Laser Wakefield Acceleration in the GeV Regime using Optically-Induced Shock Injection

Katinka von Grafenstein

München 2024

Laser Wakefield Acceleration in the GeV Regime using Optically-Induced Shock Injection

Katinka von Grafenstein

Dissertation
an der Fakultät für Physik
der Ludwig-Maximilians-Universität
München

vorgelegt von
Katinka von Grafenstein
aus Dachau
München, den 21. August 2024

Erstgutachter: Prof. Dr. Stefan Karsch
Zweitgutachter: Prof. Dr. Matt Zepf
Tag der mündlichen Prüfung: 30. Oktober 2024

Zusammenfassung

Die Laser-Kielfeld-Beschleunigung (engl. laser wakefield acceleration (LWFA)) bietet einen enormen Vorteil gegenüber konventionellen Hochfrequenzbeschleunigern, da lasergetriebene Plasmawellen wesentlich höhere Beschleunigungsfelder aufrechterhalten können. Diese starken Felder von 100 GV/m und höher machen LWFA zu einem vielversprechenden Kandidaten für eine neue Generation von Beschleunigern mit einem deutlich kleineren Fußabdruck als herkömmliche Beschleuniger. Die LWFA-Gemeinschaft ist daher bestrebt, die erreichbaren Elektronenenergien auf Werte im Multi-GeV-Bereich zu erhöhen. Außerdem ist es erstrebenswert, die Qualität der laserbeschleunigten Elektronenstrahlen zu verbessern, indem schmale Bandbreiten, kleine Divergenzen und hohe Schuss-zu-Schuss Stabilitäten erreicht werden. Diese Eigenschaften sind für viele wichtige Anwendungen in verschiedenen Bereichen der Grundlagenforschung, Medizin und Industrie erforderlich.
Eine spannende Anwendung der von LWFA erzeugten Elektronen wird am Centre for Advanced Laser Applications (CALA) an der Ludwig-Maximilians-Universität München verfolgt: Quasi-monoenergetische Elektronenstrahlen mit einer Energie von 2.5 GeV werden in einem Bremsstrahlungstarget γ-Strahlen erzeugen, die mit einem hochintensiven Laser kollidieren werden. Bei dieser Kollision sollen durch den nichtlinearen Breit-Wheeler-Effekt Elektron-Positron-Paare im Vakuum erzeugt werden. Die Untersuchung des Quantenvakuums durch die Messung dieses fundamentalen Prozesses in einem nicht-perturbativen Regime, in dem sehr hohe Laserintensitäten verwendet werden, wird für den Bereich der Quantenelektrodynamik (QED) von großem Interesse sein, da das nicht-perturbative Regime noch nie experimentell untersucht wurde.
Die vorliegende Arbeit dient als Vorbereitung für das Breit-Wheeler-Experiment und als allgemeine Demonstration der Performance von LWFA, indem Strategien für die Erzeugung von stabilen Elektronenstrahlen im GeV Bereich mit schmaler Bandbreite und kleiner Divergenz untersucht werden. In dieser Arbeit wurden zwei Arten von Gastargets getestet: eine Gaszelle und schlitzförmige Überschalldüsen. Durch Selbstinjektion injizierte Elektronen wurden in der Gaszelle auf Energien über 2 GeV beschleunigt. Die erzeugten Elektronenstrahlen waren sehr stabil (3 % Standardabweichung der Höchstenergie) und wiesen sehr kleine Divergenzwinkel von 0.32 mrad auf. Allerdings war ihre Bandbreite 100 % ohne eindeutige quasi-monoenergetische Strukturen. Daher wurde die Schockinjektion, die häufig

zu quasi-monoenergetischen Strahlen führt, in der Gaszelle mit einem optisch induzierten Schock unter Verwendung eines Injektorstrahls getestet. In der Gaszelle konnte die Injektion am optisch induzierten Schock beobachtet werden.
Mit den schlitzförmigen Überschalldüsen wurde hauptsächlich die optisch induzierte Schockinjektion eingesetzt. Durch Variation der Länge der Schlitzdüsen und der Laserintensität wurden Elektronenstrahlen mit Cut-off-Energien zwischen $1 - 2.5\,\mathrm{GeV}$ und Ladungen zwischen $80 - 400\,\mathrm{pC}$ erzeugt. In vielen Fällen waren diese Elektronenstrahlen stabil (bis zu 7 % Standardabweichung der Höchstenergie) und wiesen eine schmale Bandbreite (ca. 10 % der Hauptenergie) und eine kleine Divergenz ($0.5 - 0.8\,\mathrm{mrad}$) auf. Zu höheren Elektronenenergien hin nahm die Stabilität im Allgemeinen ab. Es werden Vorschläge zur Verbesserung der Stabilität und zum Erreichen stabiler Elektronenstrahlen bei $2.5\,\mathrm{GeV}$ diskutiert.
Bei der Analyse der experimentellen Ergebnisse wird ein besonderer Schwerpunkt auf den Einfluss der Beschleunigungslänge auf die Elektronenenergie gelegt. Theoretische Modelle, die das 'bubble'-Regime von LWFA behandeln, sagen voraus, dass der Beschleunigungsprozess bei unseren experimentellen Parametern durch den Verbrauch der Energie des Treiberlasers (engl. depletion) begrenzt ist. Die Scans der Beschleunigungslänge durch Scans der Position des Injektorstrahls konnten mit dieser Vorhersage in Einklang gebracht werden. Mit diesen Scans konnte die optimale Beschleunigungslänge bestimmt werden, bei der die Länge der Düse mit der Länge, über die die Treiberenergie verbraucht wird, übereinstimmt. Scans der Plasmadichte wurden mit der längsten verfügbaren Schlitzdüse durchgeführt und stimmten gut mit einem theoretischen LWFA-Modell überein. Dieses Modell bestätigte, dass der Beschleunigungsprozess bei den aktuellen Parametern durch den Verbrauch der Energie des Treiberlasers begrenzt ist.
Zusätzlich wurde der Einfluss einer Änderung der Zeit zwischen dem Laserstrahl, welcher den Schock generiert, und dem Treiberlaserstrahl untersucht. Es wurde gezeigt, dass die Änderung der Zeit zwischen den beiden Laserstrahlen die Energie der Elektronenstrahlen beeinflusst. Dies lässt sich durch ein höheres Dichteverhältnis im Schock erklären, wenn der Treiberlaserstrahl nach längerer Zeit nach dem Schock-induzierenden Laserstrahl ankommt. Das höhere Dichteverhältnis im Schock führt zu einer Injektion von Elektronen weiter vorne im Laser-Kielfeld. Aufgrund des nach vorne abfallenden elektrischen Feldes im Laser-Kielfeld resultiert dies in einem geringeren erreichbaren Energiegewinn. Daher sind kleine Dichteverhältnisse in Schocks von Vorteil, um hochenergetische Elektronenstrahlen mit Schockinjektion zu erreichen. Die optische Erzeugung eines Schocks bietet so eine direkte Möglichkeit, um die Elektronenenergie einzustellen. Mithilfe dieser Methode konnten quasi-monoenergetische Elektronenstrahlen mit Energien von bis zu $2.5\,\mathrm{GeV}$ erzeugt werden, die für das geplante Breit-Wheeler-Experiment benötigt werden. Dies stellt einen wertvollen Schritt zur Realisierung des Breit-Wheeler-Experiments in CALA dar.

Abstract

Laser wakefield acceleration (LWFA) offers a tremendous advantage over conventional radio-frequency accelerators due to the considerably higher accelerating fields supported by laser-driven plasma waves. These ultra-strong fields of around 100 GV/m and higher are the reason why LWFA is a promising candidate for advanced accelerators with a significantly smaller footprint than conventional accelerators. Therefore, the LWFA community seeks to push the boundaries of electron energies towards values in the multi-GeV regime. At the same time, it is desirable to improve the quality of laser-accelerated electron bunches by achieving small bandwidths, small divergence angles, and high shot-to-shot stability. These properties are required for many important applications in fundamental research, medicine, and industry.

One exciting application of LWFA-generated electrons is pursued at the Centre for Advanced Laser Applications (CALA) at the Ludwig-Maximilians-Universität München: Quasi-monoenergetic beams at 2.5 GeV will generate γ-rays in a high-Z target via bremsstrahlung. Subsequently, the γ-rays will collide with a high-intensity laser. This collision should create electron-positron pairs from the vacuum via the nonlinear Breit-Wheeler effect. Probing the quantum vacuum by measuring this fundamental process in a non-perturbative regime using very high laser intensities will be highly interesting for the quantum electrodynamics (QED) community since the non-perturbative regime has never been investigated in experiments.

This thesis serves as a preparation for the Breit-Wheeler experiment, as well as a general demonstration of the LWFA performance, by exploring and demonstrating strategies for the generation of stable electron bunches in the GeV regime with low bandwidth and divergence. In this work, two types of gas targets were tested: a gas cell and various supersonic, slit-shaped nozzles. Using the gas cell, electrons injected via self-injection were accelerated to energies above 2 GeV. These beams were very stable (3 % standard deviation of the cut-off energy) and showed very small divergence angles of 0.32 mrad. However, they exhibited bandwidths of 100 % without clear quasi-monoenergetic features. Therefore, shock injection, which often yields quasi-monoenergetic beams, was tested in the gas cell with an optically-induced shock injection scheme using an injector beam. In the gas cell, injection at the optically-induced shock could be observed.

With the slit nozzle targets, mainly optically-induced shock injection was applied. By varying the length of the slit nozzles and the laser intensity on target, electron bunches with cut-off energies between $1-2.5\,\mathrm{GeV}$ and charges between $80-400\,\mathrm{pC}$ were generated. In many cases, these bunches were stable (down to 7 % standard deviation in cut-off energy) and had a small bandwidth (around 10 % of the peak energy) and a small divergence ($0.5-0.8\,\mathrm{mrad}$). Towards higher electron energies, the stability generally decreased. Suggestions for improving stability and reaching stable electron bunches at 2.5 GeV are discussed.
In the analysis of the experimental results, a special emphasis is put on the influence of the acceleration length on the electron energy. Theoretical models covering the bubble regime of LWFA predict that the acceleration process is limited by the depletion of the driver laser at our experimental parameters. The scans of the acceleration length via scans of the position of the injector beam were consistent with this prediction. With these scans, the optimal acceleration length could be determined, for which the length of the nozzle is equal to the length over which the driver laser depletes. Scans of the plasma density were performed with the longest available slit nozzle and were in good agreement with a theoretical LWFA model. This model confirmed that the acceleration process is limited by the depletion of the driver laser for the current parameters.
Additionally, the influence of the delay between the laser beam generating the shock and the driver beam was investigated. The delay was shown to affect the energy of the electron bunches. This can be explained by an increased density ratio in the shock for the driver laser arriving with increased delay after the shock-inducing beam. The higher density ratio of the shock leads to the injection of the electrons further inside the first bubble of the wakefield. The decreasing electric field further inside the wakefield bubble leads to lower achievable energy gain. Therefore, small density ratios in shocks are beneficial for achieving high-energy electron beams with shock injection. Optically-induced shock injection thus provides a straightforward way for tuning electron energies. Using this method, quasi-monoenergetic electron beams with energies up to 2.5 GeV could be generated that are needed for the planned Breit-Wheeler experiment. This poses a valuable step towards the realization of the Breit-Wheeler experiment at CALA.

Contents

1. Introduction

1.1. Pair production in the non-perturbative regime

More than 90 years ago, in 1928, Dirac published his work on 'The quantum theory of the electron' [1]. The equation he derived in this publication for the point-charge electron in an atom suggested that the quantum vacuum contains virtual electron-positron pairs on negative energy levels. When enough energy is applied, these virtual pairs can reach positive energy levels and transform into real particles. Only a few years later, in 1934, Breit and Wheeler predicted that the collision of two highly energetic photons could supply this energy and would create electron-positron pairs from the quantum vacuum [2]. In this process, the combined energy of the two colliding photons must be larger than the rest mass of the created pairs $\hbar\omega_1\hbar\omega_2 \geq (m_e c^2)^2 \approx (511\,\mathrm{keV})^2$. Therefore, the collision of two photons with an energy of, e.g., $\hbar\omega_1 = \hbar\omega_2 = 511\,\mathrm{keV}$ is needed for the linear Breit-Wheeler process to occur. Due to its very low cross-section, this linear process has never been experimentally observed and is still very difficult to achieve since it requires the collision of two very bright γ-ray beams.
Instead of colliding two photons of the same energy, the process could also occur asymmetrically with two photons of different energy. When using, e.g., a laser photon of a commonly used Ti:Sa laser with an energy of $\hbar\omega_0 \approx 1.55\,\mathrm{eV}$, the consequently needed energy of a γ-ray photon would be $\hbar\omega_\gamma \approx 168\,\mathrm{GeV}$. However, this value exceeds the γ-ray energies available so far in the laboratory.
However, similar to ionization processes, the Breit-Wheeler effect can also occur via a non-linear, multi-photon mechanism [3, 4]. In the analogy to atomic ionization, the linear Breit-Wheeler process corresponds to the photoelectric effect, while the non-linear Breit-Wheeler process corresponds to multi-photon ionization.
For the latter, a relativistic γ-ray photon can interact simultaneously with several photons from an electromagnetic field. Then, the energy threshold is overcome with $n\hbar\omega_0\hbar\omega_\gamma \geq (m_e c^2)^2$. This multi-photon process plays an important role in astrophysical phenomena [5, 6] such as the pair creation in the vicinity of black holes [7] and magnetars [8] and the absorption of high-energy photons in the universe [9].
When several laser photons are used, the needed energy of the γ-ray photon is smaller and can reach energies that are available in the laboratory, e.g., at large

accelerator facilities, such as the Stanford Linear Accelerator Center (SLAC). The non-linear Breit-Wheeler effect was first probed at SLAC in 1996 [10, 11]. A 47 GeV electron beam from the linear accelerator at SLAC collided with a focused laser beam. γ-rays with a maximum energy of 29 GeV were generated via Thomson scattering and interacted with approximately four laser photons of the intense laser field to create electron-positron pairs. This experiment occurred in the perturbative regime [12] with the laser strength parameter $a_0 \lesssim 1$.
For $a_0 \gg 1$, the process reaches the non-perturbative regime [13]. Using an ultra-intense laser field with $a_0 \gg 1$ results in the γ-photon interacting with $n \gg 1$ laser photons. Consequently, the laser intensity must be higher for this process to occur, but the γ-ray energy can be smaller than in the SLAC experiment and can be reached more easily.
The non-perturbative Breit-Wheeler process can be viewed as a combination of the two mechanisms for pair production from vacuum: the Breit-Wheeler and the Schwinger mechanisms. The pure Schwinger mechanism is analogous to barrier suppression ionization (BSI), where the binding potential is distorted, allowing electrons to escape spontaneously. For pair creation via the Schwinger mechanism, a field strong enough to perform the pair creation work over one Compton wavelength $\lambda_c = \hbar/(m_e c)$ is needed. This is the Schwinger critical field $E_S = m_e c^2/(e\lambda_c) = m_e^2 c^3/e\hbar \approx 1.3 \cdot 10^{18}\,\mathrm{V/m}$ [14], which corresponds to the intensity of an electromagnetic field of approximately $10^{29}\,\mathrm{W/cm^2}$. However, this field is not directly reachable with current laser technology. Therefore, the pure Schwinger mechanism is far from being observable in the laboratory.
The non-perturbative Breit-Wheeler process, on the other hand, is reachable with laser intensities of around $10^{22}\,\mathrm{W/cm^2}$ since the collision of a relativistic γ-photon with an electromagnetic field results in the boosted field of the laser in the co-moving frame of $E_* = \left(2\hbar\omega_\gamma/m_e c^2\right) \cdot E$, with E the field of the laser in the lab frame. Thus, the boosted field E_* can reach $E_* \approx E_S$, and the barrier between negative and positive energies is distorted. As a consequence, the virtual particles can either tunnel through the barrier to positive energy levels (analogous to tunnel ionization) for $X_\gamma = E_*/E_S < 1$ or spontaneously escape as for the pure Schwinger mechanism for $X_\gamma > 1$. The probability of this non-perturbative Breit-Wheeler effect is either exponentially suppressed, as typical for tunneling processes, with $P \sim \exp\left(-\frac{8}{3X_\gamma}\right)$ for $X_\gamma < 1$ or scales exponentially with $P \sim X_\gamma^{2/3}$ for $X_\gamma > 1$ [3].
The non-perturbative Breit-Wheeler regime, which has not been probed yet, is of particular interest to the quantum electrodynamics (QED) community: The theory of QED in the weak-field regime, where perturbation theory can be applied, has been tested and verified thoroughly in experiments [15]. The theory can be visualized with Feynman diagrams [16], which facilitates complicated calculations. However, when reaching the non-perturbative regime in very strong fields, expansion in a_0 is no longer possible, and an infinite sum of Feynman diagrams would

be needed [17]. Therefore, more exact considerations are needed: For this regime, the Furry picture [18] was invented for evaluating strong-field problems, where the field is divided into a weak field that can be treated perturbatively and a strong field that is treated classically. However, this theory covering the non-perturbative regime has never been experimentally verified. It is unknown whether the QED theory is valid in the strong-field regime. If it is not valid in the strong-field regime, a more fundamental theory, which is generally valid, might exist [19, 20]. Therefore, it would be of great interest to check the validity of QED theory in the strong-field regime in experiments [21, 22]. This goal is now within reach, as the non-perturbative Breit-Wheeler regime is nowadays accessible with PW-class lasers.

1.2. The Breit-Wheeler experiment at CALA

Joining the effort to probe the quantum vacuum and test QED theory in the strong-field regime, a Breit-Wheeler experiment is in preparation at the Centre for Advanced Laser Applications (CALA) at the Ludwig-Maximilians-Universität München. The experiment aims at measuring electron-positron pairs created via the Breit-Wheeler effect in the non-perturbative regime [3, 23]. A scheme of the planned experiment is shown in Figure 1.1. Laser pulses from the ATLAS-3000 PW-class Ti:Sa laser system at CALA will be tightly focused to generate the high-intensity field with $a_0 \gg 1$ that interacts with γ-rays to create electron-positron pairs. The γ-ray beam will be generated from a relativistic electron beam in a bremsstrahlung converter target. Bremsstrahlung results in a γ-ray beam with maximum energy at the electron bunch energy. Thus, higher γ-ray energies can be reached at fixed electron energy than by using Thomson scattering, as used in the experiment in 1996 at SLAC. In the experiment at CALA, a magnetic field will be used to deflect the relativistic electron beam after the bremsstrahlung converter, such that the collision zone will be free from all particles. Thus, the Breit-Wheeler process can be measured without any competing processes [3].
A vital issue for a successful experiment is to measure the created pairs against a background of radiation, creating secondary pairs in any material on its path. Therefore, the signal-to-noise ratio must be maximized. Extensive studies have been deployed to build a highly sensitive detector system with elaborate shielding [6, 24] and to design the experiment to maximize pair yield while minimizing background [3]. According to this design, the electron beams must fulfill specific requirements to maximize the signal-to-noise ratio, which will be discussed in the following paragraphs.
The pair yield increases with increasing γ-ray energy and, thus, electron energy. However, reaching for the highest possible electron energies also exhibits drawbacks

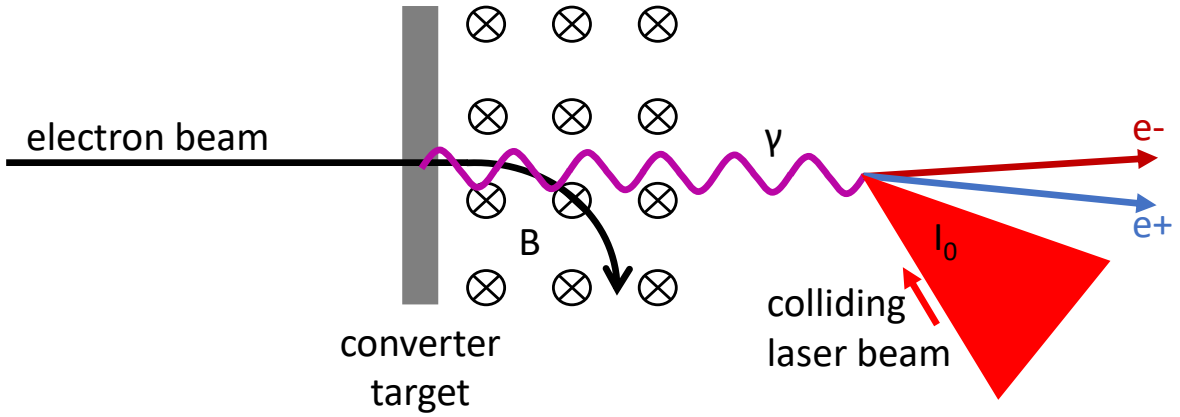

Figure 1.1.: Schematic of the Breit-Wheeler experiment planned at CALA, adapted from [25]. A relativistic electron beam generates γ-rays in a bremsstrahlung converter target. The primary electron beam is deflected in a magnetic field. The γ-ray beam collides with a tightly focused high-intensity laser. The collision generates electron-positron pairs via the nonlinear Breit-Wheeler effect in the non-perturbative regime.

since the primary electron beam has to be deflected before the collision point. At a fixed magnet strength available at CALA (0.85 T), the magnet has to have a certain length to deflect high-energy electrons sufficiently. Due to the divergence of the γ-ray beam, a longer distance to the collision point implies a decrease in γ-ray photons in the interaction region with the laser focus and, therefore, a decrease in pair yield. The result is a trade-off between electron energy and magnet length. A design point of 2.5 GeV electrons with a 60 cm long magnet was chosen [3]. As the divergence of the electron beam contributes to the divergence of the γ-beam, the electrons should exhibit the lowest possible divergence to minimize the divergence of the γ-beam and thus maximize the pair yield.
The pair yield also increases with higher charge in the electron beam — however, so does the background. Therefore, a moderate charge in the electron beam might be favorable in comparison to maximizing the beam charge at the expense of the beam quality. Charge at significantly lower energies than the desired 2.5 GeV would contribute to the background but not the creation of pairs. Therefore, quasi-monoenergetic beams at 2.5 GeV are required, containing a charge between $10 - 100$ pC.
Finally, the bunches' reproducibility and shot-to-shot stability are crucial for achieving statistically significant measurements of the pair-creation process within a reasonable time frame.
All considerations described above result in the goal of stable, quasi-monoenergetic electron beams with approximately tens of pC of charge at an energy of 2.5 GeV with the lowest possible divergence.
Such beams are available at conventional radio-frequency (RF) accelerator facili-

ties. However, access to these facilities is limited, and a high-intensity PW-class laser has to be accessible in the same laboratory. As an alternative, a new accelerator concept driven by a high-intensity laser, as available at CALA, could generate the needed electron beams: laser wakefield acceleration.

1.3. Laser wakefield acceleration

Laser wakefield acceleration (LWFA) was first suggested by Tajima and Dawson in 1979 [26]: The electric fields in plasma waves driven by high-intensity lasers could be used to accelerate electrons. The needed laser intensities came within reach when chirped-pulse amplification (CPA) [27] was invented a few years later in 1985. This technique was awarded the Nobel Prize in Physics in 2018 [28] since it facilitated lasers to become orders of magnitude more intense than what was achievable before using CPA. Reaching these intensities with lasers paved the way for many new research fields, such as generating attosecond pulses [29, 30] via high-harmonic generation (HHG). For this, another Nobel Prize in Physics was awarded in 2023 [31], as these ultra-short pulses can be used to investigate electron dynamics in matter on the attosecond level.
LWFA poses another exciting research field that was realized with the high-intensity laser pulses generated via the CPA method.

1.3.1. LWFA and its motivation

The new research field of LWFA is particularly intriguing due to the fact that the accelerating gradients in plasma waves can be orders of magnitude larger than in conventional RF accelerators, where material breakdown [32] limits the electric fields. As plasma is already a fully ionized state of matter, material breakdown is not an issue, and very high electric fields can be supported. Therefore, acceleration gradients of around 100 GV/m at plasma densities of around $10^{18}\,\mathrm{cm}^{-3}$ can accelerate electrons to the GeV level over only a few centimeters [26, 33–35].
This capability is the reason why LWFA could be the novel accelerator concept that enables a new generation of electron accelerators. The largest electron accelerator so far has been the LEP2 at CERN, reaching electron energies of 104.5 GeV per beam [36]. Plans exist for new accelerators in the Geneva region: the Future Circular Collider (FFC), a 100 km long ring for 350 GeV per beam [36] and the Compact Linear Collider (CLIC), a 50 km long linear accelerator for 3 TeV per beam [37]. Losses due to synchrotron radiation for circular accelerators and maximum available gradients due to material breakdown for linear accelerators drive the need to go to larger accelerator structures when acceleration to higher energies is needed. For now, the largest conventional accelerator to date is the Large

Hadron Collider (LHC), which is a 27 km long ring and reaches energies of 7 TeV per beam [38] - a hadron collider, where synchrotron losses are negligible. This large machine made the discovery of the Higgs particle possible [39, 40]. The FFC is planned as a Higgs factory and for high-precision measurements of other fundamental particles. However, the planned accelerators in the Geneva region could be the limit using RF technology both in feasible maximum gradient of RF structures as well as size of the accelerators supported by society regarding space and cost of these large facilities. Therefore, plasma accelerators, with their much higher accelerating gradients, are the subject of research in many groups worldwide to increase the availability of less space- and cost-consuming accelerators.
Even though LWFA still lags behind conventional accelerators regarding the energy, luminosity, quality, and stability of accelerated bunches, the community has made much progress, reaching nearly 8 GeV in one accelerator stage [41], sub-percent energy spreads [42] and under 3 % energy stability over 100 000 shots [43], albeit not all at the same time. Additionally, staging concepts of 10 GeV-stages were proposed to reach energies in the TeV regime [44].
However, the LWFA community can also achieve other important goals: Very short [45] electron bunches from LWFA can generate light pulses via inverse Compton scattering [46] (also called Thomson scattering in the Thomson limit), betatron radiation [47], bremsstrahlung using high-Z targets, undulator radiation [42] and coherent transition radiation (CTR) in the THz regime [48]. There are several possible applications for these very short pulses of radiation in different areas [49]. Biological and medical applications include X-ray diffraction experiments, medical isotope production using photofission, and diagnostic radiology using imaging techniques like computed tomography and X-ray phase contrast imaging. The latter has already been demonstrated with biological samples using betatron radiation from LWFA [50, 51]. In industry, light sources generated with LWFA could be used for γ-ray radiography for non-destructive inspections, which has been shown using inverse Compton scattering [52] and bremsstrahlung from LWFA [53]. Inverse Compton scattering sources could also be used to detect radioactive isotopes with nuclear resonance fluorescence and for phototransmutation [54] for nuclear waste disposal. Another application could be backscattered inspection [49, 55] for the detection of explosives and drugs. In condensed matter and high energy density science, radiography could probe phase transitions using ultra-fast crystallography [56] or investigate shocks for fusion research using X-ray phase contrast imaging [57], taking advantage of the ultra-fast nature of light sources generated with LWFA. Since X-rays generated from LWFA are intrinsically synchronized with a laser beam, they are also ideal for time-resolved pump-probe absorption [58] or diffraction [59] experiments.
Many of these applications would benefit from the micron-level source size and ultra-fast nature of the radiation generated from LWFA to achieve high spatial

and temporal resolution.
Most of these applications can also be realized at large synchrotron and X-ray free electron laser (XFEL) facilities. However, due to their size and cost, less than a hundred synchrotrons [60] and only a hand-full XFELs driven by conventional accelerators [61–67] exist so far or are in commissioning. This makes access highly competitive and limits applications primarily to scientific research. As LWFA matures, more universities and laboratories are now operating, constructing, or planning for PW-class lasers based on ND:glass, Ti:Sa, or OPCPA technologies, and already more than 50 facilities operate or construct one or more PW-class laser systems [68, 69]. Therefore, LWFA-driven light sources could make many applications more accessible, increase the academic output in different scientific areas, and make industrial applications possible. Additionally, LWFA exceeds synchrotrons regarding temporal and spatial resolution since it offers shorter X-ray pulses from smaller source sizes and with generally higher photon energies [70] than those available at synchrotrons.
Furthermore, electron beams accelerated via LWFA with sub-percent bandwidths could be used to drive XFELs. The sub-percent bandwidth of the electron bunches is a prerequisite for driving an XFEL, as a spread in the electron beam energy would prevent the electrons in the FEL undulator structure from microbunching, which is necessary for achieving FEL gain. Recently, first works towards this goal have been achieved by Wang et al. [42] and Labat et al. [71], who observed FEL gain using LWFA-driven electron bunches. If LWFA-driven XFELs would increase the number of XFELs worldwide significantly, even applications in energy storage could be possible, as XFELs could be used to release energy stored in nuclear isomers via nuclear excitation by electron capture [49].
Over the last decades, considerable progress has been made with LWFA to achieve electron bunches suitable for the abovementioned applications. Electron energies [41, 72] and charge levels [73, 74] have been pushed to the GeV- and nC-levels. The quality of accelerated bunches has significantly been improved: Sub-percent energy spreads [42] have been reached, and a stability in electron energy of 2.4 % over 100 000 shots has been achieved [43]. However, reliably combining these separate goals is still an ongoing effort in the community. Stable, quasi-monoenergetic beams at a wide range of energies and charges would significantly increase LWFA's usability as the next generation of accelerators for various applications.
Specifically, achieving high-quality beams at high energies with LWFA could enable mid-scale facilities such as CALA to also conduct fundamental experiments probing the quantum vacuum, such as the above-described pair-production experiments. For the planned Breit-Wheeler experiment at CALA, a specific combination of requirements for electron beams was identified (cf. Section 1.2): stable, quasi-monoenergetic beams with $10 - 100\,\mathrm{pC}$ of charge at an energy of $2.5\,\mathrm{GeV}$ with the lowest possible divergence. The following section will investigate whether such

beams have already been achieved using LWFA.

1.3.2. Achievements of LWFA

To gain an overview of the performance of electron beams achieved with LWFA so far, different parameters of electron beams accelerated with LWFA in the last 20 years are plotted in Figure 1.2. As quasi-monoenergetic beams are desired for the Breit-Wheeler experiment, only data from publications where quasi-monoenergetic features were observed are plotted here, beginning in 2004, when the first quasi-monoenergetic beams from LWFA were generated [75–77]. In each plot of Figure 1.2, the charge in the highest-energy quasi-monoenergetic feature of the electron beams is plotted versus their peak energy. The color code stands for the achieved bandwidth (Figure 1.2a), the divergence (Figure 1.2b), and the stability in electron energy (Figure 1.2c) of this electron beam feature, respectively. It has to be noted that this definition provides only a loose prerequisite for the usability of these electron beams for the Breit-Wheeler experiment as it does not exclude beams with a high-energy quasi-monoenergetic peak but with possibly other features with non-negligible charge at lower energies. Such beams would not be ideal for the Breit-Wheeler experiment as discussed in Section 1.2.
From all plots, it can be seen that many publications show data with electron energies below 1 GeV. At these energies, many different charge levels have been achieved, reaching up to several hundred pC. However, not many publications have reached energies over 1 GeV with quasi-monoenergetic features. Quasi-monoenergetic features at energies above 2 GeV, as required for the Breit-Wheeler experiment, have only been published a few times (to the best knowledge of the author).
Regarding energy bandwidth, shown in color code in Figure 1.2a, very small bandwidths below 5 % have been reached for energies around and below 1 GeV. For energies above 2 GeV, the bandwidth of electron beams is slightly higher (between 5 and 15 %).
In Figure 1.2b, the color code depicts the divergence of the electron beams. Here, divergence angles below 1 mrad are frequently achieved for electron energies above 100 MeV. At high energies above 2 GeV, the divergence is below 2 mrad for almost all publications.
Figure 1.2c shows the energy stability of electron beams in publications where this quantity was quoted. Around and below 1 GeV energy stabilities below 10 % were frequently reached. However, for energies above 2 GeV, most publications do not quote the stability of the electron energy or the stability was above 10 %, which could indicate that achieving good energy stability is still difficult at high energies.
These plots show that small bandwidths below 10 %, small divergence angles below 2 mrad, or stable beams with an energy stability below 10 %, as needed for the Breit-Wheeler experiment, have separately been achieved frequently with

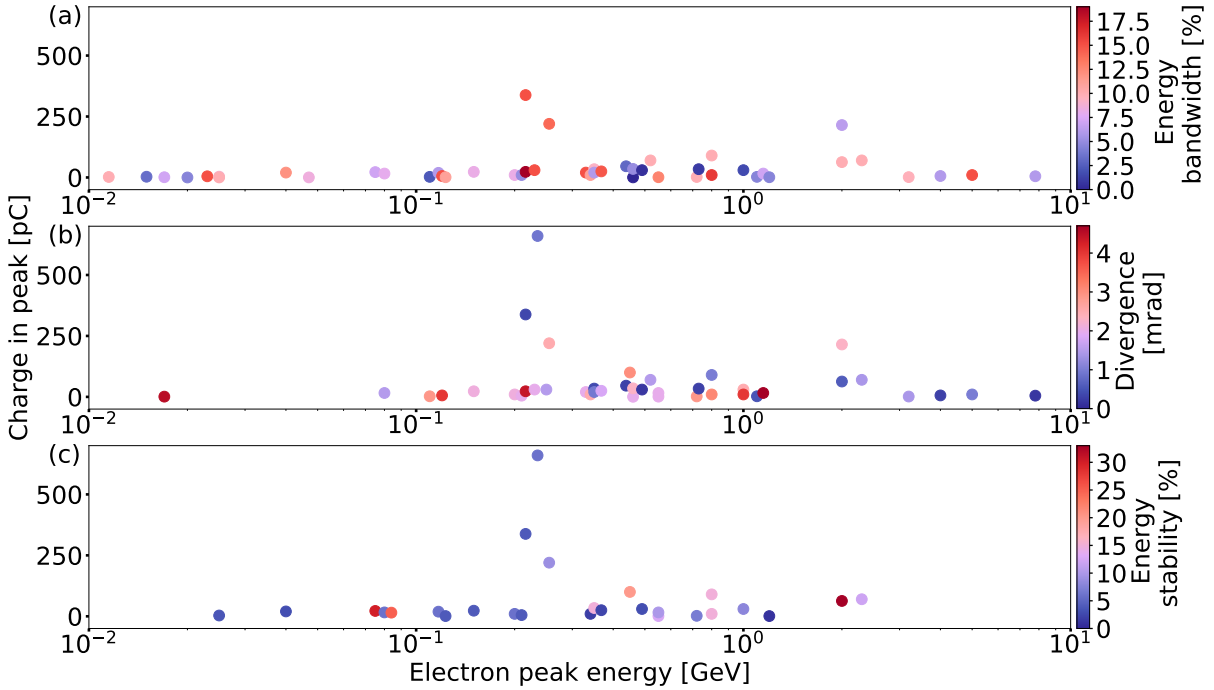

Figure 1.2.: Performance of electrons accelerated via LWFA in roughly 50 publications of the years between 2004 - 2023 [34, 35, 41–43, 45, 72–75, 78–119]. This collection only contains publications in which quasi-monoenergetic features were observed, and the peak energy as well as the charge in the peak were quoted. The peak energy is plotted against the charge in the peak for all three panels. The color code in each panel stands for different electron qualities (**(a)** energy bandwidth, **(b)** divergence, **(c)** energy stability). If a certain metric is not specified in one of the referenced publications or quoted values were larger than 20 % for energy bandwidth or larger than 5 mrad for divergence, the data point is omitted in the respective panel.

LWFA. However, all of these requirements have rarely been accomplished simultaneously. Especially small bandwidths and good energy stabilities have not often been achieved at high energies.

As energies above 2 GeV are required for the Breit-Wheeler experiment, we can take a closer look at the corresponding publications [34, 41, 72, 99, 103, 109, 115]: for most of the electron beams in these publications, the charge is at the lower limit (10 pC or lower) of what is required for the Breit-Wheeler experiment. Also, most of these publications did not specify a value for the stability of the energy for several consecutive shots. Only one publication by Kim et al. [103] seems to get close to combining all requirements for the Breit-Wheeler experiment (peak energy 2.3 GeV ± 12 %, bandwidth 10 %, charge 70 pC, divergence 1.4 mrad). Evidently, the requirements for the Breit-Wheeler experiment are achievable with LWFA, but accomplishing them simultaneously is still a challenge. Also, in Kim et al.'s publication, the peak at 2.3 GeV was rather a quasi-monoenergetic feature with non-negligible remaining charge at lower energies. For the Breit-Wheeler experi-

ment, a distinct quasi-monoenergetic peak at 2.5 GeV with only a small background of charge at lower energies would be desirable.
This work will discuss the first steps towards generating stable, quasi-monoenergetic electron beams with approximately tens of pC of charge at an energy of 2.5 GeV with low divergence at CALA. Energies in that regime or higher have either been accomplished by applying external guiding structures such as capillaries [41, 99, 109] or HOFI-channels [72] or by using PW-class lasers [34, 103, 115]. As the ATLAS-3000 laser at CALA is a PW system, this work did not employ a guiding structure since it proved to be difficult to implement a guiding structure without pointing stabilization of the drive laser, which has not yet been implemented at the ATLAS-3000. Additionally, the setup for the Breit-Wheeler experiment with collimators, the bremsstrahlung target, the magnet to deflect the electron beam, and the collider beamline [3] is complex, and a guiding structure would complicate the setup further.
To achieve the beams required for the Breit-Wheeler experiment, different gas targets - a gas cell and supersonic gas jets - have been tested in this work, using different laser energies on target and focusing geometries of the LWFA driver laser. As shock injection is often used for the controlled and stable acceleration of quasi-monoenergetic beams [42, 120], an optically-induced shock injection scheme has been investigated, which can be used in both gas cells and gas jets. Using this method in supersonic gas jets, quasi-monoenergetic electron beams with energies up to 2.5 GeV could be generated.
These experiments have been performed with the full beam from the ATLAS-3000 laser system to investigate the fundamental requirements on laser energy and target length for the required 2.5 GeV electron beams. However, these studies will have to be continued using only part of the laser beam from the ATLAS-3000, e.g., a ring beam, with a significant part picked from the center to act as the collider beam in the Breit-Wheeler experiment. While the energy from the ATLAS-3000 can be increased to compensate for the picked collider beam, it will have to be investigated whether the ring beam configuration can also yield high-quality electron bunches at 2.5 GeV.

1.4. Thesis structure

The remainder of this work is structured as follows:

Chapter 2:

Introduction to the basic principles of LWFA.

Chapter 3:

Description of the experimental setup at CALA, including those components that are relevant to this work. Special attention is given to the design of slit nozzles as LWFA targets and optically-induced shock injection.

Chapter 4:

Description of LWFA experiments performed with a gas cell target in combination with self-injection and optically-induced shock injection. Discussion of the experimental results with regard to the requirements of the Breit-Wheeler experiment.

Chapter 5:

Description of three experiments with different slit nozzles, laser parameters, plasma densities, and injector properties. Discussion of the respective results, particularly regarding the acceleration limits in each case. Comparison of the electron performance achieved in this work to reports in the literature.

Chapter 6:

Review of the experiments discussed in chapters 4 and 5, respectively. Evaluation of the current status and the required next steps in the context of the Breit-Wheeler project.

2. Theoretical Framework

In this work, LWFA is used to accelerate electrons to GeV energies. In LWFA, an intense laser pulse propagates through a gas, generates a plasma, and drives a plasma wave in its wake. In this plasma wave, high electric fields are sustained that can accelerate electrons to high energies. This chapter will give a short overview of the physics behind LWFA, starting with the description of laser pulses and their interaction with matter, specifically plasma. Subsequently, the generation of plasma waves and the injection of electrons into the accelerating fields of plasma waves will be introduced. Finally, the fundamental limits of the acceleration process will be discussed. Most information in this chapter can be found in standard textbooks about electrodynamics, laser physics, plasma physics, and laser-plasma interactions (e.g., [121–125]).

2.1. Laser light

The driving force of a laser-wakefield accelerator is an intense laser pulse, which interacts with a plasma. To describe this process, we can start with a general description of an electromagnetic field interacting with matter. This interaction is governed by Maxwell's equations [121, 122]

$$\nabla \times \mathbf{B} = \frac{1}{c^2}\partial_t \mathbf{E} + \mu_0 \mathbf{J}, \tag{2.1a}$$

$$\nabla \times \mathbf{E} = -\partial_t \mathbf{B}, \tag{2.1b}$$

$$\nabla \cdot \mathbf{E} = \frac{\rho_e}{\epsilon_0}, \tag{2.1c}$$

$$\nabla \cdot \mathbf{B} = 0, \tag{2.1d}$$

where $\mathbf{B}$ and $\mathbf{E}$ are the electric and magnetic field, respectively. c is the speed of light in vacuum, ρ_e the charge density, and $\mathbf{J}$ the current density. ϵ_0 and μ_0 are the vacuum permittivity and permeability, respectively, which are connected to the speed of light via $c^2 = (\mu_0 \epsilon_0)^{-1}$. When describing the interaction of light

with matter, it can be useful to write Maxwell's equations in terms of the vector potential $\mathbf{A}$ and the scalar potential Φ:

$$\mathbf{B} = \nabla \times \mathbf{A}, \tag{2.2}$$

$$\mathbf{E} = -\partial_t \mathbf{A} - \nabla\Phi. \tag{2.3}$$

Inserting these in Equations 2.1a and 2.1c, using the vector identity $\nabla \times (\nabla \times \mathbf{A}) = \nabla(\nabla \cdot \mathbf{A}) - \nabla^2\mathbf{A}$ and applying the Lorenz gauge $\nabla \cdot \mathbf{A} = -\frac{1}{c^2}\partial_t\Phi$, gives the following wave equations for the two potentials:

$$\frac{1}{c^2}\partial_t^2\Phi - \nabla^2\Phi = \frac{\rho_e}{\epsilon_0}, \tag{2.4}$$

$$\frac{1}{c^2}\partial_t^2\mathbf{A} - \nabla^2\mathbf{A} = \mu_0\mathbf{J}. \tag{2.5}$$

In the absence of matter, i.e., in vacuum, the right sides of these equations are zero, and solutions for $\mathbf{A}$ and Φ are plane waves, e.g.,

$$\Phi = 0, \tag{2.6}$$

$$\mathbf{A} = \mathbf{A}_0 \cos(\omega t - \mathbf{kr} + \varphi), \tag{2.7}$$

traveling in the direction of wave vector $\mathbf{k}$ with amplitude $\mathbf{A}_0$, frequency ω and phase φ. Here, $\mathbf{r} = (x, y, z)$ is a vector in space and t is the time. The value of $\mathbf{k}$ is $k = 2\pi/\lambda$ with λ the wavelength of the wave. The phase velocity of the wave in vacuum is $v_{ph} = \frac{\omega}{k} = c$ [122]. Using Equations 2.2 and 2.3, the magnetic and electric fields are

$$\mathbf{B} = \mathbf{k} \times \mathbf{A}_0 \sin(\omega t - \mathbf{kr} + \varphi) \tag{2.8}$$

and

$$\mathbf{E} = \mathbf{A}_0\omega \sin(\omega t - \mathbf{kr} + \varphi) \tag{2.9}$$

with the amplitude of the electric field $\mathbf{E}_0 = \mathbf{A}_0\omega$. From these equations, we can see that $|\mathbf{B}_0| = |\mathbf{E}_0|/c$. The Poynting vector

$$\mathbf{S} = \frac{1}{\mu_0}\mathbf{E} \times \mathbf{B} \tag{2.10}$$

represents the energy flow carried by this wave.
The intensity of the wave is then defined as the temporal average over the Poynting vector:

$$I = \langle \mathbf{S} \rangle = \epsilon_0 c^2 \langle \mathbf{E} \times \mathbf{B} \rangle = \epsilon_0 c \langle \mathbf{E}^2 \rangle = \frac{\epsilon_0 c}{2} E_0(t)^2. \tag{2.11}$$

The electromagnetic fields used for LWFA in this work do not appear in the idealized form of plane waves in space and time but as linear superpositions of an infinite number of plane waves with different frequencies and k-vector orientations, forming beams and pulses. The amplitude of the electric field of a temporal pulse is then the Fourier transform of the spectral amplitude:

$$E_0(t) = FT(E_0(\omega)) = \frac{1}{\sqrt{2\pi}} \int_{-\infty}^{\infty} d\omega E_0(\omega) \cdot e^{i\omega t}. \tag{2.12}$$

For a Gaussian-shaped temporal pulse

$$E_0(t) = E_0 e^{-t^2/\tau_L^2} \tag{2.13}$$

the inverse Fourier transform to Equation (2.12) can be applied, which results in $E_0(\omega) \propto e^{-\tau_L^2 \omega^2/4} = e^{-\omega^2/\Omega_L^2}$. From this, one can obtain the time-bandwidth product for a Gaussian pulse:

$$\Delta\tau_I \cdot \frac{\Delta\omega_I}{2\pi} \approx 0.441 \tag{2.14}$$

with $\Delta\tau_I = \sqrt{2\ln 2} \cdot \tau_L$ and $\Delta\omega_I = \sqrt{2\ln 2} \cdot \Omega_L$ the FWHM widths of the temporal and spectral intensity profile, respectively. This shows that a short pulse must have a broad spectral amplitude and vice versa.
The spatial profile of a laser can often be described by a Gaussian beam, which is a solution of the wave equation in the paraxial approximation. The beam shows a Gaussian profile with axial and radial symmetry:

$$E_0(r) = E_0 e^{-r^2/w_0^2}, \tag{2.15}$$

where $r = \sqrt{x^2 + y^2}$ if the laser is assumed to travel along the z-direction. The following equation can be derived for the laser profile along z [122]:

$$E_0(r, z) = E_0 \frac{w_0}{w(z)} e^{ik(z + \frac{r^2}{2R(z)}) - i\varphi - \frac{r^2}{w(z)^2}}. \tag{2.16}$$

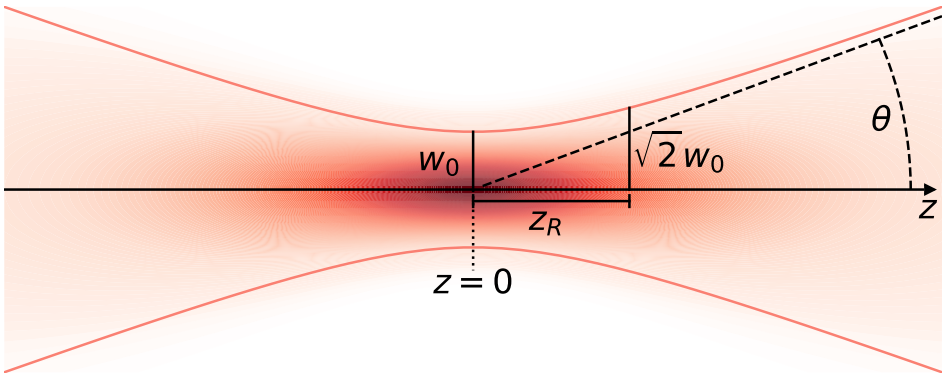

Figure 2.1.: Sketch of a Gaussian beam with waist w_0 and Rayleigh length z_R. The divergence θ of the beam is indicated for $z \gg z_R$.

Here, $R(z) = z(1 + z_R^2/z^2)$ is the radius of curvature of the wavefronts and

$$w(z) = w_0\sqrt{1 + \left(\frac{z}{z_R}\right)^2} \tag{2.17}$$

is the width of the beam, where the field is decreased by a factor of e^{-1} with respect to the on-axis field. The width of the beam at $z = 0$ is the so-called waist w_0. A sketch of a Gaussian beam is shown in Figure 2.1. The Rayleigh length is defined as $z_R = \frac{\pi w_0^2}{\lambda}$. The width of the beam at $z = z_R$ has increased to $w(z_R) = \sqrt{2}w_0$, which means that the energy fluence and, hence, the intensity through a plane at $z = z_R$ is exactly half of that in focus with $z = 0$. The divergence angle of the asymptotic beam is $\theta \approx \frac{w_0}{z_R}$.
Finally, we define the power of the laser pulse as the integral of the intensity over the area of the pulse

$$P = \iint I\,dx\,dy, \tag{2.18}$$

and the pulse energy as the integral of the intensity over the area and the length of the pulse

$$E = \iiint I\,dx\,dy\,dt. \tag{2.19}$$

2.2. Electron motion in an intense laser pulse

After describing the laser pulse that will drive the LWFA process, we go back to a plane wave to understand the basic effect of an intense electromagnetic field on a single electron. Later, considerations will be expanded to more realistic laser pulses and, subsequently, from the effect on a single electron to the effect on many electrons in a plasma.
The motion of an electron in an electromagnetic wave is described by the Lorentz equation

$$\mathbf{F} = -e(\mathbf{E} + \mathbf{v} \times \mathbf{B}), \tag{2.20}$$

where $\mathbf{F}$ is the Lorentz force acting on the electron, e is the elementary charge and $\mathbf{v}$ the velocity of the electron.
A linear polarized plane wave is assumed with a normalized vector potential of $\mathbf{a}(\omega, k) = (a_0 \cos\varphi, 0, 0)$ with $\varphi = \omega t - kz$, traveling along z and with the polarization in x-direction. a_0 is the amplitude of the normalized vector potential $\mathbf{a} = e\mathbf{A}/m_e c$, where m_e is the mass of an electron. Using Equations 2.2 and 2.3, the Lorentz equation can be written in terms of $\mathbf{a}$:

$$\mathbf{F} = m_e c \left(\partial_t \mathbf{a} - \mathbf{v} \times (\nabla \times \mathbf{a})\right). \tag{2.21}$$

Together with the energy equation

$$m_e c^2 \frac{d\gamma}{dt} = -e(\mathbf{v} \cdot \mathbf{E}), \tag{2.22}$$

where $\gamma = 1/\sqrt{1-\beta^2}$ is the Lorentz factor with $\beta = v/c$ the normalized velocity, the motion of an electron in a plane wave can be solved with the following result [125]:

$$x = \frac{c a_0}{\omega} \sin\varphi, \tag{2.23a}$$

$$y = 0, \tag{2.23b}$$

$$z = \frac{c a_0^2}{4\omega} \left[\varphi + \frac{1}{2} \sin 2\varphi\right]. \tag{2.23c}$$

From Equation (2.23a), an oscillation of the electron in x-direction following the laser phase is evident. The last part of Equation (2.23c) shows another oscillation

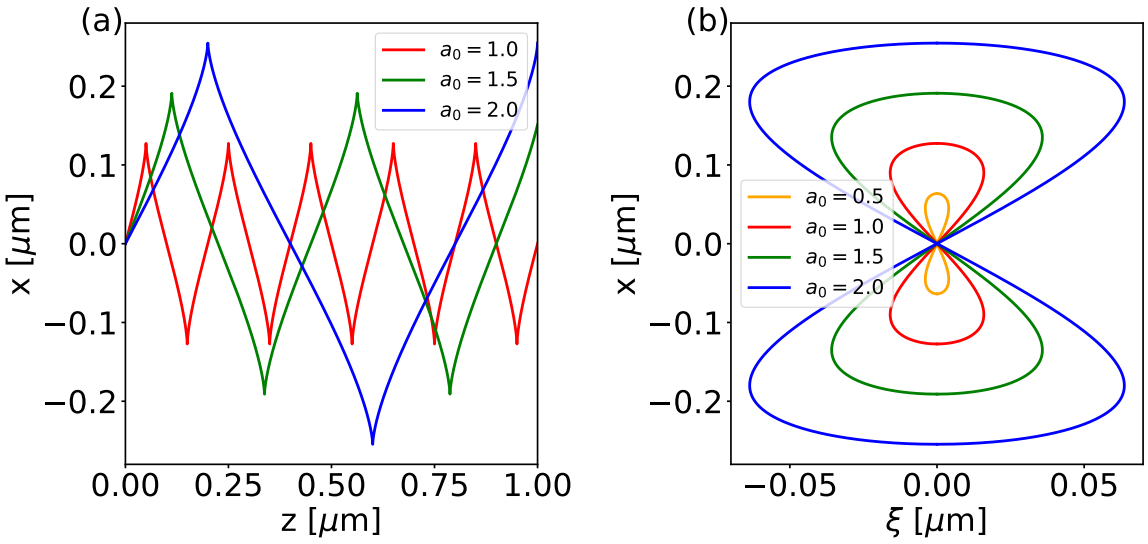

Figure 2.2.: Electron motion in a plane wave with fixed frequency for different values of a_0. **(a)** The electron motion is shown in the laboratory frame. **(b)** shows the motion in a co-moving frame.

along the laser propagation direction z with twice the laser phase, while the first part of Equation (2.23c) denotes a constant longitudinal drift. This combined motion is shown in Figure 2.2 for different values of a_0 in the laboratory frame (Figure 2.2a) and for a co-moving frame traveling along z with the co-moving variable $\xi = z - ct$ (Figure 2.2b). In the co-moving frame, the so-called figure-of-8 motion is obtained. In both plots, the increasing amplitude of the oscillation with increasing laser intensity is visible. Notably, the number of oscillations per distance in the lab frame decreases with increasing a_0. This shows that the velocity of the electron increases for increasing a_0.
If the finite pulse duration of an actual laser pulse is considered, the electron undergoes the motion described by Equation (2.23) during the interaction with the laser pulse. Once the pulse has passed, the electron returns to rest, displaced in space but without any net energy gain [125].
To complete the picture of a real laser pulse, the finite transverse extent of the laser must be considered as well. An electric field with a radial intensity dependence is assumed, and the electric field is written in a Taylor expansion considering first- and second-order terms:

$$E(x) \simeq E_0(x) \sin\varphi + x\partial_x E_0(x) \sin\varphi. \tag{2.24}$$

For simplicity, only the polarization direction x is taken into account.
Considering first the non-relativistic case for an electron velocity $v/c \ll 1$, the

equation of motion for an electron in the electric field of the focused laser reduces to

$$\partial_t v_x = -\frac{e}{m_e} E(x). \tag{2.25}$$

The solution to the lowest order using only the first-order term of Equation (2.24) is the linear term of the velocity $v_x^{(1)} = v_q \cos\varphi$, where $v_q = \frac{eE_0}{m_e\omega}$ is the electron quiver velocity and the superscript (1) denotes the first order. From this, the linear term for the position $x^{(1)} = \frac{v_q}{\omega} \sin\varphi$ can be obtained. Inserting these solutions into the second order term of Equation (2.24) and then in Equation (2.25), multiplying by m_e and averaging over one cycle $T = \frac{2\pi}{\omega}$ yields the second-order term of the equation of motion [125]:

$$m_e \langle \partial_t v_x^{(2)} \rangle = -\frac{e^2}{4m_e\omega^2} \partial_x E_0^2 \equiv F_p, \tag{2.26}$$

which is the non-relativistic ponderomotive force. As can be seen from this equation, the ponderomotive force is proportional to the gradient of the intensity of a laser field. Therefore, an electron will be pushed away from areas of high intensity, implying that an electron in a focused laser beam will drift away from the focus.
In the relativistic case, the **B**-field in the equation of motion has to be taken into account, and after a lengthy derivation (see Ref. [125]), the relativistic ponderomotive force

$$F_p = -m_e c^2 \nabla \langle \gamma \rangle \tag{2.27}$$

is obtained. Here, $\langle \gamma \rangle = \sqrt{1 + p_s^2/m_e^2c^2 + a^2/2}$ is the time-averaged relativistic factor of the electron motion, where p_s is the slow component of the electron motion. The resulting electron trajectory in a focused laser beam for both the relativistic and non-relativistic cases must be found numerically. However, it can be shown that the final kinetic energy of the electron is given by $\Delta E = (\gamma - 1) m_e c^2$ and the emission angle by $\tan\theta = \sqrt{2/(\gamma - 1)}$.
The ponderomotive force is responsible for pushing electrons in a plasma out of the way of a high-intensity focused laser beam. Thus, a charge separation between the heavier ions and the electrons in the plasma is created. This enables the generation of a plasma wave behind an intense laser pulse. In the next sections, the creation of plasma by an intense laser and basic plasma definitions will be described before the process of plasma wave generation will be addressed.

2.3. Ionization processes

In LWFA experiments, the laser usually does not interact with a preformed plasma but is sent into a neutral gas. Depending on the intensity of the laser pulse, different mechanisms [125] are responsible for the ionization of the gas atoms.
For the ionization by a single high-frequency photon via the photoelectric effect, the energy of the photon must match or surpass the binding energy of the electron $\hbar\omega = \hbar\frac{2\pi c}{\lambda} \geq E_{\text{ion}}$. If $\hbar\omega < E_{\text{ion}}$, as is the case for laser photons from a Ti:Sa laser ($\lambda = 800\,\text{nm}$; $\hbar\frac{2\pi c}{\lambda} \approx 1.55\,\text{eV}$) for ionizing hydrogen ($E_{\text{ion}} \approx 13.6\,\text{eV}$) as used in this work, the atoms cannot be ionized by absorbing a single photon. However, ionization can still take place in an intense laser pulse via multiphoton ionization (MPI), where n photons provide the energy to overcome the binding energy: $n\hbar\omega \geq E_{\text{ion}}$. With increasing intensity, the atomic binding potential is distorted in such a way that there exists a finite probability that an electron can tunnel through the Coulomb barrier. This mechanism is called tunneling ionization (TI). The Keldysh parameter [126] $\gamma_K = \omega\sqrt{\frac{2E_{\text{ion}}}{I}}$ is used to distinguish between the MPI ($\gamma_K > 1$) and the TI ($\gamma_K < 1$) regime.
If the intensity is even higher, the binding potential is distorted so strongly that the Coulomb barrier drops below the binding energy, allowing the electron to escape spontaneously. This process is known as barrier suppression ionization (BSI). The binding potential distorted by the electric field E of the laser takes the following form:

$$V(x) = -\frac{1}{4\pi\epsilon_0}\frac{Ze^2}{x} - eEx \tag{2.28}$$

with Z the atomic number. The electric field that is necessary to distort the potential sufficiently for BSI can be found by setting the maximum of the potential at $x_{\text{max}} = \sqrt{\frac{Ze}{4\pi\epsilon_o E}}$ equal to E_{ion}. This yields

$$E_{\text{BSI}} = \frac{\pi\epsilon_0 E_{\text{ion}}^2}{Ze^3}. \tag{2.29}$$

The intensity threshold for BSI can then be calculated from Equation (2.11) to be $I_{\text{BSI}} \approx 1.4 \cdot 10^{14}\,\text{W/cm}^2$ for hydrogen.
In this work, peak intensities exceeding $10^{18}\,\text{W/cm}^2$ are reached, which is four orders of magnitude above the BSI threshold. Therefore, already the foot of the laser pulse fully ionizes the hydrogen gas used in this work. As a consequence, the peak of the pulse can be assumed to interact with fully ionized gas, which forms a plasma if it fulfills a few basic plasma definitions that will be introduced in the next section.

2.4. Basic plasma definitions

A few basic plasma definitions will be given in this chapter, following Ref. [123, 124]. First, plasma is considered to be quasi-neutral, which means that oppositely charged fluids in the plasma (electrons and ions) neutralize each other. Furthermore, the charges in plasma are coupled by self-consistent electric and magnetic fields. Thereby, the charges show collective behavior. Due to this collective behavior, a perturbing point charge is shielded by a cloud of surrounding charges with a radius of the Debye length

$$\lambda_D = \sqrt{\frac{\epsilon_0 k_B T}{n_0 e^2}}, \tag{2.30}$$

where k_B is the Boltzmann constant, n_0 is the ambient electron plasma density, and T is the temperature of the electrons, which is proportional to their mean kinetic energy. This effect is called Debye shielding, which is the manifestation of collective behavior in the presence of a static electric field.
If time-dependent fields are present, e.g., when a slab of electrons is momentarily displaced from its quasi-neutral position, for example, by the ponderomotive force of an intense laser, the collective behavior will manifest itself in an oscillation of the plasma electrons. The frequency of the oscillation will be the plasma frequency

$$\omega_p = \sqrt{\frac{n_0 e^2}{\epsilon_0 m_e}}. \tag{2.31}$$

During this oscillation, an electron will travel the distance of one Debye length λ_D during one plasma period.
If an electromagnetic wave passes through a cold plasma, the interaction is governed by the dispersion relation

$$\omega^2 = \omega_p^2 + k^2 c^2. \tag{2.32}$$

Using this relation and the definition for the phase velocity of the laser $v_{ph} = \frac{\omega}{k} = \frac{c}{\eta}$, the plasma refractive index is found to be

$$\eta = \sqrt{1 - \frac{\omega_p^2}{\omega^2}}. \tag{2.33}$$

This equation implies that $\eta < 1$ for $\omega > \omega_p$ and the electromagnetic wave propagates through the plasma with a phase velocity $v_{ph} > c$ and a group velocity

$v_g = \frac{\partial\omega}{\partial k} = c\eta < c$. For $\omega < \omega_p$, η becomes imaginary, and an electromagnetic wave with frequency ω cannot propagate through the plasma and is reflected. Due to the dependence of the plasma frequency on the plasma density n_0, the two regimes, $\omega \lessgtr \omega_p$, can also be distinguished by the plasma density for a given laser frequency. This yields the critical plasma density

$$n_c = \frac{\omega^2 \epsilon_0 m_e}{e^2}. \tag{2.34}$$

For plasma densities $n_0 > n_c$, the plasma is called overdense and light cannot propagate. For $n_0 < n_c$, the plasma is in the underdense regime, and a laser with frequency ω can propagate through the plasma. For a Ti:Sa laser with a wavelength of $\lambda = 800\,\mathrm{nm}$, the critical density is $n_c \approx 1.7 \cdot 10^{21}\,\mathrm{cm}^{-3}$. The interactions between a Ti:Sa laser and plasma with plasma densities of between $10^{17}\,\mathrm{cm}^{-3}$ and $10^{18}\,\mathrm{cm}^{-3}$ used in this work therefore take place in the underdense regime.

2.5. Relativistic guiding

For interactions of an intense laser pulse with underdense plasma, relativistic effects have to be taken into account once the quiver velocity of electrons in the laser field approaches the speed of light. This is the case for laser intensities above $10^{18}\,\mathrm{W/cm}^2$, which are reached in this work. In this case, nonlinear effects, such as self-focusing [127, 128], occur. The plasma refractive index becomes dependent on the relativistic electron motion, such that Equation (2.33) changes to [129]

$$\eta(r) \simeq 1 - \frac{\omega_p^2}{2\omega^2} \frac{n_e(r)}{n_0 \gamma(r)} \tag{2.35}$$

in an underdense plasma with $\omega_p^2/\omega^2 \ll 1$. $n_e(r)$ is the local plasma electron density and $\gamma(r)$ the local relativistic factor of the electron motion. This is a more general expression for the refractive index than Equation (2.33), which also considers the effect of a local density change. This density change can either result from a modified density profile before the interaction with the main laser pulse or the main laser's ponderomotive force and generation of a plasma wave.
The leading order of the electron motion in the laser field is the transverse quiver motion with momentum $\mathbf{p}_\perp = \gamma_\perp m_e \mathbf{v}_\perp$, which is related to the normalized vector potential of the laser by $\mathbf{a} = \mathbf{p}_\perp / m_e c$. Therefore, $\gamma(r)$ can be approximated by $\gamma(r) \approx \gamma_\perp(r) = \sqrt{1 + p_\perp^2/(m_e c)^2} = \sqrt{1 + a^2(r)}$.
Inserting this into Equation (2.35) shows that for $\partial_r a^2(r) < 0$, as is the case for a Gaussian laser pulse, also $\partial_r \eta(r) < 0$. Therefore, the refractive index on-axis is

larger than off-axis, leading to the laser's phase velocity $v_{ph} = \frac{c}{\eta}$ being smaller on-axis than off-axis. This results in a curvature of the phase fronts of the laser and, thus, a focusing effect on the beam. If this relativistic self-focusing effect balances out the diffraction of the Gaussian beam, the beam can be self-guided over several Rayleigh lengths. This happens approximately at a power of [129]

$$P_c = \frac{2c}{4\pi\epsilon_0}\frac{e^2}{r_e^2}\frac{\omega^2}{\omega_p^2} \simeq 17.4\,\mathrm{GW}\left(\frac{\omega}{\omega_p}\right)^2 \tag{2.36}$$

with $r_e = e^2/(4\pi\epsilon_0 m_e c^2)$ the classical electron radius. More accurate numerical studies were conducted by Sun et al. [130]. They include the effect of the ponderomotive force of the laser, which expels electrons from the axis and creates a density channel with $\partial_r n_e(r) > 0$, leading likewise to $\partial_r \eta(r) < 0$. This effect is called ponderomotive self-channeling and reduces the critical power of self-guiding slightly to

$$P_c \approx 16.8\,\mathrm{GW}\left(\frac{\omega}{\omega_p}\right)^2. \tag{2.37}$$

A channel with $\partial_r n_e(r) > 0$ to guide a laser in a plasma can also be generated before sending the laser through the plasma. For this, a reduction of the electron density on the axis has to be reached, which can either be achieved by a discharge current in a capillary to form an approximately parabolic plasma channel [131] or another laser pulse is used that arrives before the main pulse and forms a hydrodynamic optical-field-ionized plasma channel [132].

2.6. Laser wakefield acceleration

After discussing basic properties of laser light and plasma, and the effect of intense laser fields on single electrons, we can continue with introducing the generation of plasma waves behind an intense laser beam in an underdense plasma. Due to the ponderomotive force (cf. Section 2.2), the density of plasma electrons is perturbed when an intense laser pulse is focused into plasma. The plasma ions are much heavier than the electrons and are, therefore, assumed to be stationary, acting as a neutralizing background. The density perturbation of the plasma electrons gives rise to a charge separation between the electrons and the ions, forcing the electrons back on-axis once the laser pulse has passed. Thereby, an oscillation of the plasma electrons is induced, and a plasma wave forms behind the laser. This trailing plasma wave is called a wakefield and is generated most efficiently when

the laser pulse length $L = c\Delta\tau_I$ is approximately half the plasma wavelength $\lambda_p = 2\pi c/\omega_p$ [26]. Between the plasma electrons forming the wave and the stationary ions, extremely high electric fields build both in the axial and radial directions. The axial fields can be used to accelerate electrons, while the radial fields can focus the electrons to achieve electron bunches with few-micron diameters. In this chapter, basic equations will be introduced to model laser wakefields.

2.6.1. Generation of a laser wakefield

To gain an overview of laser wakefields, we start here with the derivation of a laser wakefield in the weak field limit and will then expand to non-linear wakefields and the bubble regime, in which the wakefields used in this work can be placed. First, a wave equation for the perturbed electron density $\delta n = n_e - n_0$ of driven plasma waves in the weak field limit can be derived by using Maxwell's equations (2.1) and the Lorentz equation for electrons in a cold plasma (2.20) [125, 133]:

$$\partial_t^2 \delta n + \omega_p^2 \delta n = \frac{n_0}{2} \nabla^2 \mathbf{v}_\perp^2. \tag{2.38}$$

Here, $\mathbf{v}_\perp$ is the transverse component of the electron velocity and $\nabla = \hat{e}_r \partial_r + \hat{e}_z \partial_z$ with the laser traveling along z and r the radial component. A coordinate transformation to a co-moving frame with the laser's group velocity $v_g \simeq c$ will be applied, using the co-moving coordinates $\xi = z - ct$ and $\tau = t$. The partial derivatives transform to

$$\partial_z = \partial_\xi \tag{2.39}$$

and

$$\partial_t = \partial_\tau - c\partial_\xi \simeq -c\partial_\xi. \tag{2.40}$$

In the last step, ∂_τ was set to zero, applying the quasi-static approximation (QSA), which assumes a temporal steady state since the plasma in this coordinate system flows through a laser pulse that is only slowly varying in τ and is considered to be nearly stationary [134, 135]. This is due to the fact that only the envelope of the field contributes to the ponderomotive force as the fast oscillations are averaged out (cf. Section 2.2).
Applying the transformation to Equation (2.38) and using $\mathbf{a} = \mathbf{p}_\perp/m_e c = \mathbf{v}_\perp/c$, the wave equation for the density perturbation becomes:

$$(\partial_\xi^2 + k_p^2)\delta n = \frac{n_0}{2} \nabla^2 \mathbf{a}^2 \tag{2.41}$$

with $k_p = \omega_p/c$ the wavenumber of the plasma wave. To obtain equations for the electric field and potential of the wakefield, we use the Poisson equation

$$\nabla^2\Phi = -\nabla E = \frac{e\delta n}{\epsilon_0}, \tag{2.42}$$

which is derived from the Maxwell equations under the Coulomb gauge $\nabla \cdot \mathbf{A} = 0$, as shown in Ref. [121].
Using the Poisson equation and the definition of the plasma frequency (Equation (2.31)), the wakefield equations read [125, 134]

$$(\partial_\xi^2 + k_p^2)\Phi(r,\xi) = -k_p^2\Phi_p(r,\xi), \tag{2.43}$$

$$(\partial_\xi^2 + k_p^2)\mathbf{E}(r,\xi) = k_p^2\nabla\Phi_p(r,\xi) \tag{2.44}$$

with the ponderomotive potential $\Phi_p(r,\xi) = -(m_e c^2/2e)a^2(r,\xi)$. Both expressions describe a driven oscillator with the laser's ponderomotive potential and force as a driver, respectively.
For a laser profile with a shape

$$a\left(r,\xi\right) = \begin{cases} a_0 \sin\left(\frac{\pi\xi}{L}\right) \exp\left(-\frac{r^2}{r_I^2}\right) & \text{for } 0 \leq \xi \leq L \\ 0 & \text{otherwise} \end{cases} \tag{2.45}$$

with r_I the $1/e$-pulse width of the intensity envelope, the potential and electric field of the axial wakefield behind the pulse ($\xi < 0$) can be solved to

$$\Phi\left(r,\xi\right) = \frac{2\pi^2\Phi_{p0}(r)}{4\pi^2 - k_p^2L^2}\left[\cos k_p\left(\xi - L\right) - \cos k_p\xi\right], \tag{2.46}$$

$$E_z\left(r,\xi\right) = -\partial_\xi\Phi = \frac{2\pi^2\Phi_{p0}(r)k_p}{4\pi^2 - k_p^2L^2}\left[\sin k_p\left(\xi - L\right) - \sin k_p\xi\right] \tag{2.47}$$

with $\Phi_{p0}(r,\xi) = -(m_e c^2/2e)a_0^2 \exp\left(-\frac{2r^2}{r_I^2}\right)$. The solution within the pulse ($0 \leq \xi \leq L$) can be found in Ref. [134]. An analytical solution for a temporally Gaussian pulse shape $a(\xi) = a_0 \exp\left(-\xi^2/2L^2\right)$ also exists and can be looked up in Ref. [133]. From the solution for the potential and the electric field, the density perturbation δn can be calculated via the Poisson equation 2.42.
This derivation assumed $a_0 < 1$, which corresponds to the linear regime, and results

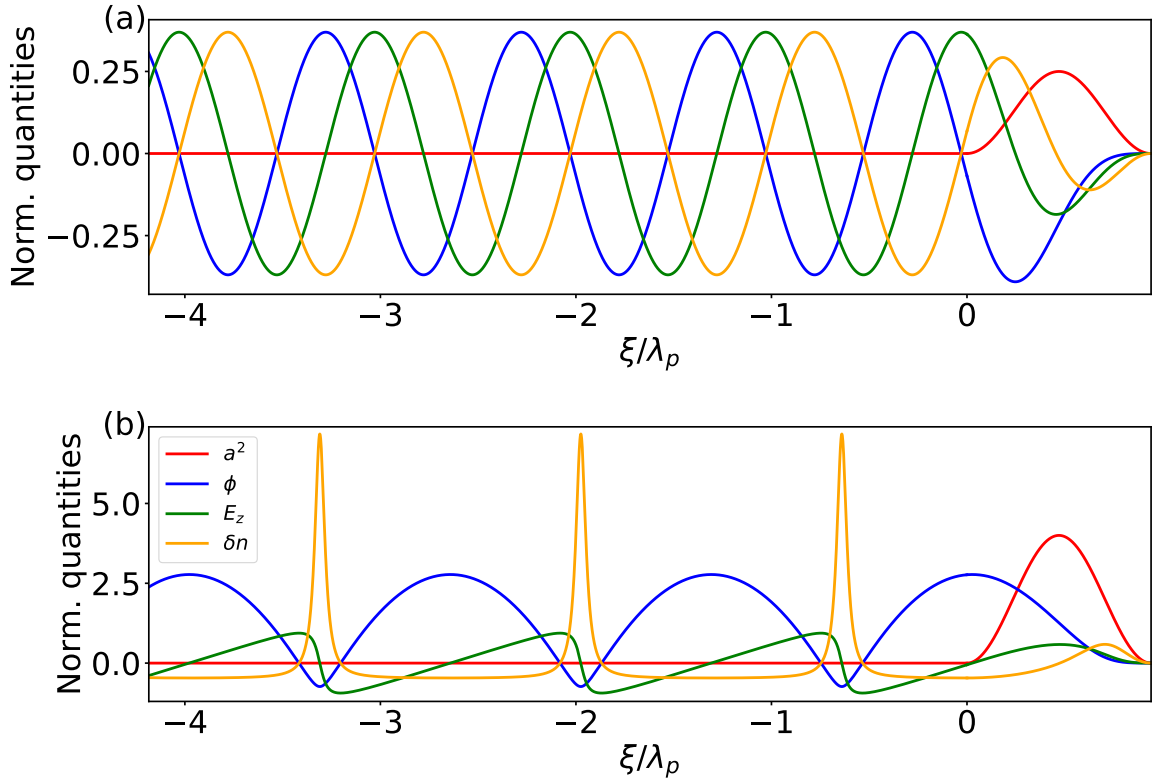

Figure 2.3.: Linear and nonlinear wakefields. **(a)** shows the wakefield potential ϕ, the axial electric field E_z, and the density perturbation δn of a linear wakefield forming behind a pulse with $a_0 = 0.5$. **(b)** The same quantities are depicted for $a_0 = 2$, resulting in a nonlinear wakefield. In both plots, the laser intensity is plotted with a^2.

in a sinusoidal wave behind the laser pulse, as depicted for the axial wakefield in Figure 2.3a. The radial wakefield is related to the axial wakefield with $\partial_\xi E_r = \partial_r E_z$. For a wakefield in the linear regime, the radial field is 90° out of phase with the axial field, such that a region of length $\lambda_p/4$ both accelerates and focuses electrons within the first wakefield trough.

2.6.2. Nonlinear wakefields

For laser intensities with $a_0 > 1$, as used in this work, nonlinear effects start distorting the wakefield from a sinusoidal form, yielding much larger electric fields, which are beneficial for the acceleration of electrons. Nonlinear wakefields can analytically only be solved in 1D and for a square laser pulse [136–138]. General equations can be derived that have to be solved numerically for arbitrary laser shapes:
Starting again from the Maxwell equations (2.1) and the Lorentz equation (2.20)

and using the definitions of the scalar and vector potentials (Equations 2.2 and 2.3), the equation for the longitudinal velocity $\beta_z = v_z/c$ of the plasma electrons in the relativistic regime can be derived, which yields [125]

$$\frac{d}{dt}(\gamma\beta_z) = c\partial_z\phi - \frac{c}{2\gamma}\partial_z\mathbf{a}^2, \tag{2.48}$$

where $\phi = e\Phi/m_e c^2$ is the normalized scalar potential.
Together with the continuity equation for the plasma electron density [135]

$$\partial_t n_e + c\partial_z(n_e\beta_z) = 0 \tag{2.49}$$

and the Poisson equation in terms of the normalized scalar potential

$$\partial_z^2\phi = k_p^2(n-1) \tag{2.50}$$

with $n = n_e/n_0$ the normalized electron density, relations between the electron velocity, density, and the wakefield potential can be derived (see Ref. [125]):
Applying a transformation to the co-moving coordinates $\xi = z - v_g t$ and $\tau = t$, as for the linear case in Section 2.6.1, now with an arbitrary group velocity of the laser v_g and setting $\partial_\tau = 0$ (see QSA in Section 2.6.1) yields [125]

$$\partial_\xi\left[\phi - \gamma\left(1 - \beta_g\beta_z\right)\right] = 0, \tag{2.51}$$

$$\partial_\xi\left[n\left(\beta_g - \beta_z\right)\right] = 0 \tag{2.52}$$

with $\beta_g = v_g/c$ the normalized group velocity of the laser.
These two equations imply that $\phi - \gamma\left(1 - \beta_g\beta_z\right) = \text{const.}$ and $n\left(\beta_g - \beta_z\right) = \text{const.}$.
Applying appropriate boundary conditions ($\phi = 0$, $\beta_z = 0$, $\gamma = 1$ and $n = 1$ in absence of a plasma wave) gives

$$n = \frac{\beta_g}{\beta_g - \beta_z}, \tag{2.53}$$

$$\phi - \gamma\left(1 - \beta_g\beta_z\right) = -1. \tag{2.54}$$

Solving for β_z and n yields

$$\beta_z = \frac{\beta_g - \Psi}{1 - \beta_g \Psi}, \tag{2.55}$$

$$n = \gamma_g^2 \beta_g \left(\frac{1}{\Psi} - \beta_g \right) \tag{2.56}$$

with $\Psi = \left(1 - \frac{1+a^2}{\gamma_g^2(1+\phi)^2}\right)^{1/2}$ and $\gamma_g = 1/\sqrt{1-\beta_g^2}$.
Inserting these equations into the Poisson equation in co-moving coordinates, we arrive at an ordinary differential equation that can be solved numerically for given pulse profiles [125]:

$$\begin{aligned} \partial_\xi^2 \phi &= k_p^2 \gamma_g^2 \left(\frac{\beta_g}{\Psi} - 1 \right) \\ &= k_p^2 \gamma_g^2 \left\{ \frac{\beta_g (1+\phi)}{[(1+\phi)^2 - \gamma_g^{-2}(1+a^2)]^{1/2}} - 1 \right\}. \end{aligned} \tag{2.57}$$

For highly underdense plasma, where $v_g \simeq c$, the differential equation is slightly simpler and is given by [135]

$$\partial_\xi^2 \phi = -\frac{k_p^2}{2} \left(1 - \frac{(1+a^2)}{(1+\phi)^2} \right). \tag{2.58}$$

Solving Equation (2.57) or Equation (2.58) numerically results in a solution for the normalized scalar potential ϕ. Then, the density can be calculated from Equation (2.56).
In Figure 2.3b, the density distribution, potential, and axial electric field are shown for a nonlinear wakefield for a laser profile as in Equation (2.45) with $a_0 = 2$. Compared to the linear wakefield in Figure 2.3a, the wave steepens, and highly peaked density oscillations form. The electric field shows a 'sawtooth' profile with nearly linear gradients between the density peaks. The plasma period lengthens from λ_p to $\lambda_{p(\mathrm{nl})} \simeq 4(c/\omega_p)\gamma_\perp$ [137]. In a nonlinear wakefield, half of the plasma period accelerates and focuses electrons, which is beneficial for accelerating high-quality electron bunches to high energies.

2.6.3. The bubble regime

In the last two sections, the generation of wakefields behind laser pulses was divided into two regimes, the linear regime for $a_0 < 1$ and the nonlinear regime for

relativistic intensities $a_0 \gtrsim 1$. Three-dimensional particle in cell (PIC) simulations have shown that for ultra-relativistic intensities ($a_0 \gg 1$), another highly nonlinear regime is reached, the so-called blow-out or bubble regime [139]. In this regime, the ultra-intense laser can expel all electrons from the first wakefield trough, and an almost spherical bubble completely void of electrons forms behind the laser. Lu et al. [140, 141] developed a model for this regime by dividing the wakefield into a blow-out region and a sheath of electrons around the cavity. Simulations show that a perfectly spherical bubble is generated for $a_0 \gtrsim 4$. However, blow-out still occurs for $2 \lesssim a_0 \lesssim 4$, and a cavity with a nearly spherical shape is built [142].
This work used laser intensities with $a_0 \gtrsim 2$. Therefore, the theory covering the bubble regime was used to analyze LWFA experiments conducted with these laser intensities in this work.
Lu et al. [140–142] estimate the bubble radius by balancing the ponderomotive force of the laser and the ion channel force since the ponderomotive force pushes electrons outward until the positively charged ions left behind in the cavity bring them to rest. This consideration results in the following equation for the bubble radius:

$$k_p R_b = 2\sqrt{a_0}. \tag{2.59}$$

Here, the factor of 2 was obtained from simulations.
Their model works well for a regime where the waist w_0 of the laser driver is matched to the radius R_b of the bubble: $w_0 \simeq R_b$. In this regime, a well-defined narrow sheath is produced, and the laser is guided without strong variations of the pulse profile. Using Equation (2.59) for the bubble radius, a matching condition for stable guiding can be formulated:

$$k_p w_0 \simeq 2\sqrt{a_0}. \tag{2.60}$$

The matching condition can also be expressed in terms of the laser power and the critical power for self-focusing (cf. Section 2.5) with

$$a_0 \simeq 2\left(\frac{P}{P_c}\right)^{1/3}. \tag{2.61}$$

In experiments with unmatched guiding conditions, the blow-out regime can still be reached since the laser beam is focused via self-focusing until it reaches the matched spot size around which it oscillates. In this case, Equation (2.61) can be used to calculate the matched value of a_0 after self-focusing.
In PIC simulations, Lu et al. determined that the axial field inside a bubble in

the blow-out regime is approximately linear, with the maximum electric field at the back of the bubble. The maximum electric field usable for the acceleration of electrons is, then, given by [142]

$$E_{z,\max} = \frac{m_e c \omega_p}{e} \sqrt{a_0}. \tag{2.62}$$

This equation shows that the acceleration fields increase for increasing plasma densities (cf. Equation (2.31)) and for increasing laser intensities. However, maximizing these quantities does not necessarily yield the highest electron energy gain as the acceleration process is limited by different factors that also depend on these quantities. These limits will be discussed in Section 2.6.5.

2.6.4. Injection mechanisms

Before electrons can get accelerated by the axial electric field of a laser wakefield, they need to be injected into the wakefield. In the experiments of this work, electrons from the surrounding plasma are injected into the wakefield. Background electrons can only be trapped in the wakefield if they gain enough momentum to 'ride the wave' - similarly to a surfer on an ocean wave. In the plasma wave, the orbit of a single electron with momentum p is determined by the Hamiltonian in the co-moving frame [129, 143]

$$H = \left(\gamma_\perp^2 + \left(\frac{p}{m_e c} \right)^2 \right)^{1/2} - \beta_p \frac{p}{m_e c} - \phi(\xi) \tag{2.63}$$

with $\gamma_\perp = \sqrt{1 + a^2}$ the transverse component of the Lorentz factor of the electron motion, $\beta_p = v_p/c$ the normalized phase velocity and $\phi(\xi)$ the normalized scalar potential of the plasma wave. The phase space (ξ, p) with the color scale showing values of the Hamiltonian is depicted in Figure 2.4b for a wakefield with $a_0 = 1.0$ and $\beta_p = 0.991$ (corresponding wakefield quantities are shown in Figure 2.4a). Trapped and untrapped electron orbits are distinguished by the separatrix in phase space

$$H_S = \frac{\gamma_\perp}{\gamma_p} - \phi_{\min}, \tag{2.64}$$

where $\gamma_p = 1/\sqrt{1 - \beta_p^2}$ and $\phi_{\min}$ is the minimum of the normalized scalar potential of the plasma wave. The separatrix is shown in black in Figure 2.4b, trapped electron orbits in red, and untrapped orbits in blue.

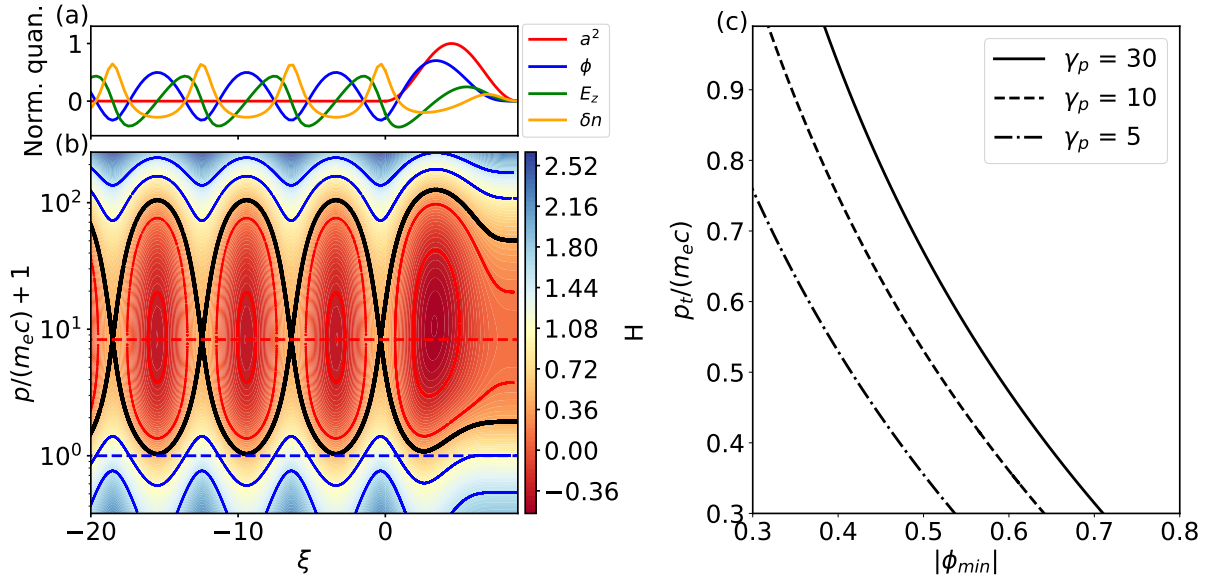

Figure 2.4.: (a) shows wakefield quantities of a nonlinear wakefield with $a_0 = 1.0$ and $\beta_p = 0.991$. **(b)** depicts the corresponding (ξ, p) phase space with the color scale showing values of the Hamiltonian. Blue solid lines show untrapped orbits of electrons, while red solid lines represent trapped orbits. The black solid line is the separatrix between trapped and untrapped orbits. The red dashed line indicates $p/m_ec = \gamma_p\beta_p$ and the blue dashed line $p = 0$. The momentum axis is shifted by $+1$ to achieve better representation on the logarithmic scale. **(c)** shows the minimum initial electron momentum for trapping against the minimum of the wakefield potential for different values of the γ_p-factor of the plasma wave.

An electron will be trapped in the wakefield if the orbit defined by an initial momentum p_t lies within the separatrix, i.e. the Hamiltonian in the absence of any fields is smaller or equal to the separatrix [129, 143]:

$$H_t = \left(1 + \left(\frac{p_t}{m_ec}\right)^2\right)^{1/2} - \beta_p \frac{p_t}{m_ec} \leq H_S. \tag{2.65}$$

By setting $H_t = H_S$, the minimum initial electron momentum for trapping is found to be [143]

$$\frac{p_t}{m_ec} = \gamma_p\beta_p(\gamma_\perp - \gamma_p\phi_{\min}) - \gamma_p[(\gamma_\perp - \gamma_p\phi_{\min})^2 - 1]^{1/2}. \tag{2.66}$$

This equation is plotted in Figure 2.4c for different values of ϕ_{min} and γ_p, assuming $\gamma_\perp = 1$. From the plot, we can see that the threshold momentum for trapping decreases with large plasma wave amplitudes (large $|\phi_{min}|$) and low plasma wave

phase velocities (small γ_p) [129]. This means that a higher laser intensity, which generates larger wave amplitudes, facilitates the trapping of electrons. Furthermore, a higher plasma density contributes to decreasing the trapping threshold since it results in a lower plasma wave phase velocity $v_p \simeq v_g = c\eta$ as the plasma refractive index η (cf. Equation (2.33)) decreases with increasing plasma frequency $\omega_p \propto \sqrt{n_0}$ (Equation (2.31)). Different mechanisms can facilitate the trapping of electrons. This section will describe mechanisms used in this work.

Self-injection

As shown above, the threshold to inject electrons into the wakefield decreases with higher plasma wave amplitudes. Electrons at the back of the wakefield trough can gain enough momentum to be injected when the wave amplitude approaches the wave-breaking amplitude, which is the maximum amplitude before the wave loses its coherence and breaks. This process is called self-injection. For a cold plasma with relativistic plasma wave phase velocities, the wave-breaking field is [125, 129]

$$E_{\mathrm{WB}} = \frac{m_e c \omega_p}{e} \sqrt{2(\gamma_p - 1)} = E_{\mathrm{WB0}} \sqrt{2(\gamma_p - 1)}, \tag{2.67}$$

with E_{WB0} the cold non-relativistic wave-breaking field [144]. The wave-breaking field is reduced in a warm plasma due to strong adiabatic heating [145]. These equations were obtained in 1D. In reality, 3D effects further reduce the limit for self-injection due to so-called transverse wave-breaking. Since a Gaussian laser pulse drives the wake stronger on the axis, the trailing plasma waves are curved, which results in the crossing of electron trajectories and the destruction of the regular structure of the wave. This transverse wave-breaking enables electrons to enter the wakefield transversely [146].
Even though self-injection poses an easy injection mechanism in LWFA experiments, it has a significant drawback: If the conditions for wave-breaking and self-injection are reached, the injection is continuous as long as these conditions are maintained, often resulting in a broadband electron energy spectrum, unfit for many applications that require small energy spreads. It has been shown that self-injection can also produce mono-energetic features [75–77]. However, they often suffer from shot-to-shot instabilities due to their sensitivity to nonlinear pulse evolution or depend on additional requirements that render independent energy or charge control difficult. In any case, self-injection is still widely used for producing high-energy electrons [41, 103] and is also used in this work for first tests of a gas cell target.
To achieve further controllability, different controlled injection methods have been

developed [129]. Methods relevant to this work will be described in the next sections.

Density down-ramp injection

Density down-ramp injection was first proposed by Bulanov et al. [147]. Here, the injection of electrons into the laser wakefield is facilitated by the manipulation of the gas profile to exhibit a down-ramp in density. At this density down-ramp, electrons can be injected into the wakefield due to a decrease of the local phase velocity of the wake. This can be understood by examining the evolution of the local phase velocity $v_p = \omega_{p,\mathrm{eff}}/k_{p,\mathrm{eff}}$ in the down-ramp [129]. The effective plasma frequency and wavenumber are defined by $\omega_{p,\mathrm{eff}} = -\partial_t \Psi$ and $k_{p,\mathrm{eff}} = \partial_z \Psi$ with the local phase of the wake $\Psi = k_p(z)\xi = k_p(z)(z - ct)$. Here, the effect of the density down-ramp on the laser's group velocity is expected to be small ($\omega_p^2/\omega^2 \ll 1$ in Equation (2.33)) in underdense plasma, so that $v_g \simeq c$ was assumed. Thus, for the local phase velocity, we arrive at

$$v_p = \frac{c}{1 + \frac{\xi}{k_p}\partial_z k_p} \simeq c\left(1 - \frac{\xi}{k_p}\partial_z k_p\right) = c\left(1 - \frac{\xi}{2n}\partial_z n\right), \tag{2.68}$$

where a Taylor expansion for a small variation was applied. Equation (2.68) shows that, behind the laser pulse ($\xi < 0$), the local phase velocity will decrease for decreasing density ($\partial_z n < 0$) in the density down-ramp. This enables the trapping of electrons when the local phase velocity approaches the velocity of the plasma electrons.

Shock injection

Shock injection [120] is a special case of density down-ramp injection. For shock injection, the injection occurs at the down-ramp of a density shock. Such a shock can, for example, be generated hydrodynamically by introducing an obstacle, e.g., a wire or a sharp razor blade made from a silicon wafer, into a supersonic gas flow. Due to the very sharp down-ramp in the density shock, the injection occurs at very small time scales and at a local injection point. In certain conditions, this local injection point can result in mono-energetic beams with very small energy spreads [42, 82, 120], which can be controlled in energy by adjusting the position of the shock in the gas target.
Often, shock injection is explained by the evolution of the wakefield bubble: From Equation (2.59), we see that the radius of the bubble in the blow-out regime is inversely dependent on $k_p = \omega_p/c$ and, thus, inversely dependent on the density

(cf. Equation (2.31)) with $R_b \propto 1/\sqrt{n_0}$. Therefore, the bubble radius is smaller at the density peak of the shock than after the shock. In the sharp density down-ramp of the shock, the bubble rapidly expands. Electrons that were at the back of the bubble at the density peak are suddenly inside the now larger bubble. As shown in the previous section for a gradual down-ramp, the local phase velocity is rapidly reduced in the down-ramp, such that the momentum of these electrons falls into the region inside the separatrix in phase space (cf. Figure 2.4), and they find themselves on trapped orbits, where the axial electric fields in the bubble can accelerate them.
Next to density down-ramp injection and shock injection, other controlled injection mechanisms such as ionization injection [35, 148, 149] and colliding pulse injection [97, 150, 151] have been developed. As these were not used in the experiments for this work, their explanation is omitted here and can be looked up in one of the above-mentioned references.

2.6.5. Acceleration limits

Once electrons are injected into the wakefield via one of the above-discussed injection mechanisms, they can be accelerated in the axial field of the wakefield. This acceleration process is then limited by several effects. These effects are mainly the depletion of the driver energy, the dephasing between the laser driver and the accelerated electrons, and the diffraction of the laser beam. These three effects will be introduced in this section.

Depletion

A fundamental limit for acceleration in a driven plasma wave is the depletion of the driver. The driver transfers its energy to the plasma wave until all its energy has depleted. Decker et al. found that the front of a laser driver erodes with an etching velocity [152]

$$v_{\mathrm{etch}} \simeq c\frac{\omega_p^2}{\omega^2}. \tag{2.69}$$

After a time t, for which $v_{\mathrm{etch}}t = L = c\Delta\tau_I$, the pulse length L of the laser is completely eroded. The length over which this happens is the depletion length L_{depl}. In highly underdense plasma with $v_g \simeq c$, the depletion length is therefore

$$L_{\mathrm{depl}} \simeq ct = c\frac{c\Delta\tau_I}{v_{\mathrm{etch}}} \simeq \frac{\omega^2}{\omega_p^2}c\Delta\tau_I. \tag{2.70}$$

For given laser parameters, the depletion length depends on the plasma density with $L_{\mathrm{depl}} \propto n_0^{-1}$ (cf. Equation (2.31)). Therefore, lower plasma densities can be used to extend the depletion length.

Dephasing

In laser-driven wakefields, another limiting factor for the acceleration of electrons is the dephasing between the electrons and the wakefield. Electrons accelerated to a few 100 MeV move with velocities exceeding $0.9999c$, while the laser's group velocity (assuming a Ti:Sa laser with $\lambda = 800\,\mathrm{nm}$) in a plasma with a density of $10^{18}\,\mathrm{cm}^{-3}$ is approximately $0.9997c$ (cf. Section 2.4). Consequently, an accelerated electron bunch catches up with the laser until it reaches the point in the wakefield, where the electric field changes sign and starts to decelerate the bunch (cf. Figure 2.3). This can also be seen in the phase space plot of Figure 2.4b: Electrons on trapped orbits gain momentum on one half of the orbit and lose momentum on the other half.
The dephasing length is the length after which the electron bunch reaches the dephasing point. Lu et al. [142] found for the bubble regime and highly underdense plasma, a dephasing length of

$$L_{\mathrm{deph}} \simeq \frac{2}{3}\frac{\omega^2}{\omega_p^2} R_b = \frac{2}{3}\frac{\omega^2}{\omega_p^2}\frac{2\sqrt{a_0}}{k_p} \tag{2.71}$$

validated in simulations for $2 \lesssim a_0 \lesssim 2\sqrt{\frac{n_c}{n_0}}$. This equation already includes the effects of driver depletion on the dephasing length.
Using Equation (2.31) for the plasma frequency, the dephasing length is seen to increase with decreasing plasma density: $L_{\mathrm{deph}} \propto n_0^{-3/2}$. Furthermore, higher laser intensities result in a longer dephasing length: $L_{\mathrm{deph}} \propto \sqrt{a_0}$.
From Equations 2.70 and 2.71, we can see that $L_{\mathrm{deph}} \lesseqgtr L_{\mathrm{depl}}$ for

$$\frac{2}{3}\frac{2\sqrt{a_0}}{k_p} \lesseqgtr c\Delta\tau_I. \tag{2.72}$$

Therefore, for a fixed laser pulse length, the acceleration process is limited either by dephasing or by depletion depending on the laser intensity and the plasma density ($k_p \propto \sqrt{n_0}$). For high laser intensities and low plasma densities, the acceleration process is expected to reach a regime, in which it is limited by the depletion of the laser, as the dephasing length will be longer than the depletion length.

Diffraction

Lastly, the acceleration process is also limited by the diffraction of the laser driver, as acceleration can only be maintained as long as the laser is intense enough to drive a wakefield. Commonly, focused laser beams for LWFA can be approximated by Gaussian beams (cf. Section 2.1). The evolution of the beam size due to diffraction is governed by Equation (2.17), and the acceleration process is limited to at most a few Rayleigh length z_R [129], for which the intensity is still high enough to drive a wakefield.
However, with relativistic intensities, as used in this work, the laser beam is self-guided as long as the power is higher than the critical power for self-focusing (cf. Section 2.5). When the power drops beneath the critical power due to depletion, diffraction starts to dominate over self-focusing, and the acceleration process will eventually terminate. In experiments, where very small densities are used to extend depletion and dephasing lengths, the threshold for relativistic self-focusing is higher, such that self-focusing is not strong enough to outweigh diffraction. Then, external guiding structures have to be applied, such as hydrodynamic optically-field-ionized (HOFI) channels [153, 154] or channels generated by capillary discharges [117, 131, 155]. Using these external guiding structures has led to record peak electron energies from LWFA of 5 GeV [72] and 8 GeV [41].
However, external guiding structures usually add complexity to the experimental setup and require a very good pointing stability of the driver laser to obtain an overlap of the guiding structure and the laser that is to be guided at every laser shot. Therefore, an external guiding structure was omitted in the experiments presented in this work. Instead, our experiments rely solely on self-guiding to surpass the diffraction limit. Additionally, a weak focusing geometry, resulting in a long Rayleigh length, was used to maximize the length over which acceleration can be maintained.

A goal of this work was to reach electron energies in the GeV regime. To accomplish this, operating at low plasma densities is beneficial as the depletion and dephasing lengths are longer, enabling the acceleration of electrons over longer lengths and, thus, to higher energies. As mentioned above, the threshold for relativistic self-guiding is higher for low plasma densities (Equation (2.37)). To counteract this, higher laser power can be used to extend the length for which the power is higher than the critical power for self-focusing and over which the laser can be guided.
To approximate the length needed to accelerate electrons to GeV energies, Equations 2.62 and 2.71 can be used. Assuming a Ti:Sa laser with $\lambda = 800\,\mathrm{nm}$ and $a_0 = 2.0$ and a density of $10^{18}\,\mathrm{cm}^{-3}$, the maximum acceleration gradient is $E_{z,\max} \approx 136\,\mathrm{GV/m} = 0.136\,\mathrm{GeV/mm}$ (note that the vacuum intensity was used for this calculation, neglecting any self-focusing effects for this approximation). In the bubble regime, the axial field is approximately linear inside the bubble. There-

fore, the electron will experience an average field of $E_{z,\max}/2 \approx 0.068\,\mathrm{GeV/mm}$ over the dephasing length while moving through the bubble up to the dephasing point[142]. Therefore, an energy gain of $0.068\,\mathrm{GeV/mm} \cdot 17.5\,\mathrm{mm} \approx 1.2\,\mathrm{GeV}$ would be reached over the dephasing length of 17.5 mm for these parameters. From this, we can see that a length in the cm range is needed to accelerate to GeV energies. Note that this calculation only gives an estimate of the length scale needed for the acceleration to GeV energies. Depending on the pulse length of the laser, Equation (2.70) results for our parameters ($\Delta\tau_I \approx 30\,\mathrm{fs}$) in a depletion length of 15.7 mm, such that the full dephasing length would not be available for acceleration and the expected energy gain would be lower.
In this work, we will discuss LWFA results in the GeV regime and compare them to the predictions of the theoretical models presented above. Before showing the results, the experiment and its components will be introduced in the next chapter.

3. Experimental Setup

The LWFA experiments conducted in this work took place at the Centre for Advanced Laser Applications (CALA) at the Ludwig-Maximilians-Universität in Munich. At CALA, the PW-class Advanced Titan-Sapphire Laser System ATLAS-3000 delivers ultra-intense laser pulses with a center wavelength of 800 nm that can drive plasma waves for the acceleration of electrons. In this chapter, the ATLAS-3000 system and the setup used for LWFA experiments in this work will be described.

3.1. ATLAS-3000

The laser system ATLAS-3000 uses the technique of chirped pulse amplification (CPA) [27] to amplify laser pulses to high energies in order to reach intensities needed for driving plasma waves. To understand the basic setup of the laser used for the experiments in this work, Figure 3.1 shows a schematic of the ATLAS-3000. First, pulses with a pulse length <10 fs are generated in a mode-locked oscillator with a repetition rate of 80 MHz. After boosting the energy in a first amplifier stage, the pulses are stretched to approximately 1 ns in a grating stretcher. Thereby, the intensity is reduced by approximately five orders of magnitude. This enables the amplification of the pulse energy without damaging optics along the beam path, which is the fundamental idea of CPA. Furthermore, Pockels cells (PC) sample down the pulses to 10 Hz in the first three amplifier stages (called front-end) to facilitate alignment and control, and subsequently to 1 Hz to address the limitations of the pump lasers and the data rates in the experiments. After the stretcher, the pulse is sent through an acousto-optic programmable dispersive filter [156] (DAZZLER^{TM} by FASTLITE), which pre-compensates high-order dispersion of the laser pulse in the laser chain for optimum compression after amplification. In the regenerative amplifier (regen), the pulse is amplified in a cavity, resulting in a clean Gaussian spatial profile since only resonator modes are amplified efficiently. In the regen, an acousto-optic programmable gain filter [157] (MAZZLER^{TM} by FASTLITE) controls the spectral gain of the amplifier. Thus, the resulting spectrum can be optimized to exhibit a broad spectral width, which is necessary for achieving short pulses after compression (cf. Equation (2.14)). After the regen, six

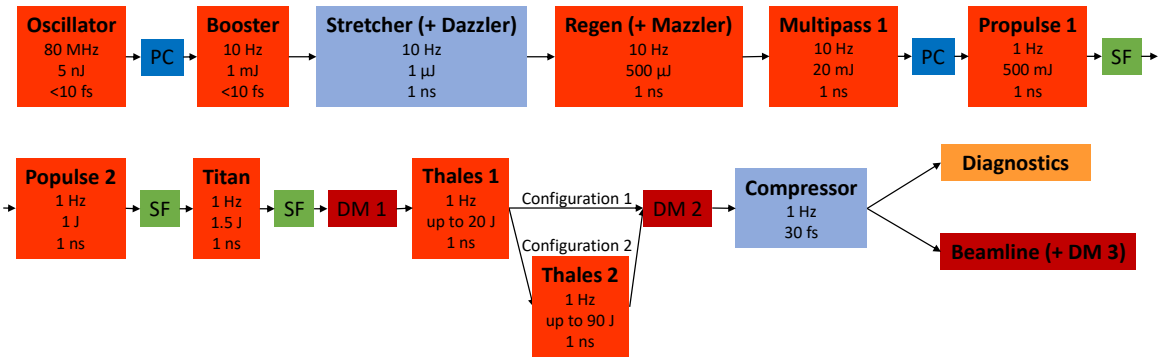

Figure 3.1.: Schematic of the ATLAS-3000 laser system as used in this work. PC stands for Pockels cell, SF for spatial filter, and DM for deformable mirror. At each amplifier stage, the repetition rate and the approximate pulse energy and pulse length are quoted.

more amplifier stages amplify the pulse further. The amplified beam is telescoped up to larger beam sizes for each amplifier stage to further reduce the intensity on optical components. Spatial filters (SF) smoothen the spatial profile after different amplifiers by sending the focused beam through a pinhole to filter out high spatial frequencies. Before and after the last two amplifiers (Thales 1 & 2), deformable mirrors (DM 1 & 2) are used to flatten the wavefront of the beam in a closed loop with feedback from wavefront sensors based on quadriwave lateral shearing interferometry [158] (SID4 by PHASICS).
In the course of this work, two configurations of the amplifier chain were used (indicated in Figure 3.1). For the first configuration, the last amplifier (Thales 2) alongside the corresponding telescope is bypassed, resulting in a beam size in the compressor and beamline of 18 cm and maximum energy before compression of 20 J. The other configuration uses Thales 2 to amplify up to 90 J (up to 31 J in this work), and a beam size of 27 cm is obtained.
After the last amplification stage, the pulse is recompressed in vacuum by a grating compressor to approximately 30 fs FWHM duration. For the diagnostic of the pulse length, a self-referenced spectral interferometer (WIZZLER^{TM} by FASTLITE) using cross-polarized wave generation [159] and a second-harmonic-generation frequency-resolved optical gating device (SHG-FROG) [160] (GRENOUILLE^{TM} by Swamp Optics) are installed. The optimal compression is obtained using the DAZZLER in a closed loop with the measurement of the WIZZLER as feedback.
Afterward, the beam is sent through the evacuated beamline towards the experimental caves. The transmission through the compressor and the beamline with cleaned beamline mirrors was measured to be approximately 67 %. However, the mirrors undergo blackening from contaminations in the beamline, which reduces their reflectivity. The transmission was not measured before every experiment as no measurement device was available to be used in vacuum. The measurement in

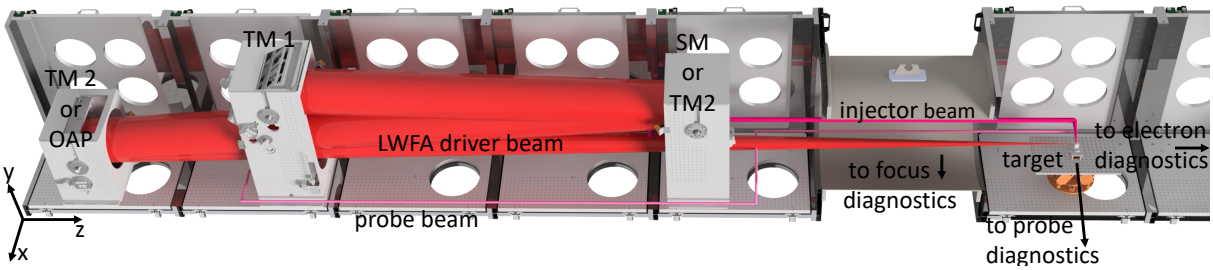

Figure 3.2.: Experimental chamber in ETTF showing the beam path of the main laser beam (red) over two turning mirrors (TM 1/2) and a spherical mirror (SM) or an off-axis parabola (OAP) towards the target. Before the target, a pick-off mirror can be moved into the beam path to send the beam to the focus diagnostics (not shown here). The probe beam (light pink) and the injector beam (dark pink) are picked from the main beam. The beam paths of the probe and injector beams have been simplified here, omitting delay stages and periscopes.

air is also affected by uncertainties since the whole beam does not fit through the windows in the vacuum shutters. Therefore, the transmission was measured using a smaller beam size, which adds uncertainty due to the potential inhomogeneity of the reflectivity of the beamline mirrors. Considering this, the transmission for this work is assumed to be lower than the measured 67 % and with a large error margin: (60 ± 10) %.

3.2. Experimental chamber

The LWFA experiments in this work were conducted in the experimental cave of CALA called Electron and Thomson Test Facility (ETTF). The details of the setup in the vacuum chamber of ETTF with its diagnostics and gas targets will be described in the next sections. First, an overview of the laser path and locations of the gas target and different diagnostics in the 14 m long vacuum chamber in ETTF is shown in Figure 3.2. A spherical mirror (SM) with 10 m focal length focuses the beam from ATLAS-3000 in an f/56 or f/37 configuration depending on the initial beam size for the two different configurations (see Section 3.1) to a FWHM spot size of (57 ± 1) µm and (38 ± 1) µm, respectively. Data in Sections 4.1, 4.2 and 5.2 were obtained with the f/56 configuration, while in experiments shown in Sections 5.3 and 5.4 the f/37 configuration was used. For the data shown in Section 4.3, an off-axis parabola (OAP) with 6 m focal length focused the beam in an f/33 geometry (ATLAS configuration 1).
Before conducting an LWFA experiment, the focus and the wavefront of the attenuated driver beam in vacuo can be measured using the focus diagnostics (see Section 3.3), which is located before the target area. Then, in the LWFA experiment, the focused beam propagates through a gas target (see Section 3.4) and ionizes it,

generating a plasma, in which a plasma wave can be driven by the laser. In this plasma wave, electrons can be accelerated via LWFA. A probe beam is picked from the main beam and propagates through the gas target perpendicularly to the main beam to image the target area and measure the plasma density (see Section 3.5). An injector beam is used to ionize gas locally, which facilitates electron injection into the laser wakefield (see Section 3.6). Accelerated electrons travel downstream to an electron spectrometer (see Section 3.7). All of these parts are described in more detail in the next sections.

3.3. Focus diagnostics

To measure the focal spot size and the vacuum intensity of the LWFA driver beam, the beam from ATLAS-3000 is attenuated and sent via a pick-off mirror before the target to the focus diagnostics setup. The setup is shown schematically in Figure 3.3. In the focus diagnostics, a beam splitter (BS) sends the beam to a far-field camera and a Shack-Hartmann wavefront sensor comprising a microlens array and a camera. The deformable mirror in the beamline (DM3) (cf. Figure 3.1) flattens the wavefront and optimizes the focus in a closed loop with feedback from the Shack-Hartmann wavefront sensor. A reference of a flat wavefront on the Shack-Hartmann sensor is created by flipping a pinhole into the beam path, which creates a perfect spherical wave around the beam center. The algorithm for focus optimization was developed in-house [161].
The resulting focal spot can be monitored on the far-field camera. High dynamic range (HDR) images using different attenuation levels are recorded to measure the focal spot size, Strehl ratio, and intensity. An example image of the vacuum focus for the f/56 configuration is shown in Figure 3.4a. The energy arriving in ETTF

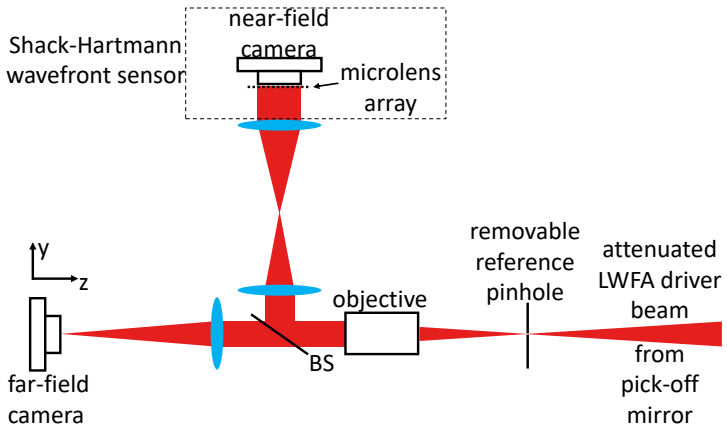

Figure 3.3.: The focus diagnostics setup is shown schematically. It comprises a far-field camera and a Shack-Hartmann sensor.

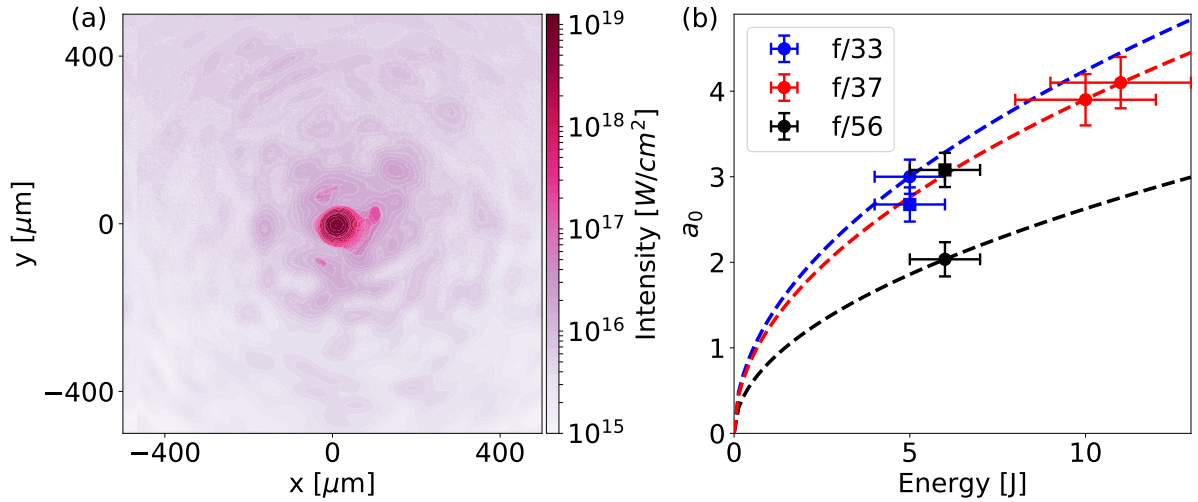

Figure 3.4.: Measurements of the focus in different configurations used in this work. **(a)** depicts an exemplary HDR image of a focal spot in the f/56 configuration with (9 ± 1) J arriving in ETTF, corresponding to (6 ± 1) J in the central disk of the focus. **(b)** shows the measured a_0 versus the energy in focus for four configurations with f/33 and (5 ± 1) J (blue circle), f/37 with (10 ± 2) J and (11 ± 2) J (red circles), and f/56 and (6 ± 1) J (black circle). The dashed lines are fitted square-root functions to the measured data points with the constraint $a_0 = 0$ for zero energy. The squares are the data of the f/33 (blue) and f/56 (black) cases normalized to the f/37 case. The data was obtained on 04/10/2021 (f/33), 26/04/2022 (f/56), 16/10/2023 (f/37,10J) and 19/10/2023 (f/37,11J).

can be calculated from the energy measured in ATLAS before compression and the transmission through the compressor and the beamline (60 %, see Section 3.1). The energy in the central disk of the focus, contributing to the LWFA process, is calculated from the energy arriving in ETTF by taking into account the measured Strehl ratio and the theoretical value of 84 % of energy contained in the central peak of an Airy focus [162].

In Figure 3.4b, the results of the HDR measurements are plotted for the different configurations discussed above for the measurement days considered in this thesis. Only one measurement day could not be evaluated (data in Section 4.1) due to a too large intensity in the objective of the focus diagnostics and resulting white light generation. However, the configuration is the same as for the data shown in Section 5.2 (f/56 configuration and (6 ± 1) J in focus).

To guide the eye, the data points for each f-number were fitted with a square-root function as a_0 depends on the intensity and thus on the energy with a square root (cf. Section 2.1). For the fits, the constraint $a_0 = 0$ for zero energy was applied. To be able to compare the three different configurations, the two data points of the f/33 configuration and the f/56 configuration were normalized to the f/37 case by multiplying the result with the respective f-number and dividing by 37. The normalized data points end up close to the fitted line of the f/37 case.

3.4. Gas targets

During an LWFA experiment, the focused laser beam will propagate through a gas target. The gas will be ionized by the foot of the laser pulse, forming a plasma, and a plasma wave will build up behind the laser, in which electrons can be accelerated. This work aimed at accelerating electrons with LWFA to GeV energies, obtaining stable and quasi-monoenergetic electron beams. To this end, a gas target with a length in the cm range is needed (cf. Section 2.6.5), providing a stable and homogeneous density profile to ensure a stable acceleration process. Often, two types of gas targets are used in LWFA experiments: gas cells (e.g., [34, 92, 100]) and nozzles producing supersonic gas jets (e.g., [74, 97, 119]). Both target types have advantages that qualify them as targets for this work.
Steady-state gas cells provide very homogeneous and reproducible density profiles [118]. Furthermore, gas cells can easily be scaled to provide longer interaction lengths for the acceleration to GeV energies. Supersonic gas jets, on the other hand, are often used because they facilitate obstacle-induced shock injection (cf. Section 2.6.4), resulting in quasi-monoenergetic electron beams. They also usually simplify the experiment setup and the alignment procedure due to the better accessibility of the focus area. Additionally, direct interferometry measurements of the plasma density are feasible since a perpendicular probe beam can propagate freely through the gas jet. However, both target types also have disadvantages, which were addressed in the designs of a gas cell and slit-shaped supersonic nozzles in this work. These new designs will be presented in the next sections.

3.4.1. Gas cell

First, a new design of a variable-length gas cell is presented. A drawing of this design can be seen in Figure 3.5. In comparison to classical designs of gas cells for LWFA, we addressed some disadvantages of gas cells in this design. First, the entrance pinhole of a gas cell can get ablated and widened if a high-intensity laser beam with remaining intensity outside the focus passes through it repeatedly. With a widening entrance pinhole over time, the length of the density gradient at the entrance of the cell increases [163]. If the gradient length exceeds the laser's Rayleigh length, out-of-focus beam profile fluctuations could result in an unstable propagation of the laser. To prevent this effect, we use a rotatable disk with pinholes in front of the gas cell. By sending the driver beam through a pinhole in this disk, remaining intensity outside the focus is filtered out before reaching the entrance pinhole, preventing it from getting ablated and widened quickly. To prolong this effect, the pinhole can be exchanged by rotating the disk approximately every one hundred shots. The entrance pinhole of the cell is manually exchangeable for each new experiment day. Both the pinhole disk and the cell entrance holes are placed

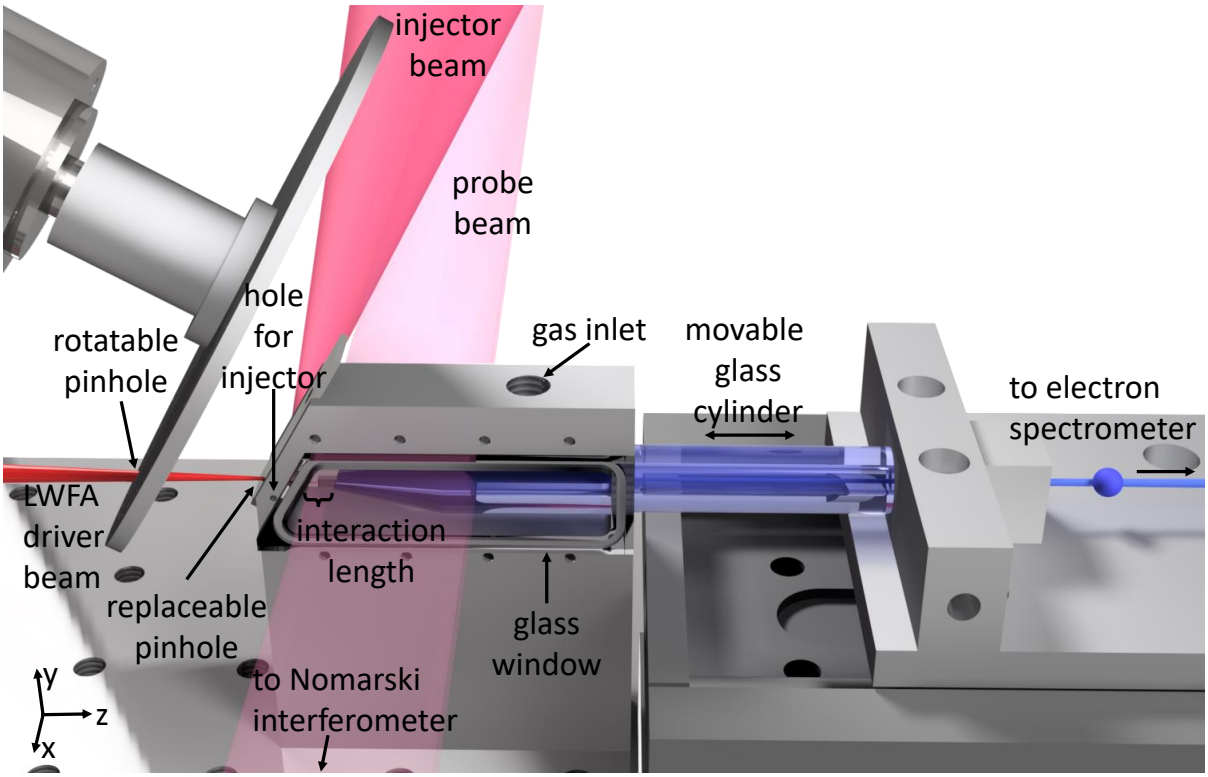

Figure 3.5.: Gas cell target. The LWFA driver beam passes a first pinhole with a 0.5 mm diameter in a rotatable mount before entering the gas cell through another pinhole of the same size. Inside the gas cell, the interaction length between laser and gas is between 5 and 30 mm long and can be changed by moving the glass cylinder. Electrons accelerated in the interaction length travel further downstream toward the electron spectrometer. The gas cell has glass windows for the probe beam to pass perpendicularly. At the front of the gas cell, a hole is drilled in x-direction for the injector beam to pass through.

at an oblique angle to the laser beam to avoid direct back-reflection of the laser pulses into the laser, where they would cause damage to the laser optics.
Another issue with often opaque gas cells is the direct measurement of the plasma density during the experiment. To address this, our gas cell design includes windows at the side of the gas cell enabling a probe beam to pass perpendicularly through the gas to measure the density via interferometry.
The exit of the gas cell is a 1 mm diameter hole in a glass cylinder. The cylinder can be moved in and out of the gas cell, changing the length of the cell and, thus, the interaction length for LWFA. Glass was chosen as a material for the cylinder after some initial tests with an aluminum cylinder. After only a few shots, the laser ablated the aluminum, and debris covered the cell's windows, preventing probing the interaction region through the windows. Using glass as a material for the cylinder mitigated this issue noticeably.
Lastly, we address our need to obtain quasi-monoenergetic beams for the Breit-

Wheeler project (cf. Chapter 1). Often, self-injection or ionization injection mechanisms are used in gas cells, typically lacking a high level of control and resulting in broadband energy distributions. In our design, a hole is drilled at the front of the gas cell in x-direction. This hole allows another laser beam (injector beam) to pass through the cell perpendicularly, which can be used to inject quasi-monoenergetic bunches in a controlled way (see Section 3.6). First tests of this injection mechanism in the gas cell are discussed in Chapter 4, where all results of LWFA experiments with the gas cell are shown.

3.4.2. Slit nozzles

In addition to the gas cell, new supersonic nozzles with exit lengths in the cm range needed for the acceleration to GeV energies were designed in this work. To this end, computational fluid dynamics (CFD) simulations were conducted. Before introducing the new designs, we will first give some basic equations that are needed in CFD simulations, using Ref. [164–166]. Furthermore, some basic equations characterizing supersonic nozzles will be given that are needed to understand our choice of designing slit-shaped nozzles instead of conventionally round supersonic nozzles.

Assuming an adiabatic, reversible, and steady flow in one dimension of a compressible, ideal gas through a tube, the following conservation equations hold [165]:

Mass conservation:

$$\rho A v = const., \tag{3.1}$$

in terms of the mass flow per time, where ρ is the mass density, A the cross section of the tube, and v the velocity of the gas.

Momentum conservation:

$$pA + \rho A v^2 = const. \tag{3.2}$$

with p the pressure of the gas. Here, the momentum flux with a unit of $[\mathrm{kg} \cdot \mathrm{m/s^2}]$ is used in analogy to the mass flow from Equation (3.1), assuming a steady 1D flow [164].

Energy conservation:

$$h + \frac{1}{2}v^2 = c_p T + \frac{1}{2}v^2 = const. \tag{3.3}$$

Here, h is the specific enthalpy in units of [J/kg], c_p is the specific heat at constant pressure, and T is the gas temperature. The energy equation is written in the common form used for steady adiabatic compressible flows, where mass conservation is already taken into account [164].
For the relation between the gas density ρ, the temperature T and the pressure p, the ideal gas law can be used:

$$p = \frac{\rho R T}{m_M} \tag{3.4}$$

where R denotes the molar gas constant and m_M the molar mass of the gas.
The speed of sound in a medium is defined as [164]

$$c_s = \sqrt{\gamma \left(\frac{\partial p}{\partial \rho}\right)_T} \tag{3.5}$$

with $\gamma = c_p/c_V$ the adiabatic index, where c_V is the specific heat at constant volume. Using the ideal gas law, the sound velocity c_s in an ideal gas can be calculated with

$$c_{s(\mathrm{IG})} = \sqrt{\gamma R T / m_M}. \tag{3.6}$$

A disturbance in the gas flow will travel with the sound velocity c_s.
The Mach number M is the velocity of the gas in a compressible flow normalized to the sound velocity:

$$M = v/c_s. \tag{3.7}$$

Using the Mach number M, two regimes can be defined for a compressible gas flow: In the **subsonic** ($M < 1$) regime, a disturbance in the gas flow can propagate freely. In the **supersonic** ($M > 1$) regime, disturbances cannot propagate freely, and shocks can occur. This implies that shock-fronts can be generated in supersonic gas flows by introducing an obstacle into the flow. This property is frequently used for generating shocks for shock injection (cf. Section 2.6.4) in LWFA experiments.
To achieve a supersonic flow, nozzles with convergent-divergent shapes are used. A convergent-divergent shape is shown schematically in Figure 3.6a. In the converging part, the flow speed is accelerated and reaches the sound velocity ($M = 1$) in the nozzle's throat. The flow is further accelerated to supersonic velocities ($M > 1$) in the diverging part. A thorough explanation and derivation of this effect can be

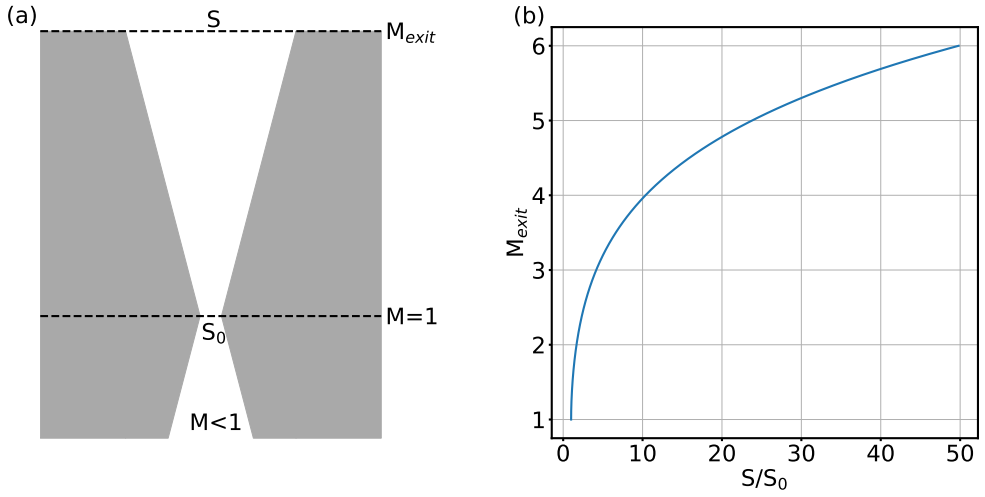

Figure 3.6.: (a) Schematic of a convergent-divergent nozzle. **(b)** Exit Mach number against exit-to-throat area ratio for hydrogen ($\gamma = 1.41$).

found, for example, in Ref. [164, 165]. The Mach number at the nozzle exit can be calculated from the ratio of the throat area S_0 and the exit area S with

$$\frac{S}{S_0} = \frac{1}{M_{\text{exit}}} \left[\frac{2 + (\gamma - 1) M_{\text{exit}}^2}{\gamma + 1} \right]^{\frac{\gamma+1}{2(\gamma-1)}} . \tag{3.8}$$

This relation is plotted in Figure 3.6b for $\gamma = 1.41$ [164] for hydrogen at 20 °C. Note, that this equation is just an approximation for the exit Mach number of a convergent-divergent nozzle, as it is only valid for constant γ. However, for diatomic gases, such as hydrogen, γ is temperature dependent as rotational degrees of freedom of the molecules freeze out at low temperatures [165]. Around a temperature of 80 K, the value of γ for hydrogen rises to the value for monoatomic gases ($\gamma = 1.67$). As the temperature rapidly drops in the diverging part of a convergent-divergent nozzle, γ for hydrogen cannot be assumed to be constant. However, this effect is not covered by the common theory for compressible flow through a convergent-divergent nozzle. In CFD-simulations conducted in this work, we observe that the simulated exit Mach number is approximately $10 - 30\,\%$ lower than the theoretical value calculated from Equation (3.8) (see summary of nozzle designs used in experiments in this work in Table A.1 in the appendix).
The density ratio before and after a shock front in a supersonic flow for a shock that is normal to the flow direction can be calculated by [165, 166]

$$\frac{\rho_2}{\rho_1} = \frac{(\gamma+1)M_1^2}{2+(\gamma-1)M_1^2} \tag{3.9}$$

with ρ_1 and ρ_2 the density before and after the shock-front, respectively, and M_1 the Mach number before the shock. For oblique shocks that are produced by introducing an obstacle into a supersonic flow, the Mach number must be replaced by $M_{1\perp} = M_1 \sin\beta$ with β the shock angle between the incoming flow and the shock-front [165]. Just like Equation (3.8), Equation (3.9) is only strictly valid for monoatomic gas, where γ can be assumed to be constant, and can only be taken as an approximation in the case of hydrogen that is used in the LWFA experiments in this work.

For the CFD-simulations, the CFD-software Ansys Fluent was used to simulate compressible flows through different convergent-divergent nozzles. For the simulations, the geometry of the volume inside the nozzles was drawn and meshed into small simulation volumes. Drawing a quarter of the geometry was sufficient due to the symmetry of the nozzles. Ansys Fluent then solves the conservation equations for mass, momentum, and energy (Equations 3.1,3.2 and 3.3) in these simulation volumes, as described in [167]. The ideal gas law (Equation (3.4)) is used for the relation between gas density, temperature, and pressure. In the simulations, hydrogen was used as a gas species.

Next, the new designs of supersonic nozzles are introduced, and their simulated density distributions will be discussed. To design supersonic nozzles with exit lengths in the cm range, as needed for the acceleration to GeV energies, a simple scale-up of the nozzle exit of conventionally round supersonic nozzles would quickly lead to high Mach numbers (cf. Equation (3.8)) if the throat diameter is kept constant. According to Equation (3.9), high Mach numbers lead to higher density ratios before and after obstacle-induced shocks, which can lead to excessive injection at these shocks and lower electron energies, as will be discussed in Section 5.1. Increasing the throat diameter and exit size simultaneously would cause the gas load, scaling with the square of the throat diameter, to become too large for many vacuum systems.

A straightforward way to reach long interaction distances while circumventing these issues is to reduce the dimensionality of the flow. Therefore, slit-shaped nozzles were designed, where the LWFA drive beam will be oriented along the long axis of the slit. The convergent-divergent shape in the slit nozzles was chosen to be in the longitudinal direction since it was assumed that fabrication would be easier than with a convergent-divergent shape in the transverse direction. In Figure 3.7a,b, the inside of such a slit nozzle is shown at a longitudinal and a transverse cut through the center, respectively. Parameters defining the nozzle design (i.e., exit length, throat length, opening angle, and width) are indicated. The nozzle depicted in Figure 3.7a,b has an opening angle of 22.6° and a width of 3 mm. The exit length

is 20 mm and the throat length 750 µm. With these values and Equation (3.8), the value of the exit Mach number can be approximated ($M = 5.15$ for hydrogen (cf. Figure 3.6b)). According to simulations, the exit Mach number will be slightly lower than this theoretical value, as discussed above. All slit nozzles that were used in this work have the same exit-to-throat ratio and, consequently, the same theoretical exit Mach number. However, a slightly lower exit Mach number resulting in a smaller density ratio of an obstacle-induced shock might be beneficial for future designs, that are intended for obstacle-induced shock injection, as will be discussed in Section 5.1.

For now, the usability as LWFA targets of the new nozzle designs will be discussed by looking at the density distribution above the nozzle exit, through which the LWFA driver laser will propagate. For a stable LWFA process, a homogeneous density plateau along the laser propagation direction (z) is desirable. Furthermore, a shallow gradient in the y-direction is favorable. Strong gradients in the y-direction would cause the laser to refract upwards. Consequently, trailing electrons in the laser's wakefield would deviate from straight pointing. The same applies to the x-direction. Therefore, a plateau in x-direction with constant density is desirable, even more so, as a gradient in x-direction would have a defocusing effect on the laser.

In Figure 3.7a,b, the density distribution inside and above the nozzle obtained from the simulation is shown. Line-outs of the density distribution along the laser axis and transverse to the laser axis are plotted for different heights above the nozzle in Figure 3.7c,d, respectively. For creating the line-outs, a linear interpolation between data points obtained from the simulation was used, since not enough simulation points are exactly on the same height above the nozzle. However, the line-outs can also be obtained by using data points that lie within ±50 µm of a certain height above the nozzle. This method yielded basically the same line-outs as the interpolation method.

As seen in the line-outs in Figure 3.7c, this nozzle design shows rather homogeneous plateaus in z-direction, with only a slight dent closer to the nozzle exit. The density line-outs in x-direction (Figure 3.7d) exhibit a plateau only for distances closer to the nozzle than 2 mm. Following the arguments discussed above, a small distance between the laser axis and the nozzle exit is, therefore, favorable. This can, however, be limited by the laser damaging the nozzle and the need to fit a blade or a wire between the laser and the nozzle for obstacle-induced shock injection. Therefore, in experiments shown in this work, the distance between laser and nozzles was rather around 4 mm. However, a systematic study in future works to test how close the laser can be to the nozzle without causing damage to the nozzle or a wire/blade could be useful to minimize the distance.

To study the influence of different opening angles and widths of the slit nozzles, several simulations, as described above, were performed. First, the influence of

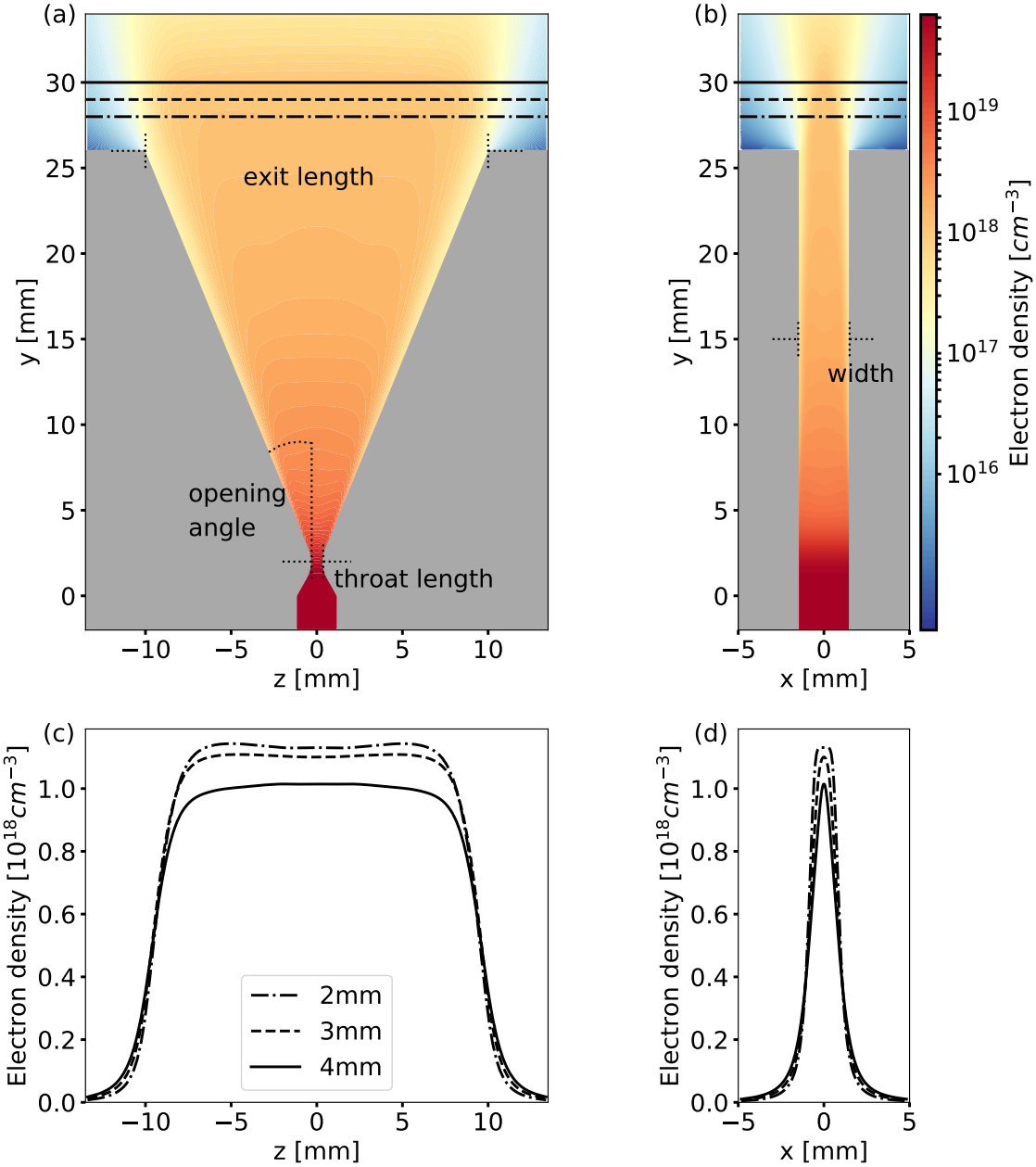

Figure 3.7.: Example of slit nozzle and corresponding simulated density distribution. **(a)**,**(b)** Simulated density distributions at cuts through the center of the nozzle along the longitudinal and transverse direction, respectively. The nozzle has an exit length of 20 mm, a throat length of 750 µm, an opening angle of 22.6°, and a width of 3 mm (indicated with black dotted lines). The solid, dashed and dashed-dotted black lines indicate positions for line-outs of the density at different distances to the nozzle exit shown in (c),(d). The LWFA driver laser will propagate along the longitudinal direction. **(c)**,**(d)** Density line-outs of the simulated density distribution at different heights above the nozzle (indicated in (a),(b)) along the longitudinal and transverse direction, respectively. The inlet pressure in the simulation was 2.6 bar. A similar figure showing this nozzle design was published in [168].

different opening angles will be discussed. To this end, the gas flow through seven slit nozzle designs with different opening angles was simulated. All these nozzle designs have an exit length of 20 mm, a throat length of 750 µm, and a width of 2 mm. Figure 3.8a-c show the density line-outs above the nozzles along the longitudinal (z-), transverse (x-), and vertical (y-) directions, respectively. The line-outs in z-direction (Figure 3.8a) and x-direction (Figure 3.8b) are depicted for a height of 3 mm above the nozzles.
Regarding the density distribution in z-direction, along which the laser would propagate, all opening angles produce rather homogeneous density profiles with only slight deviations from perfect plateaus. Therefore, all of these opening angles are acceptable for LWFA experiments. From an opening angle of 33.7°, the density distribution starts to exhibit a dent in the center of the plateau. According to the Method of Characteristics [169], large opening angles can lead to shock waves inside the nozzle and flow separation at the nozzle walls. Therefore, no nozzles with larger opening angles were simulated.
For a small opening angle of 14°, a density peak is visible in the plateau's center. However, this small feature is not expected to have much influence on the acceleration process. In any case, going to much smaller opening angles was not necessary, as the larger ones do result in nice density plateaus. Smaller opening angles would imply higher nozzles, which can be impractical in the experimental setup with a

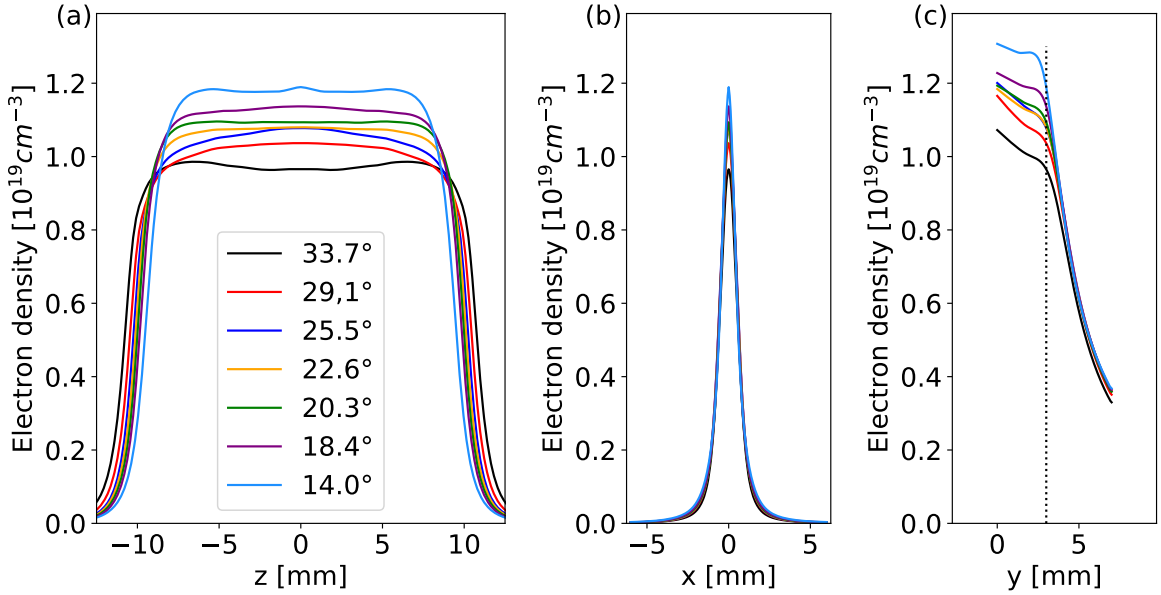

Figure 3.8.: Density line-outs along the **(a)** z-, **(b)** x- and **(c)** y-direction for slit nozzles with different opening angles. The exit length of the slit nozzles is 20 mm and the width 2 mm. In **(c)**, a black dotted line indicates a height of 3 mm above the nozzle, corresponding to the height of the line-outs in z- and x-direction. The inlet pressure in the simulations was 30 bar.

fixed distance between the chamber floor and the laser axis.
In x-direction (Figure 3.8b), different opening angles do not significantly influence the density profile but only have an influence on the peak density. In y-direction (Figure 3.8c), all designs exhibit a small gradient close to the nozzle exit with a steeper gradient from around a height of 3 mm above the nozzle. Therefore, a height of 3 mm or less between the LWFA driver laser and the nozzle is favorable to avoid a strong gradient and, thus, refraction of the laser. This coincides with the requirement to work close to the nozzle due to a plateau building in x-direction for distances close to the nozzle as discussed for Figure 3.7. In fact, the change in gradient in y-direction happens approximately at the height above the nozzle where the plateau in x-direction vanishes.
In Figure 3.9, density line-outs for nozzles with different widths are shown. The nozzles all have an exit length of 20 mm, a throat length of 750 µm and an opening angle of 25.5°. The line-outs in z- (Figure 3.9a) and x-direction (Figure 3.9b) are depicted for 3 mm above the nozzles. In z-direction, the width does not influence the quality of the plateau significantly. In both the x-direction and y-direction (Figure 3.9c), a wider slit seems favorable: For a wider slit, a plateau in x-direction exists for a larger range above the nozzle, and the region with small gradients in the y-direction is longer, as discussed above. However, the throat area scales with the width, and with an increasing throat area, the gas load in the vacuum chamber

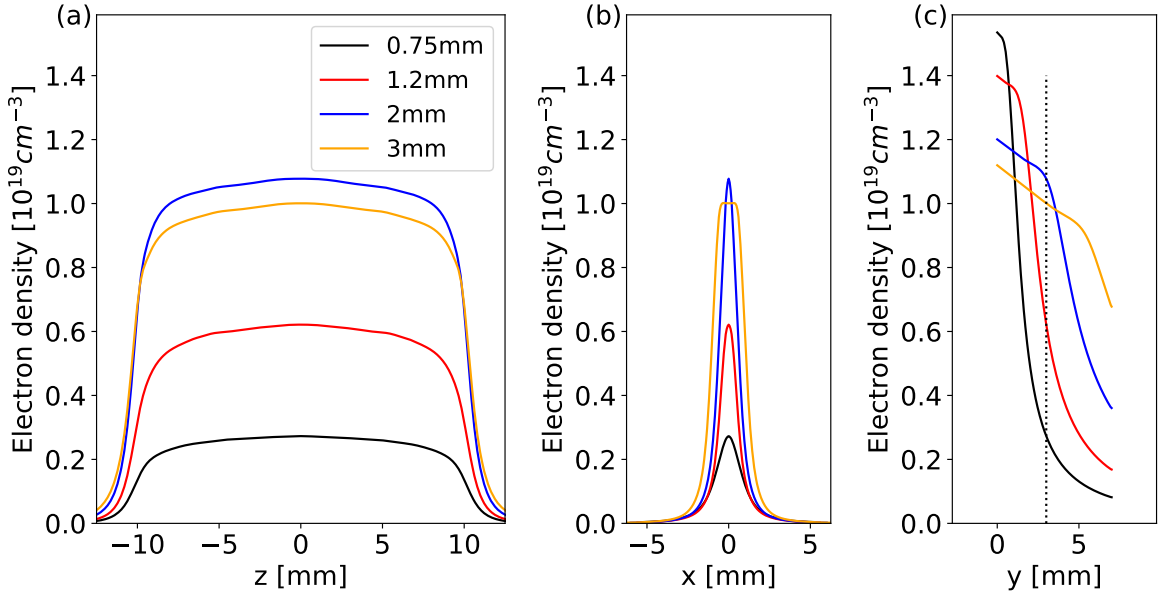

Figure 3.9.: Density line-outs along the **(a)** z-, **(b)** x- and **(c)** y-direction for slit nozzles with different widths. The exit length of the slit nozzles is 20 mm and the opening angle 25.5°. In **(c)**, a black dotted line indicates a height of 3 mm above the nozzle, corresponding to the height of the line-outs in z- and x-direction. The inlet pressure in the simulations was 30 bar.

will increase. Therefore, it is not advisable to use extremely wide slits. Widths of 2 and 3 mm seem suitable since the plateau in x-direction exists and the gradient in y-direction is small up to heights of approximately 3 and 5 mm above the nozzle, respectively, which gives enough space for the laser to propagate through this region without damaging the nozzle and with space for a wire or a blade.
In conclusion, for slit nozzles with an exit length of 20 mm, opening angles between roughly 14° and 34° and widths between roughly 2 and 3 mm result in density profiles that are suitable for stable propagation of the LWFA driver laser. For other exit lengths, similar values can be used, as was tested, for example, for a 40 mm long slit nozzle used in this work (see Section 5.4).
To test different designs of the slit nozzles in LWFA experiments, several designs were 3D-printed from the photopolymer material VeroWhitePlus^{TM} (RGD835). 3D printing was a time- and cost-efficient fabrication method, enabling the testing of many prototypes. The photopolymer material was tested for high vacuum and proved suitable for pressures down to 10^{-5} mbar. However, the surface roughness of the nozzle's inside is higher than for nozzles fabricated from stainless steel, which can result in a turbulence layer, flow separation, and a more inhomogeneous density profile [119]. The fabrication from stainless steel could, therefore, yield more stable and homogeneous density profiles in future experiments.
An example of a slit nozzle in an LWFA target setup is depicted in Figure 3.10.

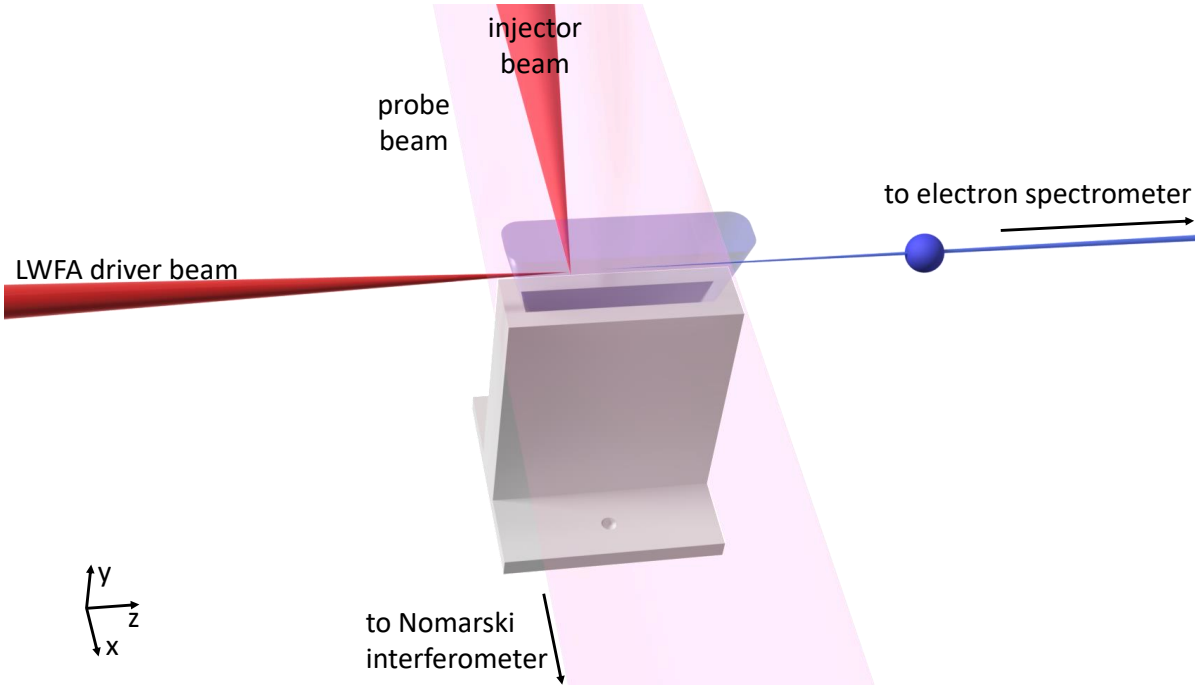

Figure 3.10.: Example of a slit nozzle as a gas target for LWFA. The LWFA drive beam is shown arriving from the left. The injector and probe beams propagate perpendicular to the drive beam. Accelerated electron bunches travel downstream toward the electron spectrometer.

Here, the laser travels along the z-direction of the slit nozzle. Electrons accelerated in the wakefield behind the laser travel further downstream towards an electron spectrometer. In this setup, an injector beam produces a shock for shock injection. This scheme will be introduced in Section 3.6.
Results from LWFA experiments using three different designs of slit nozzles (summary of designs in Table A.1 in the appendix) will be discussed in Chapter 5, where their measured and simulated density profiles will be shown.

3.5. Probe diagnostics

The density profiles of the targets described in the previous sections can be measured directly in the LWFA experiment using a probe beam and an interferometry setup. This section will briefly introduce the probe diagnostics and the analysis procedure of the interferometry data employed in this work.
In the experiment, the probe beam is picked from the main beam before TM1 (see Figure 3.2) and sent over a delay stage to the target, passing it in the x-direction, as shown in Figures 3.5 and 3.10. At the target, the probe beam is approximately half an inch in size. In Figure 3.11, the setup of the probe diagnostics behind the target is shown. On the one hand, the target is imaged onto a CMOS camera, creating a shadowgraphy image to gain an overview of the target area. An exemplary shadowgraphy image is shown in Figure 3.12a. The shadow of a part of a slit nozzle used as target in this experiment can be seen on the bottom. The plasma channel created by the LWFA driver beam propagating through the gas above the nozzle is visible as well. A silicon blade to generate a shock for shock injection (cf. Section 2.6.4) is seen on the left. However, in the experiment in which Figure 3.12a was recorded, the blade was not used to generate a shock. Instead, a strongly astigmatic laser beam produced a bi-planar shock via hydrodynamic optical-field-ionization (HOFI) (see Section 3.6). This shock is the one

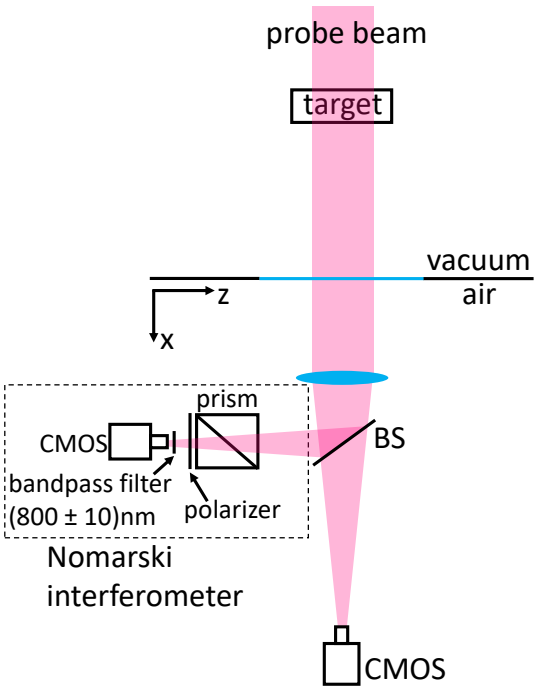

Figure 3.11.: Probe diagnostics setup comprising a shadowgraphy camera and a Nomarski interferometer.

visible in the shadowgraphy image.
Using a beam splitter, the probe beam is also sent through a Nomarski-type interferometer [170] to generate an interferogram of the plasma channel. The interferometer comprises a Wollaston prism and a polarizer, as seen in Figure 3.11. The Wollaston prism is oriented such that the polarization of the linearly polarized probe beam is 45° to the optical axes of the two birefringent parts of the Wollaston prism[171, 172]. This ensures that the two parts of the beam with orthogonal polarization that are split in the Wollaston prism are of equal intensity. The polarizer then filters both beam copies for the component of the polarization with the same orientation so that the two beams can interfere and create an interferogram. To obtain better coherence, the spectrum of the laser pulse is filtered with a 10 nm bandpass filter around 800 nm. The plasma density can be measured by evaluating the interferograms recorded with the CMOS camera. An exemplary interferogram is shown in Figure 3.12b, corresponding to the same laser shot as the shadowgraphy image in Figure 3.12a. All features described for the shadowgraphy image are visible twice due to the two copies of the probe beam generated in the Wollaston prism. In this experiment, the alignment of the prism was not optimal, resulting in the two copies of the plasma channel overlapping. In this case, only one half of one channel is analyzed and then mirrored, assuming a symmetric channel, to obtain data for the full channel.
To analyze interferograms obtained with the Nomarski interferometer, a few analysis steps have to be followed, which, in the current work, were programmed with basic packages in the programming language Python^{TM}. A short overview of the analysis steps will be given here. Details can be looked up in previous works [165, 172], where the software IDEA by the Technische Universität Graz [173] was used for analysis. For details on the procedure of this work, see Appendix B.
First, noise is filtered out from the raw interferometry images by Fourier filtering. The next step is the reconstruction of the relative phase ϕ, which can be calculated from the inverse Fourier transform after filtering with

$$\phi = \arctan\left(\frac{Im}{Re}\right) \tag{3.10}$$

with Im and Re the imaginary and real parts of the inverse Fourier transform, respectively. Here, the inverse Fourier transform is computed in complex numbers, even if the original image only contained real numbers [174].
Equation (3.10) gives modulo-2π values of the relative phase, which, therefore, have to be unwrapped to obtain correct values. Different methods exist for phase unwrapping, which are, for example, compared in Ref. [175]. One simple method is to check for the difference between two adjacent phase values. For a difference larger than $+\pi$, 2π is subtracted from the second value and all values following

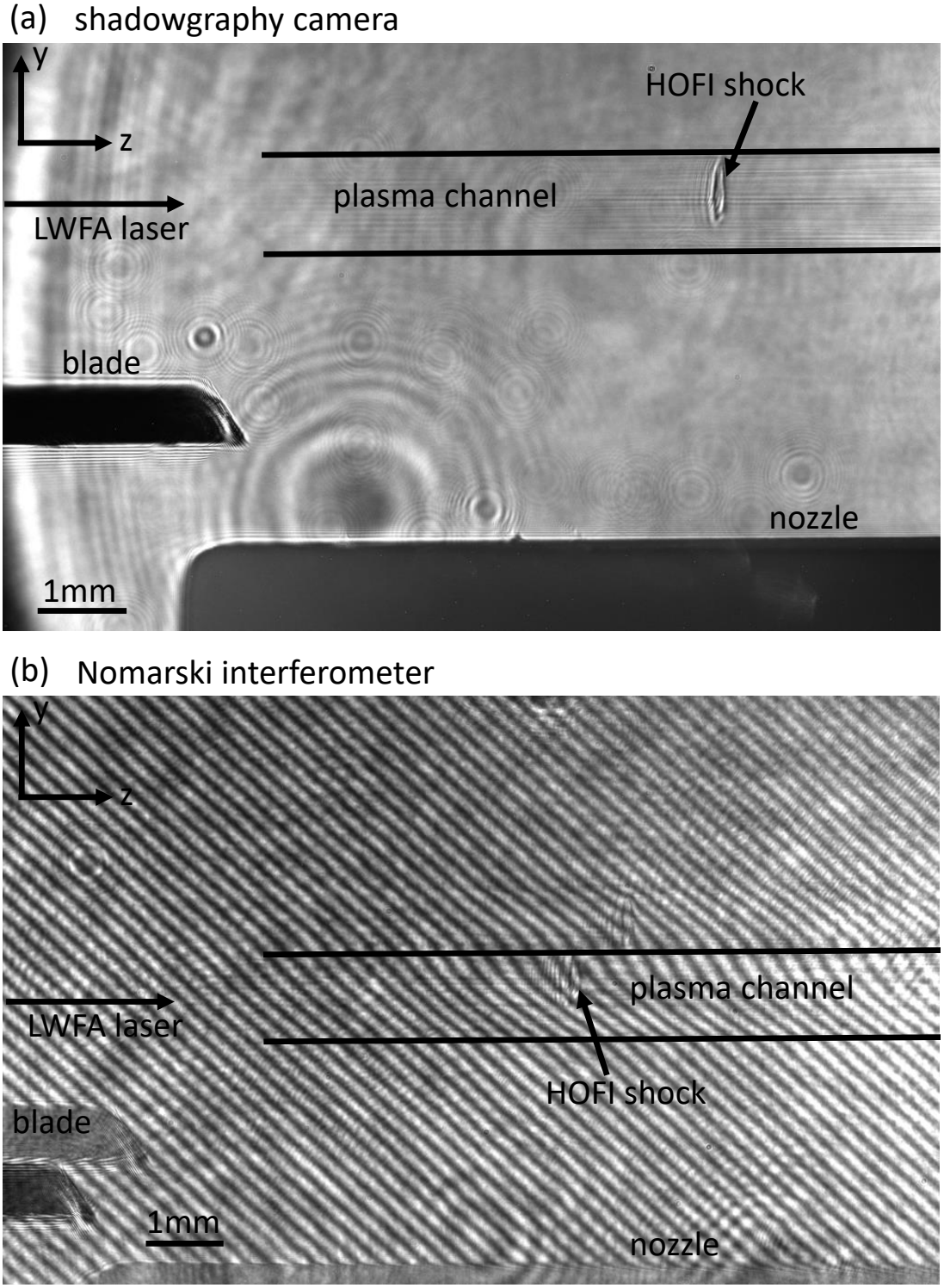

Figure 3.12.: Exemplary images of **(a)** the shadowgraphy and **(b)** the interferometer camera, showing the nozzle, the plasma channel generated by the LWFA driver beam coming from the left, the HOFI shock and a blade that can be used to generate a shock hydrodynamically. The rings visible in several positions in the images are interference patterns originating from contaminations on the mirrors of the probe beamline.

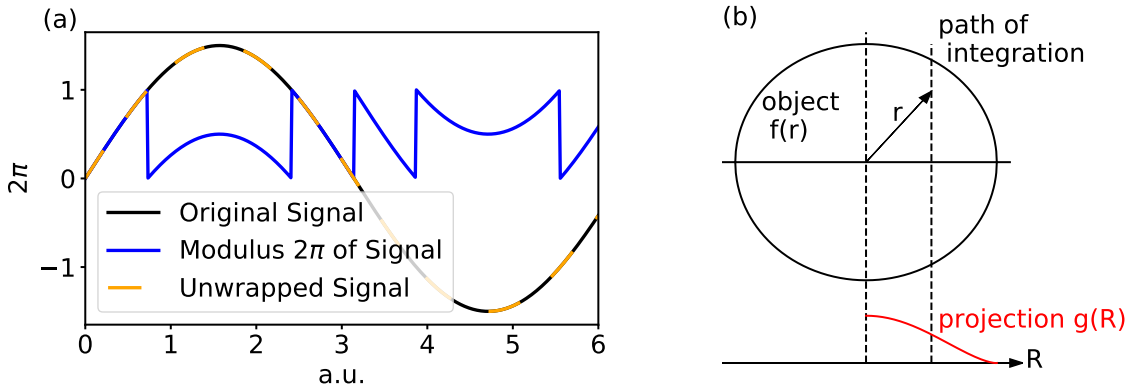

Figure 3.13.: Illustrations of **(a)** phase unwrapping (adapted from [177]) and **(b)** Abel transformation (adapted from [178]).

this value. For a difference smaller than $-\pi$, 2π is added to the second value and all following values. The procedure is repeated for all adjacent phase pairs. An illustration of phase unwrapping is shown in Figure 3.13a. For the analysis used in this work, a Python package was used for unwrapping the 2D interferometry image [176].
After unwrapping, a background image without gas, for which the same steps described above were applied, can be subtracted to obtain the relative phase difference in two dimensions introduced by the plasma channel. These 2D values are an integration over all 3D phase values along the probe beam path. Assuming a cylindrically symmetric plasma channel, this projection is the forward Abel transform of the real distribution of the phase values, as illustrated in Figure 3.13b. The projection $g(R)$ is calculated from the object function $f(r)$ by[178]

$$g(R) = 2\int_R^\infty \frac{f(r)\ r\ dr}{\sqrt{(r^2 - R^2)}} \tag{3.11}$$

and the reconstruction of the object function $f(r)$ is obtained from the projection $g(R)$ by applying the inverse Abel transform (Abel inversion):

$$f(r) = -\frac{1}{\pi}\int_r^\infty \frac{g'(R)\ dR}{\sqrt{(R^2 - r^2)}}. \tag{3.12}$$

In this work, a Python package[179] applying the recursive Hansen-Law method for Abel inversion[178] was used to retrieve the 3D phase values. In this method, a previously computed point and a new data point are the basis for each succeeding

point of the Abel inversion.
Before applying the Abel inversion, a point outside of the plasma channel has to be chosen to define zero plasma density, i.e., zero phase. Thereby, absolute phase values Φ can be obtained from the Abel inversion.
Finally, the plasma density can be calculated according to

$$n_0 = \frac{\lambda_0 n_c \Phi}{2\pi s_{px}} \tag{3.13}$$

with s_{px} the pixel size in the interferometry image.
Some measured density profiles of different slit nozzles used in this work will be shown in the results section in Chapter 5.

3.6. Injector beam and optically-induced shock injection

A goal of this work was to obtain quasi-monoenergetic beams for the planned Breit-Wheeler experiment at CALA. This can, for example, be achieved by injecting electrons at a defined location in the gas profile, e.g., at a density shock. This process is called shock injection, which is described in Section 2.6.4. Often, a shock is generated by introducing an obstacle into a supersonic gas flow, as mentioned in Section 3.4.2. However, this mechanism does not work in subsonic flows, e.g., in gas cells. To enable shock injection in a gas cell, a different scheme for shock generation is needed. To this end, we use another laser beam to generate a shock in the gas via hydrodynamic optical-field-ionization (HOFI) [154, 180, 181]. This scheme was first used in our group by Foerster et al. [110]. For this shock injection scheme, a so-called injector beam arrives before the main LWFA driver laser and propagates through the gas target perpendicularly to the driver laser (cf. Figures 3.5 and 3.10). It is focused to a highly astigmatic focus by a spherical mirror under an angle. The astigmatic focus ionizes and heats the hydrogen gas locally. The heated plasma electrons propagate away at the speed of sound [110], which is higher than the speed of sound of the surrounding neutral gas. This leads to line-shaped shock waves at the edge of the expanding region. At the density transitions of these shocks [182], electrons can be injected into the wakefield of the driver beam. In the course of this work, this scheme will be called optically-induced shock injection. The line-shape of the shocks mitigates potential pointing instabilities between the injector beam and the driver beam, which improved the optical injection scheme compared to other works [183, 184]. At the time of the development of the scheme, our group was unaware of an earlier work by Brijesh et al. [91], which also used an astigmatic focus, generated by a pair of cylindrical lenses.

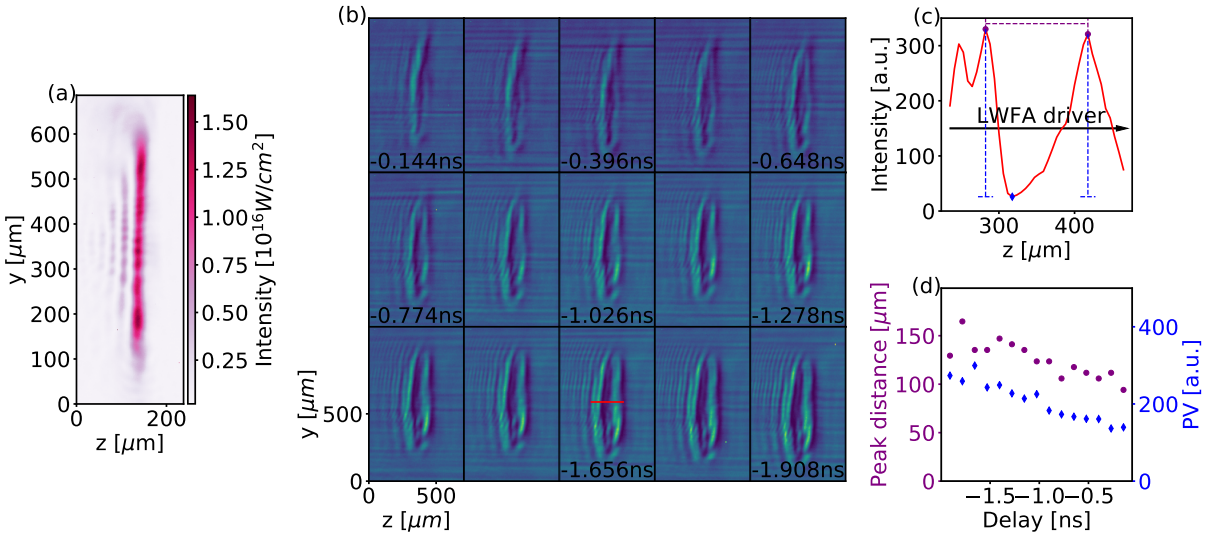

Figure 3.14.: (a) Image of the injector beam in vacuo. **(b)** Shadowgraphy images of the HOFI shock generated by the injector beam for different delays between the LWFA driver beam and the injector beam with increasing absolute values of the delay in each row from left to right (equal steps between images). The driver beam is defined to come at time 0. **(c)** Line-out across the HOFI-shock for the shadowgraphy image with the injector arriving 1.656 ns before the driver laser (location of line-out indicated with a red line in (b)). **(d)** The distance of the two peaks (purple dots) and the mean peak-to-valley (PV) value of the two peaks (blue diamonds) are plotted for the shocks at different delay values. The shadowgraphy images were obtained on 26/04/2022 (Set 26).

As shown in Foerster's work [110], the optically-induced shocks proved to be more stable than shocks generated by introducing an obstacle into a supersonic gas flow. Therefore, the optically-induced shock injection scheme is not only tested in a gas cell (see Section 4.3) in this work but also used in supersonic gas jets (see Chapter 5).

To generate a HOFI shock in the LWFA experiment, the injector beam is picked from the main beam before SM1 or TM2 (cf. Figure 3.2). The delay between the LWFA driver beam and the injector beam is adjustable by a delay stage, such that the injector beam arrives $0 - 2$ ns before the driver beam. In this work, the beam contained between 70 and 90 mJ of energy. It is focused with a 150 mm focal length spherical mirror under an angle of incidence of $(20 \pm 5)°$, generating an astigmatic focus with a FWHM spot size of $(20 \times 450)\,\mu m^2$ and a peak intensity of $1.6 \cdot 10^{16}\,W/cm^2$. An image of the injector beam focus in vacuum is shown in Figure 3.14a.

The HOFI shocks can be investigated by evaluating shadowgraphy images. Figure 3.14b shows shadowgraphy images of shocks for different delays between the injector and the driver beams. As expected, the density peaks of the shocks propagate away from each other with increasing time between the injector and the driver beam. To investigate the shock properties at different delays further, line-

outs along the z-axis were evaluated. One example of a line-out is shown in Figure 3.14c. For this shock, the injector arrived 1.656 ns before the driver beam. The line along which the line-out was taken is indicated in red in Figure 3.14b.
In Figure 3.14d, the distances of the peaks for different delay values are plotted. The peak distances increase for increasing absolute delay values with roughly 30 µm/ns. This value is on the order of the speed of sound of the heated plasma as estimated by Foerster et al. [110].
Furthermore, the peak-to-valley (PV) values are plotted for different delays in Figure 3.14d. An increase of the PV values and, thus, an increase of the density ratio of the shocks with increasing absolute delay values is observed. The density ratio of shocks has an influence on the charge and energy of electrons injected at the shocks, as was shown in simulations by Massimo et al. [185]. This implies that electron properties can be controlled by changing the delay between the injector and the driver beams in the optically-induced shock injection scheme. This feature will be investigated in Chapter 5.
Due to the long extent of the shocks along the propagation direction of the probe beam and the limited depth of focus of the imaging system, the shocks could not be resolved in the interferometry images in this work. By improving this in future works, the qualitative analysis discussed above could be extended to quantitative statements. For now, only empirical correlations can be deduced from the qualitative analysis shown above. However, by combining the measured intensity ratio in the shadowgraphy images with a LWFA model to calculate the energy gain in Section 5.4.2, we were able to extend the qualitative analysis to quantitative values.

3.7. Electron beam diagnostics

In this section, the diagnostic in ETTF measuring energy, charge, and divergence of accelerated electron beams is introduced. The same diagnostic was already used in previous works [172, 186, 187], where it is described in detail. Therefore, only a short introduction is given here.
In ETTF, a 80 cm long dipole magnet with an in-gap magnetic field strength of approximately $B = 0.85\,\mathrm{T}$ [172] is used as an electron spectrometer. The magnet is situated downstream of the target at a distance of 2.9 m. A drawing of the dipole magnet is shown in Figure 3.15 along a longitudinal cut through the center of the magnet. Electrons entering the dipole magnet are deflected downwards in its magnetic field. Trajectories of electrons with different energies coming from the LWFA target on the left (not shown) have been plotted inside the magnet. The trajectories were calculated by assuming a homogeneous magnetic field in the magnet. The gyroradius [123]

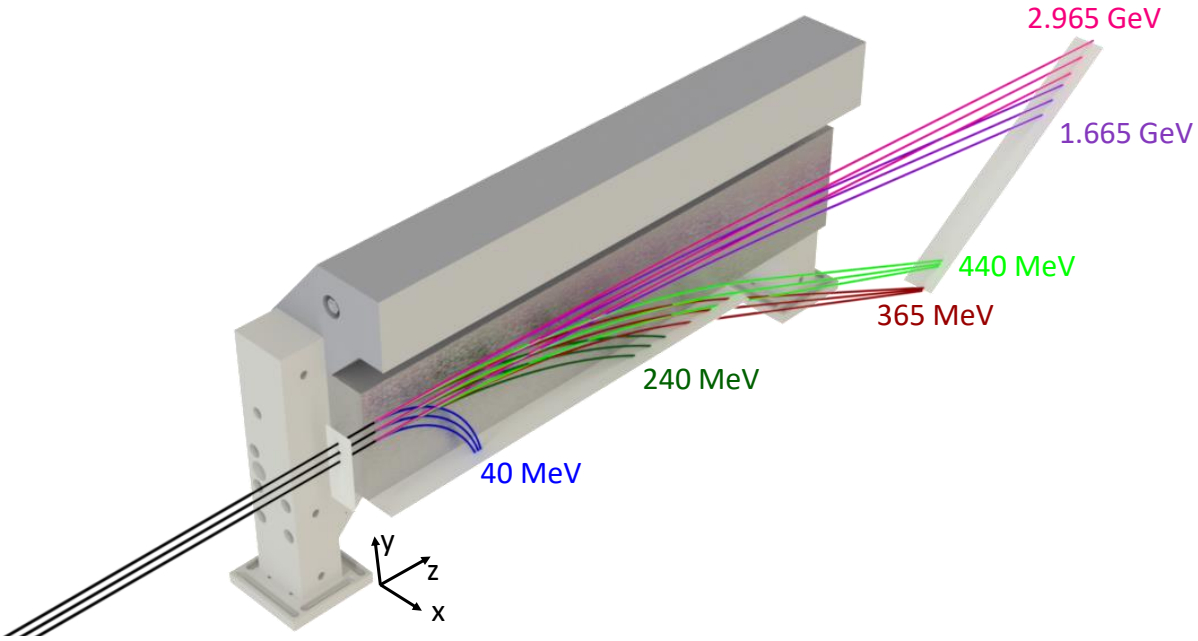

Figure 3.15.: Electron Spectrometer. A half-view of the 80 cm-long dipole magnet acting as an electron spectrometer is shown. Different electron trajectories are depicted schematically. Black lines indicate incoming electron beams. Three different trajectories for different pointings are shown (from bottom to top −4.3 mrad, 0 mrad and 4.3 mrad). The incoming electron beams intersect with a lanex-screen, from which their pointing can be measured. Inside the magnet, different colors denote different electron energies that are deflected differently. Depending on their energy, they hit lanex-screens placed underneath ('LowE-lanex') and behind ('HighE-lanex') the magnet. All lanex-screens are imaged onto 12-bit CMOS cameras (not shown here).

$$r_g = \frac{m_e \gamma v}{eB} = \frac{E[eV]}{cB} \tag{3.14}$$

was used to calculate the electron trajectories for different energies inside the magnet. When leaving the magnet, the electrons are assumed to propagate on straight trajectories.
In Figure 3.15, three trajectories are shown for each electron energy: an electron beam pointing straight from the target and electron beams pointing ±4.3 mrad up and down, respectively. This range was chosen as most electron beams measured in this work were pointing within this range.
From Figure 3.15, it can be seen that electrons with different energies and pointings propagate on different paths in the magnet and impinge on different points on scintillating screens located below and behind the magnet, which then emit fluorescence light. The screens are imaged by 12-bit CMOS cameras. The fluorescence

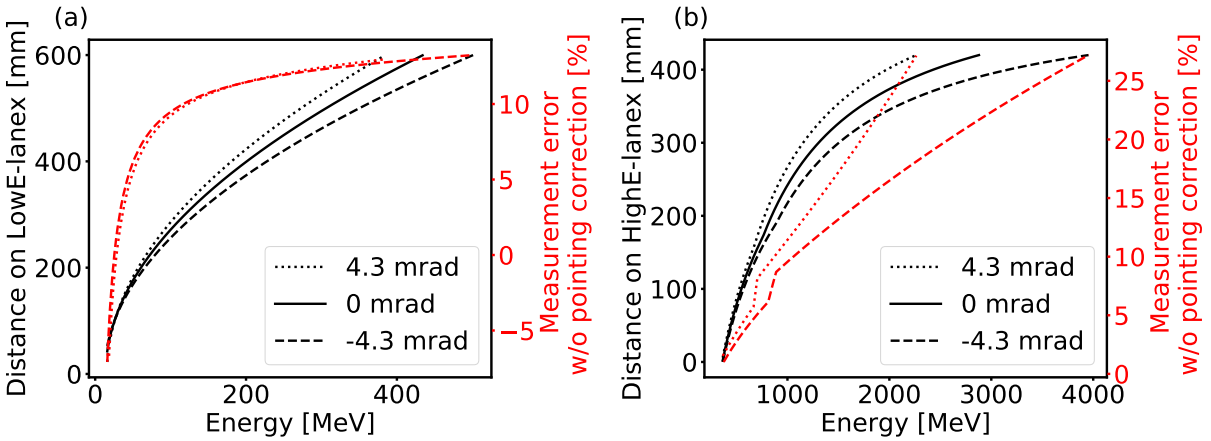

Figure 3.16.: Distance on the **(a)** 'LowE-lanex' and on the **(b)** 'HighE-lanex' for electrons with different energies between approximately 12 MeV and 3 GeV that could be measured with the current setup. The relation is plotted for a straight pointing of the electron beam and as an example for electron beams pointing ±4.3 mrad up and down, respectively.

emission was calibrated [172, 188] to constant light sources, i.e., Tritium capsules, that are located next to the screens. By comparing the intensity of the fluorescence to the intensity of these light sources, the amount of electrons impinging on the screens, hence the charge of electron beams, can be evaluated. The divergence of electron beams can be obtained by measuring the width of the fluorescence emission on the screens.

From the position along the z-direction of the fluorescence light on the screens, the energy of the electrons can be evaluated. In Figure 3.16, the energy of electrons is plotted against the distance on the lanex-screens below the magnet ('LowE-lanex': Figure 3.16a) and behind the magnet ('HighE-lanex': Figure 3.16b), which is obtained from the electron trajectories calculated using Equation (3.14).

Another scintillating screen (pointing screen) is placed before the entrance of the magnet and imaged onto a 12-bit CMOS camera. From this, the pointing of the electron beams and, hence, the entrance location and angle of the beams into the magnet could be obtained. This information is needed due to electrons with different pointing propagating on different paths in the magnet, as seen in Figure 3.15.

As an example, the relation between the distance on the lanex-screens and the electron energy for high-pointing (4.3 mrad) and low-pointing (−4.3 mrad) beams is plotted in Figure 3.16. Most measurements in this work were within the range of pointing ±4.3 mrad up or down. Only very few shots were reaching values of up to ±8 mrad. The pointing screen was able to measure pointings of approximately ±8.8 mrad. The measurement error for evaluating the electron energy without taking the pointing of the electron beams into account is plotted in red for different energies for beams pointing ±4.3 mrad up and down, respectively. Without measuring the pointing, the measured distance on the lanex-screens would under-

estimate the electron energy for low-pointing beams and overestimate the energy for high-pointing beams. Only for very low energies (below $\sim 30\,\mathrm{MeV}$), the electrons change direction in z while still in the magnet. In this case, the energy is underestimated for high-pointing and overestimated for low-pointing, which results in negative values of the measurement error in Figure 3.16a. For energies over $\sim 30\,\mathrm{MeV}$ on the LowE-lanex, the error is small for low energies and gets larger with increasing electron energies. This is due to the focusing effect of the magnet, which bends the electron trajectory of high-pointing beams stronger than low-pointing beams. The focus for low energy electrons is close to the lanex-screens and moves further away for high energy electrons as can be seen in Figure 3.15. For the LowE-lanex, the measurement error for pointings of $\pm 4.3\,\mathrm{mrad}$ reaches over 10 % for energies around 300 MeV. On the HighE-lanex, the measurement error also increases with increasing electron energies. Here, a step in the measurement error around 750 MeV is notable. This step results from electrons below 750 MeV leaving the magnetic field at the bottom of the magnet, while electrons with higher energies leave the field at the end of the magnet.
From this step onwards, the measurement error rises steeply, reaching over 10 % for 1 GeV and reaching roughly 25 % for 2 GeV beams pointing up by 4.3 mrad. Therefore, it is advisable to account for the pointing of electron beams for evaluating energies close to 2 GeV. As energies above 2 GeV were a goal of this work, the pointing of electron beams was always measured in this work, and the electron energy was evaluated with taking the pointing into account. This was done for all data that will be presented in Sections 4 and 5.
It has to be noted that the measurement of the pointing results in an increase in the divergence of the electron beams due to their passing through the pointing screen. This results in a broadening of the measured spectra in both horizontal and vertical directions. The broadening in the vertical direction reduces the energy resolution of the spectrometer. A correction of this effect is not possible as the pointing screen offers no information on the electron energy. The energy resolution can be estimated by the measured horizontal divergence of the electron beams, which was in this work between roughly 0.35 and 0.8 mrad (RMS of Gaussian fit) for electron beams around 2 GeV and approximately 0.5 mrad for beams around 1 GeV. Assuming these values also in the vertical direction, the energy resolution around 1 GeV was approximately 18 MeV and around 2 GeV between 47 MeV and 104 MeV.

4. Electrons from two Injection Mechanisms in a Gas Cell

In our pursuit of generating stable, quasi-monoenergetic electron beams at an energy of 2.5 GeV with low divergence for the planned Breit-Wheeler experiment at CALA (cf. Chapter 1), we tested various gas targets and injection mechanisms. In this chapter, we present experimental results on the performance of gas cells, which are common targets in LWFA experiments [33, 88, 103, 118]. The steady-state flows in properly designed gas cells provide homogeneous density profiles [118]. This quality facilitates the reproducible acceleration of electrons and can result in stable electron beams. Therefore, gas cells are promising candidates as targets for the Breit-Wheeler experiment. Furthermore, we can easily extend the length of gas cells to provide the required acceleration lengths for the acceleration to GeV energies.
In this chapter, we present self-injection results obtained with a newly designed gas cell (Section 4.1) and show a length scan of the gas cell to investigate the limits of the acceleration process (Section 4.2). The details of the gas cell design are described in Section 3.4.1. Furthermore, we show the first attempts of using optically-induced shock injection (cf. Section 3.6) in a gas cell with the goal of injecting electrons in a controllable way and obtaining quasi-monoenergetic electron beams (Section 4.3).

4.1. Self-injected electrons beyond 2 GeV

For a first characterization, the gas cell was tested in the self-injection regime (cf. Section 2.6.4). In this experiment, the laser was used in the first configuration (see Figure 3.1) with (6 ± 1) J energy in the central disk of the focus and a f/56 focusing geometry.
Figure 4.1 shows electron spectra from a set of 20 consecutive shots. During this experiment, the plasma density was $(1.0 \pm 0.1) \cdot 10^{18}\,\mathrm{cm}^{-3}$ and the cell length 20 mm. As visible in Figure 4.1, the energies of the self-injected electrons reach energies exceeding 2 GeV. Table 4.1 contains averaged key parameters of the data set plotted in Figure 4.1. A cut-off energy of (2.223 ± 0.070) GeV (mean value and

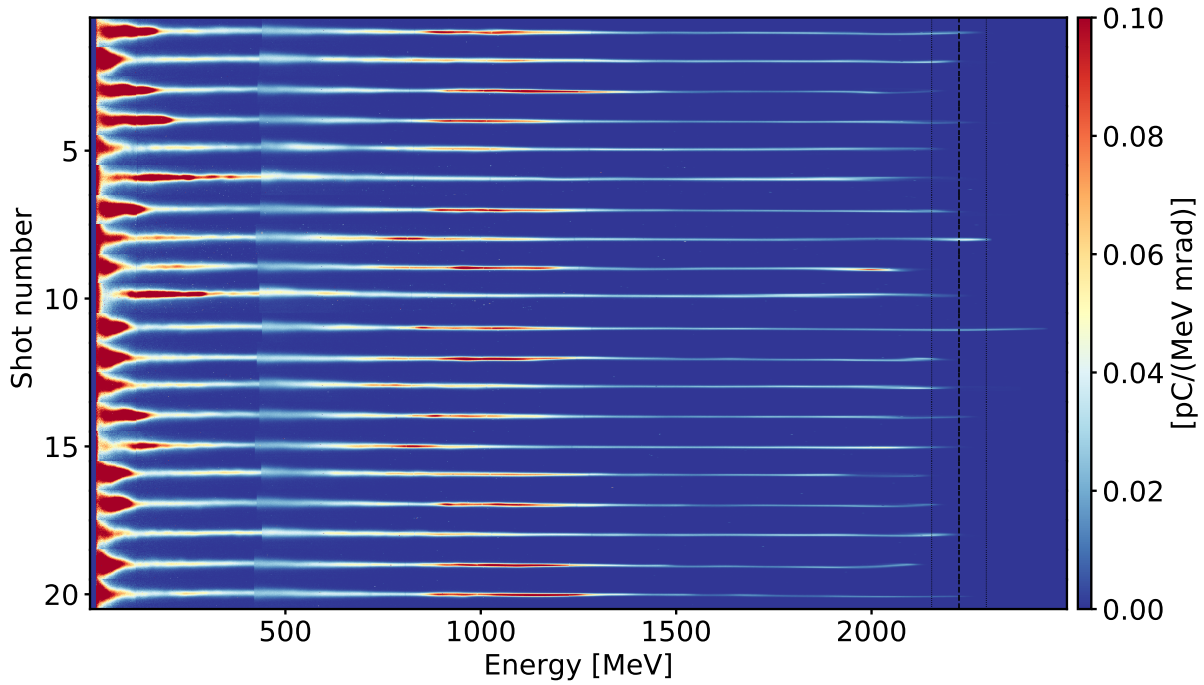

Figure 4.1.: Electron spectra from a set of 20 consecutive shots of self-injected electrons obtained with the gas cell at a cell length of 20 mm and a plasma density of $(1.0 \pm 0.1) \cdot 10^{18}\,\mathrm{cm}^{-3}$. Black dashed lines indicate the mean cut-off energy and corresponding standard deviation. The range of divergence angles covered in the plots is ± 5.4 mrad. This data set was obtained on 29/03/2022 (Set 25).

standard deviation) is reached. Here, the cut-off energy is defined as the energy where the spectral charge density falls to 2 % of the measured peak spectral charge density over 500 MeV. A Gaussian fitted RMS-divergence of (0.32 ± 0.05) mrad (mean value and standard deviation in a range of 500 MeV below the cut-off energy) is measured.
In the literature, other examples are found (e.g. [34, 103, 189]) where energies between 2 and 2.5 GeV were reached with self-injection in gas cells. All three publications show higher divergence (between 0.6 and 1.4 mrad) than in our case.

Cut-off energy	(2.223 ± 0.070) GeV
Total charge	(199 ± 22) pC
Charge over 1 GeV	(37 ± 4) pC
Charge over 1.5 GeV	(12 ± 4) pC
Charge over 2 GeV	(3 ± 1) pC
Divergence	(0.32 ± 0.05) mrad

Table 4.1.: Electron parameters related to the data of Figure 4.1 (self-injection in a gas cell). The mean value of 20 shots and its standard deviation are given.

However, most electrons in our data set are accelerated to energies below 1 GeV. On average (37 ± 4) pC are measured above 1 GeV, below 20 % of the measured total charge. Additionally, no quasi-monoenergetic features are observed. In the other examples in the literature of self-injection in gas cells, Wang et al. [34] and Kim et al. [103] were able to obtain quasi-monoenergetic features but with less energy stability of 33 % and 12 %, respectively. Other injection mechanisms might have to be tested to achieve stable, quasi-monoenergetic beams with the gas cell.

4.2. Length scan of the gas cell

To investigate acceleration limits for the current experimental approach, the acceleration length was varied by changing the length of the gas cell between 5 mm and 30 mm. Figure 4.2a shows electron spectra for 6 sets of 20 consecutive laser shots, each recorded at different lengths of the gas cell. The data shows that the mean cut-off energy first increases with increasing acceleration lengths. The maximum mean cut-off energy is measured at a gas cell length of 20 mm. At longer cell lengths, the mean cut-off energy decreases.
At this point, we can check whether our data allows for conclusions about the acceleration limits. If the acceleration process in the bubble regime is limited by dephasing, the electron energy vs. the acceleration length follows a parabolic profile [142, 190] with a maximum at the dephasing length. After reaching the dephasing point, the electron energy decreases due to the electrons reaching the decelerating phase of the wakefield. If the acceleration process is limited by depletion, the energy would stay roughly constant once the acceleration process stops. If the depletion length is shorter than the dephasing length, the maximum of the parabola will not be reached. If the dephasing length and the depletion length are exactly matched, the acceleration process would stop at the maximum of the parabola. Figure 4.2b shows the cut-off energy of the data in Figure 4.2a as a function of the cell length. The data seems to follow roughly a parabolic shape with a maximum around 20 mm, which could indicate a dephasing-limited acceleration process. A parabolic fit yields a dephasing length of (22.7 ± 2.3)mm and a maximum accelerating field of (200 ± 43)GV/m via the gradient of the parabola at the zero-crossing. The gradient obtained from the fit is in good agreement with the value obtained from a model covering the bubble regime (calculated using Equation (2.62)). The value of the dephasing length is close to the theoretical value (calculated using Equation (2.71)) and deviates by roughly 14 %. All values from theory and the fit to experimental data are summarized in Table 4.2.
The theory of the bubble regime predicts that the depletion length (calculated with Equation (2.70), see Table 4.2) is smaller than the dephasing length (see also Equation (2.72): $\frac{2}{3}\frac{2\sqrt{a_0}}{k_p} > c\Delta\tau_I$ for our parameters). The acceleration process is,

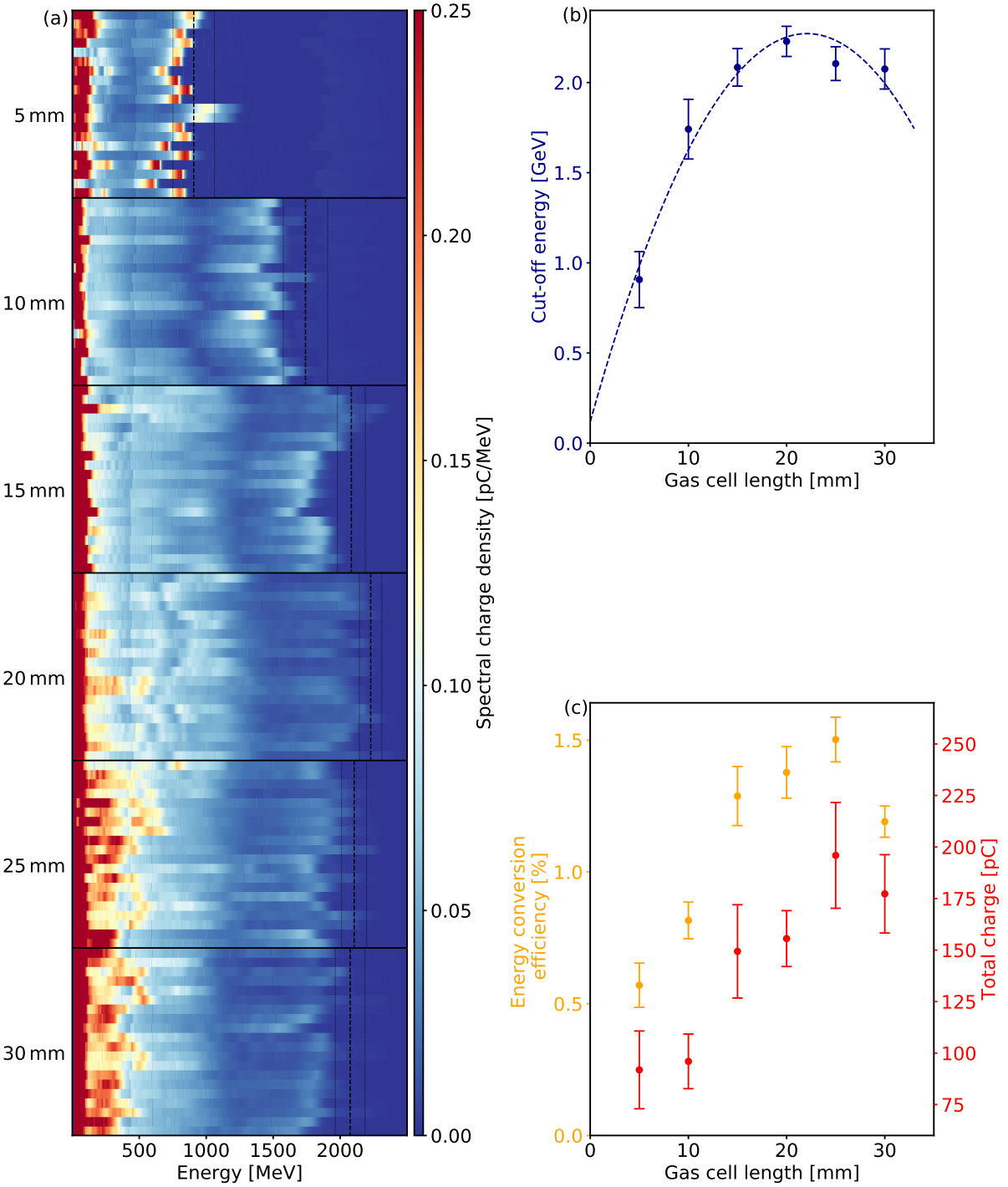

Figure 4.2.: Scan of the gas cell length. **(a)** Waterfall plot of electron spectra of 20 consecutive shots at each cell length. Black dashed lines indicate the mean cut-off energy of each set with its standard deviation. The cell length is indicated next to the figure. **(b)** Mean cut-off energy vs. the cell length. **(c)** Mean total charge and mean energy conversion efficiency vs. cell length. Error bars indicate the standard deviation of the mean values. These data sets were obtained on 29/03/2022 (Sets 32-36;40).

	Theory	Experiment (Parabolic fit)
Dephasing length	26.3 mm (Eq. 2.71)	(22.7 ± 2.3)mm
Depletion length	15.7 mm (Eq. 2.70)	-
Guiding length	14.3 mm (Eq. 4.1)	-
Rayleigh length	9.3 mm	-
$E_{z,\max}$	205 GV/m (Eq. 2.62)	(200 ± 43)GV/m

Table 4.2.: Comparison between values from theory (cf. Sections 2.6.3 and 2.6.5) and the fit to the experimental data for the scan of the gas cell length.

thus, predicted to be limited by depletion and the termination of the self-guiding process when the depleted power reaches values smaller than the critical power for self-focusing (cf. Section 2.5). A 'guiding length' can be calculated using the depletion length:

$$L_{\text{guid}} = \left(1 - \frac{P_c}{P}\right) L_{\text{depl}}. \tag{4.1}$$

The self-guiding process would terminate roughly after this length, and diffraction would start to affect the beam propagation, which contributes to the termination of the acceleration process. For our parameters, $L_{\text{guid}} = 14.3\,\text{mm}$. Therefore, according to the theory covering the bubble regime, the parabolic dependence of the electron energy on the acceleration length is predicted to stop before reaching the maximum of the acceleration parabola due to depletion and diffraction.
Indeed, the data can also be consistent with this interpretation: the cut-off energy only follows a parabolic profile for small acceleration lengths. Between acceleration lengths of $15 - 20\,\text{mm}$, the electron energy stagnates, as would be the case for a depletion-limited acceleration process. Considering the error bars of the measurements (see Figure 4.2b), this interpretation is also valid. The value of 15 mm is close to the theoretical depletion and guiding termination lengths (cf. Table 4.2). To confirm this interpretation, a longer gas cell would be beneficial to obtain more data points at longer cell lengths. This could confirm a stagnation of the energy instead of a strong decrease in energy for long acceleration lengths, as would be the case for a dephasing-limited process. Alternatively, the scan could be repeated at a higher plasma density, resulting in shorter depletion and dephasing lengths.
In any case, the parabolic fit could still be valid for small cell lengths, where the cut-off energy would follow a parabolic shape, also for the depletion-limited case. The fact that the maximum acceleration gradient determined from the parabolic fit to the data in Figure 4.2b is in good agreement with the theoretical value supports this assumption.

In Figure 4.2c, the total charge and the energy conversion efficiency are plotted against the gas cell length. For gas cell lengths from 5 mm to 20 mm, electrons are accelerated to increasing cut-off energies. At the same time, more charge is injected for longer cell lengths since electrons are injected continuously along the acceleration length. Therefore, total charge and energy conversion efficiency increase. Extending the length of the gas cell even further (30 mm) leads to a decrease in conversion efficiency and total charge due to the slightly decreasing mean cut-off energy.
The data presented so far demonstrates that self-injection in gas cells at our current laser parameters can produce electrons with energies exceeding 2 GeV, nearly reaching the energies that are needed for the Breit-Wheeler experiment. With more laser energy and a longer cell length, 2.5 GeV should readily be reached with self-injection in the gas cell. Moreover, the electron beams are relatively stable and have rather low divergence angles, which are also prerequisites for the Breit-Wheeler experiment. However, a major drawback of electron beams from self-injection is their large bandwidth, making them disadvantageous for many applications such as FELs, where small bandwidth electron beams are necessary [42]. For the Breit-Wheeler experiment planned at CALA (cf. Chapter 1), quasi-monoenergetic beams are also required since charge at lower energies contributes solely to background radiation, degrading the signal-to-noise ratio in measurements of Breit-Wheeler pairs [24]. In the next section, we present an approach to generate quasi-monoenergetic electron beams using injection at an optically-induced density shock in the gas cell.

4.3. Optically-induced shock injection in a gas cell

One way to generate quasi-monoenergetic beams is by using shock injection (cf. Section 2.6.4). However, gas cells do not support supersonic gas flow, which is a fundamental requirement for conventional obstacle-induced shock injection. To circumvent this, we employed an optically-induced shock injection scheme described in Section 3.6. To enable the formation of a shock in the up-ramp of the gas profile, an injector beam passes perpendicularly to the driver laser propagation direction through a hole in the gas cell close to the entrance pinhole (cf. Figure 3.5).
Figure 4.3 shows electron beams generated in the gas cell, once with the injector beam (Figure 4.3a) and once without the injector beam (Figure 4.3b). The sets were taken consecutively under otherwise identical experimental conditions. The plasma density could not be measured on that day due to problems with the interferometry setup. However, at 50 mbar, the backing pressure was the same as for the sets in Figure 4.1 and 4.2. Therefore, a plasma density of approximately $1 \cdot 10^{18}\,\mathrm{cm}^{-3}$ can be assumed. The cell was 10 mm in length, an f/33 focusing

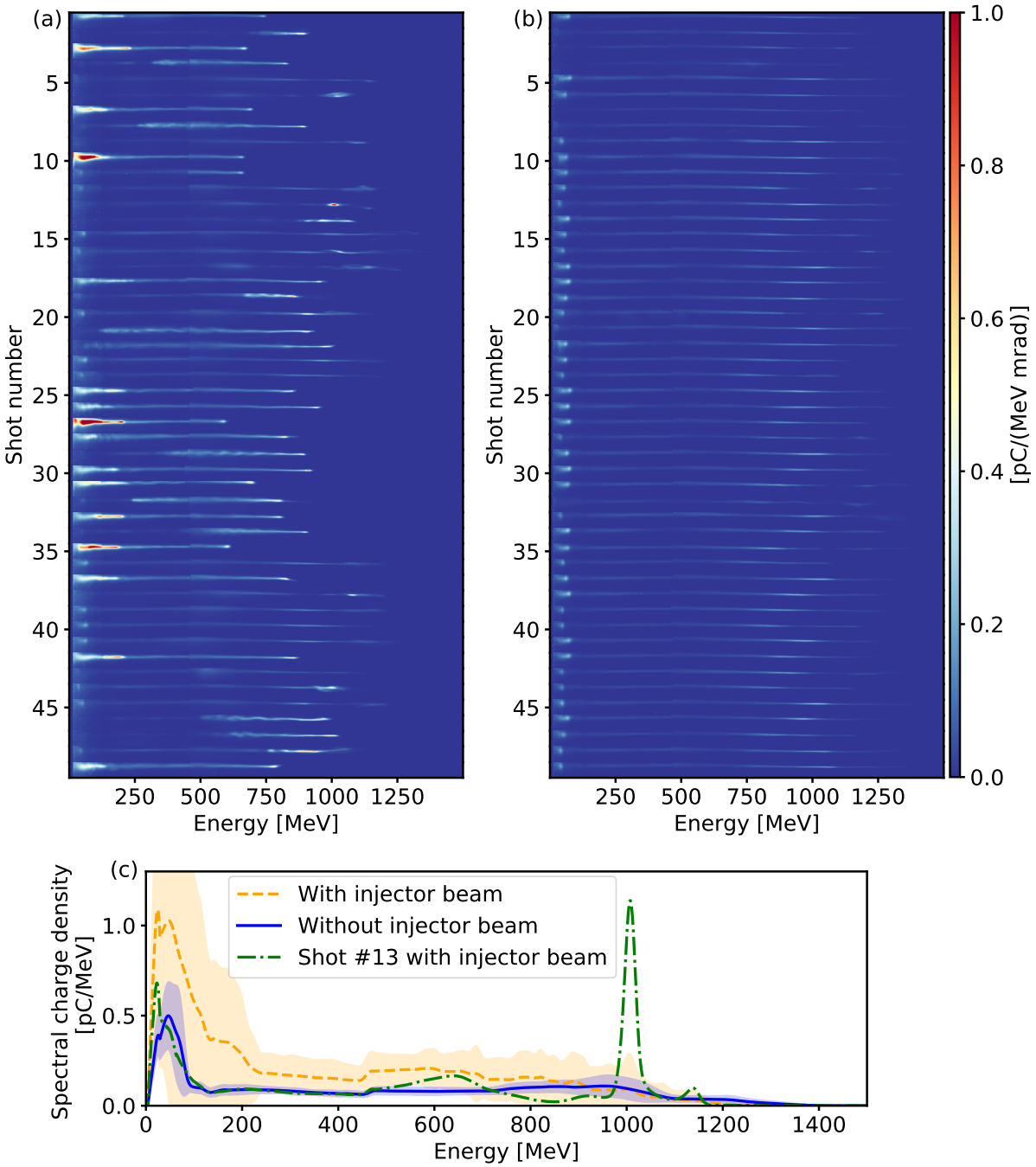

Figure 4.3.: Comparison between sets **(a)** with and **(b)** without the injector beam in the gas cell. The length of the gas cell was 10 mm. **(c)** Mean line-outs of the data with and without injector beam. The standard deviation is indicated with the shaded area. The green dashed-dotted line is the line-out of a single shot with the injector beam, where a quasi-monoenergetic beam around 1 GeV was injected. These data sets were obtained on 04/10/2021 (Sets 12/13).

geometry was used (cf. Section 3.2), and the energy in the central disk of the focus was (5 ± 1) J.
A clear difference between the set with injector and the set without injector beam is visible as more charge is injected when the injector beam is enabled (mean total charge of (253 ± 126) pC vs. (121 ± 27) pC without injector beam). This is also seen in the mean line-outs shown in Figure 4.3c. Some of the electron bunches injected with the optical injector are quasi-monoenergetic, as expected for shock injection. The line-out of a single shot from the data in Figure 4.3a is plotted in Figure 4.3c, showing a pronounced peak around 1 GeV. However, most other beams in the set with injector have lower peak energies and exhibit long tails towards low energies. This indicates that the injection process is not optimized yet. Laser intensity, plasma density, and injection position must be adjusted perfectly in order to generate high-quality shock-injected beams [168]. We assume that a combination of low intensity before self-focusing and low density in the gradient before reaching the plateau inside the gas cell is the reason for non-optimal injection (cf. Section 2.6.4). Other tests were conducted with the f/56 focusing geometry, as was used for the data in Figure 4.1. This configuration was also used to generate high-quality shock-injected beams with slit nozzles as targets (cf. [168] and Chapter 5). However, only low-charge and low-energy electron beams were observed with the gas cell setup in the latter configuration, suggesting that it yields even less suitable conditions for injection. Hence, low intensity of the driver is very likely a reason for the non-optimal injection in both cases since the f/56 focusing geometry results in a larger focal spot and, therefore, less intensity than the f/33 configuration.
More tests would have to be conducted to optimize the laser intensity and the injection position. As the hole for the injector beam is only 0.5 mm in diameter, adjusting the injector position is impossible in the current gas cell design. With the current setup, the second ATLAS configuration (cf. Section 3.2) could provide a stronger focusing geometry (f/37) and the possibility to use more energy on target. Then, a higher intensity than in the f/33 case presented above would be reached, which should provide better conditions for high-quality injection.
Furthermore, experiments with optically-induced shock injection in gas jets produced by supersonic nozzles showed that injection of high-quality electron beams starts inside the plateau rather than in the density gradient (see Sections 5.2.3 and 5.4.1). Therefore, different gas cell designs with holes for the injector further downstream in the cell were prepared to obtain a higher plasma density at the injection point.
After the first tests in the gas cell, the optically-induced shock injection scheme was thoroughly investigated using nozzles as targets, as a scan of the injection position is easier in the gas jets produced by nozzles. The results of these studies are discussed in the next chapter. As the investigation of optically-induced shock

injection in nozzles occupied much of the remaining time available for this thesis, further tests with the already prepared new gas cell designs with different positions of the hole for the injector beam were not possible within this thesis. However, to test whether optically-induced shock injection in a gas cell can produce quasi-monoenergetic beams for the Breit-Wheeler experiment with higher stability than in gas jets, more experiments should be conducted with these designs in the future. A motivation for this is that the energy stability of approximately 3 % of the self-injected electron beams shown in Figure 4.1 is the most stable that was achieved in this work (for comparison, see Table A.2 for stability values with nozzles as targets). However, the next chapter will show that much can be learned from the study of optically-induced shock injection in nozzles: Conditions to achieve quasi-monoenergetic beams at 2.5 GeV were achieved that can be used to predict the required conditions in the gas cell.

5. Optically-Induced Shock Injection with Slit Nozzles

The previous chapter discussed LWFA results obtained with a gas cell. In this chapter, data from experiments using supersonic gas jets as targets will be shown. The design of the gas nozzles that were used in these experiments is described in Section 3.4.2. Just as gas cells, gas jets produced by supersonic nozzles are common targets in LWFA experiments [42, 73, 111, 191]. With nozzles, the setup is usually more compact, and the alignment procedure is easier than with gas cells, which could be an advantage in the complex Breit-Wheeler experiment planned at CALA. Furthermore, the probe beam can propagate freely through the gas without the requirement for windows, making the measurement of the plasma density easier. This also facilitates the measurement of the density gradient at the edges of the gas profile, which was not possible with the gas cell experiments presented in the previous chapter. This helps to find the best injection position for shock injection.

The possibility of generating shocks for shock injection (cf. Section 2.6.4) by introducing an obstacle into the supersonic gas flow often drives the use of supersonic gas jets as targets for LWFA experiments. As mentioned in Chapter 4, shock injection can be advantageous over self-injection due to its high degree of controllability and the usually small bandwidth of accelerated bunches, which is beneficial for many applications (cf. Chapter 1). Typically, sharp razor blades or wires are introduced into the supersonic gas flow to generate a shock. In Section 4.3, we discussed a different method using an optical injector beam (described in Section 3.6) to generate a shock via hydrodynamic optical-field-ionization (HOFI). We demonstrated that electrons could be injected at this optically-induced shock in a gas cell (cf. Figure 4.3).

Section 5.1 compares electrons injected at an optically-induced shock to those injected at an obstacle-induced shock. The optically-induced shock shows several advantages that are promising for achieving stable, high-energy electron beams as desired for the Breit-Wheeler experiment (cf. Chapter 1). Therefore, the rest of the chapter concentrates on data obtained with optically-induced shock injection: three experiments with different nozzles, laser energy on target, and focusing geometry of the LWFA driver beam will be discussed. In these experiments, we aim

Experiment (Section)		**1** (5.2)	**2** (5.3)	**3** (5.4)
Nozzle	Length	20 mm	20 mm	40 mm
	Opening angle	22.6°	22.6°	33.7°
	Width	3 mm	2 mm	1.5 mm
Laser	f-number	56	37	37
	Energy (in centr. Airy disk)	6 J	10 J	11 J
	I_0[W/cm^2]	$8.9 \cdot 10^{18}$	$3.22 \cdot 10^{19}$	$3.54 \cdot 10^{19}$
	a_0	2.0	3.9	4.1

Table 5.1.: Summary of parameters in different experiments using slit nozzles.

to achieve stable, quasi-monoenergetic beams with low divergence at the GeV level, eventually reaching 2.5 GeV for the planned Breit-Wheeler experiment. Additionally, we study the influence of several parameters, such as the injector delay, the injector position, and the gas density. In this context, we investigate the limits of the acceleration process in each case.
A short overview of the experimental parameters for the three main experiments of this chapter is given in Table 5.1. More details of each experiment are summarized in the appendix in Tables A.1 and A.2. The latter table also summarizes results for one complete set in each experiment (Figure 5.3, 5.8 and 5.11).

5.1. Optically-induced vs. obstacle-induced shock injection

Electron injection via optically-induced shocks bears several advantages: It has already been shown by our group that shocks generated via the HOFI mechanism (cf. Section 3.6) tend to be more stable than shocks generated purely hydrodynamically via an obstacle in a supersonic gas flow [110]. A stable shock is beneficial for reliably injecting stable electron beams. In this section, we additionally demonstrate that higher electron energies were achieved with optically-induced shock injection than with obstacle-induced shock injection at otherwise unchanged experimental parameters.
Figure 5.1 shows two sets of spectra from electron beams injected at the two types of shock: For the data in Figure 5.1a, the shock is generated optically, while a wire was used to generate the shock in the experiment related to Figure 5.1b. Shadowgraphy images of the two shocks are shown in Figure 5.1c,d. The shocks were set to the same position. Both sets were measured subsequently at a plasma density of $(1.0 \pm 0.1) \cdot 10^{18}\,\mathrm{cm}^{-3}$ and the parameters of the laser driver were not changed

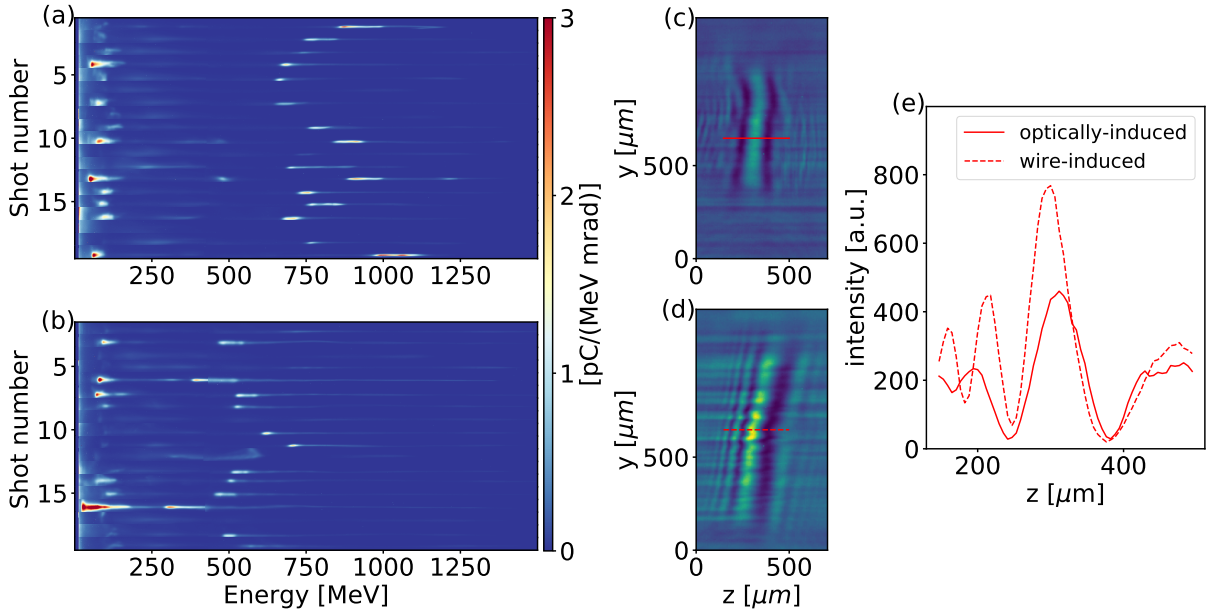

Figure 5.1.: Comparison between **(a)** electrons injected at an optically-induced shock and **(b)** electrons injected at a wire-induced shock. Wire-induced shock injection clearly yielded lower electron energies than optically-induced shock injection. Both sets show data from 19 consecutive shots. The range of divergence angles covered in the plots is ±5.4 mrad. **(c)**/**(d)** show the respective shadowgraphy images of the two shocks for the first shot of each set. The red lines indicate the positions for the line-outs shown in **(e)**. The line-outs indicate that the density ratio is larger for the wire-induced shock. These data sets were obtained on 02/05/2022 (Sets 24/27).

between the two sets. Therefore, the increase in electron energy for the electrons injected at the optically-induced shock can be attributed to shock parameters that enable the acceleration to higher energies.
A possible explanation for the lower energy in the wire-induced case is the different injection phase. In general, when electrons are injected at the density down-ramp of a shock (see explanation in Section 2.6.4), they are not injected at the back of the first bubble as for self-injection [142] but further inside the bubble. The injection phase φ_b inside the bubble for injection at the density down-ramp of a shock can be estimated via [168, 190]

$$\varphi_b = 2\pi \left(1 - \frac{R_1}{R_2}\right) = 2\pi \left(1 - \sqrt{\frac{n_2}{n_1}}\right), \tag{5.1}$$

where R_1 and R_2 denote the bubble radii and n_1 and n_2 the plasma densities before and after the density down-ramp of the shock, respectively. Here, Equation (2.59) and Equation (2.31) were used for the relation between the bubble radius and the plasma density, and it was assumed that the laser intensity a_0 is not significantly affected by self-focusing due to the change in density in the shock as it occurs over

very small length scales. The phase φ_b in the bubble is defined to be 0 at the back of the bubble and 2π at the front. Equation (5.1) suggests that electrons injected at the density down-ramp of a shock ($n_2 < n_1$) are injected at a phase position $\varphi_b \neq 0$ and, therefore, miss the highest accelerating field at the back of the bubble, and are thus limited to lower energies compared to self-injection, where electrons are injected at the back of the bubble. Equation (5.1) also shows that the injection phase is dependent on the density ratio of the shock. Electrons injected at a shock with a high density ratio are injected further inside the bubble and can, thus, gain less energy from the wakefield than electrons injected at a shock with a small density ratio. An increase in electron energy with a decreasing density ratio in shocks has also been shown in simulations by Massimo et al. [185].
The shadowgraphy images in Figure 5.1c,d and their line-outs in Figure 5.1e hint at the wire-induced shock exhibiting a higher density ratio than the optically-induced shock in this experiment. Therefore, it is reasonable to assume that the wire-induced shock injects the electrons further inside the bubble, resulting in lower energies than with the optically-induced shock.
We remark that the density ratio of the optically-induced shock can be adjusted independently, for example, by changing the delay between the LWFA driver and the injector beam as shown in Section 3.6. Thereby, the shock can be optimized to exhibit a small density ratio, such that the electrons are injected closer to the back of the bubble and can be accelerated to higher energies. Therefore, using an optically-induced shock for shock injection affords extra tuning parameters, which can be used to optimize for the desired key parameter, such as maximum energy using a small density ratio in the shock or highest charge, which is achieved with a high density ratio in the shock as was also shown in simulations in Ref. [185].
In our present experiment, we used the injector beam delay for such optimization. In Sections 5.2.4 and 5.4.2, we will discuss the influence of this parameter on the resulting electron energy and charge. The results provide further evidence for the role of the injection phase in shock injection.

5.2. Experiment 1: Electron beams at 1 GeV

In this section, we discuss the first experiment investigating the optically-induced shock injection scheme with slit nozzles. The goal of this experiment was to reach the GeV regime using slit nozzles and achieve stable, quasi-monoenergetic beams with low divergence as needed for the Breit-Wheeler experiment. Additionally, we analyzed the influence of the position and delay of the injector beam. The 1 GeV-threshold has not often been reached with shock injection. Only during the last few years, two publications [111, 114] have achieved approximately 1 GeV with shock injection. These results will be compared to our results in Section 5.5 at the end

of this chapter.
The experiment in this section was conducted using the 'ATLAS configuration 1' with a small beam size and a f/56 focusing geometry (cf. Figure 3.1). The 'ATLAS configuration 1' bypasses the last main amplifier such that the energy before compression was limited to about 20 J. However, due to the smaller beam size before the focusing optic and the longer resulting Rayleigh length, this configuration was expected to yield more stable acceleration conditions than 'ATLAS configuration 2'. For this configuration, we observed injection around a plasma density of $1 \cdot 10^{18}\,\mathrm{cm}^{-3}$. Note that for this density, a laser waist of $w_0 = (48 \pm 1)\mu\mathrm{m}$ and $a_0 = 2.0 \pm 0.2$, the guiding condition is not matched (Equation (2.60)): $k_p w_0 \approx 9.1 \gtrapprox 2\sqrt{a_0} \approx 2.8$.
As the power in the experiment ($\sim \pi I_0 w_0/2 \approx 330\,\mathrm{TW}$) was larger than the threshold for relativistic self-focusing at $1 \cdot 10^{18}\,\mathrm{cm}^{-3}$ ($P_c \approx 29\,\mathrm{TW}$), we expect the laser to self-focus to the matched spot size and reach the matched value of $a_0 \approx 4.5$ that can be calculated via Equation (2.61). With this value, the bubble regime is reached, which is valid for $a_0 \gtrsim 4$. However, a nearly spherical shape is built for $2 \lesssim a_0 \lesssim 4$ [142], such that the theory of the bubble regime also poses a valid approximation for the propagation distance where self-focusing occurs and a_0 is between the vacuum value of 2.0 and the matched value of 4.5. However, the associated guiding process that occurs while the power is higher than P_c will not be stable and the bubble size will oscillate, such that predictions from the theory might deviate from measurements in this regime. On the other hand, the theory predicted the energy gain in the gas cell experiments in the previous chapter (Chapter 4) reasonably well, which was conducted in the same regime. Therefore, the results in this section will also be compared to the theory of the bubble regime. All parameters of the experiment are summarized in Tables A.1 and A.2. The data discussed in this section was published in [168].

5.2.1. 1 GeV electron beams using a 20 mm slit nozzle

The data sets in this section were obtained using a 20 mm-long slit nozzle. In a first step, we measured the associated density profile of the plasma (shown in Figure 5.2a) using an interferometric imaging setup described in Section 3.5. In this experiment, the field of view did not cover the full extent of the slit nozzle. Under the assumption that the density profile is symmetric with respect to the center of the nozzle, we mirrored the measurements. The correct mirror plane was found with respect to the edge of the nozzle seen in the raw interferometry images (example in Figure 5.2b). The mirrored data points are indicated in Figure 5.2a. We further assume the density to be roughly constant around the central part of the nozzle. The density profile thus consists of a density plateau around the center of the nozzle with a quasi-monotonic increase/decrease of the plasma density

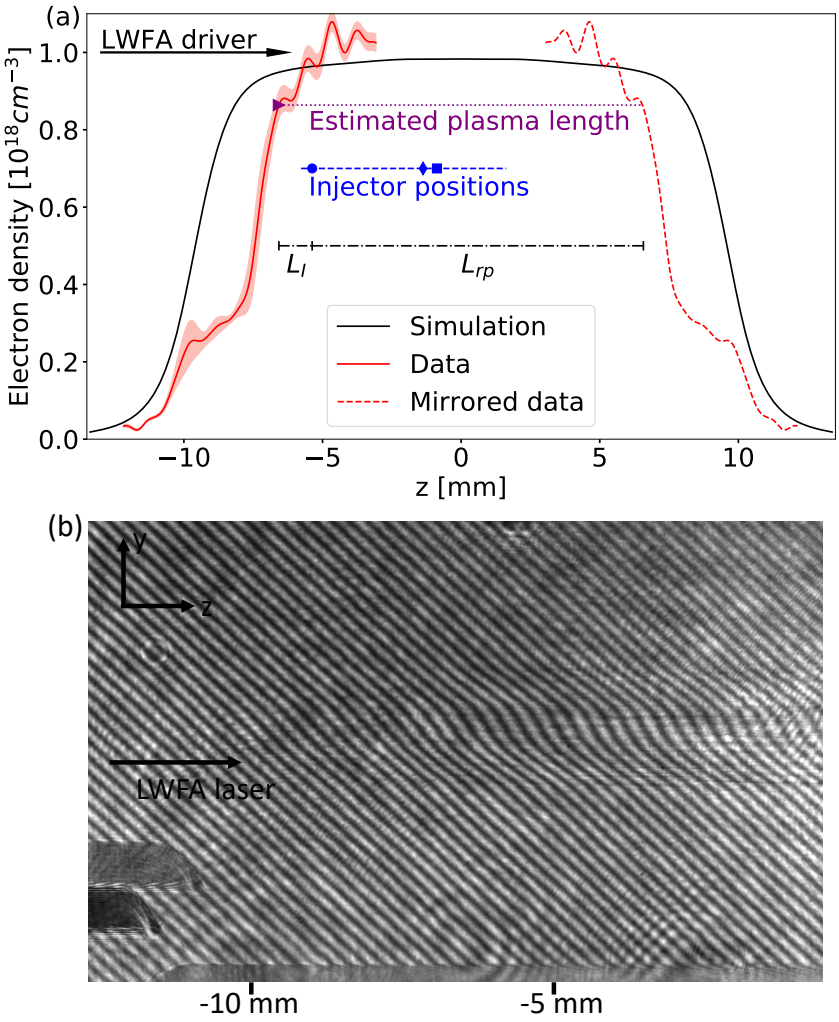

Figure 5.2.: (a) Measured and simulated plasma density of the gas jet produced by the 20 mm slit nozzle used in 'experiment 1'. The interferometry measurement was performed at an inlet pressure of (2.60 ± 0.02) bar and at a distance of (4.2 ± 0.2) mm between the driver laser axis and the nozzle. The red solid line shows the mean of five measurements. The standard deviation of the measurements is indicated by the shaded area. The purple triangle marks the defined start of the plasma and the estimated plasma length is shown with a purple dotted line. The blue circle and diamond indicate injector beam positions for the experiment related to Figure 5.3, the square for the experiment related to Figure 5.6, and the dashed blue line indicates the scan range in the experiment related to Figure 5.5. The driver laser propagates through the plasma from left to right. The black line shows the result of a CFD simulation. In the simulation, the inlet pressure was set to 2.6 bar, and the line-out is shown for a height of 4.2 mm above the nozzle. A similar figure was published in [168]. **(b)** One of the raw interferometry images that was used for the analysis is shown. The data for this measurement was obtained on 26/04/2022 (Sets 38-42).

towards both sides. To estimate the length of the plateau, the plateau was defined to start at 80 % of the measured peak density (indicated with a purple triangle in Figure 5.2a). The plateau length for the gas jet produced by the 20 mm slit nozzle

is approximately (13.0 ± 0.5) mm (see Figure 5.2a).
Figure 5.2a also shows the result of a CFD simulation of the plasma density for this nozzle design (cf. Section 3.4.2). The density profile predicted by these simulations reaches a similar plateau density but exhibits some qualitative difference with respect to the measurements. In particular, the step at around -9 mm is not reproduced by the simulation. A potential reason for this discrepancy is that the nozzle was 3D-printed, resulting in a larger surface roughness of the inside face in the diverging part of the nozzle compared to nozzles fabricated from stainless steel. Therefore, the density step might be caused by a turbulence layer at the boundary between the supersonic flow and the nozzle wall, as discussed by Schmid [119]. However, for the LWFA experiment, this density step can be assumed to have a minor influence on the propagation of the laser because of its low density and short width. The oscillations in the plateau of the measured density distribution can also be caused by the surface roughness of the printed nozzle or by noise in the interferometric measurement (cf. Appendix B).

After discussing the properties of the plasma created by the 20 mm slit nozzle, we now show data of experiments testing this nozzle with the goal of reaching GeV energies. Figure 5.3 shows spectra of electron beams that were measured at a plasma density of $(1.0 \pm 0.1) \cdot 10^{18}\,\mathrm{cm}^{-3}$ (average and standard deviation over the plateau length). In this experiment, the optical injector was positioned at $L_I = 1.2$ mm from the beginning of the plasma (i.e. at $z = -5.25$ mm in Figure 5.2a). Here, we assume a systematic error of ± 0.25 mm from measuring the distance from the beginning of the plasma to the injector position in probe images and a statistical error of ± 0.05 mm from the jitter of the optical shock in the probe images. The injector beam arrived 270 ps before the main laser pulse with a systematic error of ± 2 ps and a statistical error of ± 0.17 ps.
The data in Figure 5.3a demonstrates that this configuration yields a relatively stable electron performance at the GeV level. The peak energy of the set is (980 ± 83) MeV (mean peak energy and standard deviation of the set). The cut-off energy reaches beyond 1 GeV and is (1.086 ± 0.076) GeV (mean and standard deviation). Here, the cut-off energy is defined as the energy where the spectral charge density decreased to 20 % of the measured peak spectral charge density. This definition will be used in the rest of this chapter. However, the value of 20 % of the measured peak spectral charge density would underestimate the cut-off energy for data sets where very high peak spectral charge densities are measured while a long tail reaches to higher energies. In this case, the definition was adjusted, depending on the set, to 10, 5, 2 or 1 % of the measured peak spectral charge.
Within the energy range around the peak where the spectral charge is > 20 % of the peak spectral charge, the bunches contain a mean charge of (92 ± 56) pC with a mean Gaussian-fitted RMS divergence of (0.49 ± 0.05) mrad.
The mean FWHM energy spread around the peaks amounts to (94 ± 27) MeV. As

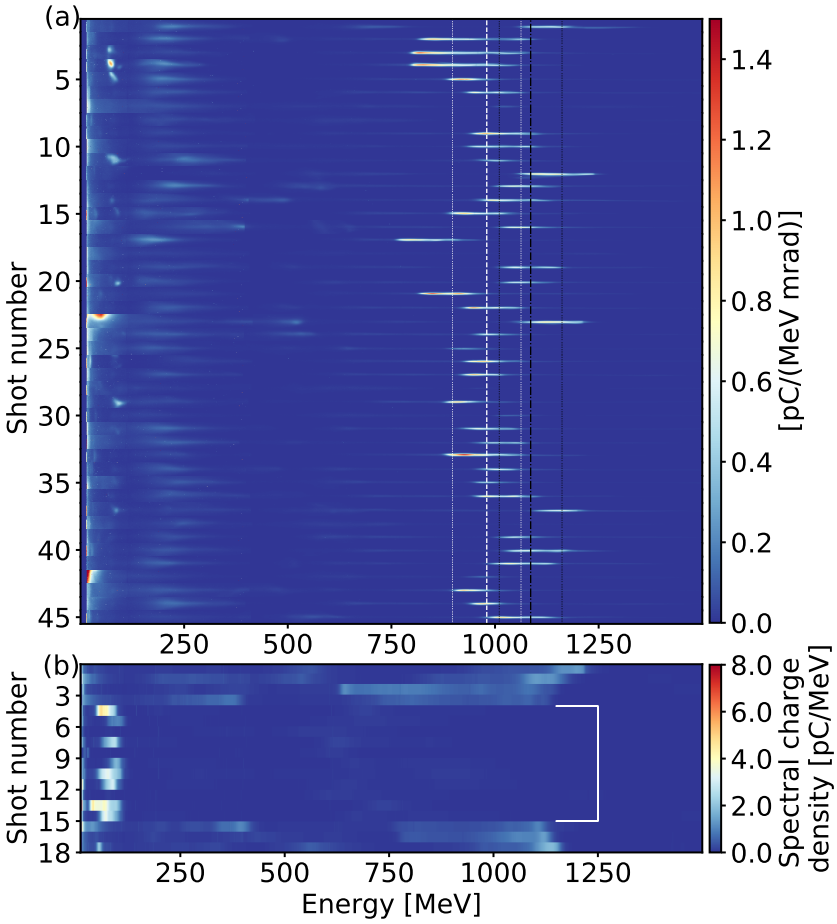

Figure 5.3.: Electron spectra obtained with a 20 mm-long slit nozzle (plasma density $(1.0 \pm 0.1) \cdot 10^{18}\,\mathrm{cm}^{-3}$) and optically-induced shock injection. **(a)** The peak electron energy reaches values around 1 GeV for almost every measurement in this set of 45 consecutive shots. The white lines indicate the mean peak energy over the full set and the corresponding standard deviation. Black lines indicate the mean cut-off energy and the corresponding standard deviation. The range of covered divergence angles is ± 5.4 mrad. **(b)** The injector beam is switched off for several shots (5-15; marked by the white bracket), demonstrating that no high-energy electrons are generated in this case. In this plot, the spectra are integrated over the width of the detector focal plane. A similar figure was published in [168]. These data sets were obtained on 26/04/2022 (Sets 16/17).

discussed in Section 3.7, the energy measurement is limited in resolution by the divergence of the beam in vertical direction, which can be estimated by the measured divergence in horizontal direction. This fact also limits the measurement of the energy spread. With a divergence of approximately 0.5 mrad at 1 GeV the energy resolution is roughly 18 MeV. Therefore, the actual FWHM bandwidth should rather be around 7.8 % than the measured 9.6 % that includes the divergence of the electron beam.

Considering the spectral distribution of the charge, we obtain a mean energy conversion efficiency of 1.5 % in the energy range around the peak where the spectral

charge is $> 20\,\%$ of the peak spectral charge. In the whole range accessible by the spectrometer in this experiment (12 MeV to 1.5 GeV), we measured a total charge of (318 ± 78) pC, yielding a total energy conversion efficiency of 2.5 %. Therefore, 60 % of the converted laser energy is transferred to the peak around 1 GeV. All values are summarized in Table A.2.
Figure 5.3a demonstrates that beams with nearly 100 pC in the peaks at 1 GeV can be reached with a laser energy of (6 ± 1) J (in central Airy disk) but without the need of an external guiding structure, such as capillary discharge waveguides [87, 192] or hydrodynamic optically-field-ionized (HOFI) channels [154, 193]. Recent results by Oubrerie et al. [111], where lower laser energy was used with a smaller spot size, yielded similar values regarding energy, bandwidth, and divergence, but less charge in the bunches (roughly 20 pC mean charge in the peaks). These experiments required an external guiding structure to overcome the diffraction limit. Our approach with higher laser energy and a long vacuum Rayleigh length (~ 9 mm) yields a higher charge in the bunches. Hence, we demonstrated that 1 GeV electron beams with similar quality as other results in the community and relatively high charge can be generated with our slit nozzle design without the additional complications of an external guiding structure.
Energy and charge could be further optimized individually in this experiment using the degrees of freedom available for the optically-induced shock, as will be shown in Section 5.2.4. However, the regime in which the data of Figure 5.3 were recorded did yield a combination that, if reached at higher energy, could be usable for the Breit-Wheeler experiment planned at CALA: Here, the goal is stable, quasi-monoenergetic electron beams with approximately tens of pC of charge at an energy of 2.5 GeV with a small divergence (see Section 1.2). It has to be noted that a combination of all of these requirements is, in this case, more important than the best possible value of one of these parameters. Specifically, a very small bandwidth, as is necessary, for example, for FELs, is not strictly necessary. To reach the goal of LWFA-driven FELs, sub-percent energy spreads were already reached with LWFA[42, 71]. However, for the Breit-Wheeler experiment, a larger energy spread should be usable as long as we achieve defined bunches in the GeV regime. Furthermore, very good energy stabilities of only a few percent were reached with LWFA[43, 114], however, either at lower energies or with much lower charge than in our case. The combination of a stability of 7 % std in cut-off energy, a divergence of 0.5 mrad and a bandwidth of less than 10 % of the peak energy at 1 GeV is a good starting point for the required combination for the Breit-Wheeler experiment. Furthermore, the charge amounts to values of several tens of pC, which is a prerequisite for the Breit-Wheeler experiment, as discussed in Section 1.2. As divergence and bandwidth are both dependent on the charge of the bunch, this requirement will most likely limit the achievable bandwidth and divergence of the bunches. A complete comparison of our results of this chapter to other results of

the community will be given at the end of this chapter in Section 5.5.

As a sanity check, we turned the injector beam off during some shots in the experiment. As Figure 5.3b shows, no electron beams with $\sim 1\,\mathrm{GeV}$ peak energy are created when the injector is off. Without the injector, the total charge on the spectrometer was measured to be $(144 \pm 81)\,\mathrm{pC}$ with a total energy conversion efficiency of $0.6\,\%$, significantly less than in the set shown in Figure 5.3a. When the injector beam is switched back on after shot 15, injection around $1\,\mathrm{GeV}$ resumes. This demonstrates that it is really the optically-induced shock that results in controlled electron injection. The measurements of Figure 5.3b were taken at almost the same parameters as the set in Figure 5.3a, with the shock position $4\,\mathrm{mm}$ further downstream compared to Figure 5.3a (cf. Figure 5.2a). This change in shock position appears to influence the bandwidth of the injected bunches, which is visibly larger with a tail down to $750\,\mathrm{MeV}$.
In the next sections, we will investigate various parameter scans in the regime of 'experiment 1' to determine acceleration limits and the influence of the injector beam delay.

5.2.2. Effect of beam-loading on peak and cut-off energy

Changing the density, injector position, and injector delay not only influences the energy of the accelerated electrons but also affects the accelerated charge. Therefore, it is possible that changes detected in the electron energy are either a direct result of a parameter change or an indirect result via beam-loading effects. Beam-loading affects the energy of accelerated electron bunches via the reduction of the electric field in the wakefield due to the presence of injected charge [129]. To evaluate the direct effects of the parameter changes on the electron energy, we either need to account for beam-loading in post-processing as was done in a publication of our group written by the author of this thesis [168]. Alternatively, we need to evaluate scans using an energy metric that is barely affected by beam-loading.
To explore suitable energy metrics, we investigate whether both the peak energy and the cut-off energy are equally affected by beam-loading. The peak energy and the cut-off energy of the electron spectra shown in Figure 5.3a are plotted versus the charge in the peaks in Figure 5.4a and Figure 5.4b, respectively. A linear fit to the data is shown in both plots. The fit in Figure 5.4a yields a negative energy-charge dependence with

$$E_{\mathrm{peak}}(Q) = (1038 \pm 23)\,\mathrm{MeV} - (0.64 \pm 0.22)\,\mathrm{MeV} \times Q[\mathrm{pC}]. \tag{5.2}$$

This indicates an influence of beam-loading as shown in Götzfried et al. [74]. However, this influence is mainly visible for the peak energy. The fit in Figure 5.4b

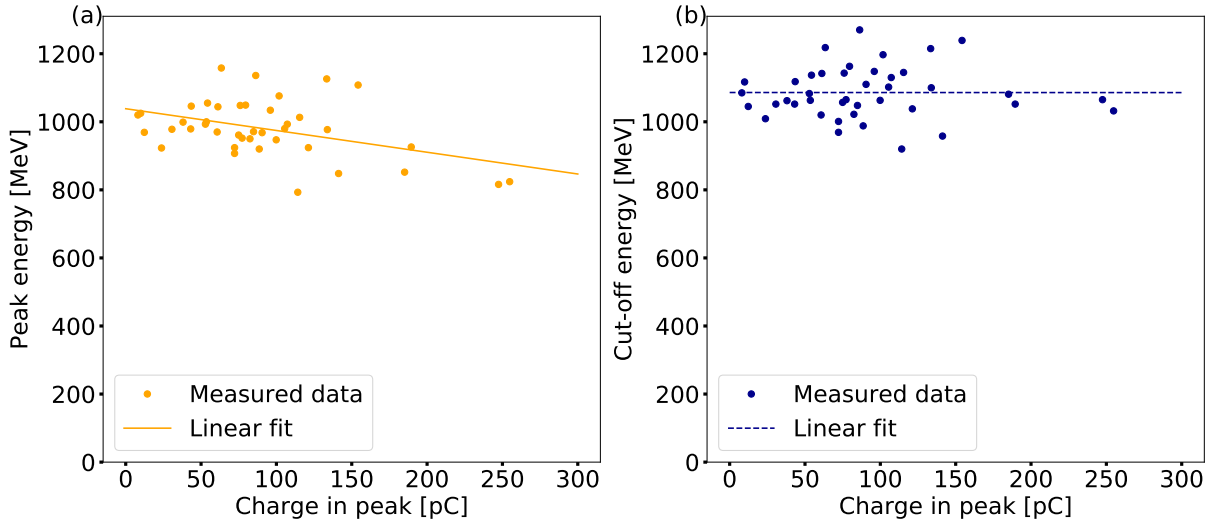

Figure 5.4.: Energy-charge dependence of data from Figure 5.3a for **(a)** the peak energy and **(b)** cut-off energy. The negative energy-charge dependence for the peak energy indicates beam-loading influences, whereas the cut-off energy shows only a very small indication of beam-loading and is less affected by the charge in the peak.

shows only a very small indication that the cut-off energy of beams with high charge is reduced due to beam-loading. The linear fit to the data in Figure 5.4b yields an energy-charge dependence of

$$E_{\mathrm{cut-off}}(Q) = (1086 \pm 23)\,\mathrm{MeV} - (0.0008 \pm 0.2)\,\mathrm{MeV} \times Q[\mathrm{pC}]. \tag{5.3}$$

The data shows that the cut-off energy is considerably less affected by beam-loading effects than the peak energy. Considering this, the parameter scans in the next sections are analyzed using the cut-off energy as energy metric. We assume then that beam-loading has a very small effect on the cut-off energy and that the parameter scans can be evaluated without correcting for beam-loading.

5.2.3. Acceleration limits

In this section, we investigate which effects limit the achievable electron energy in our experiments with the 20 mm slit nozzle in order to design future configurations for reaching even higher energies as needed for the Breit-Wheeler experiment. We perform this analysis of the acceleration limits by evaluating the energy gain as a function of the acceleration length.
As discussed in Section 4.2, the electron energy is expected to follow a parabolic profile (for acceleration in the bubble regime [142, 190]) for increasing acceleration lengths with a maximum at the dephasing length. Beyond that length,

electrons get decelerated, and the electron energy decreases again. If the acceleration process is limited by the depletion or diffraction of the driver laser before the dephasing point, the energy gain would stagnate before reaching the maximum possible energy. At our experiment parameters, the theory covering the bubble regime (cf. Sections 2.6.3 and 2.6.5) predicts a depletion-limited process as the depletion length is shorter than the dephasing length (see Table 5.2, calculated with Equations (2.70) and (2.71)). Even before the complete depletion of the driver laser energy, the relativistic self-guiding process is expected to terminate when the power reaches values below the critical power for self-focusing (cf. Section 2.5). A length over which self-guiding is expected to be maintained was calculated using Equation (4.1). All numerical values of these lengths are found in Table 5.2. Therefore, in our experiment, we expect the electron energy to stagnate before reaching the maximum of the acceleration parabola.
For all scans of the acceleration length in all three main experiments of this chapter, the position of the injector beam was fixed with respect to the driver beam. The gas nozzle was then moved along the axis of the driver beam (z-direction). The experimental setup can be seen in Figure 3.10. The remaining plasma length L_{rp} can be calculated by $L_{\mathrm{rp}} = L_{\mathrm{pl}} - L_I$ with L_{pl} the plasma length deduced from interferometry measurements and L_I the length between the beginning of the plasma and the position of the injector beam, which could also be deduced from interferometry images (see Figure 5.2a, where the injector positions are indicated along the plasma profile).
Figure 5.5 shows the data of the acceleration length scan in combination with the 20 mm slit nozzle in 'experiment 1'. The electron cut-off energy increases for increasing acceleration lengths with a maximum at a remaining plasma length of 8.5 mm. Subsequently, a decrease in cut-off energy is observed for further increasing plasma lengths. The relatively strong decrease of the electron energy is not in agreement with the theoretical prediction of a depletion-limited acceleration process in the bubble regime but would be expected from a dephasing-limited process.

	Theory	Experiment	
		Parabolic fit	Linear fit
Dephasing length	26.1 mm (Eq. 2.71)	(6.4 ± 0.5)mm	~ 8.5 mm
Depletion length	15.7 mm (Eq. 2.70)	-	
Guiding length	14.3 mm (Eq. 4.1)	-	
Rayleigh length	9.3 mm	-	
$E_{z,\max}$	203 GV/m (Eq. 2.62)	(398 ± 83)GV/m	(161 ± 13)GV/m

Table 5.2.: Comparison between values from theory (cf. Sections 2.6.3 and 2.6.5) and fits to the measured data for the acceleration length scan.

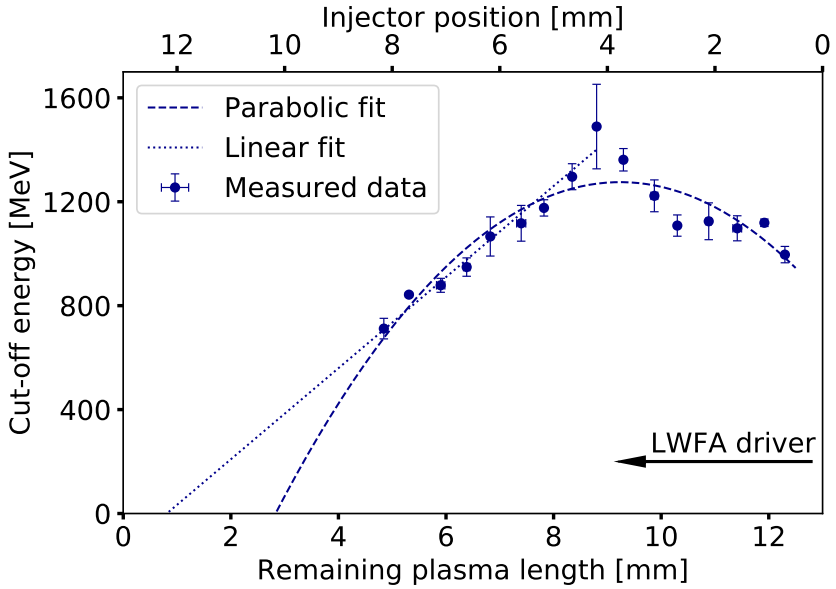

Figure 5.5.: Cut-off energy as a function of the remaining plasma length. The injector position with respect to the start of the plasma is indicated at the top (cf. Figure 5.2a). The driver laser arrives from the right. For this scan, the injector pulse arrived (270 ± 2) ps before the main beam and the plasma density was $(1.0 \pm 0.1) \cdot 10^{18}\,\mathrm{cm}^{-3}$. For the plot, the measurements for close-by injector positions were binned and averaged. The error bars show the standard error in the remaining plasma length and cut-off energy. This data was published in [168] and obtained on 26/04/2022 (Set 17).

For a dephasing-limited process, we could directly fit a parabola to the data. Such a fit yields a maximum acceleration gradient (slope of the parabola at zero-crossing) of (398 ± 83)GV/m and a dephasing length (length from zero-crossing to maximum) of (6.4 ± 0.5)mm. These values differ considerably from the theoretical predictions: for acceleration in the bubble regime a maximum acceleration gradient of 203 GV/m (Equation (2.62)) and a dephasing length of 26.1 mm (summarized in Table 5.2) is expected for our experiment parameters.
This discrepancy might be expected due to the unmatched guiding conditions and, therefore, reduced comparability to the theoretical model of the bubble regime. However, the same regime yielded results close to the theoretical predictions in the gas cell experiments shown in Chapter 4.
The very large discrepancy to theoretical values and especially the much larger maximum acceleration gradient that would rather be expected to be smaller than the theoretical prediction for unmatched guiding conditions hints at the parabola not being a suitable fit for the data. The stagnation/decrease in electron energy at long acceleration lengths could also partly be due to the depletion or diffraction of the laser. The maximum electron energy is measured at a remaining plasma length of 8.5 mm, which is close to the vacuum Rayleigh length in this experiment (9.3 mm).

In this case, a linear fit to the first part of the data at remaining plasma lengths between $5 - 8.5\,\mathrm{mm}$ can approximate the maximum acceleration gradient. The range of data with rising electron energies then corresponds to the nearly linear part of the actual, unknown acceleration parabola. A linear fit to the data (up to the data point at a remaining plasma length of 8.5 mm) yields a gradient of $(161 \pm 13)\mathrm{GV/m}$, which is closer to the theoretical value of $203\,\mathrm{GV/m}$ than the maximum acceleration gradient obtained from the parabolic fit. The fact that it is lower than the theoretical value is, on the one hand, due to the approximation by the linear fit, as the maximum acceleration gradient is actually only measured at the start of the real acceleration parabola. However, another factor, the injection phase (cf. Section 5.1), can also contribute to limiting the energy gain: With a finite density ratio in the shock, the electrons would be injected inside the bubble (cf. Equation (5.1)). They would miss the highest accelerating field at the back of the bubble. This would contribute to a lower measured maximum acceleration gradient than predicted by the theory that assumes injection at the back of the bubble. In comparison, the self-injected electron beams in the gas cell case would be injected at the rear of the bubble, where they experience the highest acceleration fields [142].
We conclude that the acceleration process is likely limited by the depletion and diffraction of the laser and that the comparison to the theory of the bubble regime is difficult in this regime due to unmatched guiding conditions. Furthermore, we suspect the advanced injection phase due to the shock injection mechanism to limit the maximum acceleration gradient and achievable energy gain. The following sections will give further evidence for this interpretation.

5.2.4. Influence of the injector delay

As discussed in Section 5.1, the optically-induced shock can be advantageous over an obstacle-induced shock since the density ratio in the shock can be adjusted independently via the delay between the injector and driver beams. The density ratio of the shock is expected to influence the injection phase (Equation (5.1)) and thus the energy gain. To investigate this further, a scan of the injector delay was conducted in 'experiment 1'.
Figure 5.6 shows the mean injected charge, the mean cut-off energy, and the mean peak energy of accelerated bunches versus the injector delay. The injected charge increases with increasing delay between the injector beam and the main beam (more negative delay means that the injector beam arrives at earlier times). A linear fit to the data yields a slope of $(-277 \pm 62)\,\mathrm{pC/ns}$. As discussed in Section 3.6, the density ratio of the optically-induced shock is larger for longer delay values between the injector beam and the driver beam. It has been shown in simulations by Massimo et al. [185] that more charge can be injected for a higher density ratio

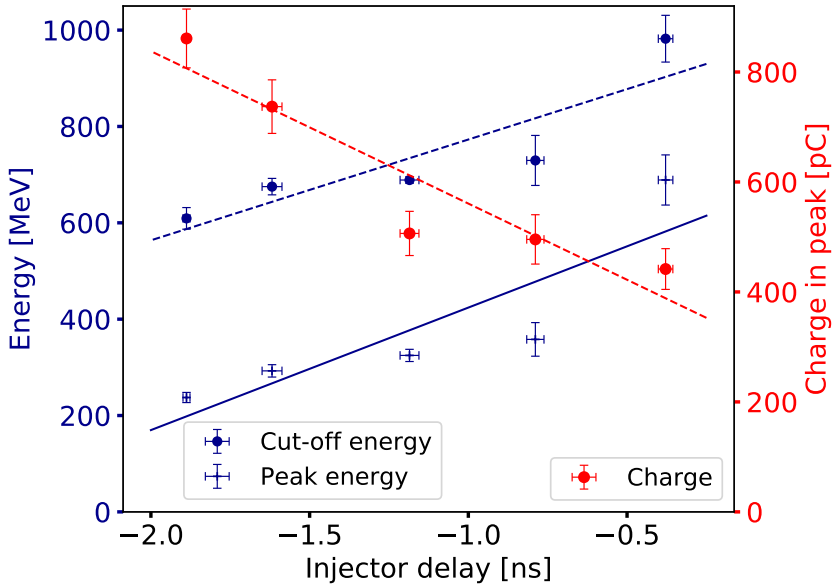

Figure 5.6.: Dependence of cut-off energy, peak energy, and charge on the injector delay. The drive laser arrives at time 0. The injector position in this scan was $L_I = 5.7\,\text{mm}$ from the start of the plasma, corresponding to a remaining plasma length of $L_{\text{rp}} = 7.3\,\text{mm}$. The plasma density was $(1.1 \pm 0.1) \cdot 10^{18}\,\text{cm}^{-3}$. For the plot, the measurements for close injector timings were binned and averaged. The error bars show the standard error in injector delay, cut-off energy, peak energy, and charge. A similar figure was published in [168] and the data was obtained on 26/04/2022 (Set 26).

in the shock. Therefore, we expect more charge to be injected at longer delay values. This is exactly the trend we observed in our experiment.
Additionally, we observed a decrease in the energy of the injected bunches with increasing delay values between the driver and injector beams. We have plotted the mean cut-off energy and the mean peak energy at different delays in Figure 5.6. Linear fits to the data yield gradients of $(209 \pm 63)\,\text{MeV/ns}$ for the cut-off energy and of $(254 \pm 83)\,\text{MeV/ns}$ for the peak energy. Following the argument discussed in Section 5.2.2, the cut-off energy is assumed to be only slightly influenced by the injected charge. Therefore, we can infer that the decrease in cut-off energy with increasing charge is, for the most part, not caused by beam-loading effects. Since all other parameters are kept constant, the decrease in cut-off energy most likely stems from changing shock properties, i.e. the changing density ratio in the shock with increasing delay. With an increasing density ratio, the electrons are injected further inside the bubble (cf. Equation (5.1)) and, thus, reach lower energies. Therefore, the highest electron energies with shock injection can be reached with small density ratios in the shock, which implies small delay values between the injector and driver beams when using optically-induced shock injection. For the peak energy, the influence of beam-loading is stronger, as shown in Section 5.2.2, which explains the stronger gradient with increasing delay for the peak energy, as the energy is

further reduced by the increasing injected charge.

5.2.5. Conclusion

The experiment discussed in Section 5.2 demonstrates the successful use of optically-induced shock injection to accelerate quasi-monoenergetic electron beams to the GeV regime. We investigated several tuning opportunities of this scheme by varying the injector position and the injector delay.
The scan of the acceleration length could be interpreted as the acceleration process being limited by the depletion of the driver laser, as the theoretical model for the bubble regime predicts. However, due to unmatched guiding conditions, the comparison to the theory is difficult. More data sets at matched guiding conditions will be analyzed in the following sections to support the interpretation of a depletion-limited acceleration process. Furthermore, the unmatched guiding conditions and the injection phase into the wakefield due to injection at a shock are suspected to influence the achievable energy gain for the current experimental setup.
The scan of the injector delay influenced the injected charge and the energy gain, which can be explained by changing density ratios of the optically-induced shock with different delay values. With longer delay values, the density ratio in the shock is higher, which facilitates more electrons to be injected but results in lower energies due to an advanced injection phase into the wakefield. Furthermore, the peak energy is reduced even stronger than the cut-off energy due to beam-loading effects.

5.3. Experiment 2: Electron beams approaching 2 GeV

To reach 2.5 GeV for the planned Breit-Wheeler experiment, we performed further experiments with higher laser energy. Increasing the laser energy was a straightforward option since 'experiment 1' was performed with 15.5 J before compression, and the ATLAS-3000 system is capable of amplifying laser pulses to energies up to 90 J before compression.
As described in Section 3.1, amplification to pulse energies higher than 20 J requires 'configuration 2' of the ATLAS system. In this case, the last amplifier is included in the amplification chain, and a larger beam diameter is obtained. The experiments discussed up to this point in the thesis used 'configuration 1' since the smaller beam diameter before the focusing optic is less susceptible to air fluctuations.
For the experiments discussed in Section 5.3 and 5.4, we used 'configuration 2'

with $30 - 31\,\mathrm{J}$ before compression. The larger beam diameter before focusing leads to a smaller f#, smaller focal spot size, and smaller Rayleigh length. Combining higher pulse energy and smaller focal size yields intensities in excess of $3 \cdot 10^{19}\,\mathrm{W/cm^2}$. The higher intensity will reduce the injection threshold (cf. Section 2.6.4), which could lead to excessive injection. Therefore, lower densities will be used to counteract this. When using lower densities at these new parameters, we can reach matched guiding conditions (for $0.4 \cdot 10^{18}\,\mathrm{cm^{-3}}$, $w_0 = 33\,\mu\mathrm{m}$ and $a_0 = 3.9$: $k_p w_0 = 3.89 \approx 3.94 = 2\sqrt{a_0}$ (Equation (2.60))) and expect a stable guiding and acceleration process along the gas length [142] and accordingly a good agreement with the theoretical predictions of the theory of the bubble regime (cf. Section 2.6.3) that is valid for $a_0 > 2$ and matched guiding conditions. Additionally, the lower density will also extend the depletion and dephasing lengths further.
However, using lower plasma density will increase the threshold for relativistic guiding (cf. Section 2.5). This will reduce the length, over which guiding can be maintained. However, this will be counteracted by the higher laser energy and associated higher power. Also, the reduced accelerating fields in the bubble (cf. Equation (2.62)) with lower density will be counteracted to some degree by the increased laser intensity.

5.3.1. Generation of high charge beams close to 2 GeV

First tests with 'laser configuration 2' were conducted with a 20 mm slit nozzle (similar to the one in 'experiment 1' but with a width of 2 mm instead of 3 mm, see Table A.1). Figure 5.7 shows a measurement of the density profile of this nozzle for a backing pressure of $(3.40 \pm 0.02)\,\mathrm{bar}$ used in the experiments. As in 'experiment 1', one half of the gas profile was measured, and the data points were mirrored, assuming the profile to be symmetric with respect to the center of the nozzle. Here, the plasma was defined to start at 30 % of the measured peak density. The definition of 80 % used in the first experiment would have underestimated the plasma length due to the shape of the plasma profile deviating from a defined plateau shape. Using the definition of 30 %, the plasma was estimated to be $(19.0 \pm 0.5)\,\mathrm{mm}$ long.
The measured density profile differs from the prediction by CFD simulations shown in Figure 5.7a. As a main difference, the simulations predict the electron density to be higher than in the measurement. This could be the result of a combination of effects: On the one hand, the throat area of the 3D-printed nozzle was measured to be actually roughly 27 % smaller than the design area due to the inaccuracy of the 3D print. The smaller throat size of the actual nozzle compared to the intended throat size used in the simulation can explain the smaller measured density. An additional effect could have been caused by a slightly leaky connection

between the nozzle and the valve, resulting in an effectively lower experimental backing pressure. It was observed that the base of the 3D-printed nozzles tended to bend upwards when used for a longer time. This could lead to a slightly leaky seal between the nozzle and the valve and to an additional small reduction of the

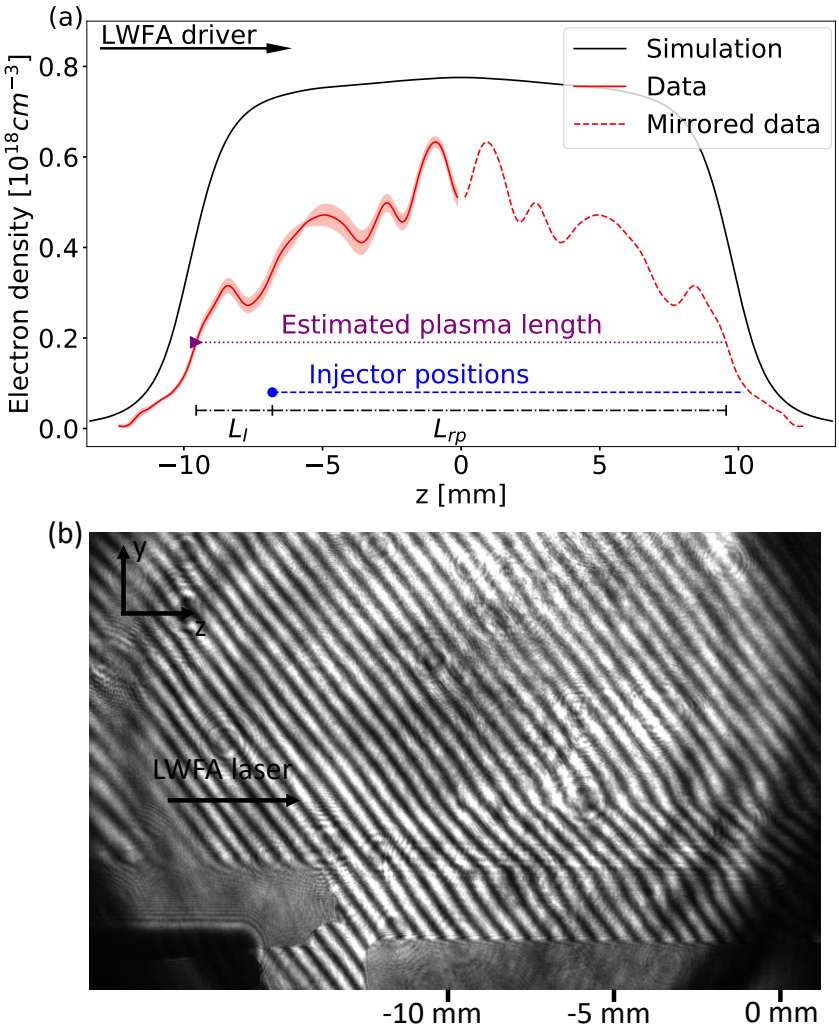

Figure 5.7.: (a) Measured and simulated plasma density of the 20 mm nozzle used in the experiment described in Section 5.3. The interferometry measurement was performed at an inlet pressure of (3.40 ± 0.02) bar and at a distance of (4.3 ± 0.2) mm between laser axis and nozzle. The red solid line shows the mean of four measured laser shots. The standard deviation of the measurements is indicated by the red-shaded area. The purple triangle marks the defined start of the plasma and the estimated plasma length is shown with a purple dotted line. The blue circle indicates the injector beam position for the experiment related to Figure 5.8, and the dashed blue line indicates the scan range in the experiment related to Figure 5.9. The driver laser propagates through the plasma from left to right. The black line shows the result of a CFD simulation. In the simulation, the inlet pressure was set to 3.4 bar, and the line-out is shown for a height of 4.3 mm above the nozzle. **(b)** One of the raw interferometry images that was used for the analysis is shown. The data for this measurement was obtained on 17/10/2023 (Sets 3/5).

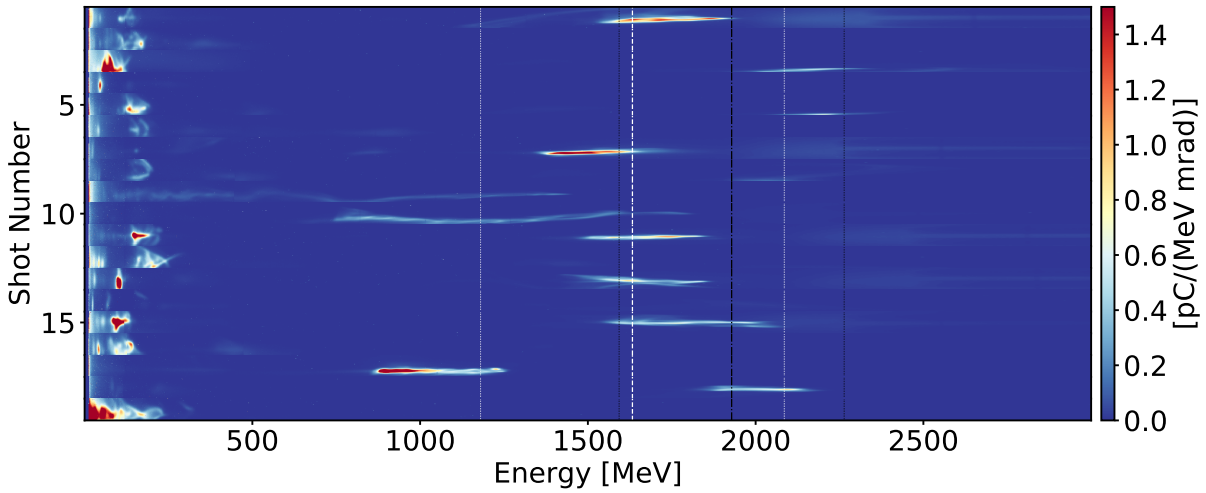

Figure 5.8.: Electron spectra with bunch energies approaching 2 GeV, obtained with a 20 mm slit nozzle and optically-induced shock injection. The white dashed lines indicate the mean peak energy of the set and the corresponding standard deviation. Black dashed lines indicate the mean cut-off energy and corresponding standard deviation. The range of divergence angles covered in the plots is ±5.4 mrad. This data set was obtained on 16/10/2023 (Set 41).

measured density in comparison to the simulation. New nozzles were designed with thicker bases to avoid this.
A discussion about the origin of the peaks seen in the density profile can be found in Appendix B.
The nozzle characterized by Figure 5.7 was used in first tests with 'laser configuration 2' to reach higher electron energies than in 'experiment 1' discussed in Section 5.2. Electron spectra from a set of 19 consecutive shots in this experiment are shown in Figure 5.8. They were recorded at a plasma density of $(0.4\pm0.1)\cdot10^{18}\,\mathrm{cm}^{-3}$ (average and standard deviation over the length of the plasma). The injector beam was adjusted to arrive 1.1 ns before the driver beam and was positioned $L_I = 3.0\,\mathrm{mm}$ from the beginning of the plasma (i.e. at $z = -6.5\,\mathrm{mm}$ in Figure 5.7a). As in 'experiment 1', we assume a systematic error of ±2 ps and a statistical error of ±0.17 ps for the delay and a systematic error of ±0.25 mm and a statistical error of ±0.05 mm for the injector position.
This configuration resulted in shock-injected electron bunches close to 2 GeV. The mean peak energy of injected bunches with peak energies above 650 MeV was measured to be $(1.633 \pm 0.453)\,\mathrm{GeV}$. The mean cut-off energy is close to 2 GeV: $(1.929 \pm 0.335)\,\mathrm{GeV}$. Here, the cut-off energy is defined as the energy where the spectral charge density decreased to 20 % of the measured peak spectral charge density. Only for shot 17 of the set, the value of 20 % of the measured peak spectral charge density would underestimate the cut-off energy strongly since the shot has a high peak spectral charge density while a long tail reaches to higher energies. Therefore, the definition for the cut-off energy was adjusted to the energy where

the spectral charge decreased to 1 % of the measured peak spectral charge for this shot to account for the different quality of the electron beam.
Within the energy range around the peak where the spectral charge is > 20 % of the peak spectral charge, the mean charge of the bunches was measured to be (394 ± 207) pC, and the RMS divergence (Gaussian fit) of the bunches is (0.8 ± 0.3) mrad. The FWHM energy spread around the peaks amounts to (263 ± 115) MeV. Table A.2 summarizes these values.
The energy spread in 'experiment 2' is higher than the energy spread of 9.6 % achieved in the 1 GeV set in 'experiment 1' (see Figure 5.3). The divergence in this experiment is also slightly higher compared to the set in 'experiment 1'. The considerably higher charge around the peaks, which is more than four times the charge measured in the configuration of 'experiment 1', is likely to contribute to this increase in bandwidth and divergence of the electron bunches.
As discussed in Section 3.7, the energy measurement is limited in resolution by the divergence of the beam in vertical direction, which can be estimated by the measured divergence in horizontal direction. This fact also limits the measurement of the energy spread. With a divergence of 0.8 mrad at 2 GeV the energy resolution for the data shown in Figure 5.8 is only roughly 100 MeV, which implies an actual smaller bandwidth than the measured 16 %, as was the case for 'experiment 1'.
In the current ´laser configuration 2', the energy in the central Airy disk was 10 J, while it was 6 J in ´laser configuration 1'. A comparison of Figures 5.3 and Figure 5.8 shows that this new configuration results in both higher electron energy and charge. In the current configuration, a mean energy conversion efficiency of 6.0 % was reached in the energy range around the peak where the spectral charge is > 20 % of the peak spectral charge. Therefore, the energy conversion efficiency into the bunches is four times higher than the energy conversion efficiency obtained in 'experiment 1'. The lower conversion efficiency in 'experiment 1' is likely due to an already limited acceleration process due to depletion and guiding termination (cf. Figure 5.5). Furthermore, the guiding conditions are nearly perfectly matched in 'experiment 2' due to a lower plasma density, smaller spot size, and higher laser intensity ($k_p w_0 = 3.89 \approx 3.94 = 2\sqrt{a_0}$), which is expected to lead to a more stable acceleration process along the gas length [142].
Regarding energy stability ($\sim$ 17 % in cut-off energy) and injection probability ($\sim$ 53 %), the 2 GeV set in 'experiment 2' lags behind the 1 GeV set in 'experiment 1' ($\sim$ 7 % and $\sim$ 91 %, respectively). A summary of these values can be found in Table A.2 in the appendix.
Multiple reasons can contribute to this decreased stability and injection probability. The larger beam diameter in ´configuration 2' is expected to be more susceptible to air fluctuations along the beam path. This can lead to fluctuations in the wavefront of the laser, leading to fluctuations of the field distribution in focus and, thus, the electron energy. Associated fluctuations of the intensity can also contribute to

the reduced injection probability. Furthermore, the larger beam diameter results in a smaller Rayleigh length (4.2 mm). If the Rayleigh length is on the order of the length of the density gradient at the start of the gas jet, out-of-focus beam fluctuations can contribute to unstable laser propagation, which can also influence the injection probability and the electron energy. The long gradient of the hill-shaped density profile of the nozzle used in 'experiment 2' (Figure 5.7a) contributes to this effect.
One possibility to increase the injection probability with optically-induced shock injection is to use longer delay values between the injector and driver beams. This was observed by Faure et al. [183]. Therefore, in this experiment, a longer delay of 1.1 ns before the driver laser compared to 'experiment 1' (0.27 ns) was used to achieve at least the injection probability of $\sim 53\,\%$.

5.3.2. Acceleration limits

With the goal of designing 'experiment 3' for reaching the desired 2.5 GeV for the planned Breit-Wheeler experiment, we performed a scan of the acceleration length at the experimental conditions of 'experiment 2' to test the limitations of the acceleration process. For the scan of the acceleration length, the position of the injector beam was fixed with respect to the driver beam. Then, the gas nozzle was moved along the axis of the driver beam (z-direction), as was done in 'experiment 1'. The experimental setup can be seen in Figure 3.10. The acceleration length scan was conducted at the same parameters at which the data shown in Figure 5.8 was obtained (average plasma density and standard deviation along the plasma length $(0.4 \pm 0.1) \cdot 10^{18}\,\mathrm{cm}^{-3}$, injector beam 1.100 ± 0.002 ns before main beam). The measured cut-off energy versus remaining plasma lengths $L_{\mathrm{rp}} = L_{\mathrm{pl}} - L_I$ is shown in Figure 5.9. The cut-off energy increases roughly linearly with the remaining plasma length, and no stagnation or decrease of the cut-off energy is visible for the range of injector positions where injection could be observed. This indicates that the acceleration process at the parameters of 'experiment 2' is not limited by dephasing, depletion, or the termination of guiding. This is in agreement with the theoretical values for the dephasing, depletion, and guiding termination lengths at the density used in 'experiment 2' (summarized in Table 5.3). These values are indeed larger than the plasma length of 19 mm in 'experiment 2' such that no fundamental limitation of the acceleration process is expected.
To estimate the maximum acceleration gradient in this experiment, the data of Figure 5.9 was fitted with a linear function that can be interpreted as the nearly linear part of the actual acceleration parabola. The fit yields a maximum acceleration gradient of (75 ± 6)GV/m. This value is smaller than the theoretical value of 120 GV/m. This might be expected since the maximum acceleration gradient would only be reached at the start of the acceleration parabola. However, the large

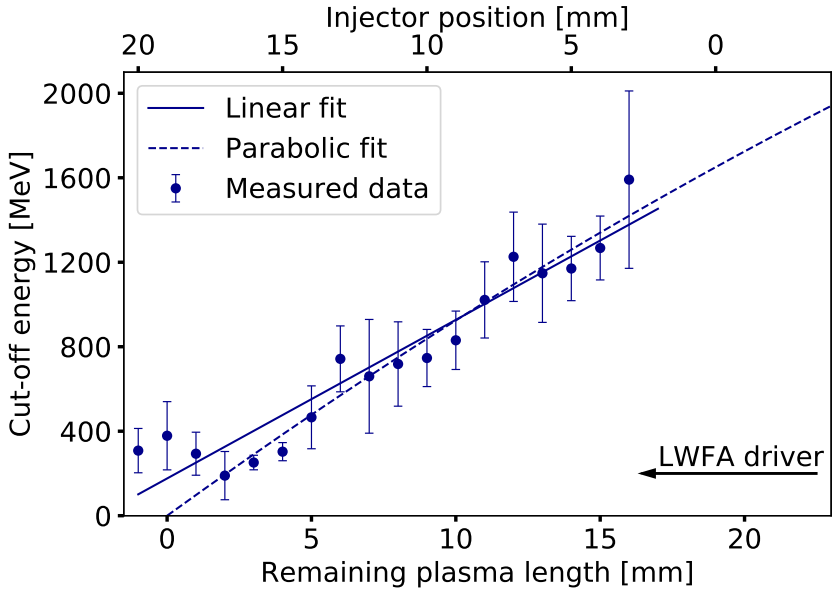

Figure 5.9.: Cut-off energy as a function of the remaining plasma length. The injector position with respect to the start of the plasma is indicated at the top. The driver laser arrives from the right. In this measurement, the injector pulse arrived (1.100 ± 0.002) ns before the main beam and the plasma density was $(0.4 \pm 0.1) \cdot 10^{18}\,\mathrm{cm}^{-3}$. Each data point shows the average of 14 - 21 shots. The error bars show the corresponding standard error. This data was obtained on 16/10/2023 (Sets 43/44;47-62).

deviation of 38 % suggests that another limiting factor could contribute. As the parameters are well-matched for guiding in 'experiment 2', the large discrepancy between the theoretical maximum acceleration gradient and the gradient obtained from the linear fit likely stems from the advanced injection phase, as discussed before. An advanced injection phase reduces both the maximum acceleration gradient and the dephasing length. For a roughly linear electric field in the wakefield bubble [142], we can calculate the effect of the injection phase on the maximum acceleration gradient and on the dephasing length with a simple parameter p, which we call 'energy reduction factor' (ERF), which changes Equations 2.62 and 2.71 to:

$$E_{z,\mathrm{max,ERF}} = p \cdot E_{z,\mathrm{max}} = p \frac{m_e c \omega_p}{e} \sqrt{a_0} \tag{5.4}$$

$$L_{\mathrm{deph,ERF}} = p \cdot L_{\mathrm{deph}} = p \frac{2}{3} \frac{\omega^2}{\omega_p^2} \frac{2\sqrt{a_0}}{k_p}. \tag{5.5}$$

To support the hypothesis of the advanced injection phase, we fitted an acceleration parabola to the data in Figure 5.9. As the data only spans over a small region of

	Theory	Experiment	
		Linear fit	Parabolic fit
Dephasing length	96.3 mm (Eq. 2.71)		(79 ± 3)mm
Depletion length	39.2 mm (Eq. 2.70)	-	
Guiding length	33.9 mm (Eq. 4.1)		-
Rayleigh length	4.2 mm		
$E_{z,\max}$	120 GV/m (Eq. 2.62)	(75 ± 6)GV/m	(99 ± 4)GV/m

Table 5.3.: Comparison between values from theory and the fits to the data of the acceleration length scan (see Figure 5.9).

the actual acceleration parabola, a few constraints had to be chosen to obtain a reasonable fit:

- Zero cut-off energy at zero remaining plasma length
- Maximum of the parabola at the reduced dephasing length $L_{\mathrm{deph,ERF}}$
- Maximum gradient of the parabola of $E_{z,\mathrm{max,ERF}}$

With these constraints, the remaining fit parameter is the ERF, from which the reduced maximum acceleration gradient and the reduced dephasing length can then be calculated. If the acceleration process would not be limited by the injection phase, the ERF would be 1.
From the parabolic fit shown in Figure 5.9, an ERF of 0.82 ± 0.04 is obtained, which results in $E_{z,\mathrm{max,ERF}} = (99 \pm 4)$GV/m and $L_{\mathrm{deph,ERF}} = (79 \pm 3)$mm. We see that the gradient obtained from the parabolic fit is not as small as the approximation from the linear fit but still shows a reduction of roughly 20 % compared to the theoretical value, which is due to the advanced injection phase. This also reduces the dephasing length by 20 %. However, this reduced dephasing length is still larger than the theoretical depletion and guiding termination lengths, which indicates that the acceleration process would still be limited by depletion for a longer plasma length, and the dephasing point would not be reached.

5.3.3. Conclusion

We conclude that operating at a lower density and using higher laser intensity facilitated the acceleration of electrons to energies of up to nearly 2 GeV. Additionally, higher charge was measured than in 'experiment 1', and we could demonstrate a conversion efficiency of 6.0 %. However, this configuration still needs to be optimized regarding energy stability and injection probability by stabilizing the laser performance and optimizing the gas target.
The scan of the acceleration length showed that the acceleration process is not lim-

ited yet by depletion, dephasing, or diffraction at a plasma density of $0.4 \cdot 10^{18}\,\mathrm{cm}^{-3}$ and at the available lengths in the nozzle. However, the maximum acceleration gradient obtained from fits to the data indicated that the achievable energy gain for shock injection is likely limited by the advanced injection phase.
To investigate whether we can obtain electrons with even higher energies by extending the acceleration length further, we also performed measurements with a 40 mm-long slit nozzle. This length is close to the theoretical depletion length of 39.2 mm for the parameters of 'experiment 2'. The results of these measurements will be discussed in Section 5.4.

5.4. Experiment 3: Electron beams approaching 2.5 GeV

In 'experiment 3', we worked with roughly the same laser parameters as in 'experiment 2' (summary in Table A.2), but with a 40 mm-long nozzle to increase the acceleration length up to the theoretical depletion length of 39.2 mm at these parameters and to reach 2.5 GeV for the Breit-Wheeler experiment.
In a first step, we measured the density profile created by the 40 mm nozzle. The measurement was divided into four steps to measure the complete density profile of the 40 mm nozzle while not diminishing the resolution of the interferometric imaging setup. One part of the gas profile at $z = 7 - 15\,\mathrm{mm}$ could not be measured, as the image was obscured by a part of the setup at this position. Furthermore, the quality of the interference fringes was not good over the whole image area on this day due to an imperfect alignment of the setup. This is visible in an example image in Figure 5.10b. Therefore, only small parts of the images could be analyzed, and the resulting density profile shows some gaps between the measurements. The results of the measurements are shown in Figure 5.10a. The profile exhibits a density plateau with a quasi-monotonic increase/decrease of the plasma density towards both sides. The simulated profile is plotted in Figure 5.10a, alongside the measured profile. It predicts a smooth increase towards an approximately flat plateau, which is reproduced by the measurement. However, the measured density of the plateau is slightly higher than the density predicted by the simulation. The actual throat area was measured to differ by roughly 12 % from the intended throat size that was used in the simulation, which can explain the difference between the simulated and the measured density.
A discussion about the origin of peaks seen in density profiles in this work can be found in Appendix B.
The plateau was defined to start at 60 % of the measured peak density. The plateau length was, thus, estimated to be $(35.0 \pm 0.5)\,\mathrm{mm}$.
We then tested whether the 40 mm nozzle allows for the generation of electron

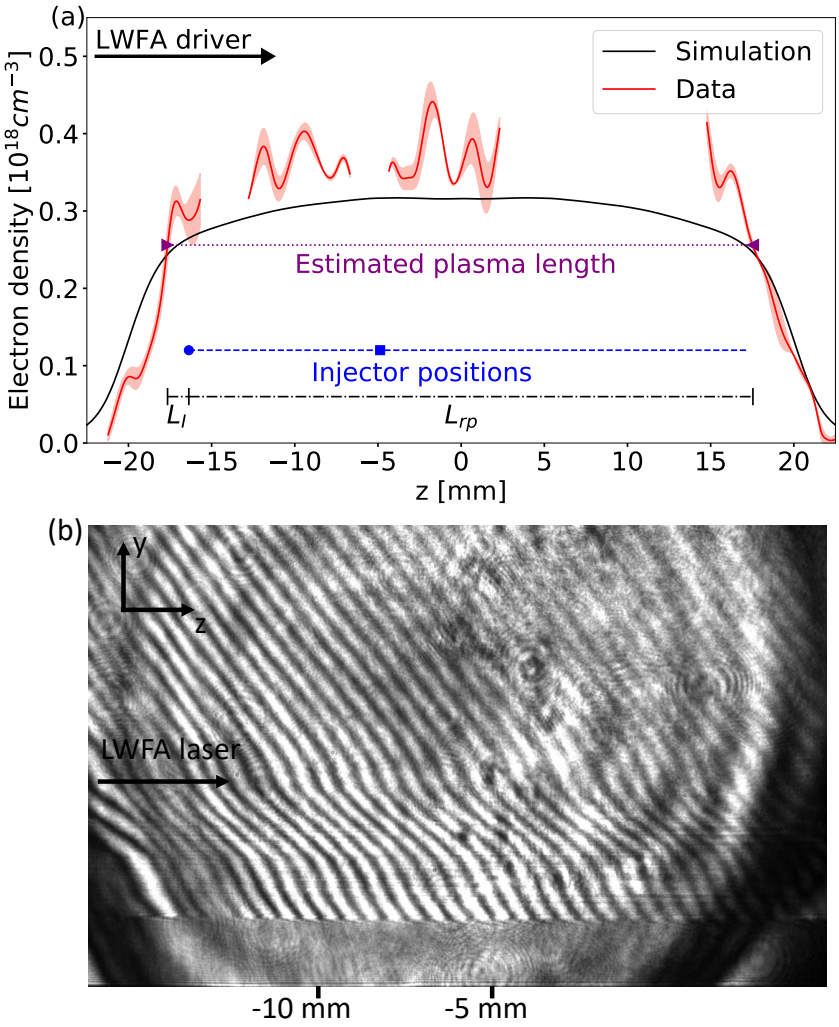

Figure 5.10.: (a) Measured and simulated plasma density of the 40 mm nozzle. The interferometry measurements were performed at an inlet pressure of (2.50 ± 0.05) bar and at a distance of (4.3 ± 0.2) mm between laser axis and nozzle. The red solid lines show the mean of four measured laser shots for each measured part of the profile. The standard deviation of the measurements is indicated by the shaded area. The purple triangle marks the defined start of the plasma and the estimated plasma length is shown with a purple dotted line. The blue circle indicates the injector beam position for the experiment related to Figure 5.11, the square for the experiment related to Figures 5.14/5.16, and the dashed blue line indicates the scan range in the experiment related to Figures 5.12/5.13. The driver laser propagates through the plasma from left to right. The black line shows the result of a CFD simulation. The inlet pressure in the simulation was 2.5 bar, and the line-out is shown for a height of 4.3 mm above the nozzle. **(b)** One of the raw interferometry images that was used for the analysis is shown. The data for this measurement was obtained on 19/10/2023 (Sets 79-82;84-91;93-96).

bunches with energies exceeding those of experiments 1 & 2. As in Section 5.3, we used 'laser configuration 2' for these measurements. Electron spectra of a set of 19 consecutive shots recorded with the 40 mm nozzle are shown in Figure 5.11. They were measured at a plasma density of $(0.4 \pm 0.1) \cdot 10^{18}\,\mathrm{cm}^{-3}$ (aver-

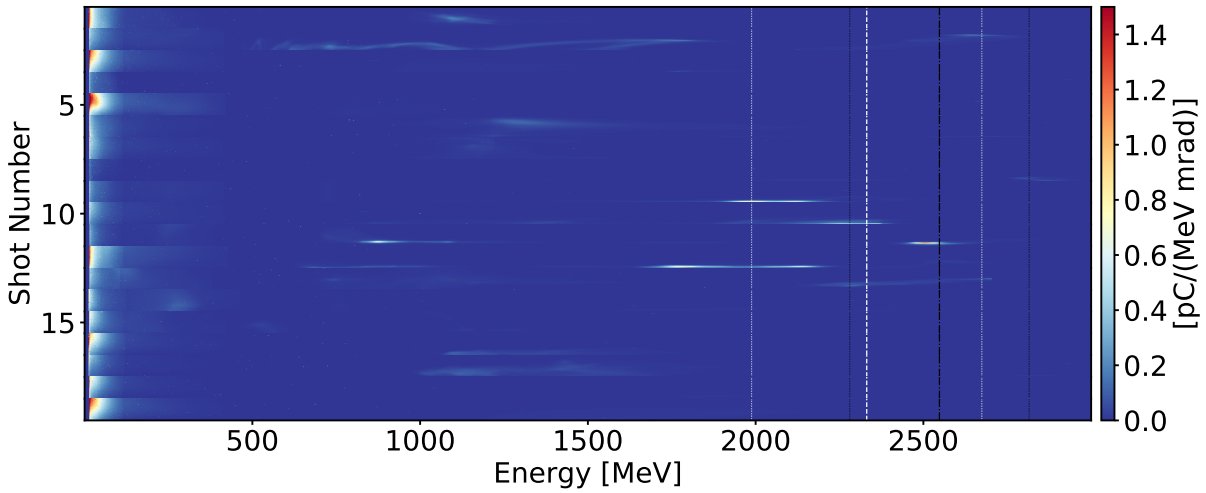

Figure 5.11.: Set of electron spectra with bunches approaching 2.5 GeV obtained with the 40 mm nozzle and using optically-induced shock injection. The white dashed lines indicate the mean peak energy of bunches injected above 1.750 GeV and the corresponding standard deviation. Black dashed lines indicate the mean cut-off energy of these bunches and the corresponding standard deviation. The range of divergence angles covered in the plots is ±5.4 mrad. This data set was obtained on 19/10/2023 (Set 123).

age and standard deviation over the plateau length). The injector was positioned $L_I = (1.0 \pm 0.25)$ mm from the start of the plateau, leaving a plasma length of approximately $L_{\mathrm{rp}} = 34$ mm for electron acceleration. The delay between the injector and the driver beam was set to (1.100 ± 0.002) ns.
In this configuration, a mean peak energy of (2.331 ± 0.343) GeV (bunches injected above 1.750 GeV) was reached. The mean cut-off energy was measured to be (2.548 ± 0.267) GeV. Here, the cut-off energy is defined as the energy where the spectral charge density decreased to 20 % of the measured peak spectral charge density. The injected bunches show FWHM energy spreads of (163 ± 50) MeV. The mean charge of the bunches was measured to be (80 ± 51) pC within the energy range around the peak where the spectral charge is > 20 % of the peak spectral charge. The Gaussian-fitted divergence (RMS) of the bunches amounts to (0.8 ± 0.5) mrad. All of these values are summarized in Table A.2.
With a mean cut-off energy of over 2.5 GeV, FWHM energy spreads of 7.0 % of the peak energy, tens of pC of charge and a divergence under 1 mrad, nearly all goals for beams for the Breit-Wheeler experiment planned at CALA are reached. However, in this configuration, only 7 out of 19 electron spectra show properly injected bunches, corresponding to an injection probability of less than 40 %. The injection probability of these beams needs to be increased for them to be usable as a reliable source for the Breit-Wheeler experiment. Reasons for a low injection probability have been discussed in Section 5.3.1. To improve the injection probability and energy stability, laser stabilization schemes [43] could be implemented to stabilize

the laser performance. Moreover, nozzles could be fabricated from stainless steel to achieve a more homogeneous and stable gas flow.
In the set in Figure 5.11, a mean energy conversion efficiency of 1.6 % was reached in the energy range around the peak where the spectral charge is $> 20\,\%$ of the peak spectral charge, similar to the energy conversion efficiency of 'experiment 1', but significantly lower than in 'experiment 2'. In 'experiment 2', electron bunches with lower energy than in 'experiment 3' but very high charge were measured, yielding an overall higher energy conversion efficiency.
The next section will investigate the acceleration limits of the regime for the 40 mm nozzle to determine the ideal acceleration length to produce quasi-monoenergetic beams at 2.5 GeV.

5.4.1. Acceleration limits

To investigate which effects limit the acceleration process in 'experiment 3', we conducted a scan of the acceleration length for the 40 mm slit nozzle. For the scan of the acceleration length, the position of the injector beam was fixed with respect to the driver beam. Then, the gas nozzle was moved along the axis of the driver beam (z-direction), as was done in 'experiment 1' and '2'. Electron spectra obtained from the scan are shown in Figure 5.12. For remaining plasma lengths between 22 mm and 34 mm, sets were taken in mm-steps of the remaining plasma length. For this range in Figure 5.12, only every second set is shown.
Theoretical values for dephasing, depletion, and guiding termination lengths are summarized in Table 5.4. The dephasing length calculated with Equation (2.71) is much larger than the depletion length (Equation (2.70)) and the length after which self-guiding is expected to terminate (Equation (4.1)). Therefore, we expect the acceleration process to be limited by the depletion of the laser energy and the termination of the guiding process induced by the depletion of the laser.
This prediction is in agreement with the data shown in Figure 5.12 and Figure 5.13, where the mean cut-off energies of the sets are plotted against the remaining plasma length: the cut-off energy increases with increasing remaining plasma length and stagnates around a remaining plasma length of $26 - 34$ mm.
Expecting the advanced injection phase to limit the energy gain due to the injection at a shock as in the previous experiments, we fit the data in Figure 5.13 with an acceleration parabola with the following constraints as in 'experiment 2':

- Zero cut-off energy at zero remaining plasma length
- Maximum of the parabola at the reduced dephasing length $L_{\mathrm{deph,ERF}}$
- Maximum gradient of the parabola of $E_{z,\mathrm{max,ERF}}$

For $E_{z,\mathrm{max,ERF}}$ and $L_{\mathrm{deph,ERF}}$, we use Equations 5.4 and 5.5 defined in 'experiment 2'

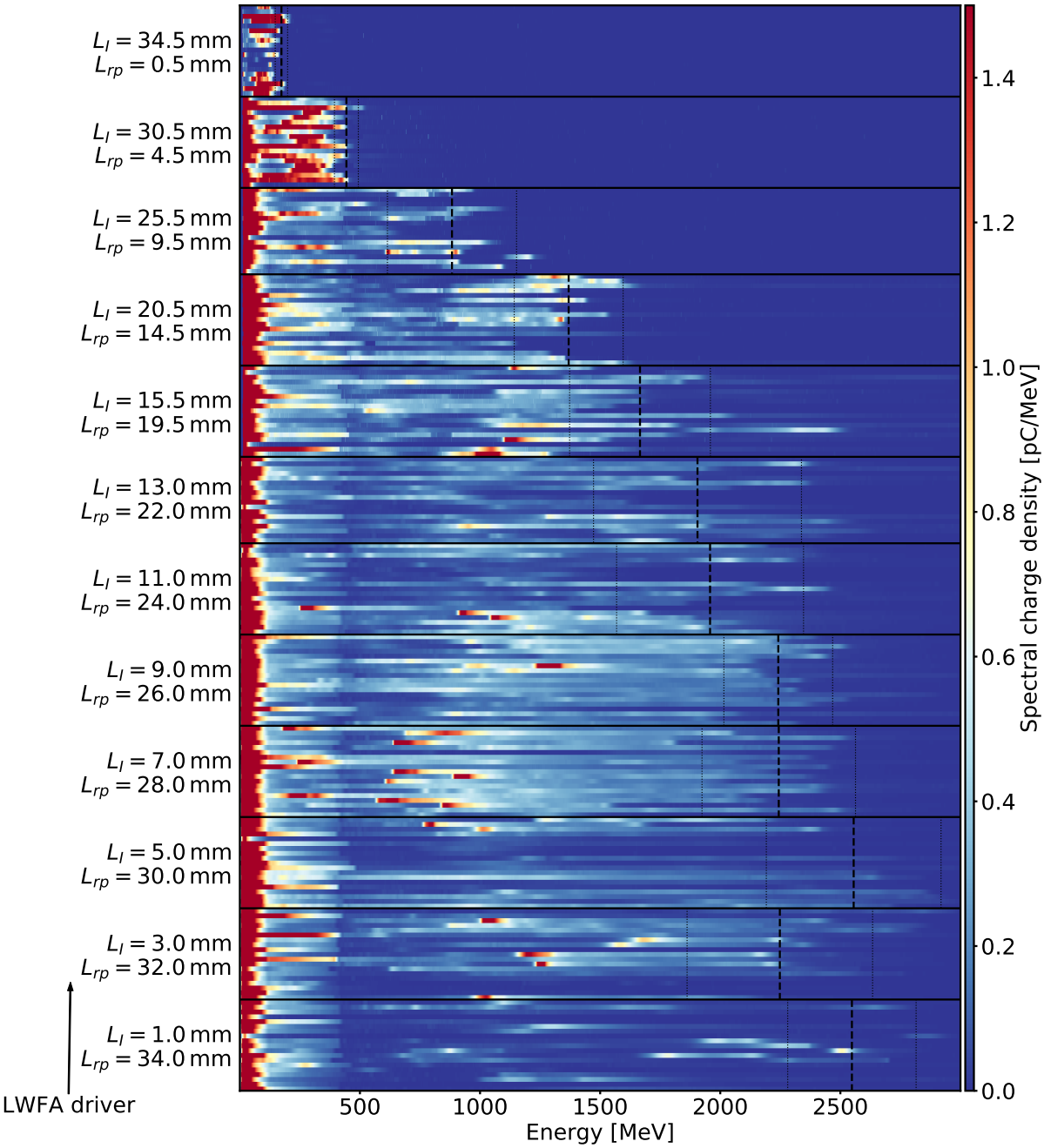

Figure 5.12.: Waterfall plot of the data of the acceleration length scan in combination with the 40 mm slit nozzle. At each position, 18-19 consecutive shots were taken. The injector pulse arrived (1.100 ± 0.002) ns before the main beam and the plasma density was $(0.4 \pm 0.1) \cdot 10^{18}\,\mathrm{cm}^{-3}$. The data was integrated over the width of the detector focal plane. The black dashed lines show each set's mean cut-off energy and corresponding standard deviation. The numbers on the left side of the plot indicate the injector position L_I with respect to the start of the plasma and the remaining plasma length L_{rp} for each set (cf. Figure 5.10). The driver laser arrives from the bottom of the plot. For remaining plasma lengths between 22 mm and 34 mm, sets were taken in mm-steps of the remaining plasma length. For this range, only every second set is shown here. This data was obtained on 19/10/2023 (Sets 106-123).

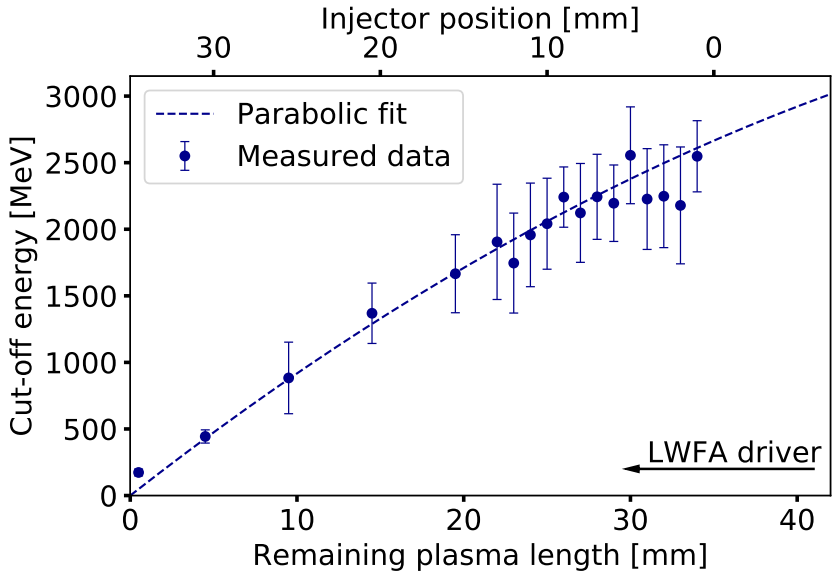

Figure 5.13.: Scan of the acceleration length in combination with the 40 mm slit nozzle. The cut-off energy is plotted as a function of the remaining plasma length. The injector position with respect to the start of the plasma is indicated at the top (cf. Figure 5.10). Here, the driver laser arrives from the right. The injector pulse arrived (1.100 ± 0.002) ns before the main beam and the plasma density was $(0.4 \pm 0.1) \cdot 10^{18}\,\mathrm{cm}^{-3}$. Each data point shows the average over $7 - 19$ shots. The error bars show the corresponding standard error. The blue dashed line indicates a parabolic fit to the rising part of the data. This data was obtained on 19/10/2023 (Sets 106-123).

for the reduced maximum acceleration gradient and the reduced dephasing length due to an advanced injection phase.
The parabola is fitted up to a remaining plasma length of 26 mm, as from this value, no clear increase in energy is observed, and depletion could already limit the energy gain.
From the parabolic fit shown in Figure 5.13, an ERF of 0.81 ± 0.01 is obtained, which results in $E_{z,\mathrm{max,ERF}} = (98 \pm 1)\mathrm{GV/m}$ and $L_{\mathrm{deph,ERF}} = (79 \pm 1)\mathrm{mm}$. These values are very close to the values obtained in 'experiment 2', which is expected

	Theory	Experiment
Dephasing length	91.0 mm (Eq. 2.71)	(79 ± 1)mm
Depletion length	37.3 mm (Eq. 2.70)	26 to 34 mm
Guiding length	32.7 mm (Eq. 4.1)	
Rayleigh length	4.0 mm	
$E_{z,\mathrm{max}}$	125 GV/m (Eq. 2.62)	(98 ± 1)GV/m

Table 5.4.: Comparison between theoretical values and parameters obtained from a parabolic fit to the data from the scan of the acceleration length (see Figure 5.13).

since, except for the acceleration length, the parameters in both experiments were very similar (see Table A.2).
As already expected in 'experiment 2', the reduced dephasing length is still larger than the depletion and guiding termination lengths, which is why the acceleration process is limited by depletion and the electron energy stagnates around an acceleration length of $26 - 34\,\mathrm{mm}$.
In Figure 5.12, it is notable that the set at a remaining plasma length of 35 mm (also shown in Figure 5.11) exhibits a much lower injection probability than the other sets ($37\,\%$ vs. $70 - 100\,\%$). This indicates that the injection probability can drop considerably for injection close to the beginning of the plasma, as the injection threshold (cf. Section 2.6.4) is more difficult to overcome in the contracting bubble (cf. Equation (2.59)) in the density up-ramp of the plasma profile (cf. Figure 5.10). Stronger shot-to-shot fluctuations of the density in the gradient are also a potential reason for a lower injection probability. The injection point can be moved further inside the gas profile to increase the injection probability. However, it can be seen in the plot that all bunches injected further inside the gas profile show larger bandwidths with tails down to the region around 1 GeV, which is undesirable for many applications (cf. Chapter 1). We assume that more charge is injected further inside the plasma due to higher density which affects the bandwidth of the bunches via beam-loading.
To achieve small-bandwidth bunches around 2.5 GeV with high injection probability, more experiments with different nozzles have to be conducted. Based on the observations in 'experiment 3', it seems reasonable to use nozzles with lengths close to the stagnation length ($30 - 35\,\mathrm{mm}$; see also Figure 5.13). Alternatively, the bandwidth of the electron bunches injected further inside the plateau could be reduced by injecting less charge, for example, by adjusting the density ratio in the shock via the injector delay. However, this will, in turn, reduce the injection probability, as was shown by Faure et al. [183].
Furthermore, nozzles with a smoother surface need to be tested to achieve a stable and homogeneous density profile for optimal injection and acceleration conditions. These tests could be the subject of further investigations.

5.4.2. Influences of plasma density and injector delay

To investigate the regime of 'experiment 3' further, we conducted scans of the plasma density and the injector delay.
For the parameter scans in this section, the plasma density was scanned in steps of approximately $0.03 \cdot 10^{18}\,\mathrm{cm}^{-3}$ between $0.36 \cdot 10^{18}\,\mathrm{cm}^{-3}$ and $0.50 \cdot 10^{18}\,\mathrm{cm}^{-3}$. This scan was repeated at seven different injector delay values (between 0.4 ns and 1.9 ns before the driver laser in steps of approximately 0.3 ns). At a delay of 1.1 ns before the driver, measurements were conducted at three additional density values up to

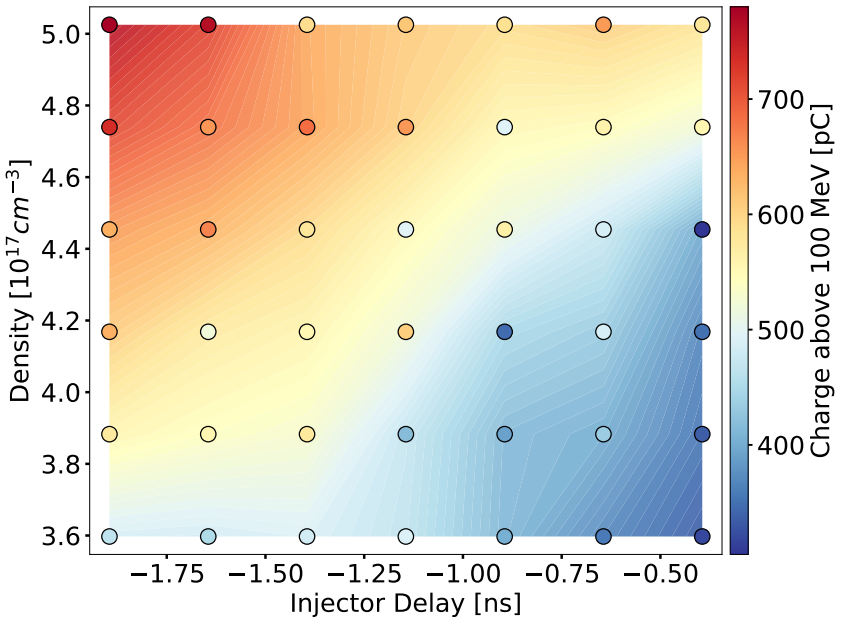

Figure 5.14.: Charge of electron bunches accelerated to energies above 100 MeV, measured at various plasma densities and injector delay values. Each data point shows the average over $8-19$ shots with standard errors between 4 and 18 %. The background is shaded with a contour plot of the smoothed data using a Gaussian filter with a standard deviation of 0.7. The charge increases with plasma density and with increasing delay between the driver and injector beam. This data was obtained on 19/10/2023 (Sets 17;19;21;23;27;29;31-38;41-54;57-70;72-74).

$0.61 \cdot 10^{18}\,\mathrm{cm}^{-3}$ in steps of approximately $0.03 \cdot 10^{18}\,\mathrm{cm}^{-3}$.
First, we determine the influence of these parameter changes on the injected charge. Figure 5.14 shows the average charge above 100 MeV for $8-19$ shots per data point with standard errors between 4 and 18 % versus the density and the injector delay. The injected charge increases with the density and increasing delay values between the driver and the injector beam. Linear fits to the raw data yield gradients of $85-200\,\mathrm{pC}/10^{17}\mathrm{cm}^{-3}$ for the density and of $100-200\,\mathrm{pC/ns}$ for the injector delay. The increase in charge with both parameters can be explained as follows: The injection threshold decreases with higher density (cf. Section 2.6.4). Therefore, more electrons are injected at higher densities. With longer delay values between the driver and injector beam, the density ratio in the shock increases (cf. Figure 3.14). A shock with a high density ratio thus also facilitates more charge to be injected, as discussed in Section 5.2.4 and shown in simulations in Ref. [185].
Plasma density and injector delay also affect the energy of the electron bunches. First, we discuss a model that describes the expected dependence of the electron energy of accelerated bunches on the plasma density. To this end, we adapted a model developed by Bloom et al. [194].
Assuming a dephasing-limited acceleration process in the bubble regime, the predicted maximum electron energy gain would be calculated according to Lu et

al. [142] via

$$\Delta E_{\max} = \frac{2}{3} a_0 \frac{n_c}{n_0} m_e c^2. \tag{5.6}$$

However, this equation assumes that the acceleration process is always limited by dephasing. This implies that laser parameters would have to be adapted (e.g. longer driver pulse length) at low plasma densities to ensure that the process is limited by dephasing and not depletion (cf. Equation (2.72)). Additionally, the plasma length has to be the same as the dephasing length. The hypothetical energy gain for a dephasing-limited process for the densities we used in our experiment is plotted in Figure 5.15a, assuming the above-mentioned adaptions to ensure a dephasing-limited process and a plasma length that is always as long as the dephasing length, which explains the continuously rising electron energy for lower plasma densities. Here, Equation (5.6) was used for the calculation, and for a_0 the matched value after self-focusing was calculated (Equation (2.61)) that depends on the density.
However, Equation (5.6) cannot be used for our experiment as at these densities and for our fixed laser parameters and fixed plasma length, the process is, according to Equation (2.72), expected to be limited by the depletion of the driver laser. At our laser parameters, the acceleration process would only be limited by dephasing for much higher densities from $5 \cdot 10^{18}\,\mathrm{cm}^{-3}$. Taking into account that the process is limited by the depletion of the laser energy, the energy gain is reduced as follows [194]:

$$\Delta E = \Delta E_{\max}(2\Delta_{\mathrm{acc}} - \Delta_{\mathrm{acc}}^2), \tag{5.7}$$

where $\Delta_{\mathrm{acc}} = L_{\mathrm{acc}}/L_{\mathrm{deph}}$ is the fraction of the dephasing length available for the acceleration process. Using the parameters of our experiment, the acceleration length L_{acc} is the remaining plasma length $L_{\mathrm{rp}} = L_{\mathrm{pl}} - L_I = 22.5 \pm 0.5\,\mathrm{mm}$ between the injection point at $L_I = 12.5 \pm 0.25\,\mathrm{mm}$ and the end of the gas jet, if the depletion length is longer than the plasma length $L_{\mathrm{pl}} = 35 \pm 0.5\,\mathrm{mm}$. If the depletion length is shorter than L_{pl}, the laser is depleted before the end of the gas jet, and the acceleration length is reduced to $L_{\mathrm{acc}} = L_{\mathrm{rp}} - (L_{\mathrm{pl}} - L_{\mathrm{depl}})$. Therefore, the fraction of the dephasing length available for acceleration can be written as

$$\Delta_{\mathrm{acc}} = \begin{cases} L_{\mathrm{rp}}/L_{\mathrm{deph}} & \text{for } L_{\mathrm{depl}} > L_{\mathrm{pl}}, \\ (L_{\mathrm{rp}} - (L_{\mathrm{pl}} - L_{\mathrm{depl}}))/L_{\mathrm{deph}} & \text{for } L_{\mathrm{depl}} < L_{\mathrm{pl}}. \end{cases} \tag{5.8}$$

This is illustrated in Figure 5.15b, where the theoretical dephasing and depletion lengths (calculated with Equations 2.71 and 2.70) are plotted. Additionally, the

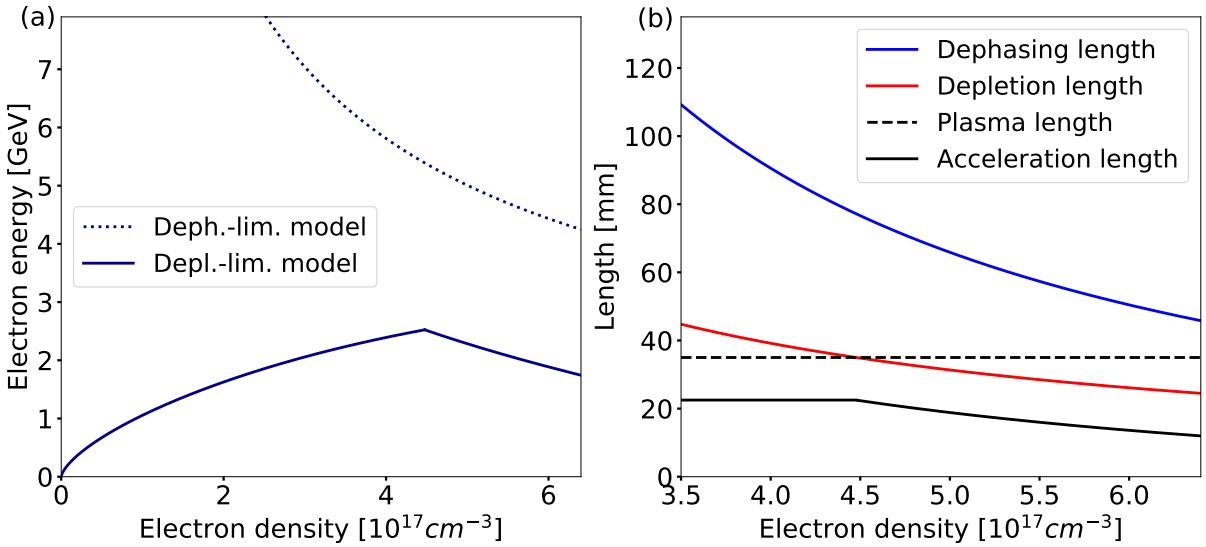

Figure 5.15.: (a) Expected energy gain for a dephasing-limited acceleration process with hypothetical adaptions to ensure a dephasing-limited process at all density values using Equation (5.6) (blue dotted line) and a depletion-limited acceleration process at our experimental parameters using Equation (5.7) (blue solid line). **(b)** Dependence of the theoretical dephasing (blue solid line) and depletion lengths (red solid line) on plasma density for our laser parameters (Equations 2.71 and 2.70). The black line shows the acceleration length in our experiment, which is, at low densities, limited by the remaining plasma length from the injector position to the end of the plasma. At higher densities, the acceleration length is limited by depletion. The length of the plasma is indicated by the black dashed line.

plasma length L_{pl} and acceleration length L_{acc} are indicated. The acceleration length L_{acc} is always smaller than the plasma length as we always inject further inside the plasma at the shock. At the density at which the depletion length reaches the length of the plasma, the acceleration length L_{acc} decreases due to the depletion of the laser.

Now using Equation (5.7), the expected energy gain for the depletion-limited process at different plasma densities for our otherwise fixed parameters is plotted in Figure 5.15a. If the depletion length is longer than the plasma length, the electron energy is expected to increase with increasing plasma density due to increasing accelerating fields. However, the depletion length decreases with increasing density. At the density at which the depletion length reaches the length of the plasma, the electron energy reaches its maximum. With further increasing density, the depletion length decreases further and, thus, the acceleration length and the energy gain decrease.

After discussing the expected energy gain at our parameters, we can compare this model to our measured results. Figure 5.16 shows the cut-off energy of measured electron bunches as a function of plasma density for different values of the injector delay. As expected, the cut-off energy first increases and then decreases with increasing density. This behavior is reproduced at all delay values. However, the

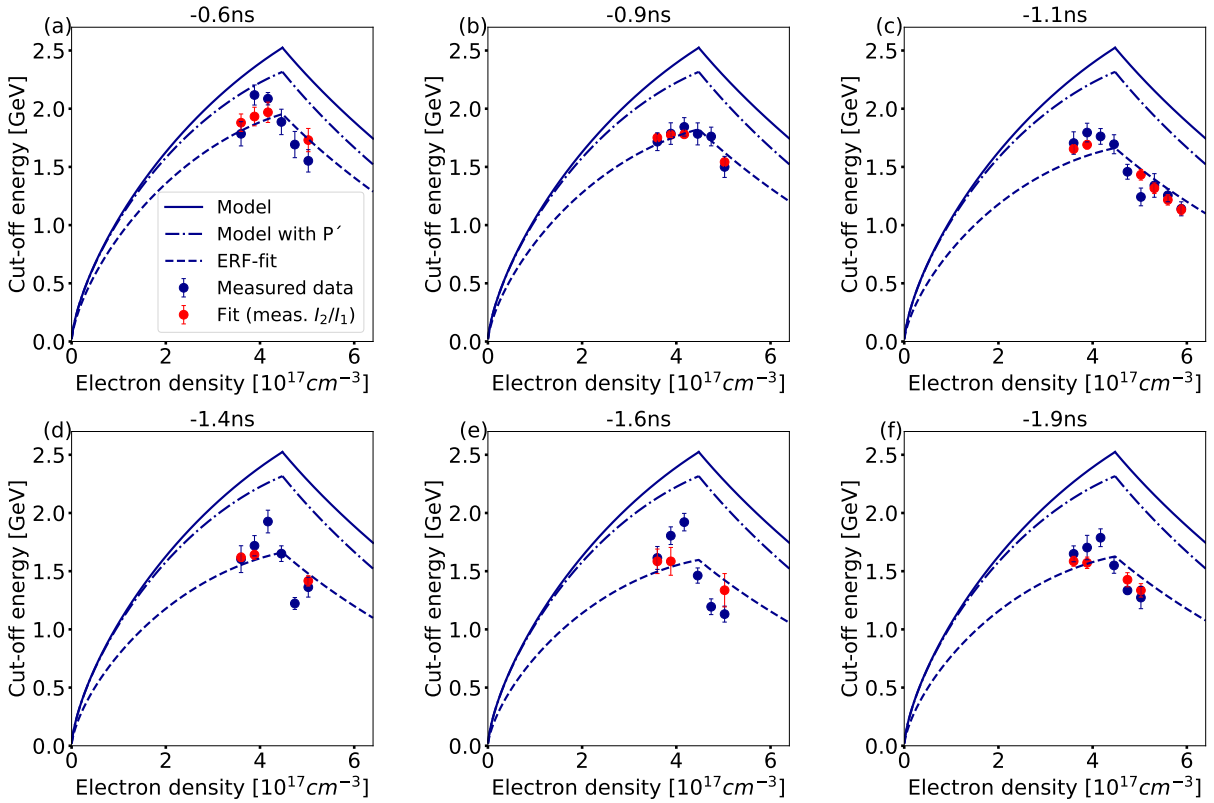

Figure 5.16.: Density scans at different injector delay values. The injector was positioned at $L_I = 12.5\,\text{mm}$ from the plasma start, leaving a remaining plasma length of $L_{\text{rp}} = 22.5\,\text{mm}$. Each blue data point shows the average over $8 - 19$ shots. The error bars show the corresponding standard error. The blue solid line indicates the expected energy gain for the model outlined in the main text. For the blue dashed/dotted line, the reduced power P' at the injection point is taken into account. These lines are the same in all plots for comparison to the actually reached energy at different delay values. The blue dashed lines indicate fits of the data using the model and the ERF fit parameter to account for the injection phase. The red points are another fit to the data that includes measurements of the shock ratios from shadowgraphy images at most delay and density values. The data in this plot was obtained on 19/10/2023 (Sets 17;19;21;23;27;29;31-38;41-54;57-70;72-74).

maximum energy is lower than what the model outlined above predicts (blue solid lines in each plot).

The model, in principle, provides a full description of the dependence between cut-off energy, plasma density, and injector position. There are, however, additional effects, such as the depletion of the laser before the injection point, that are not included in the model. Therefore, we consider this effect by using a reduced power $P' = P(1 - \frac{L_I}{L_{\text{depl}}})$ [168] at the injection point for calculating the matched value of a_0 with Equation (2.61) for the calculation of the dephasing length (Equation (2.71)) and ΔE_{max} (Equation (5.6)). The expected energy gain is plotted alongside the measured values in Figure 5.16 in all plots with the dashed/dotted lines. However, regarding absolute energy values, the model does still not agree very well with the

measurements.
One additional parameter that is not included in the theoretical model but which has a substantial effect on the gained energy is the injection phase (see also Section 5.1). In the following, we describe a method to take the effect of the injection phase into account (see also the study by Bloom et al.[194], who used a similar approach to account for the propagation length over which the laser underwent self-focusing before self-injection could occur).
For a roughly linear electric field in the wakefield bubble [142], we can calculate the effect of the injection phase on the maximum achievable energy gain and on the dephasing length with a parameter p, which we call 'energy reduction factor' (ERF), as was already done in Sections 5.3.2/5.4.1:

$$\Delta E_{\mathrm{max,ERF}} = p^2 \cdot \Delta E_{\mathrm{max}} = p^2 \frac{2}{3} a_0 \frac{n_c}{n_0} m_e c^2, \tag{5.9}$$

$$L_{\mathrm{deph,ERF}} = p \cdot L_{\mathrm{deph}} = p \frac{2}{3} \frac{\omega^2}{\omega_p^2} \frac{2\sqrt{a_0}}{k_p}. \tag{5.10}$$

In our case of a depletion-limited process, Equations 5.9 and 5.10 have to be inserted into Equation (5.7), which can then be fitted to our data to find the ERF. As seen in Figure 5.16, the fits can reproduce the increase and decrease of the cut-off energy at all delay values well. This analysis confirms that the acceleration process is limited by the depletion of the driver laser as soon as the density is high enough that the depletion length is smaller than the plasma length.
To investigate the influence of the ERF, their values for each delay obtained from the fits are plotted in Figure 5.17a. A clear dependence of the ERF on the delay is visible. This dependence is in agreement with the hypothesis that the injection phase limits the energy gain since the injection phase, and thus, the energy gain is expected to be dependent on the delay between the injector and driver beams, as already discussed in previous sections (e.g. Section 5.1).
Equation (5.10) implies that not only the energy gain but also the dephasing length is reduced by the advanced injection phase. This is illustrated in Figure 5.17b, where the dephasing length is plotted for different delay values calculated by Equation (5.10) using the ERF obtained from the fits to the data in Figure 5.16. At our parameters, the reduced dephasing lengths are still longer than the depletion length and the remaining plasma length. Therefore, at our parameters, the advanced injection phase limits the energy gain but does not reduce the dephasing length so strongly that the dephasing point would be reached before the laser has depleted.
By analyzing the corresponding shadowgraphy images of the shocks for our measurements at different densities and delay values, we can now also quantify the

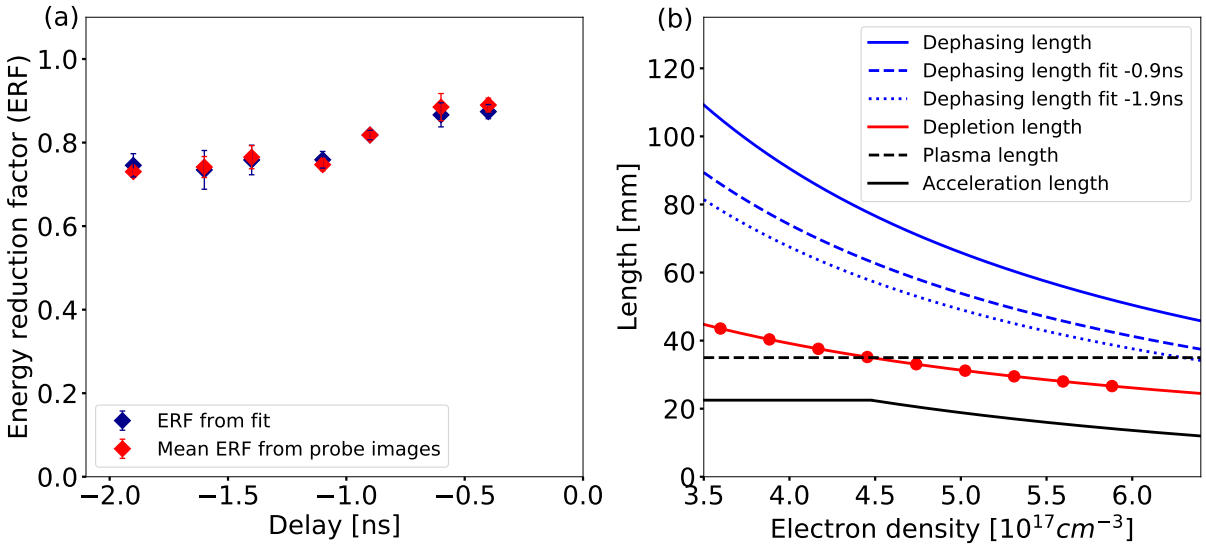

Figure 5.17.: (a) ERFs obtained from the fits in Figure 5.16 are plotted against delay values. The blue data points are values obtained from the fit where the ERF is the only fit parameter. Here, the error bar shows the fit error that is between 3 and 20 %. The red points are the calculated ERFs from the fits where the conversion factor (shock ratio factor SRF) from the measured intensity ratio of the shocks to the density ratio is the only fit parameter. Here, the plotted values are the mean values for different densities, with the error bars showing the standard deviation. **(b)** Dependence of the theoretical dephasing (blue solid line) and depletion lengths (red solid line) on plasma density (Equations 2.71 and 2.70). The red dots indicate the theoretical depletion lengths at the densities at which the measurements in this section were obtained. The black line shows the acceleration length, which is, at low densities, limited by the remaining plasma length from the injector position to the end of the plasma. At higher densities, the acceleration length is limited by depletion. The length of the plasma is indicated by the black dashed line. The effective dephasing lengths due to an advanced injection phase for different delay values are plotted in blue dashed and dotted lines.

shock ratios that correspond to the observed limit in energy gain. In Figure 5.18a, an exemplary shadowgraphy image of an optically-induced shock for a plasma density of $0.36 \cdot 10^{18}\,\mathrm{cm}^{-3}$ and a delay of $-0.4\,\mathrm{ns}$ is shown. By evaluating the line-out through the shock indicated by the red line, the intensity ratio I_2/I_1 of the shock in the shadowgraphy image can be calculated. However, the conversion from this intensity ratio to the actual density ratio n_2/n_1 is unknown. Here, I_1 and n_1 are the intensity and the density at the peak of the shock, respectively. I_2 and n_2 are the intensity and the density after the shock, respectively. Therefore, we assume n_2 to be the ambient plasma density that was measured from interferometry images when the shock is not present. Furthermore, we assume that the density ratio is linearly dependent on the measured intensity ratio obtained from shadowgraphy images and that $I_2/I_1 = 1$ corresponds to $n_2/n_1 = 1$ (no shock present). Thus, the density ratio can be calculated from the measured intensity ratio by

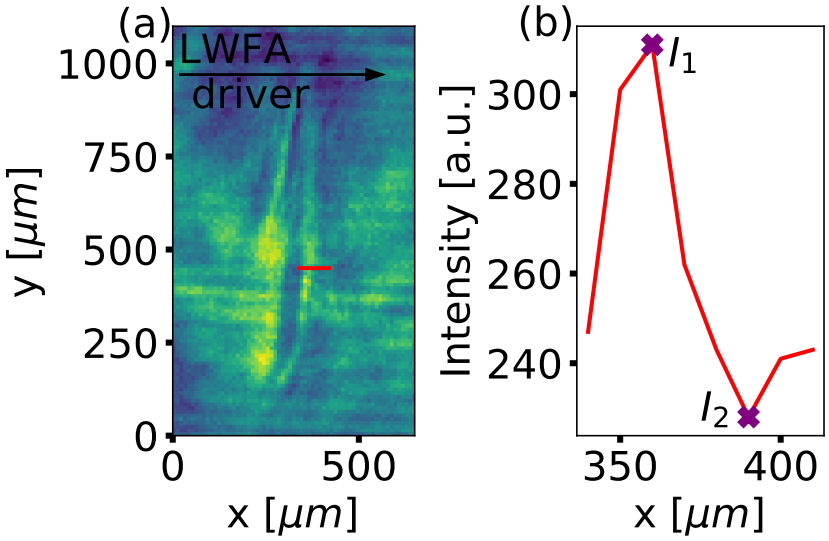

Figure 5.18.: Exemplary shock image. **(a)** Shadowgraphy image of a shock at a density of $0.36 \cdot 10^{18}\,\mathrm{cm}^{-3}$ and with the injector beam arriving 0.4 ns before the LWFA driver. The direction of the driver is indicated. The red line shows the position for the line-out shown in **(b)**. **(b)** Line-out of the shock seen in the shadowgraphy image. The maximum and minimum that were used to calculate the shock ratio I_2/I_1 in terms of intensity are indicated with purple crosses.

$$\frac{n_2}{n_1} = a\frac{I_2}{I_1} - a + 1, \tag{5.11}$$

with a an unknown factor that has to be deduced from a fit to the data. This factor we will call shock ratio factor (SRF). The conversion of the intensity ratio to the density ratio and, thus, the SRF should not be dependent on any parameters and should, thus, be the same for all measurements.
To be able to replace now the ERF as the single fit parameter to the data with the SRF and, thus, including the measurements of the shock ratios, we need to know the dependence of the ERF on the density ratio. Here, we assume a linear dependence between the injection phase φ_b and the ERF p due to the nearly linear acceleration fields [142]. Then, we can use Equation (5.1) and the constraints $\varphi_b = 0$ corresponding to $p = 1$ (injection at the rear of the bubble, no limit in energy gain due to the injection phase) and $\varphi_b = \pi$ to $p = 0$ (injection at the dephasing point, no energy gain) and arrive at the following equation between the ERF p and the density ratio in the shock:

$$p = -\frac{1}{\pi}\varphi_b + 1 = 2\sqrt{\frac{n_2}{n_1}} - 1. \tag{5.12}$$

Using now Equations 5.7- 5.12 and the SRF as the single fit parameter, the data in

Figure 5.16 can be fitted with the additional information of the measured intensity ratios in the shocks from shadowgraphy images. The red points in Figure 5.16 represent the fitted values for the density values where measurements of the shock ratios were possible. Unfortunately, in this experiment the saving of the shadowgraphy images failed for some data sets such that we do not have shock ratio values for all density and delay values. For the rest of the data points, the fit with the single fit parameter SRF reproduces the measured energy values well. From the result of the SRF from the fits and the measured intensity ratio, the density ratio

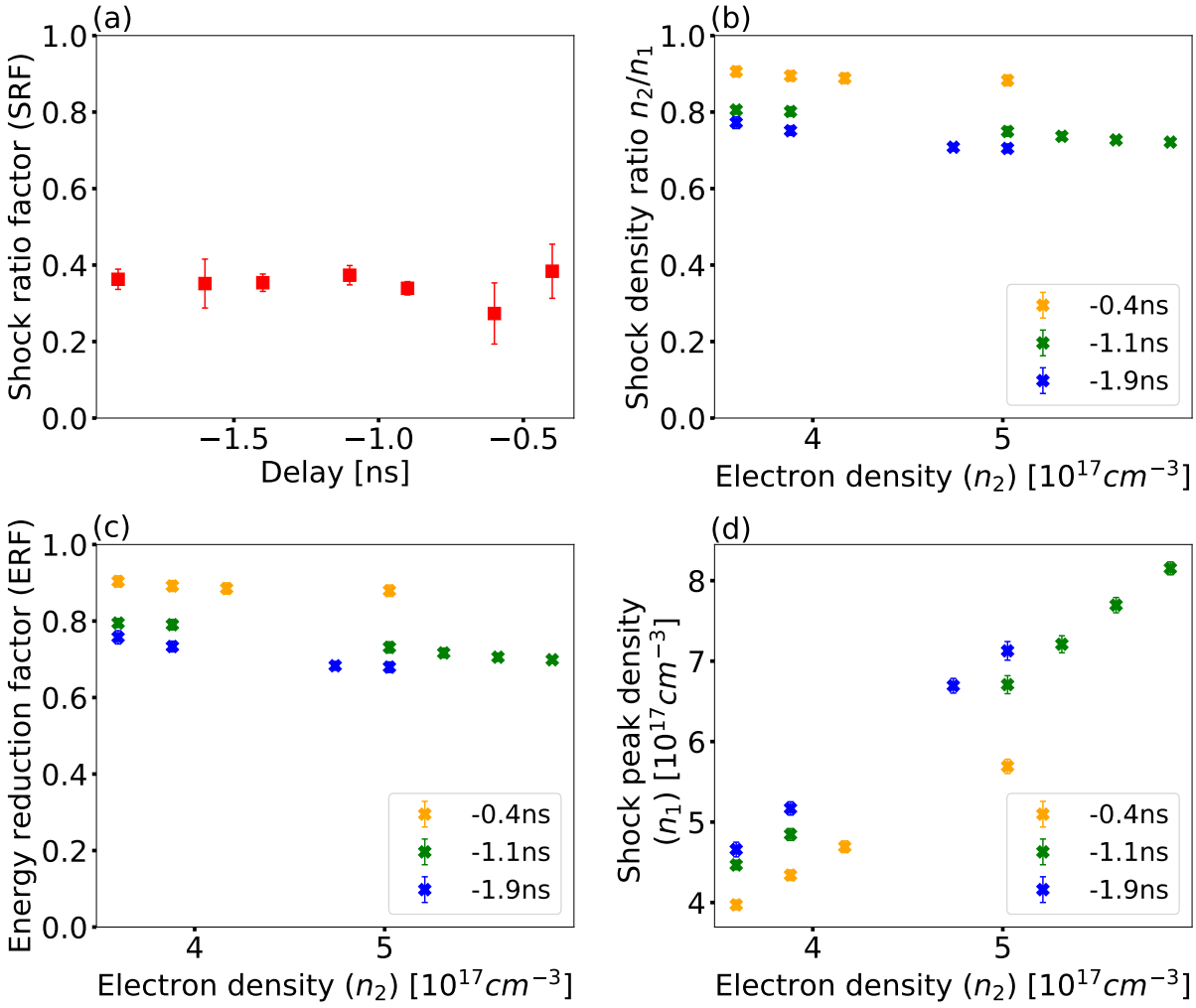

Figure 5.19.: (a) SRFs obtained from the fits in Figure 5.16 are plotted against delay values. The error bars show the fit errors that lie between 5 and 30 %. The SRFs are, as expected, roughly the same for all measurements. **(b)** The shock density ratios calculated from the SRFs are plotted for different density and delay values and are dependent on both parameters. **(c)** The ERFs calculated from the density ratios are plotted for different density and delay values and are also dependent on both parameters. **(d)** The peak densities in the shocks are plotted for different density and delay values.

for each set and the resulting ERF can be calculated with Equations 5.11 and 5.12. The calculated ERF (mean for different density values at each delay value and corresponding standard deviation) is plotted in Figure 5.17a alongside the ERF values obtained from the first fits to the data which did not include the measured shock ratios. The values agree well with the ERF values obtained from the first fits.
Additionally, more values obtained from the second fits are plotted in Figure 5.19. In Figure 5.19a, the SRF obtained from the second fits is plotted with the corresponding fit errors for different delay values. The fit errors have values between 5 and 30 %. It can be seen that the SRF obtained from the fit is nearly the same for all delay values (mean and standard deviation of 0.35 ± 0.03). This is expected since the conversion from the measured intensity ratios to density ratios should always be the same. From these SRF values and the measured intensity ratios, the density ratios can be calculated with Equation (5.11). In Figure 5.19b, the resulting density ratios are plotted for different ambient density values n_2 where the shadowgraphy images were saved. The density ratios are only plotted for selected delay values (-0.4 ns, -1.1 ns and -1.9 ns). The other values that lie in between are omitted to not overload the plot. The density ratios show that the peak density n_1 is between roughly 1.1 to 1.5 times higher than the ambient density n_2. It is visible that the shock ratio is, as expected, dependent on the delay. Additionally, it seems to be slightly dependent on the ambient electron density after the shock (n_2), such that the shock ratio n_2/n_1 decreases for higher ambient densities n_2. Therefore, also the ERF, which is calculated from the density ratio using Equation (5.12) and plotted in Figure 5.19c, decreases with higher ambient densities. This fact could not be deduced from the first fits to the data, where the ERF was the fit parameter, and only a single value was obtained for each delay value (cf. Figure 5.17a).
Furthermore, we can now also calculate the peak density n_1 of the shock from the density ratio, since the ambient electron density n_2 is known from the interferometry analysis. The result for different density and delay values is plotted in Figure 5.19d. The peak densities in the shocks reach values up to roughly $0.8 \cdot 10^{18}\,\mathrm{cm}^{-3}$.

5.4.3. Conclusion

In 'experiment 3' we were able to demonstrate that quasi-monoenergetic electron bunches at energies of nearly 2.5 GeV can be generated with the use of a 40 mm slit nozzle and optically-induced shock injection. This fulfills a number of requirements for the Breit-Wheeler project. However, the electron beams still require further optimization regarding stability and injection probability by stabilizing the laser performance and optimizing the quality and length of the slit nozzle. The

injector position scan in this regime indicated that the acceleration process at an acceleration length of 35 mm is already limited, probably by depletion and the termination of self-guiding.
The model described in the last section explains the measured electron energies at different densities and injector delay values. This allowed us to determine the limiting factors of the acceleration process in 'experiment 3': the acceleration process is either limited by the remaining plasma length or by the depletion of the drive laser if the plasma length is longer than the depletion length at high densities. Furthermore, the achievable energy gain is limited by the advanced injection phase into the wakefield for shock injection and is highest for small density ratios in the shock, which are achieved with small delay values between the driver beam and the injector beam. This implies a trade-off between highest energy and highest charge as the charge increases with high shock ratios (long delays). We could, furthermore, calculate the density ratios in the shocks that correspond to different injection phases and energy gains by measuring the intensity ratio of the shocks in shadowgraphy images and including these measurements in our model and in fits to the data.

5.5. Comparison to results in the LWFA community

In this section, we compare the results of our approach to accelerate electrons using long slit nozzles and optically-induced shock injection to the results of the LWFA community. Figure 5.20 shows the parameters reported for electron beams with mono-energetic features in the literature of the years 2004 - 2023 together with the electron performance presented in this thesis (see also Figure 1.2 and Section 1.3.2 for a discussion of the literature values). Note that the definition of quasi-monoenergetic features does not exclude beams with a high-energy quasi-monoenergetic peak but with possibly other features with non-negligible charge at lower energies. Such beams would not be ideal for the Breit-Wheeler experiment as discussed in Chapter 1 but are included here for completeness.
In Figure 5.20a, the achieved peak energies are plotted against the used peak powers (here the peak power is calculated from the energy arriving in the target area E_{target} and the pulse length $\Delta\tau_I$ with $P \approx E_{\text{target}}/\Delta\tau_I$). It is visible that our results lie within the trend of higher reachable electron energies with higher laser powers. We observe that we reached the highest energies so far using shock injection in 'experiment 2' and 'experiment 3' compared to values in the literature (to the best knowledge of the author). Results that achieved similar or higher peak energies at similar or lower laser powers used self-injection [34, 98], where the injection takes place at the rear of the bubble, and the maximum accelerating fields are exploited. Furthermore, often external guiding structures [72, 99, 109]

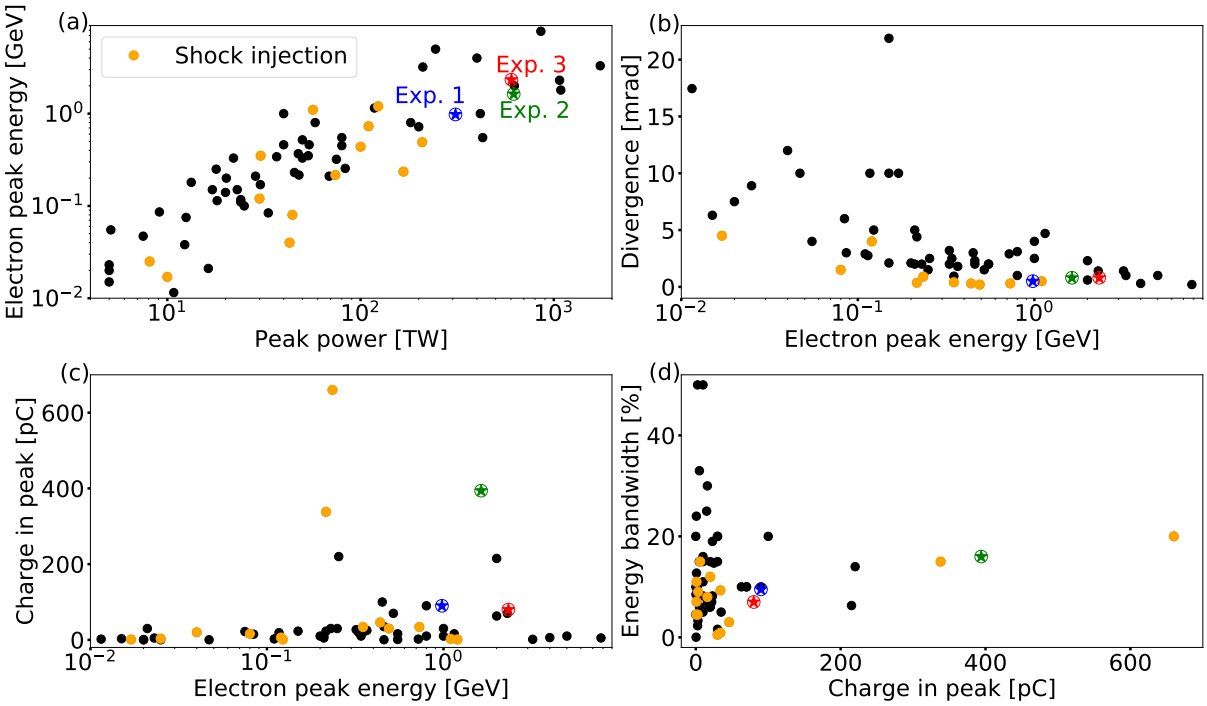

Figure 5.20.: Performance of electrons accelerated via LWFA in over 70 publications of the years between 2004 - 2023 [34, 35, 41–43, 45, 54, 72–119, 195–208]. This collection only contains publications in which quasi-monoenergetic features were observed. If a certain metric is not specified in one of the referenced publications, the data point is omitted in the respective panel. **(a)** The electron peak energy is plotted against the peak power. **(b)** The divergence is plotted against the electron peak energy. **(c)** The charge in the peak is plotted against the electron peak energy. **(d)** The energy bandwidth of the electron beams is plotted against the charge in the peaks. Data points where shock injection was used are colored orange. The data points of this work have been added as circled star-shaped points with blue for 'experiment 1', green for 'experiment 2', and red for 'experiment 3'. The data point of 'experiment 1' (blue) has been published in [168].

were used to reach energies over 3 GeV at lower or similar laser powers. Quite recently, results just over 1 GeV were reached by Oubrerie et al. [111] and Picksley et al. [114] using shock injection. Both experiments used HOFI channels to guide the drive laser. Oubrerie et al. used a blade-induced shock, and Picksley et al. used the shock generated at the front of the guiding channel.

Figure 5.20b shows the divergence plotted versus the electron peak energy. It is visible that our data is at the lower edge of divergence values measured in the field of LWFA. At similar energies, other publications measured similar or higher divergence values. Only Wang et al. [34] measured around 2 GeV a lower divergence of 0.6 mrad than our divergence of 0.8 mrad around this energy. However, this could be explained by the lower charge in the beams of Wang et al. (63 pC) compared to our charge between 80 and 394 pC in the peaks around 2 GeV.

In Figure 5.20c, the charge in the peak was plotted versus the electron peak en-

ergy. Compared to other results around 1 GeV, we accelerated more charge to 1 GeV (nearly 100 pC in the peaks) in 'experiment 1'. In 'experiment 2', we managed to accelerate an integrated charge of about 400 pC to energies above 1.5 GeV, considerably more than has previously been achieved in this energy range.
Finally, the energy bandwidth is plotted against the charge in the peak in Figure 5.20d. We can see that, especially for shock injection, the bandwidth increases with the charge in the peak. Our measurement results are within this trend and achieve lower bandwidth for lower charges in the beams.

6. Summary and Outlook

In this work, two different kinds of gas targets - a gas cell and supersonic slit nozzles - have been tested and proved to be suitable for the acceleration of electron beams to the multi-GeV level using LWFA. With self-injection in the gas cell, the electron energy goal of 2.5 GeV was readily approached with a relatively low laser energy of 6 J on target (in central Airy disk), yielding beams with very low divergence (Figure 4.1). However, their large bandwidth is not ideal for some applications and the planned Breit-Wheeler experiment at CALA (cf. Chapter 1). First tests were conducted with optically-induced shock injection to generate quasi-monoenergetic beams in the gas cell. Some quasi-monoenergetic beams close to 1 GeV were generated (Figure 4.3). However, these beams must still be optimized for higher reproducibility, shot-to-shot stability, and a small bandwidth by finding the perfect injection point in the gas profile.
Using the optically-induced shock injection scheme with slit nozzles as targets resulted in quasi-monoenergetic electron beams at the multi-GeV level (see Chapter 5). Using approximately 6 J on target (in central Airy disk), quasi-monoenergetic bunches around 1 GeV with low divergence, several tens of pC charge, high reproducibility, and shot-to-shot stability (Figure 5.3) have been achieved. These results have been published in a publication written by the author of this thesis [168]. Experiments with higher laser energy up to 11 J in the central Airy disk have been conducted, and, to our knowledge, the first shock-injected, quasi-monoenergetic electron beams up to 2.5 GeV have been achieved (Figure 5.8, Figure 5.11). With this, these beams have reached the energy needed for the Breit-Wheeler experiment. However, they have yet to be optimized for higher reproducibility and shot-to-shot stability.
We can conclude that the acceleration of quasi-monoenergetic electron beams to 2.5 GeV, as required for the Breit-Wheeler experiment, has been observed with the optically-induced shock injection scheme. Therefore, the optimization of optically-induced shock injection in either slit nozzles or the gas cell, specifically the optimization of the stability of injected electron bunches, is a promising path to achieving the required beams for the Breit-Wheeler experiment.
To this end, the optically-induced shock injection scheme has been investigated to gain valuable insights for finding the ideal conditions for electron beams at 2.5 GeV. Optically-induced shock injection was shown to be tunable in energy and charge

via the delay between the driver and injector beams. The first findings about the tunability of the optically-induced shock injection scheme have been published in [168]. Different delay values result in different density ratios of the optically-induced shock. It was shown that more charge is injected for high density ratios in the shocks. The electron energy, on the other hand, increases for a decreasing density ratio in the shock at shorter delay values. This can be explained by the injection occurring closer to the rear of the plasma bubble, where the acceleration gradients are at their maximum. We, therefore, assume that the highest energy with shock injection can be achieved using shocks with a small density ratio due to the injection at the back of the bubble and, additionally, because less charge is injected, which reduces beam-loading effects and thus also the bandwidth of injected bunches. Small density ratios are achieved with optically-induced shocks using small delays between the injector beam and the driver beam. The density ratio of obstacle-induced shocks, on the other hand, is dependent on the Mach number of the supersonic flow (cf Section 3.4.2) and, therefore, only adjustable by exchanging the nozzle, which renders the tunability less flexible. To achieve a small density ratio of the obstacle-induced shock, the Mach number of the nozzle would have to be reduced, implying a larger throat size, which also increases the gas load on the vacuum system. Together with the increased stability of optically-induced shocks as shown in Foerster et al. [110], optically-induced shock injection is, therefore, advantageous to achieve tunable and stable electron beams at high energies with moderate charge and small bandwidths, as needed for the Breit-Wheeler experiment.

Furthermore, scans of the injector beam position have shown that quasi-monoenergetic beams are predominantly generated when the injector beam is positioned close to the beginning of the plasma. We assume that more charge is injected further inside the plasma due to a higher density, which affects the bandwidth of the bunches via beam-loading. Therefore, the density and gas length have to be optimized for the injector position close to the up-ramp of the plasma to produce the desired quality of electron bunches with a small bandwidth at 2.5 GeV. The density has to be high enough to ensure stable injection. Then, the gas length can be adjusted to the length where the acceleration process just starts to be limited for a given density and given laser parameters so that the highest possible energy at these parameters can be reached.

Alternatively, with the injection position further inside the plasma, the density ratio of the shock can be adjusted via the injector delay to inject less charge and reduce beam-loading effects on the bandwidth of the bunches.

Theoretical models of the bubble regime of LWFA predict that the acceleration at our parameters is limited by the depletion of the laser energy. Scans of the acceleration length via the scans of the injector position did not conclusively confirm this prediction, as the available scanning ranges were not large enough. However, den-

sity scans were conducted, and a theoretical model for the acceleration process was adapted from Lu et al. [142] and Bloom et al. [194] and reproduced the measured data of the density scans well. The model confirmed that the acceleration process at our parameters is limited by depletion. These insights can be used in further experiments to find the ideal gas length at a given laser energy and plasma density. At laser energies of 11 J in the central Airy disk or slightly higher, a gas density around $4 \cdot 10^{17}\,\mathrm{cm}^{-3}$ and a gas length between $30 - 35\,\mathrm{mm}$, quasi-monoenergetic beams around 2.5 GeV will be feasible with shock injection, which is an important finding for the Breit-Wheeler experiment.
Regarding the choice between the gas cell and slit nozzles as targets, several points need to be considered: Optimizing the gas length at a given laser energy is easier with the gas cell. However, finding the optimal injection point with the optical injector through a hole in the gas cell can be difficult. The gas cell yields higher stability of the gas profile, increasing the stability of the electron beams. On the other hand, the setup with a slit nozzle is more compact, and the focus area is easier accessible, facilitating the alignment of the drive laser, the measurement of the density with the probe beam, and the positioning of the injector beam. This will play an important role in the setup for the Breit-Wheeler experiment, which will be a complex setup with limited space. We assume that the stability of electron beams with nozzles can be improved by the fabrication of slit nozzles from stainless steel to increase the stability of the gas flow.
Furthermore, we assume that instabilities stemming from the driver laser greatly influence the electron stability at the moment. To address this issue, work is being done at CALA to characterize instabilities by monitoring as many parameters of the laser system as possible, such as the beam pointing at different positions in the laser chain, the wavefront after the front-end and before the compressor, the temperature of the cooling systems and the large amplifier crystals, and the energy of the pump lasers. For example, a strong heating of the edge of the crystals in the two last amplifier stages has been found, which influences the thermal lens of the crystals and, thus, induces the defocus term of the wavefront to drift. Furthermore, a strong correlation between the defocus term of wavefront fluctuations to electron energy and charge has been found. Therefore, different possibilities to stabilize the system similar to Maier et al. [43] will be investigated. For example, the cooling system of the crystals will be adjusted to reach better thermalization of the crystals. We expect this to also reduce air turbulences on the beam path induced by heated air around the crystals, which will not only reduce a drift of the defocus term of the wavefront but also shot-to-shot fluctuations. With this, we expect to reduce the drift and shot-to-shot instabilities of the electron performance.
Additionally, an active pointing stabilization is planned to be implemented in the front-end of the ATLAS-3000 at CALA with the drift of the beam to be monitored with cameras and four motorized mirrors actively compensating for the measured

drift. With an improved pointing stability of the drive laser, the optically-induced shock injection scheme can also be combined with HOFI-channels [72, 114, 132] to guide the drive laser. As a consequence, the laser will also be guided at lower plasma densities. At lower plasma densities, the depletion length is longer, increasing the reachable electron energy at fixed laser parameters. This will not be necessary for the Breit-Wheeler experiment, as it is designed for 2.5 GeV. However, it will be useful to further extend the energy range of shock-injected, quasi-monoenergetic electron beams.
Another suggestion to improve the stability is to change to a focusing optic with a longer focal length. In the course of this work, a 6 m focal length OAP (cf. Section 4.3) and a 10 m focal length spherical mirror have been used. The longer focal length resulted in more stable electron beams because the longer Rayleigh length enhances stable propagation of the drive laser through the gas target, specifically through the density gradients at its edge. A change to a focal length of 13 m would be feasible in the vacuum chamber of ETTF, and we assume it will lead to an increase in the stability of the electron beams. The same holds for using the smaller beam before focusing when using 'ATLAS configuration 1', which increases the Rayleigh length and, at the same time, reduces influences of air fluctuations on the beam before focusing.
However, for the Breit-Wheeler experiment, 'ATLAS configuration 2' with the larger beam needs to be used to amplify the laser sufficiently in the last amplifier stage. Furthermore, the large beam is needed since it has to be split into two beams before individual focusing optics to both drive the LWFA process and act as the collider in the Breit-Wheeler experiment. Our first approach for this will involve a configuration where the inner part of the beam is picked and used as the collider beam. To reach sufficient energy in the collider beam, the picked beam must have a diameter of approximately 12 cm, corresponding to approximately 20 % of the total beam area. This leaves roughly 80 % of the total laser energy in the outer ring for driving the LWFA process. However, first tests have shown that, when 20 % of the energy are picked, the peak intensity of the focus generated by the ring beam is actually reduced by roughly 40 % due to a reduced focus quality. The laser energy will have to be increased to compensate for this reduction.
Alternatively to the ring beam configuration, the beam can be divided vertically, resulting in two D-shaped beam profiles. First tests have shown that this configuration reduces the focus quality of the LWFA driver and the peak intensity less than the ring beam configuration. Tests with both configurations will be the subject of further investigations to determine the most suitable configuration for the Breit-Wheeler experiment.

In conclusion, several crucial steps towards accomplishing the Breit-Wheeler experiment at CALA have been completed. Shock-injected, quasi-monoenergetic

electron beams up to 2.5 GeV were achieved, and new insights on the influence of the injection phase in shock injection have been gained. Acceleration limits have been investigated to predict optimized parameters for accomplishing the desired electron beams. Furthermore, work has been done by our collaborators [3, 6, 24] on the design for the Breit-Wheeler experiment and the detector setup to measure electron-positron pairs. Therefore, a successful Breit-Wheeler experiment at CALA has become reachable in the next few years.

A. Parameter and results overview of slit nozzle experiments

Experiment/Section		**1 (1 GeV)/5.2**	**2 (2 GeV)/5.3**	**3 (2.5 GeV)/5.4**
Nozzle Design (Figure)		**1** (5.2)	**2** (5.7)	**3** (5.10)
Geometry (cf. Figure 3.7)	Exit length	20 mm	20 mm	40 mm
	Throat length	750 µm	750 µm	1.5 mm
	Opening angle	22.6°	22.6°	33.7°
	Width	3 mm	2 mm	1.5 mm
Theory (cf. Figure 3.6)	S/S_0	26.667	26.667	26.667
	M_{exit} (H_2)	5.15	5.15	5.15
Simulation (H_2)	Inlet pressure	2.6 bar	3.4 bar	2.5 bar
	M_{exit} (peak)	4.48	4.34	3.72
	e-density in throat (peak)	$41.95 \cdot 10^{18}\,\text{cm}^{-3}$	$54.90 \cdot 10^{18}\,\text{cm}^{-3}$	$40.97 \cdot 10^{18}\,\text{cm}^{-3}$
	Exit e-density (peak)	$1.21 \cdot 10^{18}\,\text{cm}^{-3}$	$1.79 \cdot 10^{18}\,\text{cm}^{-3}$	$1.55 \cdot 10^{18}\,\text{cm}^{-3}$
	e-density above nozzle (peak)	$0.98 \cdot 10^{18}\,\text{cm}^{-3}$	$0.78 \cdot 10^{18}\,\text{cm}^{-3}$	$0.32 \cdot 10^{18}\,\text{cm}^{-3}$
	(in height above nozzle)	(4.2 mm)	(4.3 mm)	(4.3 mm)
Experiment (H_2)	Inlet pressure	(2.60 ± 0.02) bar	(3.40 ± 0.02) bar	(2.50 ± 0.05) bar
	e-density above nozzle (mean & std along plateau)	$(1.0 \pm 0.1) \cdot 10^{18}\,\text{cm}^{-3}$	$(0.4 \pm 0.1) \cdot 10^{18}\,\text{cm}^{-3}$	$(0.4 \pm 0.1) \cdot 10^{18}\,\text{cm}^{-3}$
	(in height above nozzle)	$((4.2 \pm 0.2)$ mm)	$((4.3 \pm 0.2)$ mm)	$((4.3 \pm 0.2)$ mm)

Table A.1.: Overview of slit nozzle designs used in the experiments discussed in Sections 5.2 - 5.4.

Experiment/Section		**1 (1 GeV)/5.2**			**2 (2 GeV)/5.3**		**3 (2.5 GeV)/5.4**		
Scan (Figures)		Static (5.3/5.4)	Accel. length (5.5)	Injector delay (5.6)	Static (5.8)	Accel. length (5.9)	Static (5.11)	Accel. length (5.12/5.13)	Density/Injector delay (5.14-5.19)
Nozzle	Exit length	20 mm			20 mm		40 mm		
	Width	3 mm			2 mm		1.5 mm		
Laser	f-number	56 ± 2			37 ± 1		37 ± 1		
	Foc. FWHM (HDR)	(57 ± 6)µm			(39 ± 5)µm		(38 ± 5)µm		
	Foc. w_0 (HDR)	(48 ± 5)µm			(33 ± 4)µm		(32 ± 4)µm		
	Strehl ratio (HDR)	0.77 ± 0.08			0.62 ± 0.05		0.70 ± 0.05		
	Energy bef. compr.	(15.5 ± 0.5)J			(31 ± 1)J		(30 ± 1)J		
	Energy (in centr. Airy disk)	(6 ± 1)J			(10 ± 2)J		(11 ± 2)J		
	I_0[W/cm^2] (HDR)	$(8.9 \pm 0.8) \cdot 10^{18}$			$(3.2 \pm 0.5) \cdot 10^{19}$		$(3.5 \pm 0.5) \cdot 10^{19}$		
	a_0 (HDR)	2.0 ± 0.2			3.9 ± 0.3		4.1 ± 0.3		
Plasma density [10^{18} cm^{-3}]		1.0 ± 0.1		1.1 ± 0.1	0.4 ± 0.1		0.4 ± 0.1		$0.36 - 0.59$
Matching condition	$k_p w_0$	9.1 ± 1.4		9.6 ± 1.4	3.9 ± 1.0		3.8 ± 1.0		$3.62 - 4.63$
	$2\sqrt{a_0}$	2.9 ± 0.1			3.9 ± 0.2		4.0 ± 0.2		
	matched a_0	4.5 ± 0.6		4.6 ± 0.6	3.9 ± 0.9		4.0 ± 0.9		$3.83 - 4.51$
Plasma length		(13.0 ± 0.5)mm			(19.0 ± 0.5)mm		(35.0 ± 0.5)mm		
Injector	Position [mm]	1.2 ± 0.25	$0.7 - 8.2$	5.7 ± 0.25	3 ± 0.25	$3 - 20$	1 ± 0.25	$1 - 34.5$	12.5 ± 0.25
	Delay [ps]	270 ± 2		$400 - 1900$	1100 ± 2		1100 ± 2		$400 - 1900$
	Energy [mJ]	90 ± 20			80 ± 20		70 ± 20		
Remaining plasma length [mm]		11.8 ± 0.5	$12.3 - 4.8$	7.3 ± 0.5	16.0 ± 0.5	$16 - 0$	34.0 ± 0.5	$34 - 0.5$	22.5 ± 0.5
Injection probability [%]		91			53		37		
Electron energy	Peak [MeV]	980 ±83			1633 ±453		2331 ±343		
	FWHM [MeV]	94 ± 27			263 ± 115		163 ± 50		
	Cut-off [MeV]	1086 ±76			1929 ±335		2548 ±267		
	(stability in cut-off)	(7 %)			(17 %)		(10 %)		
Electron charge in peak [pC]		92 ± 56			394 ± 207		80 ± 51		
Energy conversion efficiency (within bunch) [%]		1.5 ± 0.9			6.0 ± 2.8		1.6 ± 0.8		
Electron divergence (RMS) [mrad]		0.49 ±0.05			0.8 ±0.3		0.8 ±0.5		

Table A.2.: Summary of parameters and results from the experiments with slit nozzles discussed in Sections 5.2 - 5.4. The results of some scans are not included since they are visualized more clearly in the corresponding sections.

B. Interferometry Analysis

To give a few more details about the interferometry analysis, the steps for the analysis used in this work are described in more detail in this appendix. A short description concentrating on the theory is given in Section 3.5. In this appendix, the different steps are illustrated with images in Figure B.1 using one single shot as an example (from 'Experiment 2' taken on 17/10/2023 (shot# 306) with an inlet pressure of 3.4 bar, see Section 5.3.1), the used Python commands will be given, and the possible origin of some features in the resulting phase/density distribution will be discussed.
The raw interferometry image is shown in Figure B.1a with a resolution (pixel size) of $s_{px} = 11.1\,\mu m$ ('Exp. 2/3' Sect. 5.3.1/5.4); in 'Exp. 1' (Sect. 5.2.1) it was $s_{px} = 6.5\,\mu m$. The frequency of the interference fringes is $f = 1.68/mm$ in z-direction ('Exp. 2/3') (in 'Exp. 1' it was $f = 4.81/mm$). The raw image is Fourier transformed using the Python commands *numpy.fft.fft2()* [209] and *numpy.fft.fftshift()* [210]. The result is shown in Figure B.1b, where the natural logarithm of the squared absolute values of the FFT-data was taken to generate the image (*numpy.log(numpy.abs()^2)*). In Fourier space, the frequency of the interference fringes is found using the Python command *skimage.feature.peak_local_max()* [211]. Then, the data is filtered in Fourier space around this frequency using an n-th order Gaussian filter

$$y = \exp\left(n - \left(\frac{2(x_0 - x)}{\Delta x}\right)^{2n} \ln 2\right) \tag{B.1}$$

with x_0 the center frequency and Δx the FWHM of the Gaussian. In the example shown in Figure B.1, a 10th-order Gaussian ($n = 10$) with a FWHM of $\Delta x = 1.4/mm$ was used.
Then, the filtered data is inversely Fourier transformed using the commands *numpy.fft.ifftshift()* [212] and *numpy.fft.ifft2()* [174]. From this, the phase is calculated using Equation (3.10). The result is shown in Figure B.1c. As Equation (3.10) gives modulo-2π values of the phase, they have to be unwrapped using the command *skimage.restoration.unwrap_phase()* [176]. A continuous phase image is obtained that is shown in Figure B.1d. The same steps have to be applied to a background image without gas. This can be subtracted from the unwrapped

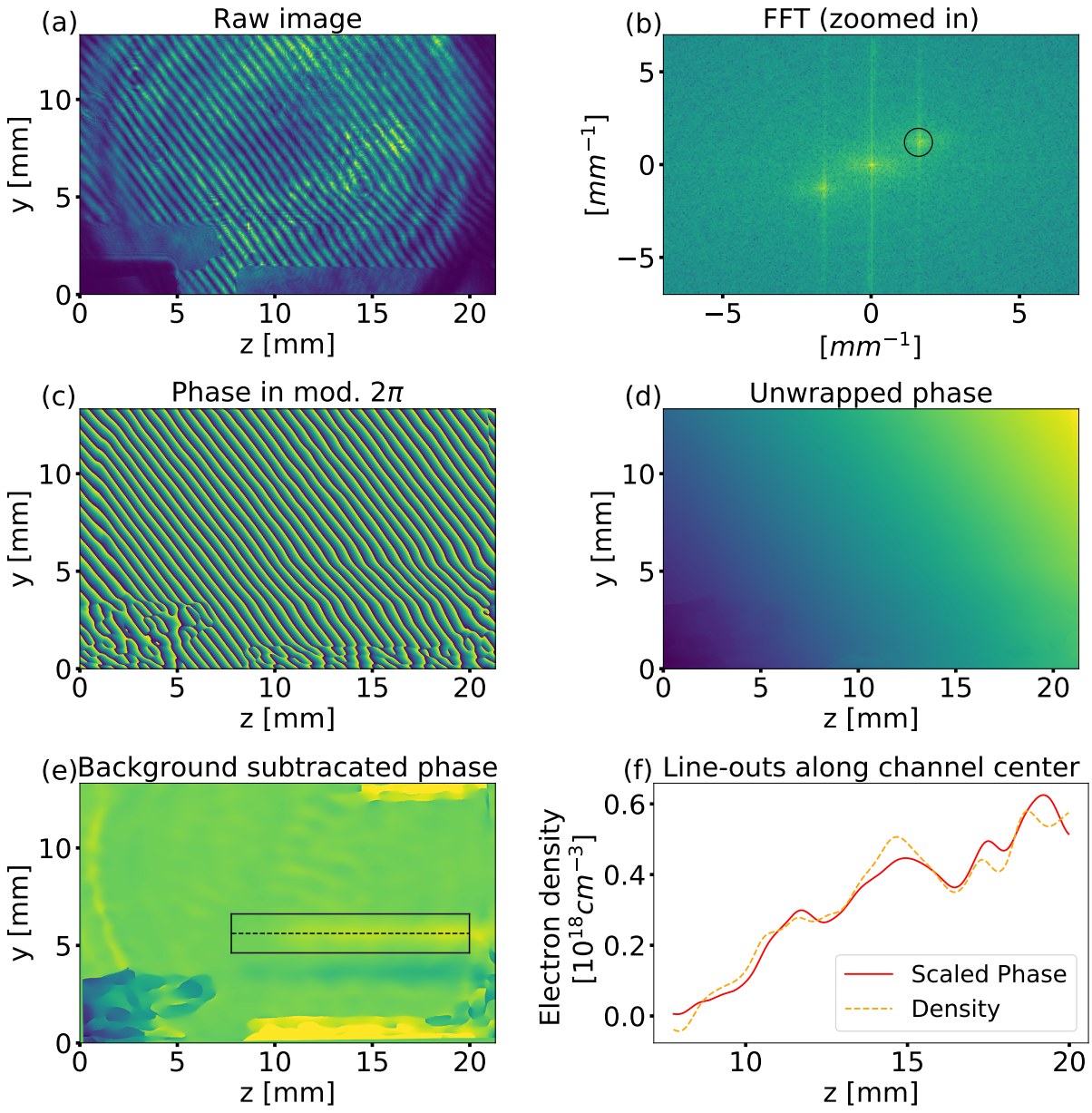

Figure B.1.: Example images of interferometry analysis steps. **(a)** Exemplary raw interferometry image of 'Experiment 2' taken on 17/10/2023, shot# 306 (Section 5.3.1) with an inlet pressure of 3.4 bar. **(b)** 2-dimensional discrete Fourier transform by means of the fast Fourier transform (FFT) of the raw image shown in **(a)**. A zoomed-in part around the zero frequency component is shown. The circle indicates the frequency of the interference fringes and the rough area around it that is not filtered out and used to calculate the phase. **(c)** The phase calculated from the filtered FFT in modulo-2π values. **(d)** The unwrapped phase. **(e)** The unwrapped background phase was subtracted from the unwrapped phase to generate the image, where the plasma channel is visible. The black solid lines indicate the area of the plasma channel used for the Abel inversion. The black dotted line indicates the center line of the channel. **(f)** Line-outs along the center of the plasma channel after more analysis steps (symmetrizing, setting the background to zero, Abel inversion). The orange dashed line is the direct result of the Abel inversion. The red solid line is the line-out of the background subtracted phase scaled to the density obtained by the Abel inversion.

phase image to obtain the image shown in Figure B.1e, where two copies of the plasma channel are visible. In this example, we use the upper channel for the rest of the analysis. The area used for this is indicated in the image with a black box. To obtain 3D values of the plasma density in the channel, the inverse Abel transform has to be applied (cf. Equation (3.12)). To be able to feed the data in the black box in Figure B.1e into the command for the inverse Abel transform (*abel.Transform()* [179]), the plasma channel should be straight within the coordinate system. If this is not the case, the commands *skimage.transform.ProjectiveTransform()* and *skimage.transform.warp()* [213] can be used to tilt the complete image such that the plasma channel lies straight within the coordinate system. Furthermore, the plasma channel has to be symmetric to the center line. As this will not be the case for real data, the channel has to be symmetrized, for example, by taking the mean of the two channel halves. Additionally, the edge of the area given to the Abel inversion algorithm has to be zero. For this, all data has to be offset accordingly. This ensures that absolute phase values are obtained from the Abel inversion. From the result of the Abel inversion, the plasma density can be calculated with Equation (3.13). A line-out of the result along the channel center is plotted in Figure B.1f with the orange dashed line. The shape of the line-out differs slightly from the line-out of the phase before the Abel inversion. Since the line-out of the phase is a more direct representation of the density profile, the phase line-out was scaled to match the density (red solid line in Figure B.1f), and used as a representation for the density profile.
On both line-outs some peaks are visible that either indicate a not completely homogeneous density profile, most likely due to the roughness of the inner surface

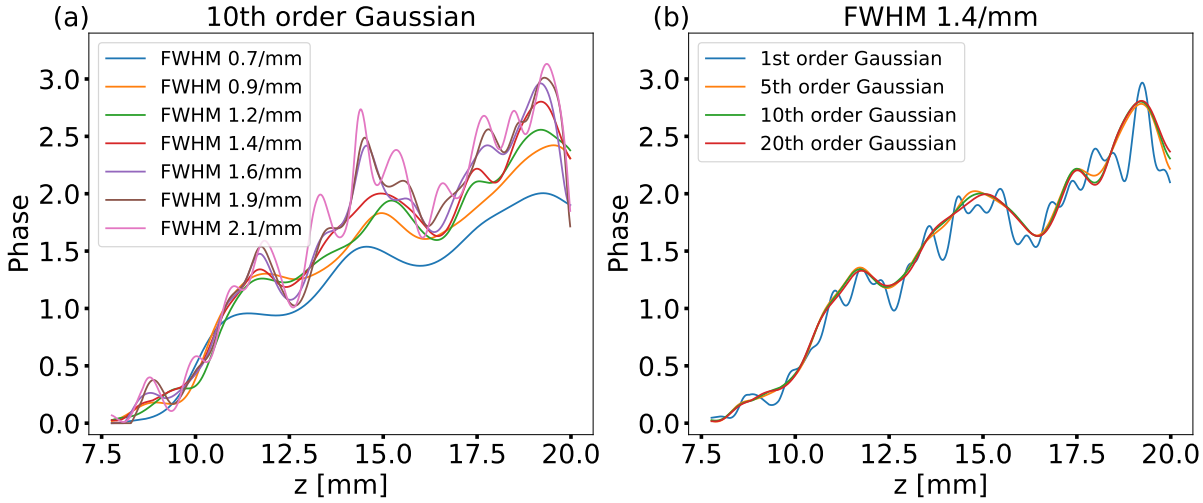

Figure B.2.: Comparison of phase line-outs along the center of the plasma channel for different Gaussian filters. **(a)** 10th-order Gaussian filters with different FWHM. **(b)** Gaussian filters with different orders and a FWHM of $1.4/\mathrm{mm}$.

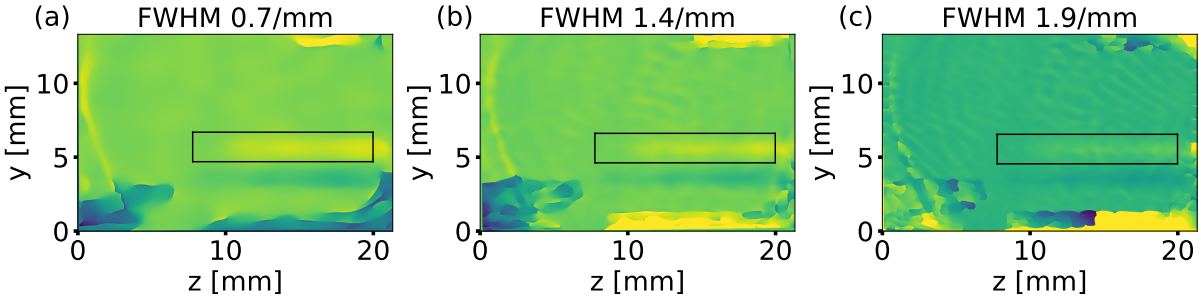

Figure B.3.: Background subtracted phase obtained by using different sizes of the filters in Fourier space. All filters here have the shape of a 10th-order Gaussian with different FWHM. **(a)** Fourier filter with a FWHM of $0.7/\mathrm{mm}$. **(b)** Fourier filter with a FWHM of $1.4/\mathrm{mm}$. **(c)** Fourier filter with a FWHM of $1.9/\mathrm{mm}$.

of the 3D-printed nozzle. However, they might also originate from noise in the interferometry data. A small filtering window in Fourier space can reduce the oscillations in the profile by filtering out more noise. However, if the frequencies of the measurement overlap with noise, a small filtering window can also result in a reduction of the measured density, indicating a loss of information. This is illustrated in Figure B.2, where the resulting phase profiles along the channel center obtained from the analysis using different Gaussian filters are plotted. In Figure B.2a, a 10th-order Gaussian was used with different FWHM. It is visible that the phase is reduced for FWHM smaller than approximately 1.4/mm. Therefore, we concluded that this is the smallest possible filtering window without a loss of information, and it was used for the analysis of the shots in Section 5.3.1. The same test was used for all interferometry data to decide on the appropriate filtering size. For larger filtering windows, the overall density does not increase significantly, but oscillations on the profiles get stronger, which is an indication that these oscillations are noise or a remainder of the interference fringes.

To also investigate the influence of the order of the Gaussian, the resulting phase profiles of Gaussians of different orders, all with a FWHM of 1.4/mm, are shown in Figure B.2b. We can see that a first-order Gaussian results in a filtering window that is too big and it seems like remainders of the interference fringes are visible in the profile. From the 5th order, the difference in the phase profiles is not significant. For the analysis of all interferometry data in this work, a 10th-order Gaussian was used.

The interpretation that remainders of the interference fringes are visible for large filtering windows is supported by looking at the background subtracted phase images for different filter sizes shown in Figure B.3. For the smallest filtering window with a FWHM of 0.7/mm (Figure B.3a), the image looks very clean. However, we could see from the phase line-outs in Figure B.2a that we are most likely already losing information. The images where filtering windows with FWHM of 1.4/mm

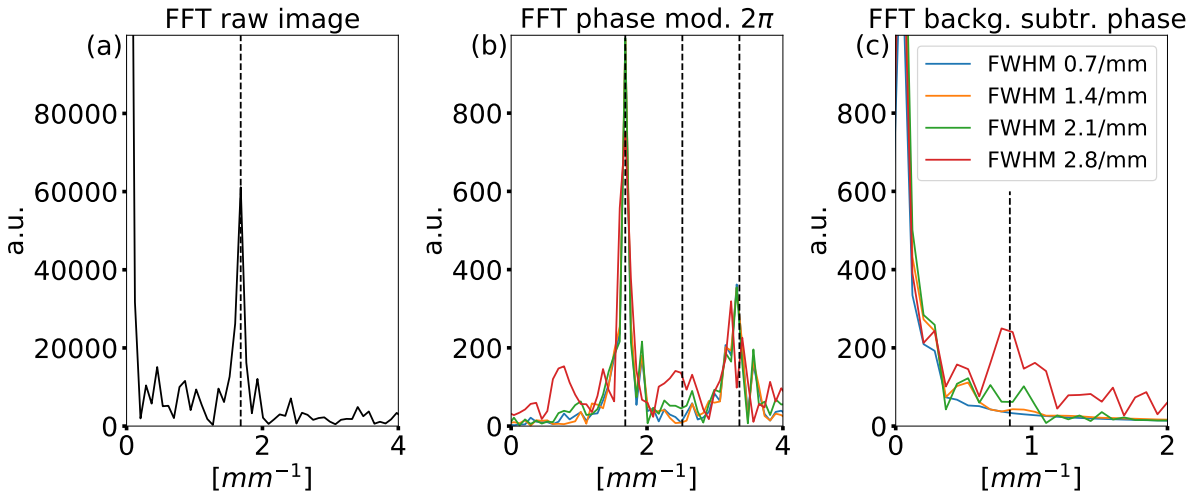

Figure B.4.: 1-dimensional Fourier transform (FFT) of the data along the plasma channel in different steps of the analysis. **(a)** FFT of the raw image along the plasma channel. The black dashed line indicates the frequency f of the interference fringes at $1.68/\mathrm{mm}$. **(b)** FFTs of the modulo-2π phase along the plasma channel for 10th-order Gaussian filters with different FWHM. The black dashed lines indicate the frequency $f = 1.68/\mathrm{mm}$ of the interference fringes and its harmonics at $1.5 \cdot f = 2.52/\mathrm{mm}$ and at $2 \cdot f = 3.36/\mathrm{mm}$. The noise around the zero-frequency and at higher frequencies is reduced. **(c)** FFTs of the background subtracted phase along the plasma channel for 10th-order Gaussian filters with different FWHM. The information about the plasma density is now shifted from the frequency of the interference fringes to the zero frequency due to the unwrapping procedure ($f - f = 0$). The black dashed line indicates the frequency $1.5 \cdot f - f = 0.84/\mathrm{mm}$, where a remaining trace of a harmonic of the interference fringes for weak filtering (large FWHM) is visible.

(Figure B.3b) and 1.9/mm (Figure B.3c) were used are noisier and, especially in Figure B.3c, traces of the interference fringes are still visible.
Additionally, we can look at the Fourier transforms in different steps of the analysis. In Figure B.4, the 1-dimensional Fourier transform along the center line of the plasma channel for the raw image (Figure B.4a), for the modulo-2π phase image (Figure B.4b), and for the background subtracted phase image (Figure B.4c) is shown. For the raw image, the frequency of the interference fringes results in the peak at a frequency of $f = 1.68/\mathrm{mm}$ in Figure B.4a. The same peak is visible for the modulo-2π phase in Figure B.4b. However, the zero-frequency is filtered out, and also noise at higher frequencies is reduced. For larger filtering windows, the harmonics of the interference fringes are visible as well at $1.5 \cdot f = 2.52/\mathrm{mm}$ and at $2 \cdot f = 3.36/\mathrm{mm}$.
The unwrapping procedure results in a shift of all frequencies by $-f$. Now the information that was encoded in the interference fringes is shifted to the zero-frequency (Figure B.4c). For a filtering window with a FWHM of 2.1/mm, we already see a rise around a frequency of $1.5 \cdot f - f = 0.84/\mathrm{mm}$, which is a remainder of the interference fringes. For a larger filtering window of 2.8/mm, the peak

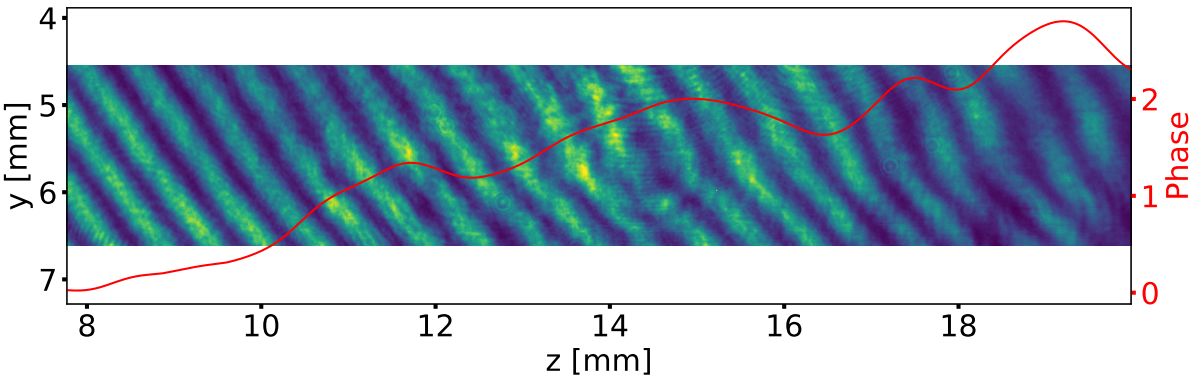

Figure B.5.: The raw image in the area of the plasma channel is shown with the resulting phase along the plasma channel plotted on top of it (filter of 10th-order Gaussian with FWHM of $1.4/\mathrm{mm}$).

is more pronounced. Using a filtering window with a FWHM of 1.4/mm, as was used for the analysis, seems to suppress this remainder sufficiently. However, noise in the raw image with a smaller frequency lies within the range of the frequencies in which the information on the plasma density is encoded. Therefore, it cannot be filtered out and cannot be discriminated from the information.
However, comparing the raw image with the phase profile can be an indication for certain features in the raw image resulting in peaks in the phase profile. In Figure B.5, the line-out of the phase is plotted on top of the area of the raw image that is used in the Abel inversion. Some interference features that result from dust or dirt on the optics of the probe setup are visible on the raw image and also the probe beam has interference fringes at its edge that are visible on the right side of the image. These features seem to correlate with the peaks in the phase profile, which is an indication that the inhomogeneity of the phase profile, i.e. the density profile, originates from noise on the interferometry image. At the same conditions, several shots were taken, which all reproduce the same peaks in the profile (cf. Figure 5.7a, where the mean of four shots and the std is shown).
However, the correlation between density peaks and features in the raw image is not as easily visible on other experiment days. For example, the interferometry images analyzed for 'experiment 1' (cf. Figure 5.2b) show less noise, and still, some peaks are visible on the analyzed phase profiles (cf. Figure 5.2a). On the other hand, they are also reproduced for all shots, which supports the assumption that they are caused by dirt on probe optics and are, therefore, present for all shots.
For future experiments, the probe optics should be as clean as possible to avoid features on the images caused by dirt. This will facilitate the measurement of real inhomogeneities. Then, measurements with 3D-printed nozzles can be compared to nozzles made from stainless steel to investigate whether more real inhomogeneities are measured for the 3D-printed nozzles that have a higher inner surface roughness.

Bibliography

[1] P. A. M. Dirac. "The Quantum Theory of the Electron." In: *Proceedings of the Royal Society of London. Series A. Mathematical and Physical Sciences* 117.778 (1928), pp. 610–624. DOI: doi/10.1098/rspa.1928.0023.

[2] G. Breit and John A. Wheeler. "Collision of two light quanta." In: *Physical Review* 46.12 (1934), pp. 1087–1091. DOI: 10.1103/PhysRev.46.1087.

[3] F. C. Salgado et al. "Towards pair production in the non-perturbative regime." In: *New Journal of Physics* 23.10 (2021). DOI: 10.1088/1367-2630/ac2921.

[4] G. V. Dunne. "New strong-field QED effects at extreme light infrastructure: Nonperturbative vacuum pair production." In: *European Physical Journal D* 55 (2009), pp. 327–340. DOI: 10.1140/epjd/e2009-00022-0.

[5] Remo Ruffini, Gregory Vereshchagin, and She Sheng Xue. "Electron-positron pairs in physics and astrophysics: From heavy nuclei to black holes." In: *Physics Reports* 487 (2010). DOI: 10.1016/j.physrep.2009.10.004.

[6] Felipe Cezar Salgado. "Design of a Single-Particle Detection System for Strong-Field QED Experiments." PhD Thesis. Friedrich-Schiller-Universität Jena, 2023.

[7] S. W. Hawking and Simon F. Ross. "Pair production of black holes on cosmic strings." In: *Physical Review Letters* 75.19 (1995), pp. 3382–3385. DOI: 10.1103/PhysRevLett.75.3382.

[8] Jeremy S. Heyl and Lars Hernquist. "Nonlinear QED effects in strong-field magnetohydrodynamics." In: *Physical Review D - Particles, Fields, Gravitation and Cosmology* 59.4 (1999). DOI: 10.1103/PhysRevD.59.045005.

[9] A I Nikishov. "Absorption of High-Energy Photons in the Universe." In: *J. Exptl. Theoret. Phys. (U.S.S.R.)* 14.2 (1962), pp. 549–550.

[10] C. Bula et al. "Observation of nonlinear effects in compton scattering." In: *Physical Review Letters* 76.17 (1996), pp. 3116–3119. DOI: 10.1103/PhysRevLett.76.3116.

[11] D. L. Burke et al. "Positron production in multiphoton light-by-light scattering." In: *Physical Review Letters* 79.9 (1997), pp. 1626–1629. DOI: 10.1103/PhysRevLett.79.1626.

[12] Howard R. Reiss. "Absorption of light by light." In: *Journal of Mathematical Physics* 3.1 (1962), pp. 59–67. DOI: 10.1063/1.1703787.

[13] A. I. Nikishov and V. I. Ritus. "Quantum processes in the field of a plane electromagnetic wave and in a constant field. I." In: *Soviet Physics JETP* 19.2 (1964).

[14] Julian Schwinger. "On gauge invariance and vacuum polarization." In: *Physical Review* 82.5 (1951), pp. 664–679. DOI: 10.1103/PhysRev.82.664.

[15] Holger Gies, Felix Karbstein, and Leonhard Klar. "All-optical quantum vacuum signals in two-beam collisions." In: *Physical Review D* 106.11 (2022). DOI: 10.1103/PhysRevD.106.116005.

[16] R. P. Feynman. "Space-time approach to quantum electrodynamics." In: *Physical Review* 76.6 (1949), pp. 769–789. DOI: 10.1103/PhysRev.76.769.

[17] Alina Golub. "Strong-field Breit-Wheeler Pair creation in various physical scenarios." PhD Thesis. Heinrich-Heine-Universität Düsseldorf, 2022.

[18] W. H. Furry. "On bound states and scattering in positron theory." In: *Physical Review* 81.1 (1951), pp. 115–124. DOI: 10.1103/PhysRev.81.115.

[19] Holger Gies and Jobst Ziebell. "Asymptotically safe QED." In: *European Physical Journal C* 80.7 (2020). DOI: 10.1140/epjc/s10052-020-8171-8.

[20] H. Abramowicz et al. "Conceptual design report for the LUXE experiment." In: *European Physical Journal: Special Topics* 230.11 (2021), pp. 2445–2560. DOI: 10.1140/epjs/s11734-021-00249-z.

[21] V. I. Ritus. "Quantum effects of the interaction of elementary particles with an intense electromagnetic field." In: *Journal of Soviet Laser Research* 6.5 (1985), pp. 497–617. DOI: 10.1007/BF01120220.

[22] Holger Gies and Klaus Klingmüller. "Pair production in inhomogeneous fields." In: *Physical Review D - Particles, Fields, Gravitation and Cosmology* 72.6 (2005). DOI: 10.1103/PhysRevD.72.065001.

[23] *DFG Research Unit FOR2783 - Probing the Quantum Vacuum at the High-Intensity Frontier*. URL: www.quantumvacuum.org (visited on 12/22/2023).

[24] F. C. Salgado et al. "Single particle detection system for strong-field QED experiments." In: *New Journal of Physics* 24.1 (2022). DOI: 10.1088/1367-2630/ac4283.

[25] T. G. Blackburn and M. Marklund. "Nonlinear Breit-Wheeler pair creation with bremsstrahlung γ rays." In: *Plasma Physics and Controlled Fusion* 60.5 (2018). DOI: 10.1088/1361-6587/aab3b4.

[26] T. Tajima and J. M. Dawson. "Laser electron accelerator." In: *Physical Review Letters* 43.4 (1979), pp. 267–270. DOI: 10.1103/PhysRevLett.43.267.

[27] Donna Strickland and Gerard Mourou. "Compression of amplified chirped optical pulses." In: *Optics Communications* 56.3 (1985), pp. 219–221. DOI: 10.1016/0030-4018(85)90120-8.

[28] Nobel Committee for Physics. *Groundbreaking inventions in laser physics*. 2018. URL: https://www.nobelprize.org/uploads/2018/10/advanced-physicsprize2018.pdf.

[29] P.M. Paul et al. "Observation of a Train of Attosecond Pulses from High Harmonic Generation." In: *Science* 292.5522 (2001), pp. 1689–1692. DOI: 10.1126/science.1059413.

[30] M. Hentschel et al. "Attosecond metrology." In: *Nature* 414.6863 (2001), pp. 509–513. DOI: 10.1038/35107000.

[31] Nobel Committee For Physics. *Experimental methods that generate attosecond pulses of light for the study of electron dynamics in matter*. 2023. URL: https://www.nobelprize.org/uploads/2023/10/advanced-physicsprize2023-2.pdf.

[32] W. D. Kilpatrick. "Criterion for vacuum sparking designed to include both rf and dc." In: *Review of Scientific Instruments* 28.10 (1957), pp. 824–826. DOI: 10.1063/1.1715731.

[33] C. E. Clayton et al. "Self-guided laser wakefield acceleration beyond 1 GeV using ionization-induced injection." In: *Physical Review Letters* 105.10 (2010). DOI: 10.1103/PhysRevLett.105.105003.

[34] Xiaoming Wang et al. "Quasi-monoenergetic laser-plasma acceleration of electrons to 2 GeV." In: *Nature Communications* 4 (2013). DOI: 10.1038/ncomms2988.

[35] M. Mirzaie et al. "Demonstration of self-truncated ionization injection for GeV electron beams." In: *Scientific Reports* 5 (2015). DOI: 10.1038/srep14659.

[36] F. Zimmermann et al. "Challenges for highest energy circular colliders." In: *IPAC 2014: Proceedings of the 5th International Particle Accelerator Conference* (2014). DOI: 10.18429/JACoW-IPAC2014-MOXAA01.

[37] M Aicheler et al. *A Multi-TeV Linear Collider Based on CLIC Technology*. Tech. rep. Geneva: CERN, 2012. DOI: 10.5170/CERN-2012-007.

[38] "Proceedings of the 2019 CERN-Accelerator-School course on High Gradient Wakefield Accelerators." In: Sesimbra (Portugal), 2020. URL: https://cas.web.cern.ch/previous-schools.

[39] Peter W. Higgs. "Broken symmetries and the masses of gauge bosons." In: *Physical Review Letters* 13.16 (1964), pp. 508–509. DOI: 10.1103/PhysRevLett.13.508.

[40] ATLAS Collaboration. "Observation of a new particle in the search for the Standard Model Higgs boson with the ATLAS detector at the LHC." In: *Physics Letters, Section B: Nuclear, Elementary Particle and High-Energy Physics* 716 (2012). DOI: 10.1016/j.physletb.2012.08.020.

[41] A. J. Gonsalves et al. "Petawatt Laser Guiding and Electron Beam Acceleration to 8 GeV in a Laser-Heated Capillary Discharge Waveguide." In: *Physical Review Letters* 122.8 (2019). DOI: 10.1103/PhysRevLett.122.084801.

[42] Wentao Wang et al. "Free-electron lasing at 27 nanometres based on a laser wakefield accelerator." In: *Nature* 595 (2021), pp. 516–520. DOI: 10.1038/s41586-021-03678-x.

[43] Andreas R Maier et al. "Decoding Sources of Energy Variability in a Laser-Plasma Accelerator." In: *Physical Review X* 10.3 (2020). DOI: 10.1103/PhysRevX.10.031039.

[44] Wim Leemans and Eric Esarey. "Laser-driven plasma-wave electron accelerators." In: *Physics Today* 62.3 (2009), pp. 44–49. DOI: 10.1063/1.3099645.

[45] O. Lundh et al. "Few femtosecond, few kiloampere electron bunch produced by a laser-plasma accelerator." In: *Nature Physics* 7.3 (2011), pp. 219–222. DOI: 10.1038/nphys1872.

[46] P. Catravas, E. Esarey, and W. P. Leemans. "Femtosecond x-rays from Thomson scattering using laser wakefield accelerators." In: *Measurement Science and Technology* 12.11 (2001), pp. 1828–1834. DOI: 10.1088/0957-0233/12/11/310.

[47] E. Esarey et al. "Synchrotron radiation from electron beams in plasma-focusing channels." In: *Physical Review E - Statistical Physics, Plasmas, Fluids, and Related Interdisciplinary Topics* 65.5 (2002). DOI: 10.1103/PhysRevE.65.056505.

[48] W. P. Leemans et al. "Observation of Terahertz Emission from a Laser-Plasma Accelerated Electron Bunch Crossing a Plasma-Vacuum Boundary." In: *Physical Review Letters* 91.7 (2003). DOI: 10.1103/PhysRevLett.91.074802.

[49] Félicie Albert and Alec G.R. Thomas. "Applications of laser wakefield accelerator-based light sources." In: *Plasma Physics and Controlled Fusion* 58.10 (2016). DOI: 10.1088/0741-3335/58/10/103001.

[50] S. Kneip et al. "X-ray phase contrast imaging of biological specimens with femtosecond pulses of betatron radiation from a compact laser plasma wakefield accelerator." In: *Applied Physics Letters* 99.9 (2011). DOI: 10.1063/1.3627216.

[51] J. Wenz et al. “Quantitative X-ray phase-contrast microtomography from a compact laser-driven betatron source.” In: *Nature Communications* 6 (2015). DOI: 10.1038/ncomms8568.

[52] K. Ta Phuoc et al. “All-optical Compton gamma-ray source.” In: *Nature Photonics* 6.5 (2012), pp. 308–311. DOI: 10.1038/nphoton.2012.82.

[53] Y. Glinec et al. “High-resolution γ-ray radiography produced by a laser-plasma driven electron source.” In: *Physical Review Letters* 94.2 (2005). DOI: 10.1103/PhysRevLett.94.025003.

[54] S. A. Reed et al. “Photonuclear fission with quasimonoenergetic electron beams from laser wakefields.” In: *Applied Physics Letters* 89.23 (2006). DOI: 10.1063/1.2400400.

[55] R. M. Deas et al. “A laser driven pulsed X-ray backscatter technique for enhanced penetrative imaging.” In: *Journal of X-Ray Science and Technology* 23 (2015), pp. 791–797. DOI: 10.3233/XST-150520.

[56] Klaus Sokolowski-Tinten et al. “Femtosecond x-ray measurement of coherent lattice vibrations near the lindemann stability limit.” In: *Nature* 422.6929 (2003), pp. 287–289. DOI: 10.1038/nature01490.

[57] Andreas Schropp et al. “Imaging Shock Waves in Diamond with Both High Temporal and Spatial Resolution at an XFEL.” In: *Scientific Reports* 5 (2015). DOI: 10.1038/srep11089.

[58] S. M. Durbin et al. “X-ray pump optical probe cross-correlation study of GaAs.” In: *Nature Photonics* 6.2 (2012), pp. 111–114. DOI: 10.1038/nphoton.2011.327.

[59] K. Ta Phuoc et al. “Demonstration of the ultrafast nature of laser produced betatron radiation.” In: *Physics of Plasmas* 14.8 (2007). DOI: 10.1063/1.2754624.

[60] *Light sources of the world*. URL: https://lightsources.org/lightsources-of-the-world/ (visited on 01/10/2024).

[61] Nanshun Huang et al. “Features and futures of X-ray free-electron lasers.” In: *Innovation* 2 (2021). DOI: 10.1016/j.xinn.2021.100097.

[62] P. Emma et al. “First lasing and operation of an ångstrom-wavelength free-electron laser.” In: *Nature Photonics* 4.9 (2010), pp. 641–647. DOI: 10.1038/nphoton.2010.176.

[63] Hitoshi Tanaka et al. “A compact X-ray free-electron laser emitting in the sub-ångström region.” In: *Nature Photonics* 6.8 (2012), pp. 540–544. DOI: 10.1038/nphoton.2012.141.

[64] Heung Sik Kang et al. "Hard X-ray free-electron laser with femtosecond-scale timing jitter." In: *Nature Photonics* 11.11 (2017), pp. 708–713. DOI: 10.1038/s41566-017-0029-8.

[65] Eduard Prat et al. "A compact and cost-effective hard X-ray free-electron laser driven by a high-brightness and low-energy electron beam." In: *Nature Photonics* 14.12 (2020), pp. 748–754. DOI: 10.1038/s41566-020-00712-8.

[66] W. Decking et al. "A MHz-repetition-rate hard X-ray free-electron laser driven by a superconducting linear accelerator." In: *Nature Photonics* 14.6 (2020), pp. 391–397. DOI: 10.1038/s41566-020-0607-z.

[67] N. S. Huang et al. "Physical design and FEL performance study for FeL-III beamline of shine." In: *Proceedings of the 39th International Free-Electron Laser Conference, FEL 2019* (2019), pp. 199–202. DOI: 10.18429/JACoW-FEL2019-TUP063.

[68] National Academies of Sciences, Engineering and Medicine. *Opportunities in Intense Ultrafast Lasers: Reaching for the Brightest Light.* Washington, DC: The National Academies Press., 2018.

[69] Colin N. Danson et al. "Petawatt and exawatt class lasers worldwide." In: *High Power Laser Science and Engineering* 7 (2019). DOI: 10.1017/hpl.2019.36.

[70] F. Albert et al. "Laser wakefield accelerator based light sources: Potential applications and requirements." In: *Plasma Physics and Controlled Fusion* 56.8 (2014). DOI: 10.1088/0741-3335/56/8/084015.

[71] Marie Labat et al. "Seeded free-electron laser driven by a compact laser plasma accelerator." In: *Nature Photonics* 17.February (2022). DOI: 10.1038/s41566-022-01104-w.

[72] B. Miao et al. "Multi-GeV Electron Bunches from an All-Optical Laser Wakefield Accelerator." In: *Physical Review X* 12.3 (2022). DOI: 10.1103/PhysRevX.12.031038.

[73] J. P. Couperus et al. "Demonstration of a beam loaded nanocoulomb-class laser wakefield accelerator." In: *Nature Communications* 8.1 (2017). DOI: 10.1038/s41467-017-00592-7.

[74] J. Götzfried et al. "Physics of High-Charge Electron Beams in Laser-Plasma Wakefields." In: *Physical Review X* 10.4 (2020). DOI: 10.1103/PhysRevX.10.041015.

[75] S. P.D. Mangles et al. "Monoenergetic beams of relativistic electrons from intense laser–plasma interactions." In: *Nature* 431 (2004), pp. 535–538. DOI: 10.1038/nature02939.

[76] C. G. R. Geddes et al. “High-quality electron beams from a laser wakefield accelerator using plasma-channel guiding.” In: *Nature* 431 (2004), pp. 538–541. DOI: 10.1038/nature02900.

[77] J. Faure et al. “A laser – plasma accelerator producing monoenergetic electron beams.” In: *Nature* 431 (2004), pp. 541–544. DOI: 10.1038/nature02963.

[78] S. Kneip et al. “Near-GeV acceleration of electrons by a nonlinear plasma wave driven by a self-guided laser pulse.” In: *Physical Review Letters* 103.3 (2009), pp. 8–11. DOI: 10.1103/PhysRevLett.103.035002.

[79] D. H. Froula et al. “Measurements of the critical power for self-injection of electrons in a laser wakefield accelerator.” In: *Physical Review Letters* 103.21 (2009). DOI: 10.1103/PhysRevLett.103.215006.

[80] A. Popp et al. “All-optical steering of laser-wakefield-accelerated electron beams.” In: *Physical Review Letters* 105.21 (2010). DOI: 10.1103/PhysRevLett.105.215001.

[81] Christopher M.S. Sears et al. “Emittance and divergence of laser wakefield accelerated electrons.” In: *Physical Review Special Topics - Accelerators and Beams* 13.9 (2010). DOI: 10.1103/PhysRevSTAB.13.092803.

[82] K. Schmid et al. “Density-transition based electron injector for laser driven wakefield accelerators.” In: *Physical Review Special Topics - Accelerators and Beams* 13.9 (2010). DOI: 10.1103/PhysRevSTAB.13.091301.

[83] C. McGuffey et al. “Ionization induced trapping in a laser wakefield accelerator.” In: *Physical Review Letters* 104.2 (2010). DOI: 10.1103/PhysRevLett.104.025004.

[84] T. P.A. Ibbotson et al. “Investigation of the role of plasma channels as waveguides for laser-wakefield accelerators.” In: *New Journal of Physics* 12 (2010). DOI: 10.1088/1367-2630/12/4/045008.

[85] A. J. Gonsalves et al. “Tunable laser plasma accelerator based on longitudinal density tailoring.” In: *Nature Physics* 7.11 (2011), pp. 862–866. DOI: 10.1038/nphys2071.

[86] J. S. Liu et al. “All-optical cascaded laser wakefield accelerator using ionization-induced injection.” In: *Physical Review Letters* 107.3 (2011). DOI: 10.1103/PhysRevLett.107.035001.

[87] W. P. Leemans et al. “GeV electron beams from a centimetre-scale accelerator.” In: *Nature Physics* 2.10 (2006), pp. 696–699. DOI: 10.1038/nphys418.

[88] B. B. Pollock et al. “Demonstration of a narrow energy spread, 0.5 GeV electron beam from a two-stage laser wakefield accelerator.” In: *Physical Review Letters* 107.4 (2011). DOI: 10.1103/PhysRevLett.107.045001.

[89] G. R. Plateau et al. "Low-emittance electron bunches from a laser-plasma accelerator measured using single-shot X-ray spectroscopy." In: *Physical Review Letters* 109.6 (2012). DOI: 10.1103/PhysRevLett.109.064802.

[90] S. Kneip et al. "Characterization of transverse beam emittance of electrons from a laser-plasma wakefield accelerator in the bubble regime using betatron x-ray radiation." In: *Physical Review Special Topics - Accelerators and Beams* 15.2 (2012). DOI: 10.1103/PhysRevSTAB.15.021302.

[91] P. Brijesh et al. "Tuning the electron energy by controlling the density perturbation position in laser plasma accelerators." In: *Physics of Plasmas* 19.6 (2012). DOI: 10.1063/1.4725421.

[92] R. Weingartner et al. "Ultralow emittance electron beams from a laser-wakefield accelerator." In: *Physical Review Special Topics - Accelerators and Beams* 15.11 (2012). DOI: 10.1103/PhysRevSTAB.15.111302.

[93] M. Z. Mo et al. "Quasimonoenergetic electron beams from laser wakefield acceleration in pure nitrogen." In: *Applied Physics Letters* 100.7 (2012). DOI: 10.1063/1.3685464.

[94] M. Z. Mo et al. "Generation of 500 MeV-1 GeV energy electrons from laser wakefield acceleration via ionization induced injection using CO2 mixed in He." In: *Applied Physics Letters* 102.13 (2013). DOI: 10.1063/1.4799280.

[95] P. A. Walker et al. "Investigation of GeV-scale electron acceleration in a gas-filled capillary discharge waveguide." In: *New Journal of Physics* 15 (2013). DOI: 10.1088/1367-2630/15/4/045024.

[96] S. Corde et al. "Femtosecond x rays from laser-plasma accelerators." In: *Reviews of Modern Physics* 85.1 (2013). DOI: 10.1103/RevModPhys.85.1.

[97] J. Faure et al. "Controlled injection and acceleration of electrons in plasma wakefields by colliding laser pulses." In: *Nature* 444 (2006), pp. 737–739. DOI: 10.1038/nature05393.

[98] Hyung Taek Kim et al. "Enhancement of electron energy to the multi-gev regime by a dual-stage laser-wakefield accelerator pumped by petawatt laser pulses." In: *Physical Review Letters* 111.16 (2013). DOI: 10.1103/PhysRevLett.111.165002.

[99] W. P. Leemans et al. "Multi-Gev electron beams from capillary-discharge-guided subpetawatt laser pulses in the self-trapping regime." In: *Physical Review Letters* 113.24 (2014). DOI: 10.1103/PhysRevLett.113.245002.

[100] G. Sarri et al. "Ultrahigh brilliance multi-MeV γ-ray beams from nonlinear relativistic thomson scattering." In: *Physical Review Letters* 113.22 (2014). DOI: 10.1103/PhysRevLett.113.224801.

[101] C. Thaury et al. “Shock assisted ionization injection in laser-plasma accelerators.” In: *Scientific Reports* 5 (2015). DOI: 10.1038/srep16310.

[102] K. Khrennikov et al. “Tunable all-optical quasimonochromatic Thomson X-ray source in the nonlinear regime.” In: *Physical Review Letters* 114.19 (2015). DOI: 10.1103/PhysRevLett.114.195003.

[103] Hyung Taek Kim et al. “Stable multi-GeV electron accelerator driven by waveform-controlled PW laser pulses.” In: *Scientific Reports* 7 (2017). DOI: 10.1038/s41598-017-09267-1.

[104] Hai En Tsai et al. “Control of quasi-monoenergetic electron beams from laser-plasma accelerators with adjustable shock density profile.” In: *Physics of Plasmas* 25.4 (2018). DOI: 10.1063/1.5023694.

[105] Changhai Yu et al. “Enhanced betatron radiation by steering a laser-driven plasma wakefield with a tilted shock front.” In: *Applied Physics Letters* 112.13 (2018). DOI: 10.1063/1.5019406.

[106] B. Hidding et al. “Generation of quasimonoenergetic electron bunches with 80-fs laser pulses.” In: *Physical Review Letters* 96.10 (2006). DOI: 10.1103/PhysRevLett.96.105004.

[107] D. Gustas et al. “High-charge relativistic electron bunches from a kHz laser-plasma accelerator.” In: *Physical Review Accelerators and Beams* 21.1 (2018). DOI: 10.1103/PhysRevAccelBeams.21.013401.

[108] Lintong Ke et al. “Optimization of electron beams based on plasma-density modulation in a laser-driven wakefield accelerator.” In: *Applied Sciences (Switzerland)* 11.6 (2021). DOI: 10.3390/app11062560.

[109] Zhiyong Qin et al. “Multi-GeV cascaded laser wakefield acceleration in a hybrid capillary discharge waveguide.” In: *New Journal of Physics* 24.7 (2022). DOI: 10.1088/1367-2630/ac81e2.

[110] F. M. Foerster et al. “Stable and High-Quality Electron Beams from Staged Laser and Plasma Wakefield Accelerators.” In: *Physical Review X* 12.4 (2022). DOI: 10.1103/physrevx.12.041016.

[111] Kosta Oubrerie et al. “Controlled acceleration of GeV electron beams in an all-optical plasma waveguide.” In: *Light: Science and Applications* 11.1 (2022). DOI: 10.1038/s41377-022-00862-0.

[112] Tomonao Hosokai et al. “Observation of strong correlation between quasi-monoenergetic electron beam generation by laser wakefield and laser guiding inside a preplasma cavity.” In: *Physical Review E - Statistical, Nonlinear, and Soft Matter Physics* 73.3 (2006). DOI: 10.1103/PhysRevE.73.036407.

[113] Driss Oumbarek Espinos et al. "Notable improvements on LWFA through precise laser wavefront tuning." In: *Scientific Reports* 13.1 (2023). DOI: 10.1038/s41598-023-45737-5.

[114] A. Picksley et al. "All-optical GeV electron bunch generation in a laser-plasma accelerator via truncated-channel injection." In: *Physical Review Letters* 131 (2023). DOI: 10.1103/PhysRevLett.131.245001.

[115] Calin Ioan Hojbota et al. "High-energy betatron source driven by a 4-PW laser with applications to non-destructive imaging." In: *European Physical Journal A* 59.10 (2023). DOI: 10.1140/epja/s10050-023-01159-5.

[116] S. Masuda et al. "Energy scaling of monoenergetic electron beams generated by the laser-driven plasma based accelerator." In: *Physics of Plasmas* 14.2 (2007). DOI: 10.1063/1.2434248.

[117] S. Karsch et al. "GeV-scale electron acceleration in a gas-filled capillary discharge waveguide." In: *New Journal of Physics* 9 (2007). DOI: 10.1088/1367-2630/9/11/415.

[118] J. Osterhoff et al. "Generation of stable, low-divergence electron beams by laser-wakefield acceleration in a steady-state-flow gas cell." In: *Physical Review Letters* 101.8 (2008). DOI: 10.1103/PhysRevLett.101.085002.

[119] Karl Schmid. "Supersonic Micro-Jets And Their Application to Few-Cycle Laser-Driven Electron Acceleration." PhD Thesis. 2009.

[120] A. Buck et al. "Shock-front injector for high-quality laser-plasma acceleration." In: *Physical Review Letters* 110.18 (2013). DOI: 10.1103/PhysRevLett.110.185006.

[121] J. D. Jackson. *Classical Electrodynamics*. 3rd. John Wileys Sons, Inc., 1999.

[122] H. J. Kull. *Laserphysik*. De Gruyter, 2014.

[123] R. Fitzpatrick. *Plasma Physics - An Introduction*. CRC Press, Taylor & Francis Group, 2015.

[124] W. L. Kruer. *The Physics of Laser Plasma Interactions*. CRC Press, Taylor & Francis Group, 2018.

[125] P. Gibbon. *Short Pulse Laser Interactions with Matter*. Press, Imperial College, 2007.

[126] L. V. Keldysh. "Ionization in the field of a strong electromagnetic wave." In: *Sov. Phys. JETP* 20.5 (1965).

[127] Claire Ellen Max, Jonathan Arons, and A. Bruce Langdon. "Self-modulation and self-focusing of electromagnetic waves in plasmas." In: *Physical Review Letters* 33.4 (1974), pp. 209–212. DOI: 10.1103/PhysRevLett.33.209.

[128] A G Litvak. "Finite-Amplitude Wave Beams in a Magnetoactive Plasma." In: *Soviet Physics JETP* 30.2 (1970), pp. 344–347.

[129] E. Esarey, C. B. Schroeder, and W. P. Leemans. "Physics of laser-driven plasma-based electron accelerators." In: *Reviews of Modern Physics* 81.3 (2009), pp. 1229–1285. DOI: 10.1103/RevModPhys.81.1229.

[130] G.-Z. Sun et al. "Self-focusing of short intense pulses in plasmas." In: *Physics of Fluids* 30.2 (1987). DOI: 10.1063/1.866349.

[131] A. Butler, D. J. Spence, and S. M. Hooker. "Guiding of High-Intensity Laser Pulses with a Hydrogen-Filled Capillary Discharge Waveguide." In: *Physical Review Letters* 89.18 (2002). DOI: 10.1103/PhysRevLett.89.185003.

[132] R. J. Shalloo et al. "Low-density hydrodynamic optical-field-ionized plasma channels generated with an axicon lens." In: *Physical Review Accelerators and Beams* 22.4 (2019). DOI: 10.1103/PhysRevAccelBeams.22.041302.

[133] L.M. Gorbunov and V.I. Kirsanov. "Excitation of plasma waves by an electromagnetic wave packet." In: *Sov. Phys. JETP* 66.2 (1987), pp. 290–294.

[134] P. Sprangle et al. "Laser wakefield acceleration and relativistic optical guiding." In: *Applied Physics Letters* 53.22 (1988), pp. 2146–2148. DOI: 10.1063/1.100300.

[135] P. Sprangle, E. Esarey, and A. Ting. "Nonlinear theory of intense laser-plasma interactions." In: *Physical Review Letters* 64.17 (1990), pp. 2011–2014. DOI: 10.1103/PhysRevLett.64.2011.

[136] V. I. Berezhiani and I. G. Murusidze. "Relativistic wake-field generation by an intense laser pulse in a plasma." In: *Physics Letters A* 148 (1990), pp. 338–340. DOI: 10.1016/0375-9601(90)90813-4.

[137] V. I. Berezhiani and I. G. Murusidze. "Interaction of highly relativistic short laser pulses with plasmas and nonlinear wake-field generation." In: *Physica Scripta* 45.2 (1992), pp. 87–90. DOI: 10.1088/0031-8949/45/2/007.

[138] D. Teychenné, G. Bonnaud, and J. L. Bobin. "Wave-breaking limit to the wake-field effect in an underdense plasma." In: *Physical Review E* 48.5 (1993), pp. 3248–3251. DOI: 10.1103/PhysRevE.48.R3248.

[139] A. Pukhov and J. Meyer-ter-Vehn. "Laser wake field acceleration: The highly non-linear broken-wave regime." In: *Applied Physics B: Lasers and Optics* 74 (2002), pp. 355–361. DOI: 10.1007/s003400200795.

[140] W. Lu et al. "Nonlinear theory for relativistic plasma wakefields in the blowout regime." In: *Physical Review Letters* 96.16 (2006). DOI: 10.1103/PhysRevLett.96.165002.

[141] W. Lu et al. "A nonlinear theory for multidimensional relativistic plasma wave wakefields." In: *Physics of Plasmas* 13.5 (2006). DOI: 10.1063/1.2203364.

[142] W. Lu et al. "Generating multi-GeV electron bunches using single stage laser wakefield acceleration in a 3D nonlinear regime." In: *Physical Review Special Topics - Accelerators and Beams* 10.6 (2007). DOI: 10.1103/PhysRevSTAB.10.061301.

[143] C. B. Schroeder et al. "Trapping, dark current, and wave breaking in nonlinear plasma waves." In: *Physics of Plasmas* 13.3 (2006). DOI: 10.1063/1.2173960.

[144] J. M. Dawson. "Nonlinear Electron Oscillations in a Cold Plasma." In: *Physical Review* 113.2 (1959), pp. 383–387.

[145] T. P. Coffey. "Breaking of large amplitude plasma oscillations." In: *Physics of Fluids* 14.7 (1971), pp. 1402–1406. DOI: 10.1063/1.1693620.

[146] S. V. Bulanov et al. "Transverse-wake wave breaking." In: *Physical Review Letters* 78.22 (1997). DOI: 10.1103/PhysRevLett.78.4205.

[147] S. Bulanov et al. "Particle injection into the wave acceleration phase due to nonlinear wake wave breaking." In: *Physical Review E - Statistical Physics, Plasmas, Fluids, and Related Interdisciplinary Topics* 58.5 (1998). DOI: 10.1103/PhysRevE.58.R5257.

[148] E. Oz et al. "Ionization-induced electron trapping in ultrarelativistic plasma wakes." In: *Physical Review Letters* 98.8 (2007). DOI: 10.1103/PhysRevLett.98.084801.

[149] M. Chen et al. "Theory of ionization-induced trapping in laser-plasma accelerators." In: *Physics of Plasmas* 19.3 (2012). DOI: 10.1063/1.3689922.

[150] D. Umstadter, J. K. Kim, and E. Dodd. "Laser injection of ultrashort electron pulses into wakefield plasma waves." In: *Physical Review Letters* 76.12 (1996), pp. 2073–2076. DOI: 10.1103/PhysRevLett.76.2073.

[151] G. Fubiani et al. "Beat wave injection of electrons into plasma waves using two interfering laser pulses." In: *Physical Review E - Statistical Physics, Plasmas, Fluids, and Related Interdisciplinary Topics* 70.1 (2004). DOI: 10.1103/PhysRevE.70.016402.

[152] C. D. Decker et al. "The evolution of ultra-intense, short-pulse lasers in underdense plasmas." In: *Physics of Plasmas* 3.5 (1996), pp. 2047–2056. DOI: 10.1063/1.872001.

[153] C. G. Durfee and H. M. Milchberg. "Light pipe for high intensity laser pulses." In: *Physical Review Letters* 71.15 (1993), pp. 2409–2412. DOI: 10.1103/PhysRevLett.71.2409.

[154] R. J. Shalloo et al. “Hydrodynamic optical-field-ionized plasma channels.” In: *Physical Review E* 97.5 (2018). DOI: 10.1103/PhysRevE.97.053203.

[155] D. J. Spence and S. M. Hooker. “Investigation of a hydrogen plasma waveguide.” In: *Physical Review E - Statistical, Nonlinear, and Soft Matter Physics* 63 (2001). DOI: 10.1103/PhysRevE.63.015401.

[156] Pierre Tournois. “Acousto-optic programmable dispersive filter for adaptive compensation of group delay time dispersion in laser systems.” In: *Optics Communications* 140 (1997), pp. 245–249. DOI: 10.1016/S0030-4018(97)00153-3.

[157] T. Oksenhendler et al. “Intracavity acousto-optic programmable gain control for ultra-wide-band regenerative amplifiers.” In: *Applied Physics B: Lasers and Optics* 83.4 (2006), pp. 491–494. DOI: 10.1007/s00340-006-2231-0.

[158] J. C. Chanteloup. “Multiple-wave lateral shearing interferometry for wavefront sensing.” In: *Applied Optics* 44.9 (2005), pp. 1559–1571. DOI: 10.1364/AO.44.001559.

[159] T. Oksenhendler et al. “Self-referenced spectral interferometry.” In: *Applied Physics B: Lasers and Optics* 99 (2010), pp. 7–12. DOI: 10.1007/s00340-010-3916-y.

[160] Patrick O’Shea et al. “Highly simplified device for ultrashort-pulse measurement.” In: *Optics Letters* 26.12 (2001). DOI: 10.1364/ol.26.000932.

[161] Leonard Doyle. “Implementation of an Adaptive Optics System for Focus Optimization at the Centre for Advanced Laser Applications.” Master Thesis. LMU München, 2019.

[162] E. Hecht. *Optik*. 5th Editio. De Gruyter, 2016.

[163] O. Kononenko et al. “2D hydrodynamic simulations of a variable length gas target for density down-ramp injection of electrons into a laser wakefield accelerator.” In: *Nuclear Instruments and Methods in Physics Research, Section A: Accelerators, Spectrometers, Detectors and Associated Equipment* 829 (2016), pp. 125–129. DOI: 10.1016/j.nima.2016.03.104.

[164] F.W. White. *Fluid Mechanics*. McGraw-Hill, 1990.

[165] Mathias Hüther. “Design and Characterisation of Supersonic Nozzles for Shock Front Electron Injection in Laser Wakefield Acceleration.” Master Thesis. LMU München, 2015.

[166] Emilien Guillaume. “Control of electron injection and acceleration in Laser-Wakefield Accelerators.” PhD Thesis. Université Paris-Saclay, 2015.

[167] ANSYS FLUENT 13 User’s Guide. “Ansys Fluent Theory Guide.” In: *ANSYS Inc., USA* (2013).

[168] K Grafenstein et al. "Laser - accelerated electron beams at 1 GeV using optically - induced shock injection." In: *Scientific Reports* 13 (2023). DOI: 10.1038/s41598-023-38805-3.

[169] Akihiro Sasoh. *Compressible Fluid Dynamics and Shock Waves*. Springer Nature Singapore, 2020.

[170] Georges Nomarski. "A double-shear differential interferometer using birefringent beamsplitter." In: *Japanese Journal of Applied Physics* 14 (1975), pp. 363–368. DOI: 10.7567/JJAPS.14S1.363.

[171] R. Benattar, C. Popovics, and R. Sigel. "Polarized light interferometer for laser fusion studies." In: *Review of Scientific Instruments* 50.12 (1979), pp. 1583–1586. DOI: 10.1063/1.1135764.

[172] H. Ding. "LWFA Diagnostics Development for ATLAS-300 and Nonlinear Plasma Wavelength Scalings." PhD Thesis. 2021.

[173] *IDEA - Interferometric Data Evaluation Algorithms*. URL: https://optics.tu-graz.ac.at/idea/idea.html (visited on 08/06/2024).

[174] *Python Numpy IFFT*. URL: https://numpy.org/doc/stable/reference/generated/numpy.fft.ifft.html (visited on 06/08/2024).

[175] Antonio Baldi, Filippo Bertolino, and Francesco Ginesu. "Phase Unwrapping Algorithms: A Comparison." In: *Interferometry in Speckle Light*. Ed. by P. Jacquot and J.-M. Fournier. Springer Berlin Heidelberg, 2000, pp. 483–490.

[176] *Python Phase Unwrapping*. URL: https://scikit-image.org/docs/stable/api/skimage.restoration.html#skimage.restoration.unwrap_phase (visited on 06/08/2024).

[177] Katinka v. Grafenstein. "Characterisation and Compensation of the Effects of Refractive Index Fluctuations in Interferometric Applications." Master Thesis. 2019.

[178] Eric W. Hansen and Phaih-Lan Law. "Recursive methods for computing the Abel transform and its inverse." In: *Journal of the Optical Society of America A* 2.4 (1985), p. 510. DOI: 10.1364/josaa.2.000510.

[179] *Hansen-Law Abel inversion method*. URL: https://pyabel.readthedocs.io/en/latest/transform_methods/hansenlaw.html (visited on 06/09/2024).

[180] P. B. Corkum, N. H. Burnett, and F. Brunel. "Above-threshold ionization in the long-wavelength limit." In: *Physical Review Letters* 62.11 (1989), pp. 1259–1262. DOI: 10.1103/PhysRevLett.62.1259.

[181] G. Taylor. "The formation of a blast wave by a very intense explosion." In: *Proceedings of the Royal Society of London. Series A. Mathematical and Physical Sciences* 201.1065 (1950), pp. 175–186. DOI: 10.1098/rspa.1950.0050.

[182] J. U. Kim, N. Hafz, and H. Suk. "Electron trapping and acceleration across a parabolic plasma density profile." In: *Physical Review E - Statistical, Nonlinear, and Soft Matter Physics* 69 (2004). DOI: 10.1103/PhysRevE.69.026409.

[183] J. Faure et al. "Injection and acceleration of quasimonoenergetic relativistic electron beams using density gradients at the edges of a plasma channel." In: *Physics of Plasmas* 17.8 (2010). DOI: 10.1063/1.3469581.

[184] S. Fourmaux et al. "Quasi-monoenergetic electron beams production in a sharp density transition." In: *Applied Physics Letters* 101.11 (2012). DOI: 10.1063/1.4752114.

[185] F. Massimo et al. "Numerical studies of density transition injection in laser wakefield acceleration." In: *Plasma Physics and Controlled Fusion* 59.8 (2017). DOI: 10.1088/1361-6587/aa717d.

[186] Max Gilljohann. "Towards Hybrid Wakefield Acceleration." PhD Thesis. 2021.

[187] Johannes Götzfried. "Beam Loading in High-Charge Laser Wakefield Accelerators." PhD Thesis. 2023.

[188] Thomas Kurz et al. "Calibration and cross-laboratory implementation of scintillating screens for electron bunch charge determination." In: *Review of Scientific Instruments* 89.9 (2018). DOI: 10.1063/1.5041755.

[189] K. Poder et al. "Experimental Signatures of the Quantum Nature of Radiation Reaction in the Field of an Ultraintense Laser." In: *Physical Review X* 8.3 (2018). DOI: 10.1103/PhysRevX.8.031004.

[190] A. Döpp et al. "Energy boost in laser wakefield accelerators using sharp density transitions." In: *Physics of Plasmas* 23.5 (2016). DOI: 10.1063/1.4946018.

[191] K. Schmid and L. Veisz. "Supersonic gas jets for laser-plasma experiments." In: *Review of Scientific Instruments* 83.5 (2012). DOI: 10.1063/1.4719915.

[192] S. M. Hooker et al. "GeV plasma accelerators driven in waveguides." In: *Plasma Physics and Controlled Fusion* 49 (2007). DOI: 10.1088/0741-3335/49/12B/S37.

[193] A. Picksley et al. "Guiding of high-intensity laser pulses in 100-mm-long hydrodynamic optical-field-ionized plasma channels." In: *Physical Review Accelerators and Beams* 23.8 (2020). DOI: 10.1103/PhysRevAccelBeams.23.081303.

[194] M. S. Bloom et al. "Bright X-ray radiation from plasma bubbles in an evolving laser wakefield accelerator." In: *Physical Review Accelerators and Beams* 23.6 (2020). DOI: 10.1103/PhysRevAccelBeams.23.061301.

[195] C. T. Hsieh et al. "Tomography of injection and acceleration of monoenergetic electrons in a laser-wakefield accelerator." In: *Physical Review Letters* 96.9 (2006). DOI: 10.1103/PhysRevLett.96.095001.

[196] S. P.D. Mangles et al. "On the stability of laser wakefield electron accelerators in the monoenergetic regime." In: *Physics of Plasmas* 14.5 (2007). DOI: 10.1063/1.2436481.

[197] T. Ohkubo et al. "Temporal characteristics of monoenergetic electron beams generated by the laser wakefield acceleration." In: *Physical Review Special Topics - Accelerators and Beams* 10.3 (2007). DOI: 10.1103/PhysRevSTAB.10.031301.

[198] T. P. Rowlands-Rees et al. "Laser-driven acceleration of electrons in a partially ionized plasma channel." In: *Physical Review Letters* 100.10 (2008). DOI: 10.1103/PhysRevLett.100.105005.

[199] Nasr A.M. Hafz et al. "Stable generation of GeV-class electron beams from self-guided laser-plasma channels." In: *Nature Photonics* 2.9 (2008), pp. 571–577. DOI: 10.1038/nphoton.2008.155.

[200] Michael Schnell et al. "Deducing the electron-beam diameter in a laser-plasma accelerator using x-ray betatron radiation." In: *Physical Review Letters* 108.7 (2012). DOI: 10.1103/PhysRevLett.108.075001.

[201] Eisuke Miura et al. "Demonstration of quasi-monoenergetic electron-beam generation in laser-driven plasma acceleration." In: *Applied Physics Letters* 86.25 (2005). DOI: 10.1063/1.1949289.

[202] N. D. Powers et al. "Quasi-monoenergetic and tunable X-rays from a laser-driven Compton light source." In: *Nature Photonics* 8.1 (2014), pp. 28–31. DOI: 10.1038/nphoton.2013.314.

[203] Michael Schnell et al. "Characterization and application of hard X-ray betatron radiation generated by relativistic electrons from a laser-wakefield accelerator." In: *Journal of Plasma Physics* 81.4 (2015). DOI: 10.1017/S0022377815000379.

[204] K. Huang et al. "Resonantly Enhanced Betatron Hard X-rays from Ionization Injected Electrons in a Laser Plasma Accelerator." In: *Scientific Reports* 6.June (2016). DOI: 10.1038/srep27633.

[205] C. I. Hojbota et al. "Accurate single-shot measurement technique for the spectral distribution of GeV electron beams from a laser wakefield accelerator." In: *AIP Advances* 9.8 (2019). DOI: 10.1063/1.5117311.

[206] Tae Gyu Pak et al. "Transverse X-ray radiation from petawatt-laser-driven electron acceleration in a gas cell." In: *Journal of the Korean Physical Society* 82.5 (2023), pp. 455–461. DOI: 10.1007/s40042-023-00730-z.

[207] S. P.D. Mangles et al. "Laser-wakefield acceleration of monoenergetic electron beams in the first plasma-wave period." In: *Physical Review Letters* 96.21 (2006). DOI: 10.1103/PhysRevLett.96.215001.

[208] M. Mori et al. "Transverse dynamics and energy tuning of fast electrons generated in sub-relativistic intensity laser pulse interaction with plasmas." In: *Physics Letters, Section A: General, Atomic and Solid State Physics* 356.2 (2006), pp. 146–151. DOI: 10.1016/j.physleta.2006.06.001.

[209] *2-dimensional discrete Fourier transform.* URL: https://numpy.org/doc/stable/reference/generated/numpy.fft.fft2.html (visited on 08/01/2024).

[210] *Fast Fourier transform shift.* URL: https://numpy.org/doc/stable/reference/generated/numpy.fft.fftshift.html (visited on 08/01/2024).

[211] *Finding local maxima.* URL: https://scikit-image.org/docs/stable/auto_examples/segmentation/plot_peak_local_max.html (visited on 08/01/2024).

[212] *Inverse fast Fourier transform shift.* URL: https://numpy.org/doc/stable/reference/generated/numpy.fft.ifftshift.html (visited on 08/01/2024).

[213] *Transformations.* URL: https://scikit-image.org/docs/stable/api/skimage.transform.html (visited on 08/01/2024).

Publications by the Author

- Salgado, F. C., **v. Grafenstein, K.**, Golub, A., Döpp, A., Eckey, A., Hollatz, D., Müller, C., Seidel, A., Seipt, D., Karsch, S., and Zepf, M. Towards pair production in the non-perturbative regime *New Journal of Physics* **23(10)** (2021).
- Foerster, F. M., Döpp, A., Haberstroh, F., **v. Grafenstein, K.**, Campbell, D., Chang, Y.-Y., Corde, S., Couperus Cabadağ, J. P., Debus, A., Gilljohann, M. F., Habib, A. F., Heinemann, T., Hidding, B., Irman, A., Irshad, F., Knetsch, A., Kononenko, O., Martinez de la Ossa, A., Nutter, A., Pausch, R., Schilling, G., Schletter, A., Schöbel, S., Schramm, U., Travac, E., Ufer, P., and Karsch, S. Stable and High-Quality Electron Beams from Staged Laser and Plasma Wakefield Accelerators *Physical Review X* **12(4)** (2022).
- **v. Grafenstein, K.**, Foerster, F. M., Haberstroh, F., Campbell, D., Irshad, F., Salgado, F. C., Schilling, G., Travac, E., Weiße, N., Zepf, M., Döpp, A., and Karsch, S. Laser-accelerated electron beams at 1 GeV using optically-induced shock injection *Scientific Reports* **13** (2023).
- Irshad, F., Eberle, C., Foerster, F. M., **v. Grafenstein, K.**, Haberstroh, F., Travac, E., Weiße, N., Karsch, S., and Döpp, A. Pareto optimization and tuning of a laser wakefield accelerator *Physical Review Letters* **133(8)** (2024).

Acknowledgements

First, I want to thank **Stefan Karsch**, who made this work possible. I am very grateful that you always found time to check in on us when we were doing experiments - no matter how late we started - and for your helpful insights.

I also want to thank **Ferenc Krausz** for the possibility of working at his chair, which provides an exceptional environment for scientific research.

Many thanks to **Andreas Döpp** who supported me with a lot of good advice and motivated me to finish up a paper and the thesis in good time. Likewise, I want to thank **Johannes Zirkelbach** for his support during the last year and his valuable comments on my thesis.

Special thanks go to **Gregor Schilling** for his constant support regarding all technical issues in ATLAS and ETTF and the countless times he turned on the laser for our experiments. I couldn't have done so many of them during my time without this help from you. I also want to thank **Andreas Münzer**, who stood in many times for Gregor when he couldn't be there.

I am so happy to have worked with so many great fellow PhD students during my time in the group. Many thanks to the ones who went the whole way with me: **Moritz Foerster**, **Florian Haberstroh**, **Enes Travac** and **Faran Irshad**. Spending so many hours with you during the experiment was a great pleasure. No matter how frustrating it could get, you were always there to make it fun. **Moritz** and **Flo**, you helped me so much in the lab, and I learned so much from you. **Enes**, you always made our office a fun place and never ceased to bring chocolate. **Faran**, I always enjoyed our great talks.

I also want to thank all colleagues who joined for a while or in the last few years: **Albert Schletter**, **David Campbell**, **Nils Weisse**, **Jinpu Lin**, **Bi Zewu** and many students. You all were or are still great additions to the group, and I enjoyed experiments, lunches, pub evenings, and gatherings with you very much.

I'm also grateful to the PhD-students of the last generation, especially **Max Gilljohann** and **Johannes Götzfried**, for explaining LWFA to me at the very beginning and for valuable tips for my time as a PhD student at CALA.

Special thanks go to **Felipe Salgado**, without whom the preparations for the

Breit-Wheeler experiment would not have been possible. Thank you very much for reviewing the parts of my thesis regarding the Breit-Wheeler experiment. Also, I always had a lot of fun when you visited CALA, and your motivation to get this complicated experiment running always inspired me.

The same can be said about **Matt Zepf**. Thank you for many great discussions about the Breit-Wheeler project with Stefan, Felipe and me, where you always stayed positive and proposed solutions for difficult obstacles.

Thanks to **Selym Villalba** for his helpful insights about QED theory.

I also want to thank **Jörg Schreiber**, **Peter Thierolf** and **Andreas Döpp** and their teams - **Leonard Doyle**, **Sonja Gerlach**, **Laura Geulig**, **Jannik Esslinger** and many more - for making the work at CALA so much fun and also for many lunch breaks and CALA user meetings.

Many thanks to **Martin Groß**, **Klaus Franke**, **Felix Rauscher** and **Katharina Adler** for their support and to **Hans-Friedrich Wirth**, **Oliver Gosau**, **Nik Gjotev** and **Florian Saran** for all the technical support in CALA. Thank you to **Johannes Wulz**, **Rolf Öhm**, and their teams for helping with many CAD designs and their fabrication.

Thanks to all the people of the IMPRS-APS for the nice meetings in Ringberg.

Und zum Schluss möchte ich mich bei denen bedanken, ohne die ich die Zeit als Doktorandin nicht durchgestanden hätte. Allen voran meinem Mann: **Basti**, du hast mich die ganzen fünf Jahre täglich mit Zuhören, Verständnis und Aufmuntern unterstützt. Ich bin dir unendlich dankbar dafür! Meinen **Freunden**, besonders meiner ehemaligen Mitbewohnerin **Johanna**, und meiner ganzen **Familie**, besonders meiner **Mutter**, gilt großer Dank, ihr seid immer für mich da!